Copper Zinc Tin Sulphide (Cu2ZnSnS4) Nanoparticle Ink Solar Cells

ALTOWAIRQI, YASIR,ABDULLAH,A

Copper Zinc Tin Sulphide (Cu_2ZnSnS_4) Nanoparticle Ink Solar Cells

Yasir Altowairqi

Physics Department

University of Durham

A thesis submitted in partial fulfilment of the requirements of the University of Durham for the Degree of Doctor of Philosophy (PhD)

2019

Declaration

I hereby declare that this thesis is a record of work undertaken by myself, that it has not been the subject of any previous application for a degree, and that all sources of information have been duly acknowledged.

* The rietveld refinement analysis in chapter 4 was done by Dr. Christopher Bosson.

* Deposit ZnO/ITO layers were done by Dr. Yongtao Qu.

Abstract

Cu_2ZnSnS_4 (CZTS) quaternary semiconductor compound has potential properties for low cost thin film solar cells. It is composed of abundant elements and non-toxic material, with desirable properties for thin film photovoltaic (PV) applications such as high absorption coefficient close to 10^{-4} cm^{-1} and a band gap close to 1.5 eV. CZTS has been successfully fabricated by non-vacuum hot injection methods with a pure sulphur source. High concentrations of CZTS nanoparticle inks were deposited onto clean glass by spin coating techniques to study the CZTS nanoparticle ink quality.

This thesis reports the study of the influence of fabrication conditions for CZTS including temperature and time on structure and optical properties. This reveals that these temperature conditions 185, 205, 225, 245 and 265 ^oC with reaction times of 0.5, 1.0, 1.5 and 2.0 hours have strong effects on CZTS properties. The nanoparticles were deposited onto glass by the spin coating method. We report measurements made by UV-VIS spectrophotometer, Scanning electron microscopy, TEM, X-ray diffraction, energy dispersive X-ray spectroscopy and Raman spectroscopy. The results confirm energy band gaps decreases with increasing reaction temperatures. For increasing reaction times from 0.5 to 2.0 h the energy band gap increases with increasing reaction time. X-ray diffraction and Raman spectroscopy were used to study the structure of CZTS nanoparticles and show the crystal structure improves with increasing reaction temperature and times. It is also observed from SEM and TEM measurements that the size of particles increases with increasing reaction conditions. CZTS nanoparticles of differing composition (stoichiometric, Cu-poor/rich and Zn-poor/rich) are prepared to investigate the impact of composition on the properties of the thin films. Films are characterised using X-ray diffraction, electron microscopy, Raman spectroscopy and photoluminescence spectroscopy. Cu-rich sample has Cu_2S secondary phases identified by a Raman peak at 475 cm^{-1}. The result confirmed that the band gaps depend on the copper and zinc content as well as the particle size. The implications for PV devices are discussed. The results confirm that the optimum conditions for synthesising high quality nanoparticles are 225 ^oC for 1.0 h. this results in nanoparticles of dimension 35 nm with band gap of 1.5 eV, which are Cu-poor and Zn-rich.

The effect of thin film annealing parameters including temperature, time, ramping rate and atmosphere on the structure and optical properties are studied. XRD, Raman Spectroscopy, SEM and EDX are used to analyse films and demonstrate that the crystallinity of CZTS and homogeneity of elements improves with annealing conditions. This is an important factor for

CZTS thin-film solar cells. The crystallinity, structure and chemical composition of CZTS thin film increased and improved under H_2S+N_2 atmosphere. It is concluded that annealing at 500 ^oC for 1 h with 10 ^oC/min under H_2S (20%) $+N_2$ (80%) atmosphere is a suitable condition for CZTS thin films used in solar cell devices.

CZTS solar cell devices which consist of substrate, back contact layer, followed by the main layer in this project; absorber layer, buffer layer, window layer, transparent oxide layer and grid layer were deposited as Mo foil/CZTS/ CdS/ i-ZnO/ ITO/ Al. Different thicknesses of CZTS layers were to study optical and electrical properties using Photoluminescence (PL) and I-V measurements. For PL measurements, the main peaks may correspond to CZTS in the range 1.35-1.55 eV. This study focused on the first four peaks, P1, P2, P3, and P4 at energies 1.38, 1.45, 1.55 and 1.63 eV for all samples. The most intense PL peak found at 1.55 eV is thought to be due to recombination of CZTS. The results confirm that all peaks have k-values less than 1. The values of k are in the range 0.75-0.92 $\pm$0.02 which are related with radiative transition involving defect states. The PL peak energy has a blue shift to higher energy with increasing excitation power. However, a small peak shifts in the range between 1.0 and 4.0 meV/decade is seen in all samples. PL results confirm radiative transitions from defect states with electronic levels which are influenced by fluctuating potentials. This limits solar device performance. SEM images of devices show some unexpected features at the interface between CZTS and other layers: CdS and ZnO. This is shown to impact I-V characteristics. Damage in the device layers leads to loss of current collection and more investigations identified the source of the damage. Cross section images show uniform CZTS layers in the majority of devices. EBSD cross sections are used to identify the quality of crystal and phase orientation in the layer.

Acknowledgements

I would like to express my special thanks of gratitude to my supervisor Dr. Douglas Halliday for his endless support during my PhD study, patience, assistance as well as valuable discussion and feedback. I would like also thank my co supervisor Dr Marek Szablewski for his encouragement, guidance, and valuable feedback.

I would like also to thank all people who provided help and training me to use many characterisation techniques here at Durham University, Dr Budhika Mendis for TEM training, Mr Leon Bowen for SEM, EDX and FIB training and help to improve images quality s and his support and valuable discussion, Dr Aidan Hindmarch for Mo sputtering training and Dr Fernando Dias. In addition, I am grateful to Prof. Andrew Beeby in chemistry department for allowing me to use the Raman facility in his labs. Also, I would like to thank Mr Gary Oswald for XRD training. Also, I thank Dr Chris Pearson for his help to setup I-V measurements.

Also, I would like to thank the technicians in physics department especially Mr Duncan McCallum and David Pattinson. Also, I express my thanks to all people in mechanical workshop for their help.

Also, I would like to thank Dr Sinan Azzawi, Dr Christopher Bosson, Mr Charles Swindells and Mr Ben Nicholson, Mr Ariam Mora-hernandez for their help to use sputter instruments. Also, I would like to thank Dr. Yongtao Qu for his help to deposit ZnO/ITO layers at Northumbria University.

I am also most grateful to my mother for her belief in me, her love, her patience and her constant prayers. Also, I thank my wife for her patience and support. I thank all my brothers, sisters and friends (you all know who I am talking about) for their great kindness and support throughout the tough times.

List of conferences and publications

1) The International Photovoltaic Science and Engineering *Conference (*PVSEC-26), *Singapore 2016,*

   Title: Optimisation of Cu_2ZnSnS_4 nanoparticles using hot injection method-structural and optical study.

2) Nanoparticle Characterisation – Challenges for the Community, Institute of Physics (IoP), London, UK, 2016.

   Title: Study the influence of different fabrication conditions (temperature and time) on optical and structure properties of Cu_2ZnSnS_4 nanoparticles fabricated by hot injection method.

3) North East Energy Materials Symposium (NEEM), Durham University, UK, 2017.

   Title: "Optical, electrical and structural measurements of Cu_2ZnSnS_4 (CZTS) nanoparticle thin films for solar cell devices.

4) Advanced Energy Materials conference (AEM2018), University of Surrey, Guildford, UK, 2018.

   Title: The effect of annealing conditions: temperature, time, ramping rate and atmosphere on nanocrystal Cu_2ZnSnS_4 (CZTS) thin film solar cell properties.

Table of Contents

Chapter 1: Introduction

1.1: Overview

Incident sunlight passes through the atmosphere and reaches the earth surface and releases light and heat. Some of this heat is reflected back toward space but other is absorbed by greenhouse gases; water vapour, CO_2, methane and nitrous oxide, which act as a thermal blanket absorbing heat and warming the surface to life supporting (15 ^{o}C) [1, 2]. On the other hand, human activities act to change the natural greenhouse balance. For instance, carbon dioxide is the primary cause for global warming which is produced from burning fossil fuels [3].

Global CO_2 emissions from fossil fuels and industry have increased every decade from an average of 3.1±0.2 GtC yr^{-1} in the 1960s to an average of 9.4±0.5 GtC yr^{-1}during 2007–2016. The growth rate in these emissions decreased between the 1960s and the 1990s, from 4.5%yr^{-1} to 1.8%yr^{-1} for the last decade (2007–2016) and to +0.4%yr^{-1} during 2014–2016. China's emissions increased by +3.8%yr^{-1} on average (+1.7 GtC yr^{-1} during the 10-year period) dominating the global trends, followed by India's emissions increasing by +5.8%yr^{-1} (+0.30 GtC yr^{-1}), while emissions decreased in EU28 by 2.2%yr^{-1} (-0.23 GtC yr^{-1}) and in the USA by 1.0%yr^{-1} (-0.19 GtC yr^{-1}) [4].

Fossil fuels including oil, natural gas and coal are still the most dominant source for energy in the world with consumption above 85 %. According to BP statistical review of world energy 2017, oil is still the first primary energy consumption which equal to 33 %, but it declined slightly in market share compared to two years of growth. Coal's market share fell to 27.6% which is the lowest level since 2004. Natural gas accounted for a record 23.4% of global primary energy consumption. However, the renewable energy (solar and wind) reached a new high of 3.6% by the end of 2017. However, the consumption of energy

sources in the world is shown in the Figure 1.1. This shows significant increased growth of the global renewable market in 2017 [5].

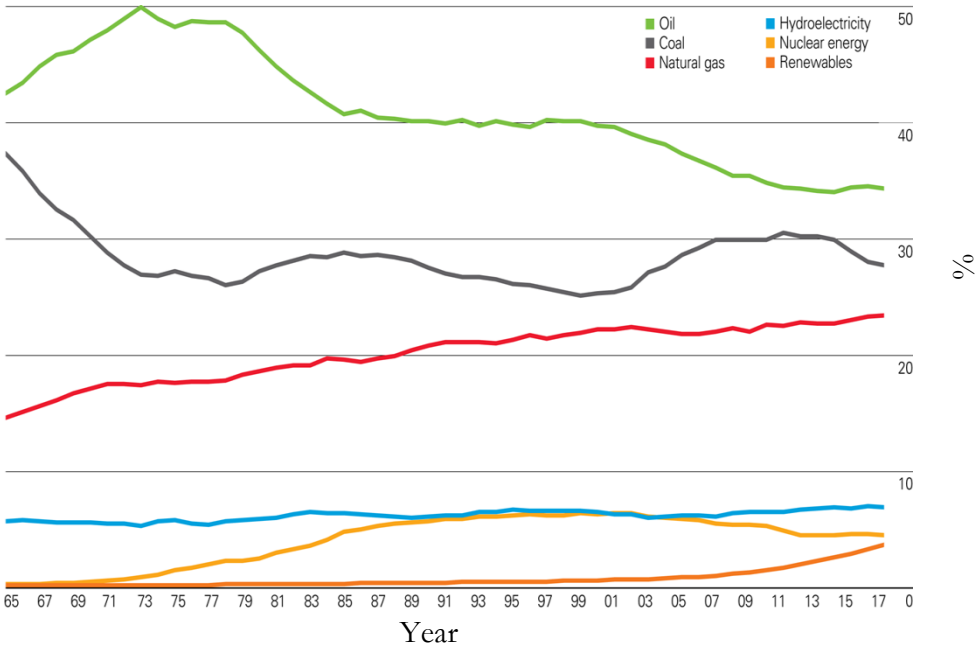

Figure 1.1 Shares of global primary energy consumption (Percentage), BP Statistical Review of World Energy 2017 [5].

Renewable energy resources have been given specific attention as alternative to fossil fuels such as hydropower, geothermal, wind, and solar which play an important role for reducing greenhouse emission, and using these resources leads to reduced fossil fuel. Moreover, renewable energy resources provide an optimal solution for the shortage of energy resources and for addressing the issue of climate change.

The total global solar power installation capacity in 2017 reached 99.1 GW which increased the accumulated global power capacity by 32% from 306.5 GW in 2016 to 404.5 GW by the end of 2017. Moreover, as shown in Figure 1.2, China is still dominant in the solar market and connected close to 52.8 GW to the grid in 2017 which increased the total capacity to 130.7 GW. United States has an annual installed capacity of 10.6 GW which fell from the record level to 14.8 GW in 2016. The third largest solar market is Japan which has an annual installation close to 8.6 GW in 2016 which continues to fall to 7.2 GW in 2017. However, the top 10 global solar photovoltaic markets with cumulative PV capacity shared

by the end of 2017, China still took over the first position of the world solar market. China owning around 33 % of the world power capacity, followed by USA which had installed capacity of 51.5 GW representing 13 %. Japan was the third of global capacity of 49.3 GW which will shrink further because decline of government support for solar [6, 7].

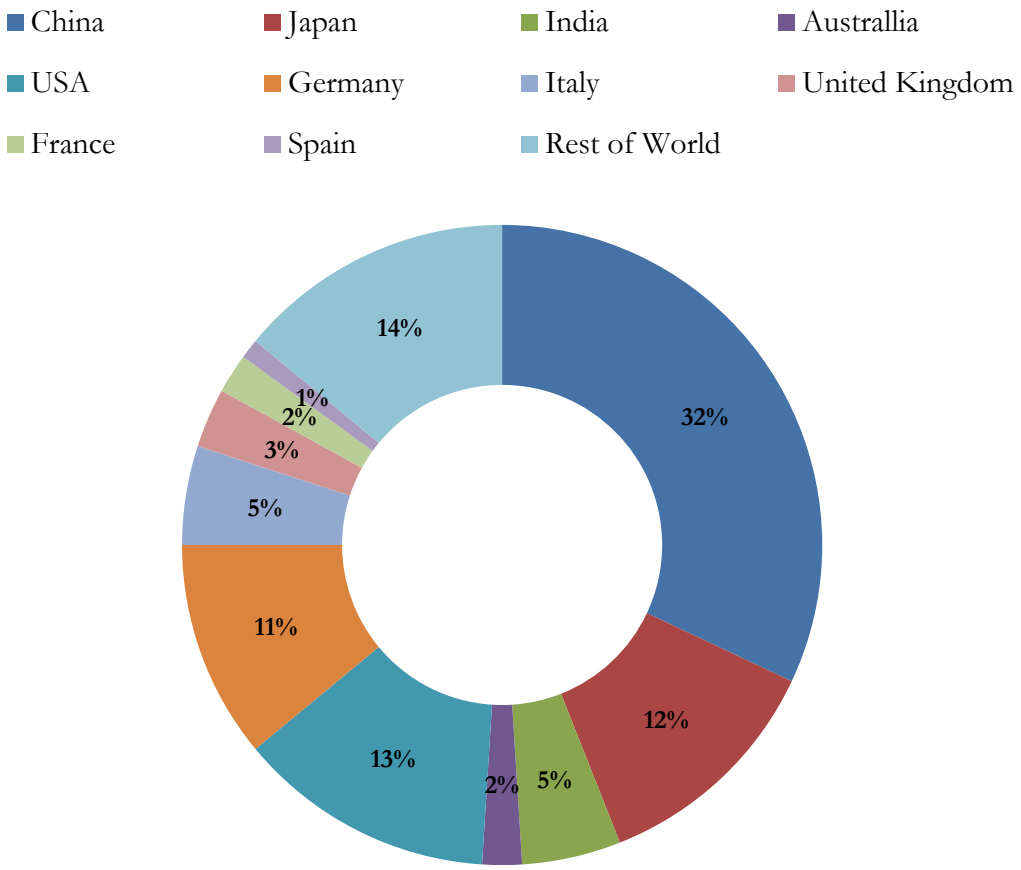

Figure 1.2 The top 10 global solar photovoltaic markets with cumulative PV capacity shared by the end of 2017 [6].

Fourth rank was Germany by 42.9 GW, equal to 11 %. Other countries shared the global capacity which exceeds 10 GW; Italy at 19.3 GW (5 %) and UK at 12.7 GW (3%), while India increase total capacity to 19.1 GW (5 %). Moreover, other countries sharing global capacity at less than 10 GW were France at 8 GW (2 %), Australia at 7.3 GW (2 %) and Spain at 5.6 GW (1 %)[6].

1.2: Element abundance and cost

Despite the fact that CIGS and CdTe have high efficiency in thin film solar cells, they still have some negative issues regarding abundance and cost. However, In, Se, Cd, and Te are less abundant elements as shown in Figure 1.3. It can be seen that the cost of In is the highest cost of materials used in thin film solar cell followed by Ga and Se. However, the most popular low-cost and abundant materials compared with other thin materials are Cu_2ZnSnS_4 (CZTS) thin film. CZTS is similar to CuInGaSe (CIGS), though it replaces Ga and In with nontoxic, abundant elements zinc and tin, more details on this are given in chapter 2. CZTS is a nontoxic material and composed of elements of high abundance in the Earth's crust.

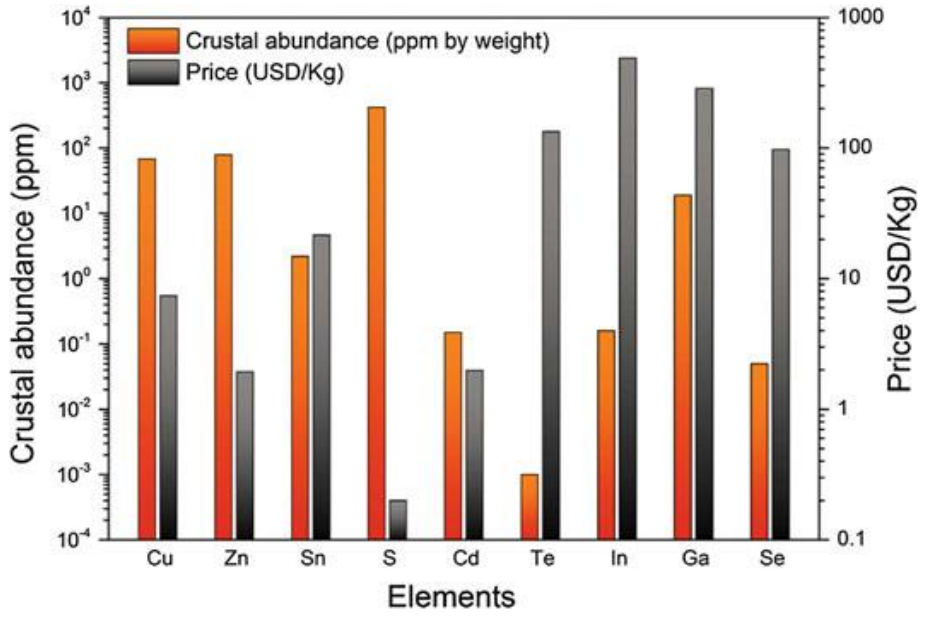

Figure 1.3 The abundance and price of different elements that used for synthesising thin film solar cells [8].

Each component of CZTS is abundant in the earth's crust (Cu: 68 ppm, Zn: 79 ppm, Sn: 2.2 ppm, S: 420 ppm) [9-11]. Moreover, copper, zinc, tin and sulphur are lower in cost compared to indium and other common PV materials as shown in Figure 1.3 [8].

1.3: Evaluation of efficiency of different solar cells materials

The Shockley-Queisser efficiency (SQ) limit [12] or detailed balance limit is a theoretical calculation of the efficiency of single absorber layer as a function of the semiconductor band gap. The Figure 1.4 shows the dependency of single layer efficiency of different semiconductor as a function of band gaps.

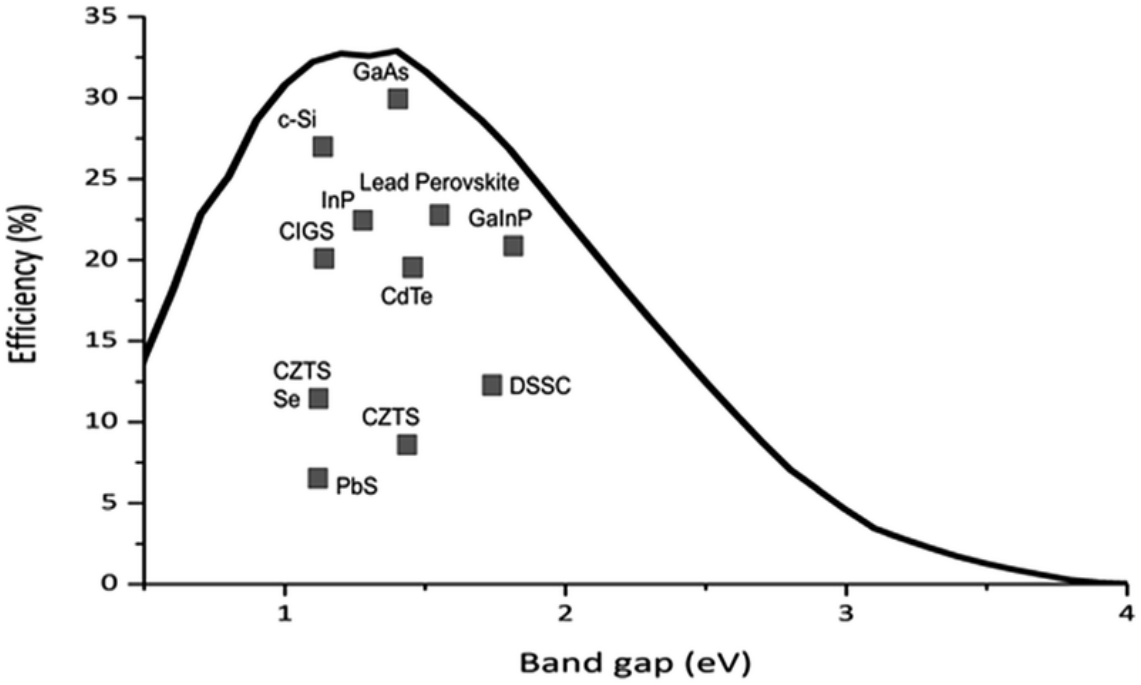

Figure 1.4 The Shockley-Queisser efficiency limit as a function of band gaps of some materials [13]. Line is theoretical limit, points indicate current record efficiencies of different solar devices

It can be seen that a band gap of absorber materials in the range 1.1 to 1.5 eV is required to achieve good photon conversion which results in a theoretical maximum efficiency of 32 % (V_{oc} and FF increase, and J_{sc} decreases with increasing band gap) under standard AM1.5G conditions [14]. However, according to the principle of detailed balance an electron and a hole which is created as a result of absorption of photon can recombine and emit a photon, this process can reduce and limit the efficiency of the cell. To overcome Shockley-Queisser limitations, multijunction tandem solar cell can be designed which achieve higher efficiency above SQ limit at 46 % [15] or by solar radiation concentrators [16] as shown in Figure 1.5.

The National Renewable Energy Laboratory (NREL) records and updates the record conversion efficiencies of various photovoltaic (PV) technologies such as multi-junction cells (concentrator and non-concentrator PV), single junction GaAs, crystalline Si cells, thin films technologies and emerging PV (dye sensitized, perovskite and organic solar cells) as shown in Figure 1.5. However, multi-junction concentrator solar cells are the most efficient solar cells technology with 46% efficiency, whereas non-concentrator solar cells with three and four junctions achieved efficiency close to 39%.

In addition, other technologies with concentrator single crystal technologies achieved a high efficiency compared with non-concentrator solar technologies but all single junction devices are still under the maximum theoretical conversion at 33% according to Shockley-Queisser limit [12].

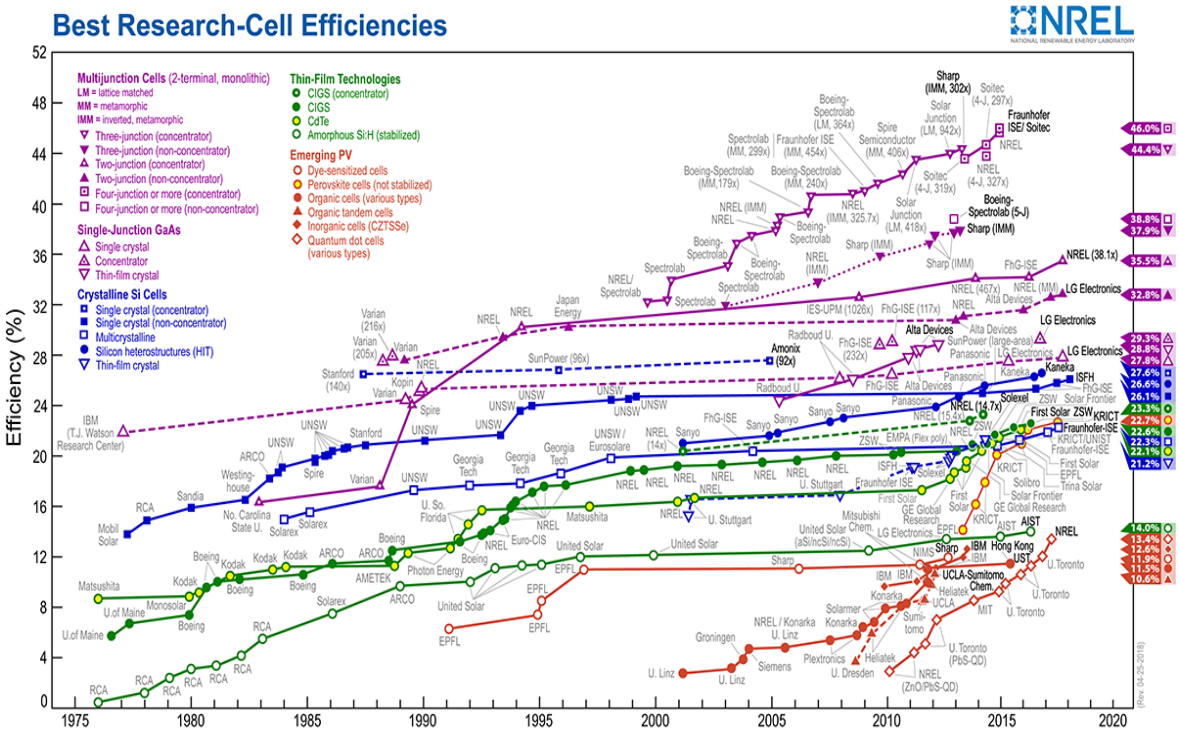

Figure 1.5 The solar cell efficiencies according to National Renewable Energy Laboratory (NREL) for different technologies: multijunction cells, single junction cells, thin film technologies and emerging PV [17].

However, other techniques are used to fabricate solar cells and give different efficiencies such as single silicon crystal ~ 20–27%[18]; despite the fact that crystalline silicon is widely available , relatively inexpensive and currently dominates the market, it has some limitations such as it requires thick layers, because it has a lower absorption cross section which will increase costs compared to amorphous silicon (a-Si) which has a higher absorption cross

section and low processing cost which has an efficiency close to 12.69 %[19]. Other thin film technologies have higher efficiency i.e. CdTe ~ 22.1% [20], CIGS ~21.0% [21]. In these materials rare elements such as indium, gallium and tellurium are used, also, some are toxic materials such as cadmium which leads to increase manufacturing cost. However, it is clear that the highest level of efficiency of CZTS was 11 %, which occurred when using co-sputtering methods [22, 23].

1.4: Aims

The aims of this work is to optimise the experimental process to synthesise CZTS nanoparticle inks by using the hot injection method and spin coating deposition techniques to produce thin films and to study the effect of different parameters such as temperature, time and composition on the CZTS properties, structure and optical properties. Also, to study the effect of annealing parameters on the CZTS properties. Lastly, to optimise the design of the cell architecture and study the device performance.

1.5: Structure of the thesis

Following this chapter the principle of solar cells physics and the literature reviews of the fundamentals of CZTS nanoparticles properties are presented. Chapter 3 describes the fabrication process of CZTS nanoparticles and films and the experimental techniques of materials synthesis and CZTS device fabrication and characterisation. Chapter 4 reports the synthesis and characterisation of CZTS under different fabrication conditions. Chapter 5 present the effect of different chemical composition on CZTS structure and optical properties. Chapter 6 describes the influence of annealing parameters on CZTS properties. Chapter 7 reports optimised design of the cell architecture and study of the device performance. Chapter 8 concludes the scientific findings of the thesis and proposes further work to be carried out.

1.6: References

1. *Climate Change 2014, Synthesis report and Summary for Policymakers, http://ipcc.ch/pdf/assessment-report/ar5/syr/AR5_SYR_FINAL_SPM.pdf.* [cited 11/04/2018].

2. *Global Climate Change, https://climate.nasa.gov/causes/*. [cited 26/4/2018].

3. Peters, G.P., et al., *Towards real-time verification of CO_2 emissions.* Nature Climate Change, 2017. **7**(12): p. 848-850.

4. Jackson, R.B., et al., *Warning signs for stabilizing global CO_2 emissions.* Environmental Research Letters, 2017. **12**(11).

5. *Statistical Review of World Energy, https://www.bp.com/content/dam/bp/en/corporate/pdf/energy-economics/statistical-review/bp-stats-review-2018-full-report.pdf* [cited 15/11/2018].

6. *Global Market Outlook for Solar Power/2018-2022, http://www.solarpowereurope.org/wp-content/uploads/2018/09/Global-Market-Outlook-2018-2022.pdf.* 2018 [cited 29/11/2018].

7. *Global Market Outlook for Solar Power/ 2017-2021, https://resources.solarbusinesshub.com/images/reports/172.pdf.* [cited 29/11/2018].

8. Das, S., K.C. Mandal, and R.N. Bhattacharya, *Earth-Abundant $Cu_2ZnSn(S,Se)_4$ (CZTSSe) Solar Cells*, in *Semiconductor Materials for Solar Photovoltaic Cells*, P.M. Paranthaman, W. Wong-Ng, and N.R. Bhattacharya, Editors. 2016, Springer International Publishing: Cham. p. 25-74.

9. Winter, M. *https://www.webelements.com/periodicity/abundance_crust/*. [cited 21/2/ 2018].

10. Katagiri, H., et al., *Characterization of Cu_2ZnSnS_4 thin films prepared by vapor phase sulfurization.* Japanese Journal of Applied Physics Part 1-Regular Papers Short Notes & Review Papers, 2001. **40**(2A): p. 500-504.

11. Mali, S.S., et al., *Novel synthesis of kesterite Cu_2ZnSnS_4 nanoflakes by successive ionic layer adsorption and reaction technique: Characterization and application.* Electrochimica Acta, 2012. **66**: p. 216-221.

12. Shockley, W. and H.J. Queisser, *Detailed Balance Limit of Efficiency of P-N Junction Solar Cells.* Journal of Applied Physics, 1961. **32**(3).

13. Matthews, P.D., et al., *Shining a light on transition metal chalcogenides for sustainable photovoltaics.* Chemical science, 2017. **8**(6): p. 4177-4187.

14. Hillhouse, H.W. and M.C. Beard, *Solar cells from colloidal nanocrystals: Fundamentals, materials, devices, and economics*. Current Opinion in Colloid & Interface Science, 2009. **14**(4): p. 245-259.

15. King, R., et al., *40% efficient metamorphic GaInP/ GaInAs/ Ge multijunction solar cells*. Applied physics letters, 2007. **90**(18): p. 183516.

16. Ross, R.T. and A.J. Nozik, *Efficiency of hot-carrier solar energy converters*. Journal of Applied Physics, 1982. **53**(5): p. 3813-3818.

17. *National Renewable Energy Laboratory (NREL), Research Cell Efficiency Records, https://www.nrel.gov/pv/assets/images/efficiency-chart.png*. 2018 [cited 10/7/2018].

18. Sukhatme, S., P & Nayak, J. K. , *Solar Energy: Principles of Thermal Collection and Storage*. 3 ed. 2008, New Delhi: Tata MCGRAW-HILL Publishing Company Limited.

19. Matsui, T., et al., *High-efficiency amorphous silicon solar cells: Impact of deposition rate on metastability*. Applied Physics Letters, 2015. **106**(5): p. 5.

20. First Solar. *First Solar sets world record for CdTe solar cell efficiency, http://investor.firstsolar.com/releases.cfm*. [cited 29/09/2014].

21. Jackson, P., et al., *Properties of Cu(In,Ga)Se_2 solar cells with new record efficiencies up to 21.7%*. Physica Status Solidi (RRL) – Rapid Research Letters, 2015. **9**(1): p. 28-31.

22. Yan, C., et al., *Cu_2ZnSnS_4 solar cells with over 10% power conversion efficiency enabled by heterojunction heat treatment*. Nature Energy, 2018. **3**(9): p. 764-772.

23. Green, M.A., et al., *Solar cell efficiency tables (version 51)*. Progress in Photovoltaics: Research and Applications, 2018. **26**(1): p. 3-12.

Chapter 2: Overview of principle physics of solar cells and literature review of Cu_2ZnSnS_4

2.1: The physics of solar cells

Solar cell devices are semiconductor devices that consist of a p-n junction that acts to convert sunlight (photons) into electrical energy. The process of the conversion of energy has many steps, such as light absorption, the excitation of the electrons from the ground state to the excited state to generate of hole-electron pairs (photogeneration). The presence of the electric field in depletion region between p-n junctions acts to separate free electrons and holes by moving them in opposite directions, which leads to these travelling through an external circuit creating a flow of electric current [1]. However, a single solar cell provides a small amount of voltage and current, it is required to connect many cells together as modules that further assemble into arrays.

2.1.1: Solar spectrum

Solar radiation consists of electromagnetic radiation that is emitted by the space. The spectrum of the solar radiation can be assumed as a black body emitted at 5800 K [2]. The amount of power incident on the earth per unit area and the spectral characteristics of sun light are important parameters for the study of solar cells. The effect of the atmosphere on the solar spectrum and the power incident density can be modelled by the air mass factor *AM*, which is defined as the path length which sun light takes through the Earth's atmosphere [3]. When the sun is at the angle with the zenith θ, the air mass is given as [4],

$$\text{Air Mass } (AM) = \frac{1}{\cos\theta} \qquad (2.1)$$

The amount of power density incident outside of the Earth's atmosphere is 1353 Wm^{-2}, which is called the solar constant. The standard solar spectra for space labelled as *AM0*, corresponds to the solar spectrum incident on the atmosphere, as shown in Figure 2.1.

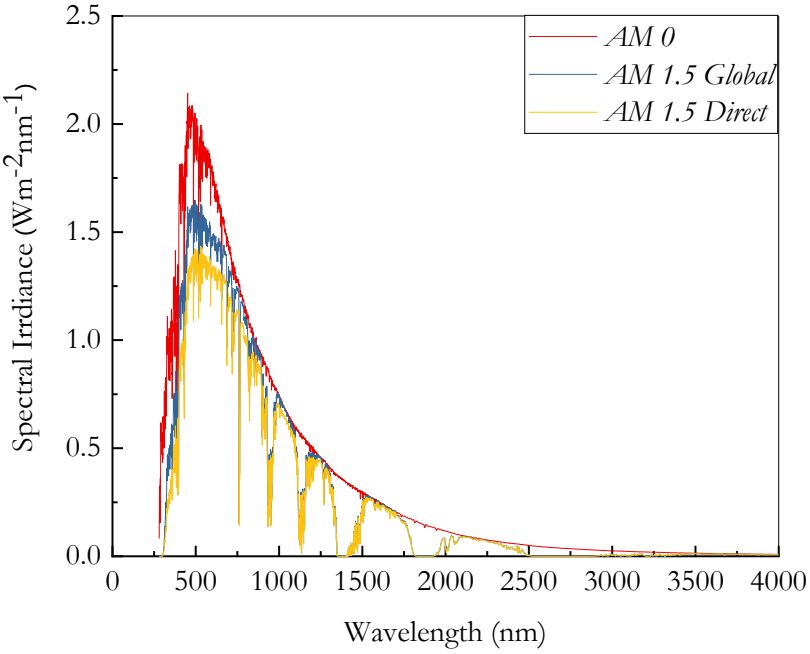

Figure 2.1 Solar cell spectra under AM0 and AM1.5 [5].

On the other hand, when the sun's spectrum reaches the Earth's atmosphere, it will experience some reflection, scattering and absorption by some elements and components of the atmosphere including main absorptions by H_2O, O_2, CO_2, and O_3. For the purpose of solar cell measurements, the average standard of the solar spectrum at AM1.5 is used $\theta = 48.19^{o}$. The standard spectrum at the Earth's surface is called *AM1.5G*, where, *G* stands for global and includes both direct and diffuse radiation or *AM1.5D*, which includes direct radiation only. Due to absorption and scattering of radiation, the intensity of *AM1.5D* radiation is lower than the *AM0* spectrum by 28%. Therefore, the global spectrum is 10% higher than the direct spectrum. These calculations give approximately 970 Wm^{-2} for *AM1.5G*. However, the standard *AM1.5G* spectrum has been normalized to give 1 kWm^{-2} due to the natural variations in incident solar radiation [6, 7].

2.1.2: Absorption of light

There are two kinds of semiconductor materials, which are defined according to their energy band gap: direct band gap semiconductors and indirect band gap semiconductors. However, in a direct band gap semiconductor, the maximum of the valence band and the minimum of the conduction band occur at the same value of the crystal momentum [8]. For any electronic transition to take place, the absorption conditions are purely based on the band gap of the material and the photon energy. The E-*k* diagram presents the direct and indirect band gap as shown in Figure 2.2 (a,b).

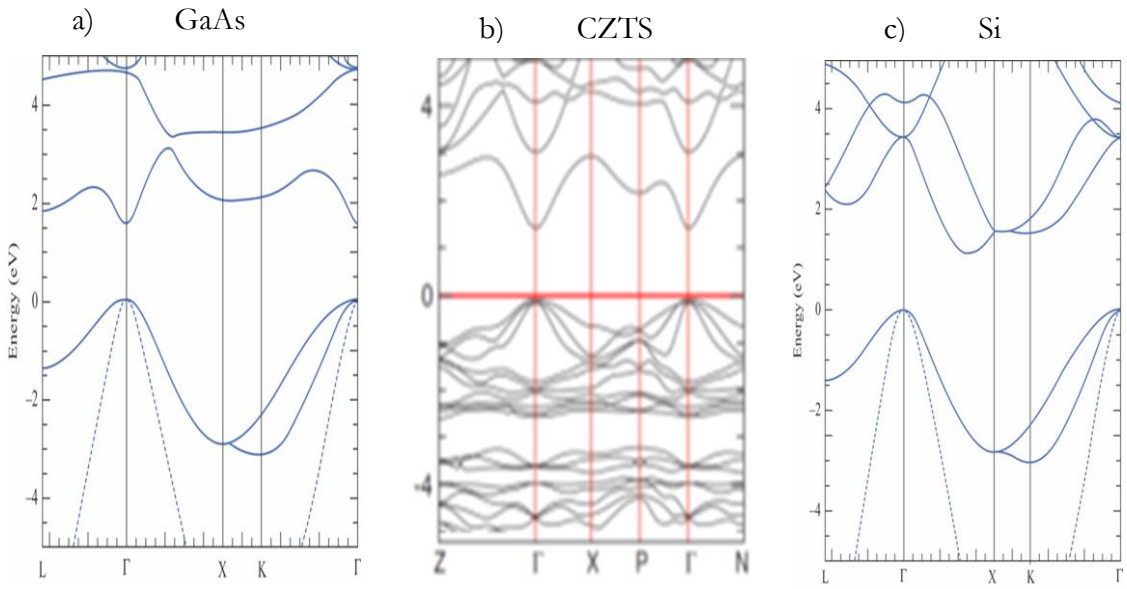

Figure 2.2 (a,b)Direct band gap of GaAs and CZTS and (c) indirect semiconductor band gap of Si [9].

In the direct band gap, the photon with energy hv gives rise to the excitation of an electron from the valence band (E_i) to the conduction band (E_f). The energy conservation is given by $E_f - E_i = hv$. Also, the momentum conservation is given by $\hbar k_i + \hbar k_{photon} = \hbar k_f$, where E_f and E_i are the electron energy at the final and initial states, respectively. Due to photons having a very small amount of momentum generally assumed to be zero; they can produce electron-hole pairs easily in a direct energy band gap. On the other hand, in an indirect band gap semiconductor, the minimum of conduction band energy and the maximum energy of the valence band occur at a different value of momentum. For any transition to take place, one needs a phonon, which can supply the crystal momentum equal to the

difference between the conduction band minimum and the valence band maximum, for example, silicon Si as shown in Figure 2.2 (c).

In an indirect band gap, the energy conservation is given by $E_f - E_i + E_{Phonon} = hv$ for emission and $E_f - E_i - E_{Phonon} = hv$ for absorption. Also, the momentum conservation is given by $\hbar k_f = \hbar k_i + \hbar k_{phonon}$, where E_f and E_i are the electron energy at the final and initial states, respectively as shown in Figure 2.2 c. However, the probability of absorption in the direct semiconductor band gap is higher than in the indirect semiconductor band gap. As a result the thickness of the direct semiconductor is lower than in the indirect band gap to give the same absorption [7].

2.1.3: Junctions in semiconductors

There are three kinds of junctions in semiconductor devices: metal (schottky and ohmic) junction, homojunction and heterojunction semiconductors, all of which are used in solar cell devices. The metal-semiconductor junction is created at the interface, and it depends on the work function (the energy between Fermi level and vacuum level) for both the metal and the semiconductor [10].

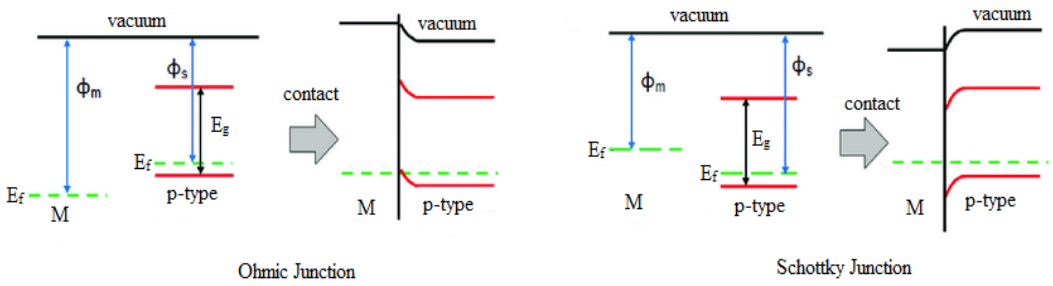

Figure 2.3 Ohmic and Schottky junctions for a p-type semiconductor before and after contact. Labels in the figure, M is metal, Ef is Fermi level, Eg is the energy bandgap, Φ_m is work function for metal and Φ_s is work function for semiconductor.

For the Schottky junction, when the metal comes into contact with the p-type semiconductor, the work function for metal is smaller than the work function of the semiconductor. Therefore, the holes diffuse to metal until the Fermi level is aligned, leaving behind the negatively charged acceptor atoms, and the depletion region is created in the

semiconductor region. In this case, the hole will face a barrier height which is called the Schottky barrier, which prevents them from crossing the junction. For the Ohmic junction, it is created when the work function of the metal is greater than the p-type semiconductor. Thus, the holes in the semiconductor will transport freely because they do not face any barrier as shown in Figure 2.3 [11, 12].

The homojunction semiconductor is created when the p-type and n-type semiconductors are made from the same material, whereas the heterojunctions are created when they are made from different materials with different energy band gaps. However, in the heterojunction, a barrier to transport (energy spike) between p-n junction is created, whereas it does not appear in the homojunction.

2.1.3.1: p-n under equilibrium

Generally, under equilibrium, when the p-type and n-type semiconductors are combined, different concentrations of charge carriers will occur. The electrons and holes diffuse across the junction; the electrons move to the p-type semiconductor and leave behind a positive charge in the n-type semiconductor and the holes will move to the n-type and leave behind a negative charge in the p-type semiconductor until the Fermi level is aligned. Thus, the electrical field is produced as a result of the junction formation, which acts to attract the charge carrier in an opposite direction to diffusion gradient.

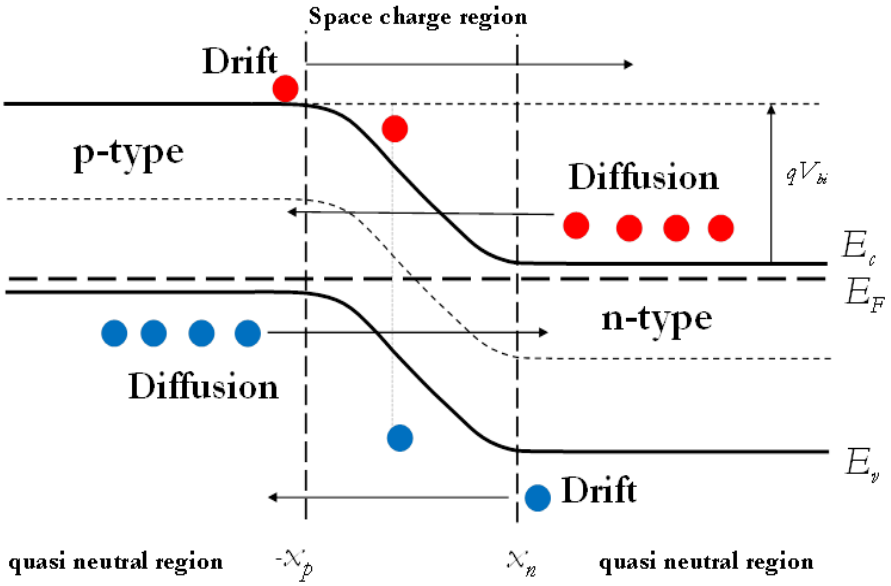

Figure 2.4 p n junction semiconductors.

The regions close to the junction become depleted of charge carriers, as shown in Figure 2.4. This region is also called the space charge region. The width of the depletion region depends on the built-in potential (which is a result of the differences between the Fermi energy levels of the p and n-types), the ionised acceptor N_A and the donor N_D concentration [8, 13].

The built in voltage can be given by the difference between the Fermi levels of both p-type and n-type sides as a result of diffusion process:

$$V_{bi} = \frac{kT}{q} \ln\left(\frac{N_A N_D}{n_i^2}\right) \tag{2.2}$$

$$n_i^2 = N_C N_V \exp\left(\frac{-E_g}{kT}\right) \tag{2.3}$$

For depletion region (space charge region) the width is given by:

$$W = x_n + x_p = \sqrt{\frac{2\varepsilon_o \varepsilon_r (V_{bi})}{q}\left(\frac{N_A + N_D}{N_A N_D}\right)} \tag{2.4}$$

Where W is the depletion width, ε is the dielectric constant, V_{bi} is the built-in potential and N_A and N_D are the doping concentration of acceptor and donor respectively, n_i^2 is the intrinsic concentration.

2.1.3.2: p-n junction under biases

2.1.3.2.1: Forward bias

When the p-n junction connects to an external voltage under forward bias, it connects the positive terminal to the p-side of the p-n junction and then connects the negative terminal to the n-side of the p-n junction, which now tends to decrease any potential barrier in the depletion region, causing its width to decrease. The positive terminal forces holes towards the junction, and the negative terminal forces electrons towards the junction. A current flows, the direction of the holes and the electrons' diffusion currents are from the p side to the n side, and the electrons' and holes' drift currents are from n side to the p-side (it is

unaffected). Therefore, the holes' and the electrons' diffusion current increases rapidly and exponentially when the applied voltage is increased [8], and the depletion width region is given by rewritten equation (2.4) as

$$W = \sqrt{\frac{2\varepsilon_o \varepsilon_r (V_{bi} - V)}{q} \left(\frac{N_A + N_D}{N_A N_D} \right)} \qquad (2.5)$$

2.1.3.2.2: Reverse bias

When the external voltage contacts are reversed, the polarity of the terminal of the voltage source is such that as it reinforces the electric field across the junction, the potential barrier across the junction increases, and the thickness of the depletion region also increases. The positive terminal pulls electrons in the n-type side away from the junction. The negative terminal pulls holes in the p-type side away from the junction. Therefore, the net junction current is only a drifting current from the p-side to n-side. Thus, the current flowing through the junction is called a reverse saturation current. The p-n junction is said to be reverse biased [8].

The theoretical equation that is used to describe the current–voltage relationship for the p-n junction is called the Shockley equation [14]. For real diode, the following equation is used:

$$J = J_S \left[\exp\left(\frac{qV}{Ak_B T} \right) - 1 \right] \qquad (2.6)$$

where J_S is the saturation current, A is the ideality factor, T is the absolute temperature, k_B is the Boltzmann constant, q is the electron charge and V is the voltage at the terminals of the cell. The ideality factor accounts for the recombination of the electrons and the holes in the depletion region, which tends to decrease the current. The value of ideality factor n is between 1 and 2; when n equal to 1 the current is mostly diffusion current, and when n equal to 2 the current is limited by minority carrier recombination.

2.1.3.3: p-n junction under illumination

When solar radiation is absorbed in the p-n junction, electron-hole pairs are generated, which leads to carrier generation in the space charge region and the quasi-neutral region. These charges in the depletion region will sweep electrons towards the n-side and holes towards the p-side due to the electric field, while the carrier generation in the bulk of the p-n junction will move randomly because there is no electric field to guide them in any direction. As a result, some of the minority carrier generations will come near the space charge region edge, where they will experience a force due to the electric field and will be pulled out at the other side. Thus, the minority carrier only crosses the junction. In other words, the minority electron from the p-side drifts to the n-side, which leaves behind its positive charge in the p-side (holes), and the minority holes from the n-side drift to the p-side, which leaves a negative charge in the n-side (electrons). Therefore, there is a net increase in the positive charge at the p-side and a net increase in the negative charge at the n-side. The build-up of the positive and negative charges causes potential differences to appear across the p-n junction due to light falling on it. This generation is called the photovoltaic effect. When photon light hits the solar cells, it results in a large drift current due to the flow of minority electrons and holes; this is called the light generation current, and it adds to the current generated by biasing. However, the generation of photovoltaic effect reduces the potential energy barrier of the junction, and there is a diffusion of the current flowing in the opposite direction of the light-generated current [8].

There are three simultaneous processes happening in the p-n junction: recombination, charge drift and charge diffusion [15]. The generation of an electron and hole pair occurs when exciting the electron from valence band to conduction band (photogeneration), whereas, the recombination process involves the direct annihilation of the electron from conduction band with holes in valence band.

During drift, the electrons and holes motion is in response of the electric field. When the electric field is applied in semiconductor, it accelerates the positively charged holes in the direction of electric field and the negatively charged electrons in opposite direction of the electric field and the current flow. The drift current is described by the average drift velocities of holes and electrons which is proportional to hole and electron mobilities, density and electric field [16].

$$J_{n.drift} = -qnv_d = qn\mu_n\xi \tag{2.7}$$

The minus sign in the above equation is due to the direction of electron drift current density which is opposite to drift velocity.

For holes

$$J_{p.drift} = qpv_d = qp\mu_p\xi \tag{2.8}$$

where, q is electron charge, n and p are electron and hole concentration, respectively, and $v_{n.drift}$ and $v_{p.drift}$ are the drift velocity of electron and hole respectively and ξ is the electric field. So, the total drift current density is

$$J_{drift} = J_{n.drift} + J_{p.drift} \tag{2.9}$$

$$J_{drift} = q\left(n\mu_n + p\mu_p\right)\xi \tag{2.10}$$

However, additional to drift current density, there is another important current component which is called the diffusion current which depends on the concentration gradient of particles, when the charges from high concentration region diffuse to the region with low charge concentration, thereby the constituting current flow. So, the diffusion current is a result of motion of electrons and holes along a concentration gradient. So, the diffusion current density for electron and holes can be expressed as

$$J_{n.diff} = qD_n\frac{\partial n}{\partial x} \tag{2.11}$$

$$J_{p.diff} = -qD_p\frac{\partial p}{\partial x} \tag{2.12}$$

The minus sign is due to the direction of the hole current being opposite to the direction of the increased concentration gradient.

Lastly, when the concentration gradient and electric field present across the p-n semiconductor junction, the diffusion and drift current flow and the total current density is given by

$$J_n = J_{n.druft} + J_{n.diff} = qn\mu_n\xi + qD_n\frac{\partial n}{\partial x} \quad (2.13)$$

$$J_p = J_{p.druft} + J_{p.diff} = qp\mu_p\xi - qD_p\frac{\partial p}{\partial x} \quad (2.14)$$

The total current density in p-n junction due to both drift and diffusion current can be given

$$J = J_n + J_P \quad (2.15)$$

$$J = qn\mu_n\xi + qD_n\frac{\partial n}{\partial x} + qp\mu_p\xi - qD_p\frac{\partial p}{\partial x} \quad (2.16)$$

Where

J is the total current density, q is charge, J_n and J_p are total electron and hole density respectively, D_n and D_p are the diffusion coefficient of electron and hole respectively, $\frac{\partial n}{\partial x}$ and $\frac{\partial p}{\partial x}$ are the electron and hole concentration gradient, ξ is the electric field, n and p are the electron and hole concentration respectively, and μ_n and μ_p are the electron and hole mobilities respectively.

2.1.4: Solar Cell Parameters

The *J-V* curve arises from the minority carrier properties which determine the solar cell behaviour. In general, the illumination shifts the *J-V* curve of the p-n junction downwards in the current axis. The *J-V* equation of an ideal solar cell is given by

$$J = J_L - J_s\left[\exp\left(\frac{qV}{Ak_BT}\right) - 1\right] \quad (2.17)$$

where, J_s is saturation current density, J_L is the photogeneration current density which is can be expressed as

$$J_L = qG\left(L_N + W + L_P\right) \quad (2.18)$$

Where, G is the generation rate, q is the charge, L_N and L_P are the minority carrier diffusion length of electron and hole respectively and W is the width of the depletion region.

Figure 2.5 shows the relationship between the current and the voltage under dark and illuminated conditions with solar parameters. The rectangle defined by V_{oc} and J_{sc} provide a convenient reference for describing the maximum power point (P_{max}) which can be defined as $P_{max} = V_{mp} \times J_{mp}$

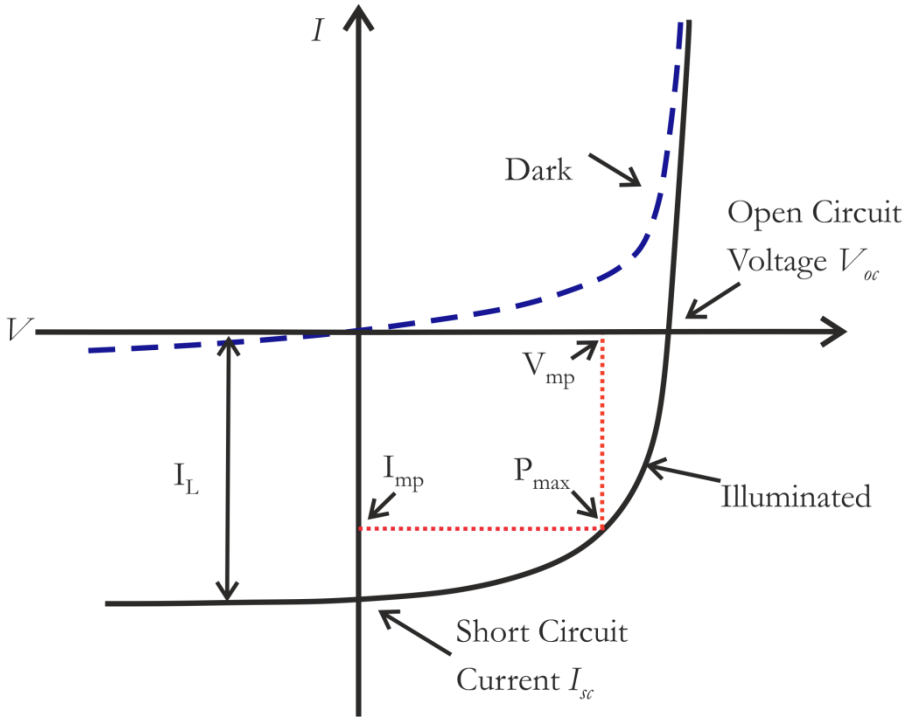

Figure 2.5 J-V curve under dark and illuminated conditions

The main parameters of solar cells are now presented:

2.1.4.1: Open Circuit Voltage (V_{oc})

The open circuit voltage is the maximum voltage that can be obtained from solar cells when they are in an open condition (no current is passing through the cells). It corresponds

to the amount of forward bias of the p-n junction due to the light-generated current [8]. The V_{oc} can be written as the following:

$$V_{oc} = \frac{Ak_BT}{q} \ln\left(\frac{J_{sc}}{J_s} + 1\right) \qquad (2.19)$$

As shown in the above equation, the V_{oc} depends on the saturation current density and photogenerated current density. As J_s depends on the recombination in the solar cell; the V_{oc} is a measure of the amount of recombination in the device. In the laboratory, CZTS thin film solar cells have V_{oc} up to 700 mV under standard $AM1.5$ conditions.

2.1.4.2: Short Circuit Current Density (J_{sc})

The short circuit current density is the maximum current produced by solar cells when they are under the short circuit condition (i.e., there is no voltage in the cell).

$$J_{sc} = J_s\left[\exp\left(\frac{qV_{oc}}{Ak_BT}\right) - 1\right] - J_L \qquad (2.20)$$

The J_{sc} depends on the photon flux density on the solar cells. Also, it depends on the absorption and total reflection of the solar cells which limits the absorbed light.

2.1.4.3: Fill Factor (FF)

The fill factor is the ratio of the maximum power to the ideal power. It is related to the resistance solar cells. The fill factor is the rectangle area within the J-V curve, which is determined by the maximum power point. It can be written as the following:

$$FF = \frac{V_{mp} \times J_{mp}}{V_{oc} \times J_{sc}} \qquad (2.21)$$

In the case of ideal single junction where both R_s and R_{sh} have negligible effect on solar cell performance, the FF can be also calculated only by using the open circuit and the equation can be written as [17]:

$$FF = \frac{V_{oc} - \ln(V_{oc} + 0.72)}{V_{oc} + 1} \quad (2.22)$$

2.1.4.4: Efficiency (η)

Efficiency is the ratio of the power output to power input. It can be written as the following:

$$\eta = \frac{V_{mp} \times J_{mp}}{P_{in}} \quad (2.23)$$

For all testing the incident power is equal to irradiance of AM1.5 spectrum, which equal to 1 kWm^{-2} and the efficiency can be defined as the function of FF, J_{sc} and V_{oc} divided by incident power (power input).

$$\eta = \frac{V_{oc} \times J_{sc} \times FF}{P_{in}} \quad (2.24)$$

2.1.5: Equivalent Circuit of Solar Cells

There are two types of resistance: series and shunt resistances. These resistances add to the equivalent circuit as they have considerable influence on solar cell devices' performance. Figure 2.6 shows the equivalent circuit diagram for photovoltaic cells [18].

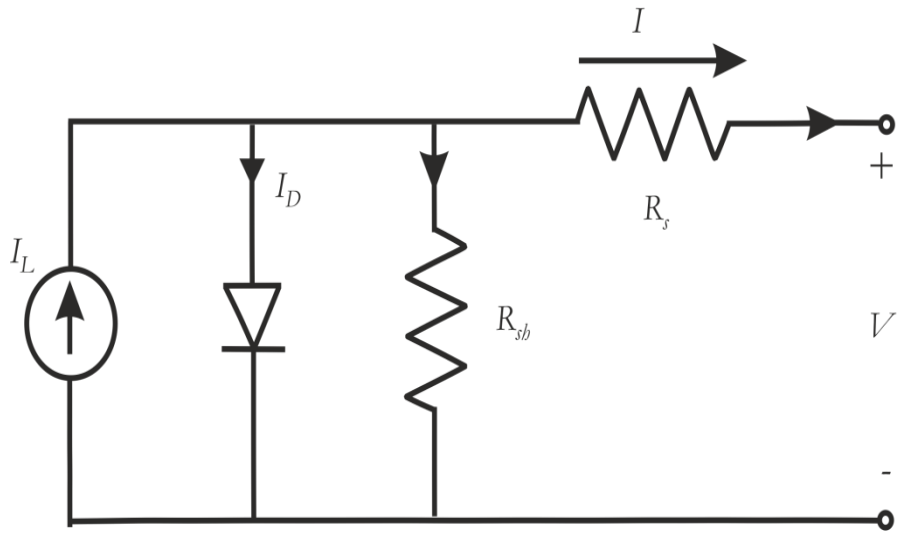

Figure 2.6 Equivalent circuit of solar cells [19].

2.1.5.1: Series Resistance (R_s)

It includes all components that come in the path of current such as semiconductor resistivity and contacts. The main effects of increasing the series resistance are the reduction of the fill factor and the amount of current flowing through the cells as shown in Figure 2.7. However, it can be seen that, the higher series resistance leads to reduce I_{sc} as well as FF without any effect on the V_{oc}.

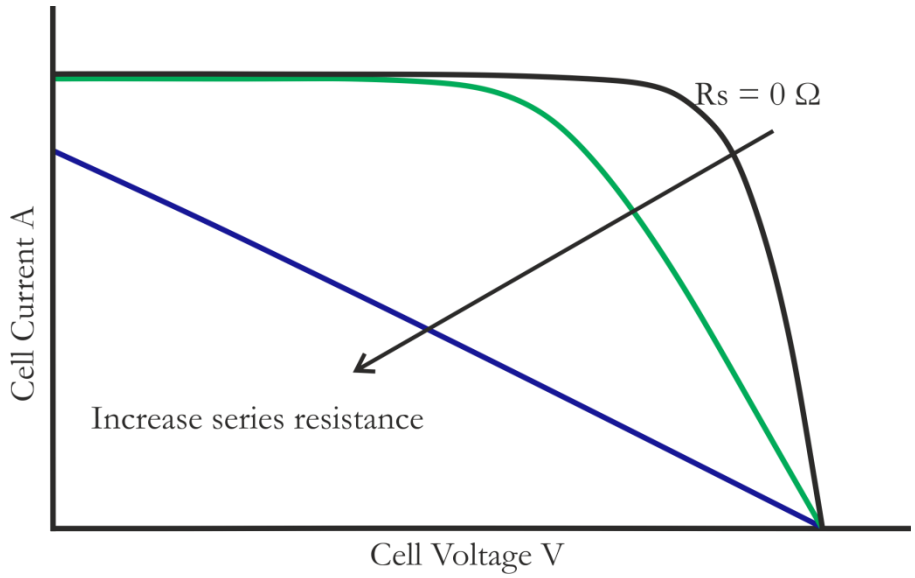

Figure 2.7 Series resistance effect.

It is calculated from the inverse gradient of the illumination of the *J-V* curve under forward bias, which is equal to $1/R_s$.[8].

2.1.5.2: Shunt resistance (R_{sh})

The R_{sh} is determined by the loss of current including recombination losses and losses along the edge of solar cells due to defects and impurities in the junction region. The presence of shunt resistance leads to power loss, as it provides an alternate current path for photogeneration current losses as shown in Figure 2.8.

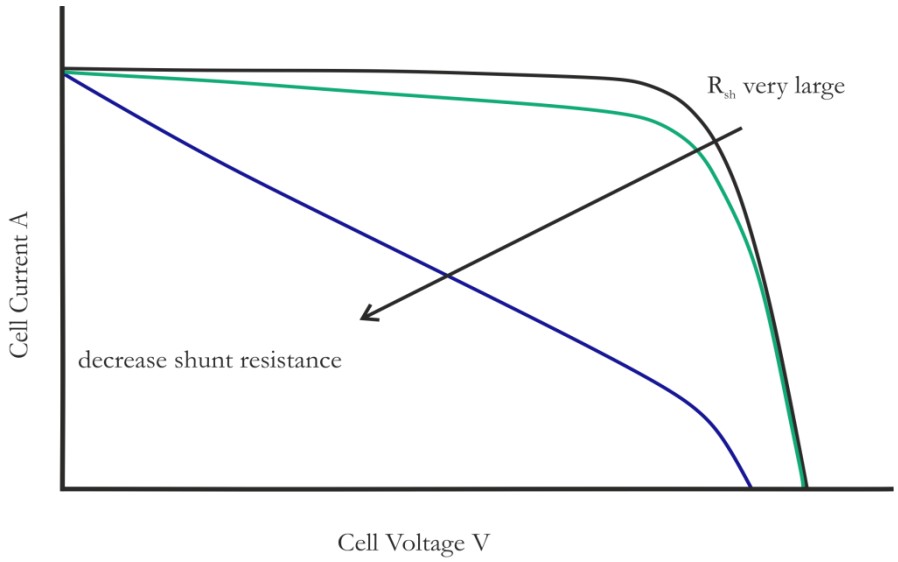

Figure 2.8 Shunt resistance effect

It can be calculated from an inverse gradient of the *J-V* curve under reverse bias, which is equal to $1/R_{sh}$ [10]. Also, the lower shunt resistance leads to reduce V_{oc} as well as *FF* without any change on J_{sc}.

Both R_s and R_{sh} can be calculated by using the following equation:

$$J = J_L - J_s\left(\exp\frac{q(V+JR_s)}{nk_BT} - 1\right) - \frac{V+JR_s}{R_{sh}} \quad (2.25)$$

where J_s is the saturation current, n is the ideality factor, T is the absolute temperature, k_B is the Boltzmann constant, q is the electron charge and V is the voltage at the terminals of

the cell. In practical solar cells the fill factor is influenced by the additional recombination occurring in p-n junction.

However, both the high series resistance and the low shunt resistance lead to a reduction of the fill factor and efficiency of solar cells. To resolve this problem and increase efficiency, the R_s should be as low as possible for higher current flow, and R_{sh} should be as high as possible to reduce losses in the cell.

2.2: Review of the existing status of Cu_2ZnSnS_4 thin-film solar cell technology

2.2.1: CZTS solar cell device

The CZTS solar cell devices consist of many layers. The first layer is a back contact, which is made from molybdenum (Mo) with a thickness between 500 and 700 nm which deposits via the sputtering technique on the soda lime glass (SLG) substrate. The second layer is the absorber layer; in this layer, the CZTS has a p-type thin film with thickness between 1.0 and 2.0 μm, and it is deposited on the Mo layer by the different methods that are discussed in section 2.2.8. Then, it is followed by the n-type CdS layer which is normally deposited by chemical bath deposition with a thickness in the range of 50–100 nm to form the p-n junction. After that, the intrinsic ZnO layer with a thickness of 50–90 nm and the transparent conducting oxide (TCO) are deposited by the sputtering technique with a thickness between 500 and 1000 nm. Lastly, the Ni/Al grid is deposited to achieve electrical contact, this is shown in Figure 2.9 [20] [21] with more details in chapter 7. However, as the absorber layer CZTS is the main point in this thesis, this chapter will focus on it and describe its structure, optical and electrical properties.

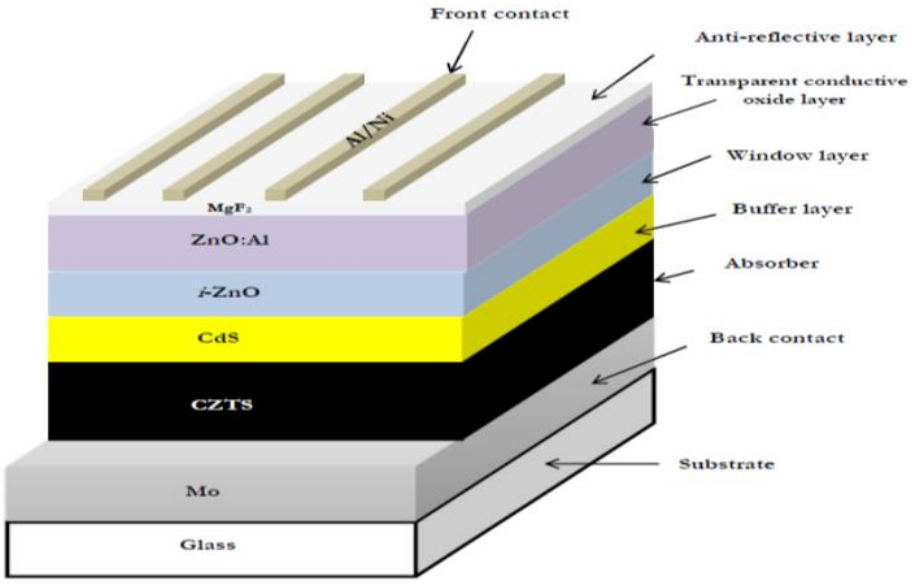

Figure 2.9 Construction of the CZTS solar cell [19, 20].

2.2.2: Absorber materials of Solar Cells

There are many semiconductor materials that can be used in solar cell devices. In the following section, a brief explanation about alternative materials including silicon and thin film materials is presented.

2.2.2.1: Silicon Si

Silicon Si is the most popular solar cell material in the photovoltaic market. It has an indirect band gap of 1.1 eV, and it is used as a homojunction semiconductor device. It has been used widely for a long time, and extensive research on Si has been done to provide in-depth knowledge about its properties and applications. Fabrication of silicon solar cells requires a high thickness (300-500 μm) , a pure crystal with more energy used of fabrication which leads to expensive solar cells [22]. There are three types of silicon used in the solar cell devices: single crystal, amorphous and polycrystalline. The single silicon crystal is recorded as having high efficiency in the range of 20 –25%. Amorphous silicon cells are thin-film solar cells, which are cheaper than the single crystal silicon. Also, their efficiency is lower than single crystals [23]. The highest efficiency for amorphous silicon solar cells is in the range of 10–12% [24].

2.2.2.2: Gallium arsenide GaAs

It is one of the III-V semiconductor materials that have a direct band gap energy close to 1.43 eV and high absorption coefficient. It has many beneficial properties, such as low electronic effective mass, high-electron mobility, and high-saturation drift velocity, which make it ideal for optoelectronic and microelectronic devices like lasers, photovoltaic cells and light emitting diodes (LED). GaAs also has a zinc blende crystal structure. The highest conversion efficiency is 27.6 % [25]. The disadvantage of this material is its high cost, so it is used in the specific application such as satellites [26-28].

2.2.2.3: Cadmium telluride CdTe

CdTe is a p-type semiconductor with large absorption coefficient ($>10^4$ cm^{-1}) and a direct band gap of 1.45 eV. It has a zinc blende structure. CdTe devices are fabricated in the superstrate configuration with high conversion efficiency. First Solar, recently announced a

new world record device efficiency of 22.1% [29]. Despite the progress made in CdTe technology by achieving cost-effective, high-efficiency devices, some issues connected with CdTe solar cells could affect their production in the future. The main issue is the toxicity and price of cadmium and relatively low abundance of tellurium, which could negatively impact production of CdTe thin film solar cells, leading to increased cell and module prices [30].

2.2.2.4: Chalcopyrite materials

Chalcopyrite is tetragonal crystal structure adopted by some semiconductors containing sulphur or other group VI elements along with group I and group III elements. Copper indium diselenide CIS is one chalcopyrite material with a direct band gap of 1.04 eV [31]. It is an alternative material for silicon and III-V materials and to improve the crystal quality and energy band gap, Ga was introduced [32], which leads to quaternary materials such as copper indium gallium diselenide (CIGS). CIGS has been the subject of extensive research and studies due to its structure and optical and electrical properties. It has a direct band gap in the range between 1.1 to 1.3 eV, which is close to the required value for optimum efficiency [31, 33]. The highest efficiency of CIGS is 22.9 % [34]. The disadvantage of CIGS is that it has a rare and toxic elements including Ga and In.

2.2.2.5: Copper Zinc Tin Sulphide CZTS

This is an important material because it is low-cost and contains abundant elements compared with other thin materials. CZTS materials have a direct band gap of 1.5 eV with a high absorption coefficient of 10^4 cm^{-1}. It is a nontoxic material and is composed of elements abundant in the Earth's crust [35]. Moreover, copper, zinc, tin and sulphur are lower cost materials compared to indium and other common PV materials and it is similar to CIGS, though it replaces Ga and In [36]. The theoretical conversion efficiency limit is 32.2%, according to the Shockley and Queisser (SQ) limit [37]. The SQ limits for V_{oc}, J_{sc}, FF and efficiency are 1.3 V, 32 $mAcm^{-2}$, 87 % and 32% respectively [37].

2.2.3: Structure of CZTS

CZTS is a crystalline material with a tetragonal structure which can exist in three different structures, which consists of either Kesterite with the space group $I\bar{4}$, stannite crystal with the space group $I\bar{4}2m$ structure, or primitive-mixed CuAu structure (PMCA) space group $P\bar{4}2m$ as shown in Figure 2.10. It can also exist as a hexaganol wurzite structure at high temperature. The Kesterite structure has lower energy than the stannite structure, and the energy difference between kesterite and stannite is 3 meV/atom [38]. The difference in structure is based on the arrangement of the Zn and Cu atoms as shown in Figure 2.10. Kesterite is characterized by alternating layers of Cu–Sn, Cu–Zn, Cu–Sn and Cu–Zn at z = 0, 1/4, 1/2 and 3/4 respectively. Thus copper occupies the 2a (0, 0, 0) position with zinc and the remaining copper atom at 2d (0, 1/2, 3/4) resulting in the space group $I\bar{4}$ [39]. On the other hand, in the stannite type structure Zn Sn layers alternate with Cu layers. The structure is consistent with the symmetry of the space group $I\bar{4}2m$, with the divalent cation located at the origin (2a) and the monovalent cation at the 4d position (0, 1/2, 1/4). Sn is located at the 2b site (0,0,1/2) in both structures [40].

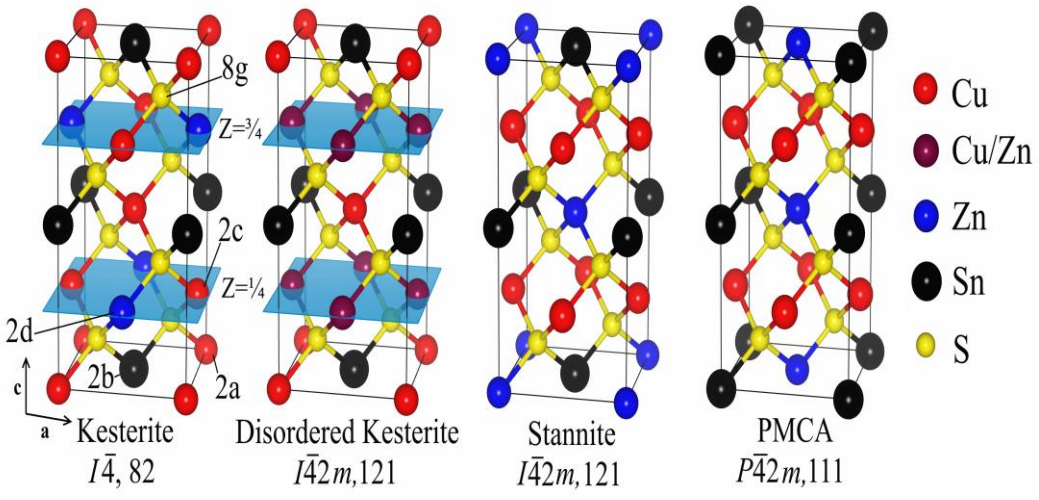

Figure 2.10 The different possible structures of CZTS. Diagrams are drawn by VESTA http://jp-minerals.org/vesta/en/.

However, due to disorder in the cation sublattice (Cu/Zn), a third possible kind of structure exists called disordered kesterite as shown in Figure 2.10 [41], in this structure Cu and Zn are randomly distributed on the 1/4 and 3/4 phases. The lattice constant of kesterite CZTS are a =0.54 nm and c=1.09 nm, but there is a range of values found by other groups [35]. In addition to KS and ST, CZTS can grow from a hexagonal-type called wurtzite structure with space group, *P63mc*. The wurtzite structure is obtained by occupying randomly coordinate of Cu, Zn and Sn cations with a half of the interstices of the sulphur anions. The d spacing was calculated as 3.32 Å and 1.91 Å [42, 43]. Lattice constant of wurtzite CZTS is in the range a = b = 3.83 Å and c = 6.33 Å [44].

2.2.4: Secondary phases and their effects on solar cells performance

There are many secondary phases that appear during synthesis of CZTS nanoparticle inks which may affect the structure and electrical properties of solar cells device. The most common secondary phases are ZnS, CuS_2, SnS, SnS_2 and Cu_2SnS_3. These secondary phases vary depending on different Cu and Zn fabrication conditions (stoichiometric and nonstoichiometric compositions) as shown in Figure 2.11. These phases act as centres of recombination and as a carrier barrier [38, 45]. In general, in the Zn-rich region, ZnS is the expected secondary phase formed by an excess of Zn precursor. The Cu-rich region covers several fields with various possible secondary phases as shown in Figure 2.11.

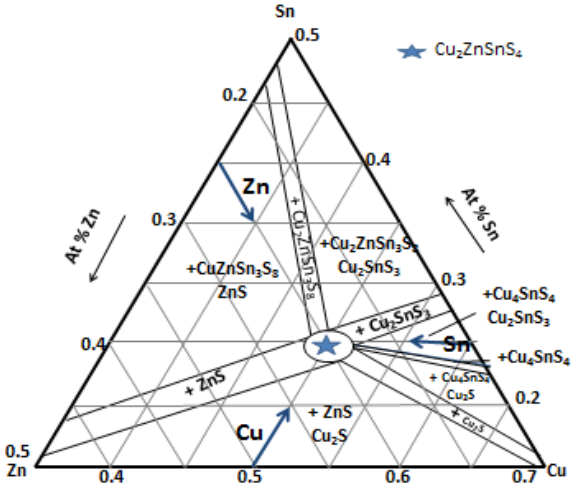

Figure 2.11 Ternary phase diagram of CZTS [46, 47].

ZnS has a sphalerite or wurtzite structure with a band gap in range of 3.54-3.68 eV, works as an insulator and also acts as resistive barriers for carriers [48] as well as reducing an active area for generating the electron hole pairs and current collection in the absorber [49]. Cu_2SnS_3 has cubic and tetragonal structures with a band gap in range of 0.98-1.35 eV [50]. It is a p-type semiconductor. Both ZnS and Cu_2SnS_3 have a similar structure to CZTS which makes them difficult to observe by XRD measurements. Moreover, regarding the phase diagram ZnS and Cu_2SnS_3 do not appear in the same region.. However, under Zn-rich and Cu-poor conditions CZTS shares the boundaries with ZnS secondary phase, whereas under Cu-rich condition it will share Cu_2SnS_3 [49].

Cu_2S is a p-type semiconductor with a band gap of 1.21 eV. It has metal behaviour because it is heavily doped with low band gap semiconductor. It appears under Cu-rich and Sn-poor or Zn-poor conditions. Due to high electrical conductivity of Cu_2S this leads to front and back contact connection across the junction which leads to loss of current by recombination. However, Cu_2S can be removed by KCN chemical treatment [49, 51].

SnS_2 is an n-type semiconductor with a Rhombohedral structure and an indirect band gap of 2.24 eV. It appears in Cu-poor and Sn-rich conditions. It can form a second diode and acts as a barrier to carrier collection and reduces solar cell performance. Also, the literature report other secondary phases from Sn and S with different properties which also may affect solar cell performance such as SnS and Sn_2S_3 with band gaps at (0.90-1.2 eV) and (0.95-1.16 eV) respectively [49, 52].

As mentioned earlier, secondary phases can be detected by using XRD and Raman spectroscopy techniques to determine the different secondary phases. However, due to a similarity in symmetry and lattice constant between ZnS, Cu_2SnS_3 and CZTS phases, [53], it is difficult to distinguish between them by using conventional XRD [54].

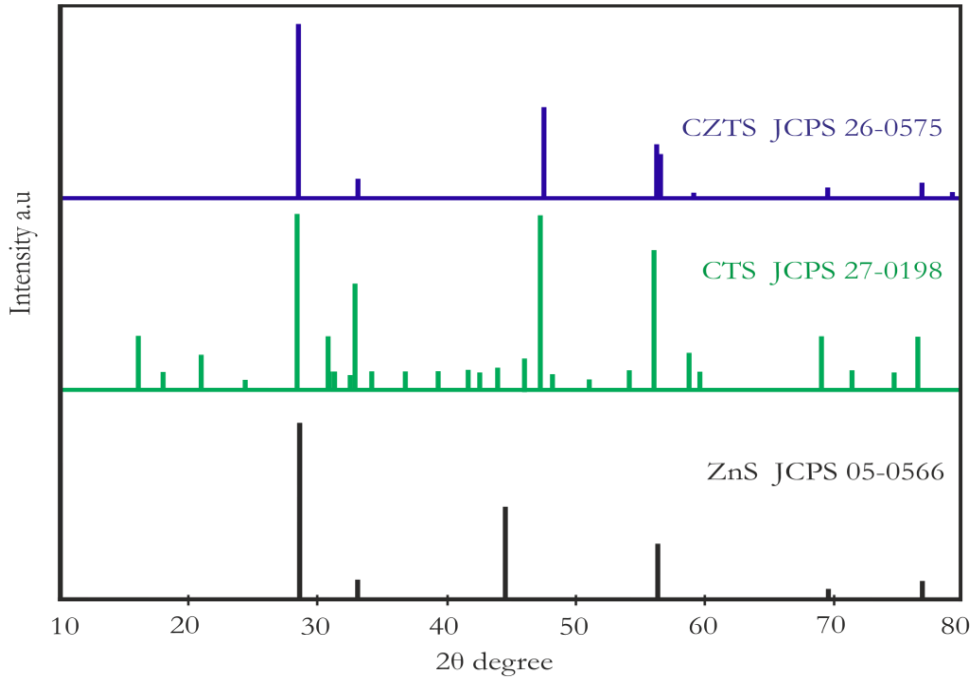

Figure 2.12 XRD peaks and Overlapping of CZTS, Cu_2SnS_3 and ZnS XRD peaks.

Table 2.1 XRD peaks and secondary phase's positions (x-ray is Cu-K_α wavelength).

CZTS		**Tetragonal Cu_2SnS_3**	**Cubic Cu_2SnS_3**	**Cubic ZnS**	**References**
2θ	hkl	2θ	2θ	2θ	
28.44	112	28.54	28.45	28.50	[55, 56]
33.02	200	33.07	32.96	33.03	[57]
47.33	220	47.47	47.31	47.40	[58]
56.09	312	56.32	56.13	56.24	[58]
56.20	116	-	-	-	[59]
76.41	332	76.68	76.39	76.56	[59]

Figure 2.12 and Table 2.1, show XRD peaks located at 28.44, 33.02 47.33 and 56.09° which correspond for (112), (200), (220) and (312) planes in CZTS. However, Raman spectroscopy was used to distinguish between secondary phases and CZTS. There are many peaks which can be observed in CZTS samples by using Raman spectroscopy as shown in table 2.2. However, Raman peaks have been observed at 257, 287,338, 351, 368, cm^{-1} corresponding to CZTS in the literatures.

Table 2.2 Raman peaks and secondary phase's positions.

Secondary phases	Shift Raman peaks(cm^{-1})	References
CZTS	287, 336, 337, 338, 351, 368, 257	[60]
ZnS	348, 352, 275	[61, 62]
Cu_2SnS_3 (tetragonal)	337, 352, 297	[54, 56, 63]
Cu_2SnS_3 (cubic)	303, 356	[63, 64]
Cu_3SnS_4	318, 295, 348	[63, 64]
$Cu_{2-x}S$	264, 476	[56, 65]
SnS	160, 190, 219	[66, 67]
Sn_2S_3	307, 356	[66, 67]
SnS_2	215, 315	[68]

2.2.5: Optical Properties of CZTS

CZTS is suitable for thin-film solar cells because it has a direct band gap in the range of 1.4–1.5 eV, which is near optimum efficiency at the peak of the solar spectrum. Also, it has a high absorption coefficient ($10^4 cm^{-1}$) in the visible region. The absorption coefficient α can be calculated from the experimental measurement of reflectance R and transmittance T using the relation 2.27:

$$\alpha(\lambda) = \frac{1}{x}\ln\left(\frac{1-R(\lambda)}{T(\lambda)}\right) \qquad (2.27)$$

Where, x is the thickness of the film. Moreover, the energy band gap can be calculated by extrapolating the straight line of the plot absorption squared $(\alpha h\nu)^2$ versus the incident photon energy $(h\nu)$ by using the equation 2.28. This is commonly referred to as a Tauc plot.

$$(\alpha h\nu) = C\left(h\nu - E_g\right)^{\frac{1}{2}} \qquad (2.28)$$

Where, C is a constant, $h\nu$ is incident photon energy and E_g is the energy band gap [69]. This is a consequence of the energy dependence of the density of the states.

2.2.6: Electrical Properties of CZTS

There are many types of intrinsic point defects that can affect the solar cells' performance, such as vacancy defects, antisite defects and interstitial defects. The most common defects in the CZTS crystal are vacancies, such as copper vacancy V_{Cu} and zinc vacancy V_{Zn}, and antisite defects like Cu_{Zn} and Zn_{Cu}. However, the V_{Cu} defects are important to achieve high efficiency of solar cells, and a p-type conductivity of CZTS comes from Cu_{Zn} antisite defects [70]. Also, a charge compensated defect pair complexes, such as $[Cu_{Zn}^{-}+Zn_{Cu}^{+}]$ for Cu-rich and Zn-poor and $[V_{Cu}^{-}+Zn_{Cu}^{+}]$ for Cu-poor and Zn-rich, which plays an important role in the electronic passivation of deep donor levels and results in an improvement in the solar cells' performances [20, 35, 71].More details are in the next section 2.2.7.

2.2.7: Defects and electronic properties:

There are many types of intrinsic point defects that can affect the PV solar cells' performance, such as vacancy defects, antisite defects, interstitial and complex defects. The most common defects in the CZTS crystal are vacancies, such as copper vacancy V_{Cu}, zinc vacancy V_{Zn}, tin vacancy V_{Sn} and sulphur vacancy V_S . Also, antisite defects like copper on zinc antisite Cu_{Zn} , zinc on copper antisite Zn_{Cu}, copper on tin antisite Cu_{Sn}, tin on copper antisite Sn_{Cu}, zinc on tin antisite Zn_{Sn} and tin on zinc antisite Sn_{Zn}. Other defect could be observed in CZTS are interstitials such as copper and zinc interstitials Cu_i and Zn_i respectively as shown in Figure 2.14. Moreover, charge compensated defect pair complexes which appear as donor and acceptor vacancies, antisites and interstitials defects, such as $[Cu_{Zn}+Zn_{Cu}]$, $[Sn_{Zn}+Zn_{Sn}]$, $[Cu_{Sn}+Sn_{Cu}]$, $[Zn_{Sn}+2Zn_{Cu}]$ and $[2Cu_{Zn}+Sn_{Zn}]$ also other complex defects such as $[V_{Cu}+Zn_{Cu}]$, $[V_{Zn}+Sn_{Zn}]$and $[2V_{Cu}+Sn_{Zn}]$. These defects introduce several levels within the band gap of CZTS; shallow acceptor level, shallow donor level, mid-gap level and deep trap levels as shown in the Figures 2.14 and 2.15 for CZTS [45, 49, 70-74].

V_{Cu} and Cu_{Zn} are shallow acceptor levels but Cu_{Zn} is deeper than V_{Cu} as a result of formation energy level at 20 meV for V_{Cu} and 120 meV for Cu_{Zn}. Availability of V_{Cu} and Cu_{Zn} with a high population produces a high concentration of hole carriers which corresponds to p-type conductivity of CZTS and increases a solar cell performance

depending on concentration of defects as well as chemical composition i.e copper poor condition when Cu/Zn+Sn ≤ 1, and zinc rich condition when Zn/Sn ≥ 1. At the same time, higher composition ratios have the a detrimental influence to CZTS performance by generating a large population of intrinsic defect and also increasing recombination losses [75] . Other accepter level defects can be found in CZTS with high energy formation such as V_{Zn}, Zn_{Sn} at 220 and 230 meV respectively. Also Cu_{Sn} is found with multi deep level acceptors with different formation energy close to mid-gap level, as well as low formation energy which act as recombination centres in CZTS having an inverse effect on solar cell performance [35, 70, 76, 77]. Figure 2.13 shows the main different between CIGS and CZTS, for instance, there are mid gap states and tail state in CZTS whereas this state disappears in CIGS. More details of recombination process are given in chapter 3.

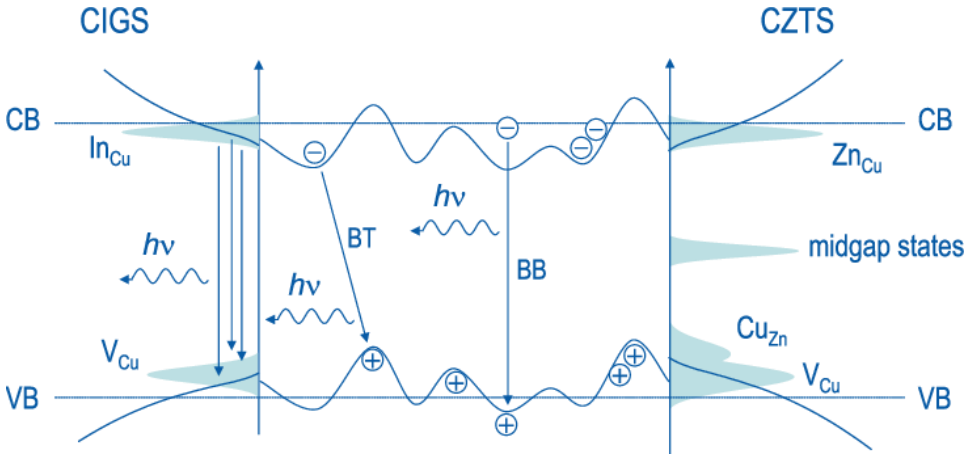

Figure 2.13 Different defects level in both CIGS and CZTS [78].

However, there are many unfavourable defects such as Zn_{Cu}, Sn_{Cu}, Sn_{Zn}, Cu_i and Zn_i. All of these defects are donor levels in the CZTS. Zn_{Cu} is a shallow donor level whereas others are deep donor levels with multi-formation energy [70]. For example, Sn_{Cu} has two levels; shallow donor energy level which is located close to conduction band and deep donor level which located close to mid-gap energy level which could be explained according to atomic orbital energies (multi-valence of Sn). Also, Cu_i and Zn_i are shallow donor level and two mid-gap levels respectively. Moreover, V_S is deep donor level which produces mid-gap states. However, all of these defects act as hole-electron pair recombination centres which could limit CZTS performance as shown in Figure 2.14 [49, 70].

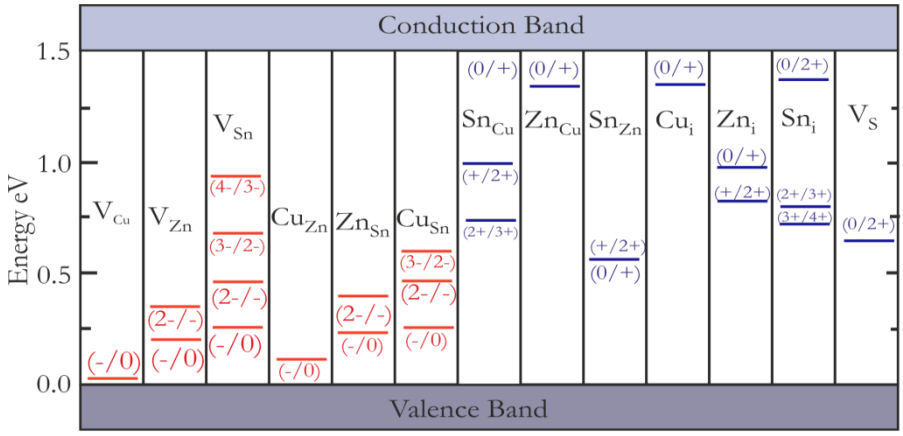

Figure 2.14 Energy formation levels of intrinsic point defects in the band gaps of CZTS. The red lines are for acceptor levels and blue lines are for donor levels [70].

Defect complexes also have a significant impact on CZTS solar cell performance as shown in Figure 2.15. For instance, $[Cu_{Zn}+Zn_{Cu}]$ is the lowest shallow acceptor and donor energies at 200 meV which leads to a decrease of the band gap of CZTS, whereas $[Sn_{Zn}+Zn_{Sn}]$ and $[Cu_{Sn}+Sn_{Cu}]$ have a high formation energy above 200 meV which leads to decrease the band gap of CZTS by 300 meV. The complex defect $[V_{Cu}+Zn_{Cu}]$ has also low formation energy but increasing the band gap of CZTS [79]. Antisite defects pairs are independent of chemical composition in CZTS. Lastly, the formation energy for $[V_{Zn}+Sn_{Zn}]$ and $[2Cu_{Zn}+Sn_{Zn}]$ are in the range of 300 and 600 meV as shown in Figure 2.15. These defects depend on the synthesis process by changing the copper and zinc ratios and all are present in CZTS under Cu-poor and Zn-rich conditions [49, 70, 80, 81].

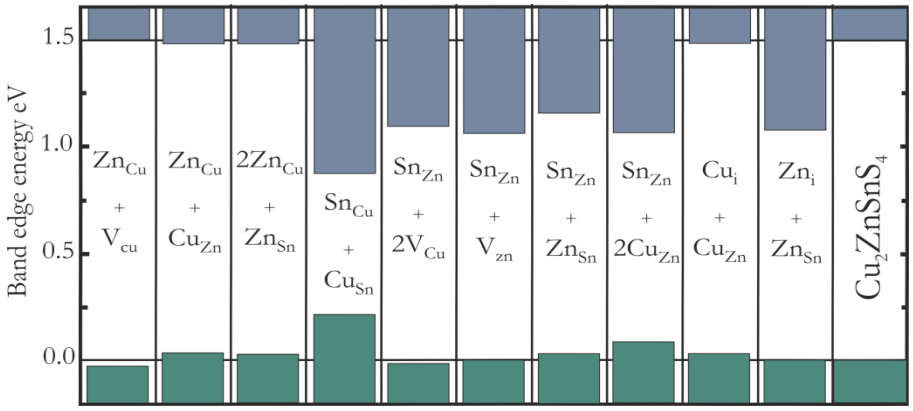

Figure 2.15 Different defect complexes lead to change of valence band (green lines) and conduction band (blue lines) position in CZTS. [70].

However, it can be seen that the tin defects (point and complex) have a high formation energy which reduces energy band gap of CZTS. The high formation energy for those defects makes them difficult to generate naturally. The formation energy of some those defects for instance $[2Cu_{Zn}+Sn_{Zn}]$, $[Sn_{Zn}+Zn_{Sn}]$ and $[Zn_{Sn}+2Zn_{Cu}]$ is at 600, 860 and 830 meV. Also, other complex defects have very high formation energy above 1.2 eV such as $[Cu_{Sn}+Sn_{Cu}]$, $[Zn_{Sn}+Zn_i]$,$[V_{Zn}+Sn_{Zn}]$ and $[2V_{Cu}+Sn_{Zn}]$.

2.2.8: Deposition Techniques for CZTS

There are two main types of deposition techniques for CZTS thin film: vacuum and non-vacuum deposition techniques. High efficiency can be achieved by vacuum techniques, but it is more expensive than non-vacuum deposition. The vacuum deposition technique can be achieved by many methods, such as sputtering, evaporation and pulsed laser deposition techniques. The non-vacuum techniques also can be achieved by several methods such as electrochemical deposition, sol-gel deposition, spray pyrolysis methods, drop casting and spin coating methods. Also, some of these methods can produce CZTS by single-stage deposited processes or in two steps. In the two-step fabrication, the film, as a precursor, is followed by the sulphurisation process at a high temperature and in a sulphur atmosphere. All of these techniques will be reviewed and show the resulting solar cell devices' properties in detail in 2.2.8.1.

2.2.8.1: Vacuum deposition techniques

2.2.8.1.1: Sputtering

The first report of CZTS thin-film solar cells was by Ito and Nakazawa in 1988. They prepared the CZTS thin film by using the atom-beam sputtering method. The PV cell devices were fabricated using the CZTS film deposited on a stainless steel substrate. A heterojuntion diode consisted of cadmium tin oxide transparent conductive film. The open circuit voltage was 165 mV, with no mention of efficiency [82].

Another group, Seol et al. (2003) deposited the CZTS thin film by RF magnetron sputtering on 7059 corning glass. The thin film then was annealed in an $Ar+S_2$ (g) atmosphere at varying temperatures from 250 to 400 ^{o}C for 1h. The stoichiometric ratio of the film was achieved, except sulphur, so the film was annealed in a sulphur vapour atmosphere above 200 ^{o}C. The XRD measurement showed the expected major peaks, which corresponded to the CZTS thin film and were of (112), (200), (220) and (312) planes when annealing the CZTS film above 250 ^{o}C. This was identified as the kesterite structure; moreover, it was discovered that the composition of the thin films was affected by both annealing and RF magnetron sputtering power [83].

Also, Tanaka et al. (2005) fabricated a CZTS thin film using the hybrid sputtering method. They deposited Sn by DC sputtering under Ar atmosphere for 80 min. Then, Zn was evaporated in a quartz crucible at 300 ^{o}C. Next, Cu was deposited by RF sputtering at power 100 W. Lastly, the film was annealed under S flux for 60 min. for the formation of CZTS with different substrate temperatures from 300 to 500 ^{o}C. The results of this study revealed that as the substrate temperatures increased, the thin films' thickness decreased. Moreover, the composition ratio of the films at different substrate temperatures was in agreement with the stoichiometric composition when the substrate temperature increased to 400 ^{o}C, but above 450 ^{o}C, the composition ratio had minimal Zn. The XRD measurement only showed the peak of secondary phases, such as CuS_2 at 300 ^{o}C, which may affect the carrier concentration, whereas the single phase of CZTS was detected at 400 ^{o}C with the stannite structure. The SEM showed the thin film with a small grain size of less than 1 micron. The resistivity, carrier concentration and Hall mobility were 0.13 Ω.cm, 8.0×10^{18} cm^{-3} and 6.0 $cm^2V^{-1}s^{-1}$, respectively, for the CZTS films prepared at 400 ^{o}C [84].

Moreover, Fernandes et al. (2009) prepared CZTS by using the DC magnetron sputtering method. The Cu, Zn and Sn were deposited on Mo- soda lime glass (SLG) substrate. Sulphurisation was done using a tubular furnace to control the sulphurisation temperature at 525 ^{o}C under N_2 +S_2 vapour atmosphere. The thickness of the metallic precursors for Cu, Zn and Sn were 150, 190 and 340 nm, respectively. Also, the sulphurisation temperature was varied at 340, 370, 425 and 505 ^{o}C. Energy dispersive x–ray (EDX) showed the chemical composition of Cu/Zn+Sn and Zn/Sn as 0.87 and 0.4, respectively. Raman measurements confirmed the secondary phases present, as SnS and SnS_2, for the sample with the sulphurisation temperature at 330 ^{o}C. For the sample with the sulphurisation temperature at 425 ^{o}C, the Raman spectroscopy confirmed the presence of $Cu_{2-x}S$, Sn_2S_3 and cubic ZnS at peaks of 264, 304 and 356 cm^{-1}, respectively. For the sample with the sulphurisation temperature at 505 ^{o}C, Raman measurements showed only a peak at 330 cm^{-1}, which corresponds to CZTS. To improve the crystal quality, the sulphurisation temperature was increased to 525 ^{o}C. The EDX analysis found the chemical composition ratio of Cu/Zn+Sn = 0.9, Zn/Sn = 0.87 and Cu+Zn+Sn/S =1.03, which means that there was a loss of Zn by the sulphurisation process. Moreover, the XRD observed the stronger peak at (112) and confirmed the presence of CZTS. The Raman spectroscopy also confirmed the presence of CZTS with the following peaks: 256 and 257, 288, 338 and 339 cm^{-1}. The secondary phases $Cu_{2-x}S$ and ZnS were found at 476 and 348 cm^{-1} respectively [63]. The same group in 2009 studied the precursor order on properties of sulphurised CZTS thin films. Mo/Zn/Sn/Cu and Mo/Zn/Cu/Sn precursor orders were used. It was found that the precursor order Mo/Zn/Sn/Cu is the best. This was due to Cu on the top, reducing the amount of loss of Zn and Sn with etching potassium cyanide (KCN) which acts to move $Cu_{2-x}S$. Also, this order gave the best results for CZTS thin-film characteristics by XRD and Raman spectroscopy. Moreover, the band gap was 1.41 eV [85]. In a later report, in 2010 [86], they prepared CZTS by sulphurisation of the DC magnetron sputtering under the precursors order as Zn/Sn/Cu and followed by sulphurisation process at 525 ^{o}C for 10 min. It was estimated that the value of the carrier concentration was 1.5×10^{17} cm^{-3} for the CZTS layer. Later, in 2012, they used admittance spectroscopy to study the electrical property of CZTS and the behaviour of the back contact. The barrier height was presented at a high temperature value of 246 meV. Moreover, the activation energies of the shallower (V_{Cu}) and deeper (Cu_{Zn}) defects were 45 and 113 meV, respectively [87].

The Leitao group in (2011), by using DC magnetron sputtering, had a pure metal precursor with an order of Zn, Cu and Sn deposited on Mo/SLG in Ar atmosphere. The thickness of deposition was at 260, 185 and 330 nm, and the deposition power of Zn, Cu and Sn were at 0.16–0.38, 0.16 and 0.11–0.16 Wcm^{-2} respectively. Then, it was followed by the sulphurisation process in a tubular furnace in the N_2+S_2 atmosphere at 525 ^oC for 10 min. Then, the sample was treated in KCN solution to remove the unwanted phase. The result was a good crystalline film with chemical composition that was Cu-poor and Zn-rich. The composition ratio of Cu/Zn+Sn was about 0.9, and Zn/Sn was 1.3 [88].The same group studied the photoluminescence at different temperatures and excitation powers. It was discovered that the peak intensity of the PL decreased with increasing temperature; whereas the peak intensity of the PL increased as the excitation power increased (the excitation was done with 488 nm line of Ar+ laser). The values of the acceptor concentration, hall mobility and holes' concentration were 2.04×10^{20} cm^{-3}, range between 0.5 and 2 $cm^2V^{-1}s^{-1}$ and 10^{18} cm^{-3} respectively. The value of the potential that fluctuated in the valance band edge was 172 meV [89].

Shin et al. (2011) fabricated a CZTS thin film using the sputtering method. The effect of the different orders of precursors was studied. Cu, SnS_2 and ZnS were deposited at room temperature with varying orders as Cu/SnS_2/ZnS/glass, ZnS/Cu/SnS_2/glass and SnS_2/ZnS/Cu/glass with thicknesses of 100, 440 and 330 nm for Cu, SnS_2 and ZnS, respectively. Then, it was followed by sulphurisation process in a tubular rapid thermal annealed (RTA) system in a N_2 (95%) +H_2S (5%) atmosphere at 550 ^oC for 10 min. XRD and Raman Spectroscopy confirmed that the sample with the order of Cu/SnS_2/ZnS achieved a high quality for solar cells. Using this order they did not observe any secondary phases, and it demonstrated a kesterite structure. Moreover, a strong Raman peak at 338 cm^{-1} was observed, which demonstrates that it is a CZTS thin film. The resistance, carrier concentration and mobility were 3.8 Ω.cm, 1.64×10^{18} cm^{-3} and 7.10 cm^2V^{-1} s^{-1} respectively. The direct band gap of this film was achieved at 1.45 eV [90].

Pawar et al. (2014) fabricated thin films by rapid thermal processing sulphurisation of stacked metallic precursor films. In this method, 200 nm of Zn, 200 nm of Sn and 350 nm of Cu were deposited by the sputtering method at room temperature. After that, the rapid thermal sulphurisation process under annealing temperature between 500 ^oC and 580 ^oC was done for 5 min. The effect of sulphurisation temperature on the film was confirmed

as the ratio of Zn/Sn increased from 1.01 to 1.16, which means that there was a loss of Sn. Also, the film was completely sulphurised at 580 °C by increasing the ratio from 0.85 to 0.99. The photovoltaic device had a structure of glass/Mo /CZTS/CdS/ i-ZnO /AZO and achieved a 5% PV efficiency and with a short circuit voltage of 561 mV [91].

Dhakal et al. (2014) fabricated thin films via the sputtering method. Cu was deposited by DC power, and ZnS and SnS were deposited by RF power on Mo-SLG. This was followed by the annealing process under an H_2S/N_2 (5%/95%) atmosphere in a tube furnace with a quartz tube at 525 °C for 3 to 4 h. XRD demonstrated the kesterite structure and the presence of secondary phases such as ZnS and SnS. The photovoltaic device had a glass/ Mo/ CZTS/ CdS/ ZnO/ TCO (AZO or ITO)/Cr–Ag structure, which achieved a power conversion efficiency of 6.2%, V_{oc} of 603 mV, J_{sc} of 19 $mAcm^{-2}$, FF of 55% and R_s and R_{sh} of 5.61 and 400 Ωcm^2, respectively [92].

Lin et al. (2016) used CuS, ZnS and SnS_2 as powders which were mixed at three different weight ratios of CuS: ZnS: SnS_2 for preparing the sputtering targets. The powders were mixed by using the ball milling method at the rotating speed of 300 rpm for 3 h, poured into a stainless steel mold, pressed into pellets and transferred to a vacuum furnace for sintering treatment. The pellet samples were annealed at 200, 300, 400, 500 and 600 °C for 8 h. The CZTS thin films were deposited at radiofrequency (RF) gun power of 75 W and various working pressures (WPs) of 1, 5 and 10 mTorr under argon (Ar) atmosphere as the inlet gas flow. After that, the films were treated by KCN to remove unwanted phases. Then, followed by sulfurisation treatment using S powder added in a graphite box and transferred to a tube furnace. In this work, the efficiency of the sample at low WP ≤ 5 mTorr was significantly higher than that of CZTS absorber fabricated at high WP of 10 mTorr. The devices were fabricated as SLG/Mo/CZTS/CdS/i-ZnO/ ITO/ Al, and PV performance for the device at WPs of 1 mTorr exhibited the high efficiency as V_{oc} = 0.52 V, the J_{sc} = 19.17 $mAcm^{-2}$, the FF = 52.7% and efficiency of 5.2% [93].

Yan et al. (2017) prepared CZTS by sputtering techniques. Two CZTS layers with high doping at bottom and low doping at the top were fabricated by rapid thermal processing (RTP) sulfurization process. The efficiency was 7.6% [94]. Other improvement was done by Feng et al. (2016). They used sputtering technique to prepare CZTS using SnS_2, ZnS and Cu targets. After that, it was followed by two sulfurization techniques. The first step was under low temperature around 260 °C at N_2+H_2S atmosphere and the second step was at

510 °C under the same atmosphere to remove secondary phases and increase the size of crystallites. The chemical ratio was 0.73 for Cu/Zn+Sn and 1.35 for Zn/Sn. The efficiency was 8.85%. The results also indicate shallower trapping, higher hole concentration and smaller defect density. Moreover, the dependence of open-circuit voltage on the element component was investigated. With the increase of Sn and Zn content, decreased in open-circuit voltage due to a high concentration of deep level defect Sn_{Cu} under excess Sn content and increase open-circuit voltage, respectively [95-97].

Recently, Yan et al. 2018 CZTS recorded the highest efficiency of CZTS device with structure Glass/Mo/ Al_2O_3 /CZTS /CdS / i-ZnO /ITO /Al / MgF_2. It was achieved V_{oc}= 730.6 mV, J_{sc}= 21.74 $mAcm^{-2}$, FF=69.27 % and the efficiency = 11.01%. The CZTS thin film with thickness around 800 nm with composition ratio Cu/Sn = 1.7~1.8 and Zn/Sn = 1.2 were fabricated by co-sputtering techniques. Cu target was deposited by DC system with power 23 W, ZnS and SnS targets were deposited by RF system with power 77 W and 53 W, respectively. After that, the films were annealed under combined sulphur and SnS atmosphere at 560 °C for three minutes. The main improvement in this method, after chemical bath deposition (CBD) of CdS layer, the film was annealed at 270 °C for 10 min under N_2 atmosphere. This approach assists elemental inter-diffusion, which leads to Zn and Cd gradients within CdS and CZTS respectively. As well as the diffusion of Cd and Zn form new phases into CZTS and CdS surface such as $Cu_2Cd_xZn_{1-x}SnS_4$ and $Zn_xCd_{1-x}S$ which is likely formation of a new phase of $Cu_{2-x}Na_xZnSnS_4$ [98] .

2.2.8.1.2: Evaporation

Katagiri et al. (1997) used an electron beam evaporation technique to deposit Cu/Zn/Sn layers on soda lime glass substrate, heated up to 150 °C. The deposition was done by elements of different thickness. The sulphurisation process was done under an N_2 (95%) +H_2S (5%) atmosphere at 500 °C in an electric furnace. The x-ray diffraction analysis of the peaks observed showed a lattice constant of 5.42 Å and 10.81 Å for a and c respectively. The chemical composition ratio was calculated using an electron probe microscope; Cu/Zn +Sn was 0.9, Zn/Sn was 0.9 and S/Cu + Zn + Sn was 1. The photovoltaic device structure was SLG/Mo /CZTS /CdS/ZnO/ Al. stack layers of CZTS were deposited on Mo-SLG by the electron beam, and CdS was deposited by CBD The *J-V* characteristics of this

device showed a power conversion efficiency of 0.66% with a band gap of 1.45 eV. Moreover, the V_{oc}, J_{sc} and FF were 400 mV, 6.0 $mAcm^{-2}$ and 27% respectively [99].

Friedlmeier et al. (1997) fabricated a CZTS thin film by thermal evaporation of the elements and binary chalcogenides. It was Cu/ZnS/SnS_2 or Sn and S with a substrate temperature up to 600 °C in a high vacuum. The film was observed in the kesterite structure. Moreover, they recorded a V_{oc} of 570 mV and efficiency of 2.3% [100].

In 2001, the Katagiri group made some improvements to their previous work by replacing the Zn layer with ZnS. They deposited ZnS onto Sn and Cu layers on Mo-SLG. In order to sulphurise, the furnace maintained a constant temperature at 550 °C under the N_2+H_2S (5%) atmosphere for 1 h. It produced CZTS thin films with thickness of 0.95, 1.34 and 1.63 μm. The optical properties of the solar cell device with a structure of SLG /Mo/CZTS /CdS/ZnO /Al at different levels of thickness in the absorber layer showed the V_{oc} and Eg increased with increasing thickness, whereas the J_{sc} and efficiency decreased with increasing thickness [101]. In another report, the Katagiri group reported a high V_{oc} of 735 meV with efficiency of 2.49% [102]. In 2003, Katagiri group made more improvements to the sulphurisation process. They used the stainless steel chamber and a turbo molecular pump (TMP), instead of a quartz glass tube furnace with a rotary pump, and they also increased the temperature to 550 °C. The different thicknesses of the ZnS layer as 330, 360 and 390 nm was deposited to examine the chemical composition with a constant thickness of Cu and Sn at 900 and 150 nm, respectively. The composition ratio of CZTS with a thick ZnS layer confirmed the S-poor and Zn-rich composition for all samples. For all of the samples, the ratios Cu/ (Zn+Sn) and S/Metal were nearly 0.92. However, the ratio of Zn/Sn of the sample with a thickness of 390 nm was slightly larger (1.19) than the other samples (1.08). For photovoltaic devices, in order to improve the efficiency of the device and to avoid the influence of the $CdSO_4$ in the fill factor, they replaced the $CdSO_4$ with CdI_2 in the chemical path solution for CdS depoition. They recorded V_{oc} of 659 mV, J_{sc} of 10.3 $mAcm^{-2}$, FF of 0.63 and efficiency of 4.25%, with device structure was as SLG/Mo/CZTS/CdS/AZO/ Al. Moreover, the study showed the effect of adding Na by fabricating the solar cell with a CZTS-based absorber layer using the Na_2S/Mo/SiO_2-SLG substrate. The results confirmed the best optical properties of the solar cell. The efficiency was 5.45%, and the fill factor was 60% [103].

Also, in 2005, Kobayashi et al. studied the effect of the Cu/Zn+Sn ratio with different annealing temperatures on the physical properties of the CZTS solar cell. They used e-beam evaporation, but they used ZnS and Sn with a constant thickness of 34 and 16 nm respectively. Also, the Cu thickness varied between 6 and 22 nm. As a result, the ratio of Cu/Zn+Sn varied from 0.5 to 1.2. In addition, the SEM image showed large particle sizes in the surface, and EDX measurements determined that when the ratio of the Cu/Zn+Sn were 0.49 and 0.69, Cu was poor, and these particles were binary and composed of Sn and S. On the other hand, when the ratio of Cu/Zn+Sn was over 1.09, Cu -rich, these particles corresponded to the secondary phase of Cu and S. By using varying sulphurisation temperatures from 510 ^{o}C to 550 ^{o}C, the CZTS thin-film solar cells were fabricated. The PV conversion efficiency and fill factor with configuration glass/Mo/CZTS/CdS/i-ZnO/ ITO/ Ni–Al grids increased to 4.53% and 58% respectively, for the sulphurisation temperature at 520 ^{o}C [104].

Schubert et al. (2010) deposited ZnS, Sn, Cu and S sources onto Mo-SLG by a fast co-evaporation process at a substrate temperature of 550 ^{o}C. SEM showed the small particles on the top of the surface of the film, which indicates the CuS secondary phase, revealing the Cu-rich thin-film growth. In order to remove the secondary phase, the KNC etching solution was used. The chemical composition ratio was Cu/ (Zn+Sn) and Zn/Sn at nearly 1. The photovoltaic devices made using these films had a PV conversion efficiency of 4.1% with a V_{oc}, J_{sc} and FF of 541 mV, 13.0 mAcm^{-2} and 59.8% respectively [105].

Wang (2010) used a vacuum process to fabricate CZTS thin films by evaporating Cu, Zn, Sn and S sources onto Mo-SLG followed by annealing on a ceramic hot plate at 540 ^{o}C for 5 min. Raman spectroscopy confirmed that the secondary phases of CuS and ZnS were absent. Also, it was confirmed that all peaks were observed at 287, 338 and 368 cm^{-1} corresponding to the CZTS thin film. The PV solar cells with a structure of SLG/Mo/CZTS/CdS /AZO/ Al was fabricated with different levels of thickness of the absorber layer at 1200, 900, 660 and 650 nm. The electrical properties showed an increase of efficiency and the fill factor with a decrease in thickness. Moreover, the series resistance decreased with decreasing thickness. The best efficiency and fill factor were recorded as 6.81% and 65%, respectively, for a solar cell with a thickness of 650 nm. The series resistance was 3.4 Ω.cm^{2} [106].

For Shin et al. (2011), CZTS thin films were prepared by thermal evaporation of a source of an element with a substrate temperature at 150 ^{o}C. After evaporation, the thin film was annealed at 570 ^{o}C. The morphology measurements confirmed the ZnS secondary phase presence near the MoS_x layer. Also, these confirmed thin films were Zn-rich. The solar cell device made from the film was found to be 8.4% efficient with the following parameters: V_{oc} = 661 mV, J_{sc} = 19.5 mAcm^{-2}, FF = 65.8 % and R_s = 4.5 Ω.cm^2 (area of solar cell device)[107].

Sakai's group fabricated CZTS with evaporation technique and followed by sulfurization treatment and annealing. They studied the effect of different based buffer layers as Cd, Zn and In deposited on Mo/CZTS layers by chemical bath deposition technique. The device with configuration Glass/Mo/CZTS/buffer layer/ZnO:B/Al have achieved different efficiency depending on buffer layers. However the back contact Mo was deposited by sputtering, the window layer ZnO:B was deposited by metal-organic chemical vapour deposition (MOCVD), front Al electrodes were deposited by evaporation. The highest efficiency of CZTS submodule was achieved with Cd based buffer layer was 9.19% with V_{oc} = 708 mV, J_{sc} = 21.6 mAcm^{-2} and FF = 60%. This is the highest efficiency reported for CZTS prepared by any evaporation method. In other study, with Zn based buffer layer with different Zn/Sn ratio, the Zn-based buffer cell has higher efficiency than Cd based buffer layer under low Zn/Sn ratio. Also, when the Zn/Sn ratio is increased, it shows strong degradation in efficiency [108-111].

Sakthivel et al. (2015) used sequential evaporation of precursors on substrates by ordering ZnS, Cu and Sn, then followed by sulfurising process in the atmosphere of N_2 +H_2S at temperature of 550 ^{o}C for 2 h. The chemical composition ratio at atomic percentage was Cu/Zn+Sn=0.83 and Zn/Sn=1.54. The device achieved efficiency close to 5.6% with device structure as ITO glass/Mo/CZTS/CdS/ZnO/i-ZnO/TCO. Other solar cell parameters were J_{sc} = 14.2 mAcm^{-2}, V_{oc} = 630 mV and FF = 63 % [112].

2.2.8.1.3: Pulsed laser deposition

In this technique, a pulsed UV laser beam is focused onto a solid target and laser ablation occurs, which result in highly non-thermal removal of the target material. The ablated material, which is an expanding plasma cloud, is finally collected onto a substrate placed a few centimetres away. In this method, there is a need to take into account many parameters

such as the background gas pressure, substrate temperature, ablation energy density because the energy source is outside of the vacuum chamber [113, 114]. Moreover, pulse repetition rate, pulse energy, target material, target-to-substrate distance, type of gas and its pressure in the chamber and substrate orientation, these parameters have a strong influence on the film properties [114].

Moriy's group in 2007 prepared CZTS thin films by mixing powders of Cu_2S, ZnS and SnS_2 and sealing them into an evacuated quartz ampule in a furnace at 750 ^oC for 24 h. This film was deposited on Mo-SLG by using the pulsed laser deposition technique. A KrF excimer laser pulse was used with a wavelength of 248 nm with controlling energy at 1.5 Jcm^{-2}, a 10 ns pulse width and a repetition rate of 30 Hz. Then the film was annealed in a furnace at varying temperatures of 300, 400 and 500 ^oC in an N_2 atmosphere. With the XRD measurement, the researchers observed that there are no peaks for CZTS films, whereas by increasing the annealing temperature, there are many X-ray peaks that correspond to the CZTS thin films: (112), (200), (220) and (312). The composition ratio of Cu/Zn+Sn and Zn/Sn increased with temperature. These films were Cu-poor and Sn-rich. The PV solar cell device was fabricated as having a structure of glass/Mo/CZTS/CdS/Al: ZnO for a sample annealing at 500 ^oC. The electrical properties of the PV device were V_{oc} = 546 mV, J_{sc} = 6.78 $mAcm^{-2}$ and FF = 48% and efficiency = 1.74%. Also, the resistance value decreased with an increase in the annealing temperature [115]. The same group in 2008 prepared CZTS thin-film precursor using a similar method, but here they used an N_2+H_2S atmosphere at 500^oC for 1 h. The result of these changes in the ratios of chemical composition became nearly stoichiometric. The devices had properties less than what was indicated on the previous report due to changing in the composition ratio after annealing under N_2+H_2S atmosphere. The devices demonstrated the following measurements:, V_{oc} = 336 mV , J_{sc} = 6.53 $mAcm^{-2}$ and FF =46% and efficiency = 0.64% [116].

Pawar et al. (2010) studied the effect of the incident laser power on the properties of CZTS thin films. In this experiment, the different incident laser powers were used in the following range: 1, 1.5, 2, 2.5 and 3 Jcm^{-2}. Then, the films were annealed in an N_2+H_2S atmosphere at 400 ^oC. The intensities of the peaks that were observed by XRD showing sharp and more intense peaks with increasing incidental power up to 2.5 Jcm^{-2}, whereas it becomes relatively weak at 3 Jcm^{-2} incidental laser power. This result may affect the quality of the crystal. Increasing incident power leads to an increase of the plasma densities and

kinetic energy, this leads to an improvement of the uniformity and smoothness in deposited crystalline structure. But increasing the incident power above 3 Jcm^{-2} leads to a decrease in the crystal quality because of the overgrowth of the grains on the surface [117].

Moreover, Moholkar et al. (2011) used the KrF excimer laser on PLD to deposit Cu_2S, ZnS and SnS_2 on Mo-coated glass substrate at different deposition times from 5 to 60 min. The quality of crystallinity was improved by increasing the deposition time up to 30 minutes, but at a greater deposition time up to 45 and 60 min, the overgrowth grains and the crystalline quality were degraded. The PV device of the CZTS solar cells deposited for 30 min with a structure of glass/Mo/CZTS/CdS/AZO/Al achieved good properties, for instance, V_{oc} = 654 mV, J_{sc} = 8.76 $mAcm^{-2}$, FF = 55% and an efficiency = 3.14% [118].

Jin's group (2016) fabricated CZTS by PLD using a single quaternary oxide target. In a typical preparation process, Sn powder was dissolved into HNO_3. Then a combination of Cu $(NO_3)_2.3H_2O$ and Zn $(NO_3)_2.6H_2O$ were dissolved by deionized water in a glass beaker. After that, the solutions were mixed together with citric acid at room temperature. The precursor mixture solution was prepared by drop-by-drop addition of ammonia until pH = 7 and was stirred for 2 h. then followed by heating process in the electric oven to form an inhomogeneous oxide powder CZTO. CZTO thin films were deposited on Mo-coated glass substrates at room temperature by PLD .The substrate was placed on a rotating holder at distance of 5 cm from the target .The deposition chamber was evacuated by using turbo molecular pump. KrF excimer laser pulses (λ=248 nm, 25 ns pulse width) were focused onto the CZTO target pellet. The deposition of CZTO precursor layers was followed by sulfurization processed with heating rate of 60 °C min^{-1}. The device performances were V_{oc} =684 mV, J_{sc} = 16.82 $mAcm^{-2}$, FF = 42.8 % and efficiency of 4.94%, under Cu poor Zn rich composition (Cu/Zn+Sn=0.92 and Zn/Sn =1.77) [119].

Cazzaniga et al. (2017) reported a 5.2% efficiency CZTS solar cell by pulsed laser deposition featuring an ultra-thin absorber layer which was less than 450 nm with V_{oc} = 616 mV, J_{sc} = 17.6 $mAcm^{-2}$ and FF = 47.9%. Mo bilayer was deposited by DC magnetron sputtering at 10 Wcm^{-1} power densities at different pressure to achieve a good adhesion to the substrate and low sheet resistance. Then, the stoichiometric ratio of 2CuS: ZnS: SnS used as the target to fabricate CZTS nanoparticles under high vacuum with pressure 5×10^{-6} mbar. The KrF excimer laser beam used 248 nm of wavelength, 20 ns of pulse-

width and 15 Hz of pulse repetition rate and focused onto a sintered target at a laser fluence of 0.6 Jcm^{-2} and a spot size of 4 mm^2 [113].

2.2.8.2: Non-vacuum deposition techniques

2.2.8.2.1: Photo electrochemical deposition method

Scragg et al. (2008) fabricated CZTS by the photoelectrochemical deposition method [120] using the Cu, Sn and Zn from an alkaline solution, which contained different amounts of NaOH, $CuCl_2$, $SnCl_2$, sorbitol and $ZnCl_2$ on Mo/SLG. Then, the samples were annealed using a quartz tube furnace in a sulphur atmosphere at 550 °C. The XRD showed the presence of secondary-phase SnS only, whereas there was no evidence of Cu_xS present, which showed the difficulty of distinguishing ZnS from CZTS. The ratio of chemical composition appeared to show that all samples were Zn-rich and the grain sizes were in the range of 0.2–0.5 μm. CZTS showed the p-type characteristics with a band gap of 1.49 eV and a carrier concentration of doping in the range of $0.5–5\times10^{16}$ cm^{-3} [121]. In 2010, CZTS was fabricated by sequential electrodeposition of a metallic precursor stack in the Cu/Sn/Cu/Zn order on the Mo-SLG using the rotation disc electrode. Then, the precursor stack was sulphured in a tube furnace at 575 °C for 2 h. The KCN was used to remove unwanted phases. The chemical composition had a Cu/ (Zn+Sn) ratio of 0.7 and a Zn/Sn ratio of 1.06. The PV device was fabricated with a structure of SLG/Mo/ CZTS/CdS/ i-ZnO/Al:ZnO /Ni/ Al had parameters of V_{oc} = 480 mV, of J_{sc}= 15.3 $mAcm^{-2}$, FF = 45% and an efficiency of 3.2% [122].

Also, Araki et al. (2009) fabricated CZTS by sulphurisation using coelectroplated Cu/Zn/Sn precursors using the electric furnace at 580 °C and 600 °C. The grain size was in the range of 1–1.5μm, and the chemical composition ratio was Zn-rich, which gave a good PV device performance. The PV device achieved a 3.14% level of efficiency. In addition, the following device characteristics were found: 46% for FF, 12.6 $mAcm^{-2}$ for J_{sc}, 540 mV for V_{oc}, 11.7 Ω for R_s and 161 Ω for R_{sh}, using a structure of glass/ Mo/ CZTS/CdS/Al:ZnO /Al at a sulphurisation temperature of 600 °C [123]. Also, Ge's group (2014) [124] by using co-electrodeposited Cu–Zn–Sn–S precursors at 590 °C for 15 min achieved an efficiency of 5.5% , V_{oc}=673.8 mV, J_{sc}=18.7 $mAcm^{-2}$, FF=44% for solar cell device built as glass/ Mo/CZTS /CdS /ZnO. Also, they found during the high

sulfurization temperature the Cu and Sn content were inadequate and bi-layered CZTS with metallic ratio Zn/Sn=1.16, Cu/ (Zn+Sn) =0.74, S/metals=0.18 was formed in the device. Also, a relatively small energy barrier height of the back contact (Schottky-type barrier) of 44 mV across the cell [124] compared with 0.32 eV [106].

Ennaoui et al. (2009) used the electroplate precursors from an alkaline, cyanide-free bath containing metal salt of Cu (II), Zn(II) and Sn (IV) in an Ar/H_2S atmosphere to fabricate the CZTS. The EDX measurements showed the element distribution maps showing the different distribution positions of secondary phases in the CZTS layers. There were several points that enhanced the Zn-rich signal in the CZTS layer, whereas these were an area of Zn-poor signal which probably due to the presence of a Cu_2SnS_3 phase near the interface. The chemical ratios were 0.97 and 1.08 for Cu/Zn+Sn and Zn/Sn, respectively. The PV device achieved a 3.4% level of PV efficiency with V_{oc} = 563 mV, J_{sc} = 14.8 $mAcm^{-2}$ and FF = 41% [125].

Moreover, Ahmed et al. (2012) fabricated CZTS using the electroplated, stacked metal with different orders of either Cu/Zn/Sn or Cu/Sn/Zn and annealed at a low temperature (210-350 ^oC) in an N_2 atmosphere. This was followed by the annealing processes in a sulphur atmosphere at 585 °C for 12 min. The chemical composition ratios were 1.83, 1.53 and 0.79 for Cu/Sn, Zn/Sn and Cu/Zn+Sn, respectively, which confirms that the film was Zn-rich and Cu-poor. The grain size was in a range of 0.5–1 μm. The secondary phases Cu_2S and ZnS appeared at a sulphurisation temperature of 550 ^oC at 30 min., while the ternary phase Cu_2SnS_3 appeared at 600 ^oC for 20 min. The PV device achieved a PV efficiency level of 7.3% [126].

2.2.8.2.2: Sprayed method

In this method, Nakayma and Ito [127] fabricated CZTS thin films using the sprayed method. The solution was made from a mixture of CuCl, $ZnCl_2$, $SnCl_4$ and thiourea in deionised water and ethanol. After that, the solution was deposited onto a soda lime glass substrate heated to 280–300 ^oC. Then, this was followed by a heating treatment in an Ar/H_2S atmosphere at 550 ^oC for 2 h. The XRD showed thin films with a stannite structure and the presence of a $ZnSnO_3$ phase. Moreover, they studied the effect of Zn concentration on the electrical properties of CZTS. It was found that the deviation of the

film composition increased when the zinc concentration increased, while tin and copper decreased, which can be controlled by varying the concentration of the spray solution.

Kamoun et al. (2007) studied the effect of temperature and time using the spray pyrolysis deposition method. The solution of copper chloride, zinc chloride, tin chloride and thiourea was deposited onto the heated substrate at different temperatures at 280, 300, 320, 340 and 360 ^{o}C for 30 and 60 min. The measurements showed that the sample prepared at the substrate temperature of 340 ^{o}C for 60 min, contained the best crystallinity structure and gave a sharp and narrow x-ray peak on the (112) plane which confirmed the presence of CZTS. The grain size was in a range between 1 and 3 μm, and the surface appeared quite smooth compared to other films grown at low substrate temperatures with band gap of 1.7 eV (as prepared film). The annealing temperature was increased to 550 ^{o}C for 2 h, which was done to improve the optical property, and the band gap was determined as 1.5 eV after this improvement [128]. This result was confirmed by Kumar et al. (2009) when they studied the effect of substrate temperature from 290 to 450 ^{o}C. The result from XRD showed the presence of ZnS in the secondary phase at 450 ^{o}C [129].

Prabhakar et al. (2010) prepared CZTS by using a spray pyrolysis solution that contained CuCl, $ZnCl_2$, $SnCl_4$ and thiourea. Then, this mixture was dissolved in DI water and deposited onto an SLG substrate at different temperatures. The study showed that the sample deposited at 340 ^{o}C gave the best smoothest, most homogeneous and uniform structure. Also, the (112) peaks' intensity become more intense, and width of peaks become narrower compared with others [130]. The PV devices were fabricated with a structure of Ag/ ZnS/ CZTS/ FTO/ SLG achieving V_{oc} =410 mV, J_{sc} = 8 mAcm^{-2} , FF =35.5% and an efficiency of 1.16% [131].

More improvement in CZTS was done by Larramona et al. (2014) [132]. $SnCl_4$, $ZnCl_2$ and CuCl in an aqueous solution of NaHS with CH_3CN mixed rapidly at room temperature were used to fabricate CZTS particles. Then the suspension was washed in water and ethanol. The CZTS was deposited on a heated Mo coated substrate at 300 ^{o}C by spray pyrolysis technique and then followed by two annealing steps under different annealing atmosphere N_2, N_2+H_2S and N_2+H_2S+HCl at 525 ^{o}C for 15 min. The device with structure SLG/Mo/ CZTS/CdS/ZnO/ ITO / Ag achieved V_{oc} = 630 mV, J_{sc} = 19.0 mAcm^{-2}, FF = 50% and an efficiency of 5% under N_2+H_2S+HCl atmosphere.

Nguyen et al. (2015) deposited the CZTS by spray pyrolysis technique on SLG/Mo substrate. CZTS was prepared by using 0.019 M of (Cu $(NO_3)_2$), 0.009 M of (Zn $(NO_3)_2$), 0.0125 M of (Sn $(CH_3SO_3)_2$) and 0.06 M of (SC $(NH_2)_2$). However, after the aqueous solution of CZTS was deposited on heated substrate at 380 °C, following by annealing process by adding 20 mg of sulphur powder in borosilicate glass ampoule at 600 °C for 30 min. the device with a structure of glass/ Mo/ CZTS/ CdS / ZnO/ ITO was fabricated. In this study, under Sn-rich composition, efficient grain growth of the resulting CZTS films achieved the highest efficiency for spray pyrolysis method which was 5.8% with V_{oc} = 647 mV, J_{sc} = 14.9 $mAcm^{-2}$ and FF = 61% under Sn rich condition [133].

2.2.8.2.3: Spin coating from Sol-gel method

Tanaka's group in 2007 fabricated CZTS thin films by the sol-gel method. The solution of the CZTS precursor was prepared from copper II acetate monohydrate, zinc II acetate dehydrate and tin II chloride dehydrate dissolved in methoxyethanol and monoethanolamine and stirred at 450 °C for 1 h. The solution then was deposited onto the SLG substrate by the spin coating method. Then, they were kept dried in the air atmosphere at 300 °C. This was followed by an annealing process in a H_2S+N_2 atmosphere at 500 °C for 1 hour. The chemical compositions showed that the solution was Zn-rich and S-poor as shown in the following ratio: Cu/Zn/Sn/S of 26:14:13:47. The band gap was 1.49 eV [134]. In 2011 [135] they studied the influence of the chemical composition of a sol-gel solution on the CZTS thin film's properties. The study demonstrated that the ratio of Cu/Zn+Sn on the CZTS thin film increases with a decreasing of the ratio of Zn/Sn compared with a sol-gel solution. Also, when the ratio of Cu/Zn+Sn of the sol-gel solution decreases, the grain size in the CZTS thin film becomes larger. The PV device achieved a 2.3% level of efficiency from the CZTS thin film deposited using the sol-gel solution with a Cu/Zn+Sn of 0.8.

Maeda et al. (2011) studied the effect of different concentrations of H_2S (3, 5, 10 and 20%) on the CZTS properties during sulphurisation stage. The chemical compositions were varied by increasing the H_2S concentrations. By increasing the H_2S concentrations from 5% to 20%, the copper content decreases, and the sulphur content increases, and when the H_2S concentrations decrease to 3%, the sulphur content increases. Moreover, the grain size

of the CZTS film annealing to 500°C for 1 h in the 3% H_2S concentration was greater than other films at different concentrations. The PV device achieved a 2.23% efficiency level in 3% H_2S concentration [136].

Yeh et al. (2009) prepared CZTS thin films by using solutions of $CuCl_2$, $ZnCl_2$, $SnCl_4$ and thiourea dissolved in deionised water and ethanol and stirred at 40 °C for 30 min. The solution was deposited onto SLG by the spin coating method and dried on a hot plate for 10 min at 110 °C [75] [137]. The effect of different synthesising temperatures (160, 200, 240, 280 and 320 °C) was studied. The suitable CZTS thin films were kept at a synthesising temperature of 280 °C or higher due to the appearance of unidentified phases at temperatures less than 280 °C. Also, the chemical composition of CZTS was nearly stoichiometric at 280 °C, and the band gap was 1.5 eV[75].

Kissani et al. (2016) synthesised CZTS thin films by a simple and low-cost spin-coating technique, using the sol-gel process without any further sulfurization. They studied the effects of annealing at 400 °C, 450° C, and 500 °C temperature for 1 h on the structural, optical, and electrical properties of the kesterite CZTS thin films. In this study, the grain size of the CZTS thin films increased with annealing temperature and the optical band-gap values were estimated in the range of 1.49 eV to 1.85 eV, depending on the annealing conditions [138].

Tiwari et al. (2014) deposited the CZTS by using sol–gel technique by spin-coating. The CZTS thin film by the replacement reaction route. In this method, the ZnS layer was deposited onto the soda lime glass substrate by chemical path deposition. Then, it was immersed into a metal solution that contained cupric chloride, zinc chloride and stannous chloride, and this mixture was then dissolved in glycerol for 10 min. For solar cells, the ZnO was deposited onto ITO coating on SLG using the sol-gel method by spin coating. Then, CdS was deposited using the CBD method. The CZTS was deposited by the replacement reaction route and then followed by colloid graphite as a top contact. The solar cells with a superstrate configuration structure of graphite/ CZTS/ CdS/ ZnO/ ITO/ SLG yielded a performance that was V_{oc} = 521 mV , J_{sc} =19.13 $mAcm^{-2}$, FF = 62% and an efficiency of 6.17%[139].

2.2.8.2.4: Drop casting and spin coating from hot injection

Guo et al. 2009 synthesised CZTS nanocrystal inks using the hot injection method. In their method, the nanoparticles were synthesised with copper (II) acetylacetonate, zinc (II) acetylacetonate and tin (IV) bis (acetylacetonate) dibromide as metal sources, which were heated in an oleylamine solvent to 130 °C under a vacuum, degassed for 30 min. and purged with argon several times. Then, the temperature was increased to 225 °C, and the solution of elemental sulphur in oleylamine was injected into the mixture. The toluene and isopropanol were added into the solution, and the nanoparticles were collected by using a centrifuge after cooling the solution to 80 °C. The final precipitate was then dispersed again for a stable ink solution in toluene. The PV devices were fabricated from CZTS nanocrystals onto Mo-SLG by the drop casting method. After that, the thin film had a selenisation process under Se vapour in a graphite box to form CZTSSe at 450 °C and 500 °C. XRD measurements showed that as the synthesised particles belonged to kesterite CZTS phase, the solar cell with a structure of SLG/Mo/CZTSSe/CdS/i-ZnO/ITO/Ag achieved a 0.73% level of efficiency for the sample selenised at 450 °C. The sample selenised at 500 °C temperature showed a slight improvement in conversion efficiency at 0.80% with V_{oc} = 210 mV, J_{sc} = 11.5 mA cm^{-2} and FF = 33.1% [140]. In the same year, Steinhagen used the same method for the replacement of tin (IV) bis (acetylacetonate) dibromide by tin (II) chloride dihydrate, and the reaction temperature rose to 280 °C. The CZTS layer was deposited by spray coating, and a device with a structure of Au/CZTS/CdS/ZnO/ITO had a low efficiency of about 0.23% [141]. The next year, the same group used the same method, but CZTS was deposited onto Mo-SLG using the knife coating method. The chemical compositions of the final films had Cu/Zn+Sn ratio of 0.79 and a Zn/Sn ratio of 1.11 [142].

Mendez-Lopez et al (2016) fabricated CZTS nanocrystals by hot injection method. In this method, 2 mmol of $CuCl_2$, 1 mmol of ZnCl, 1 mmol of $SnCl_2$, and 20 ml of oleylamine were mixed and heated to 170 °C for 1 h under argon atmosphere. Meanwhile, another solution was prepared, for which 4 mmol of thioacetamide was dissolved in 3 ml oleylamine. Afterwards, the solution was heated to 230 °C and the thioacetamide-oleylamine solution was rapidly injected. After that, the temperature of solution was kept constant during different times from 3 to 24 h. The CZTS films were deposited on a SLG

by drop coating and dried at room temperature in the air atmosphere. The ratio of Cu/Zn+Sn decreased with increasing reaction time and Zn/Sn increased. The energy band gap decreased with increasing reaction time whereas the average size of particles increased from 20 to 40 nm. Mixed structure of kesterite-wurtzite existed when the reaction time was 6 h and longer [143].

However, the spin coating technique is the main method that used in this project to deposit CZTS nanoparticle inks onto a substrate which will be described in detail in chapter 3.

2.2.8.2.5: Other non-vacuum deposition

Miskin et al., 2013 prepared CZTS nanoparticles by doing some modification on the hot injection method. Precursor composition ratios were as Cu/(Zn+ Sn)= 0.86, Zn/Sn= 1.05, and S/Metals= 1.57. A solution of copper (II) acetylacetonate (1.32 mmol), zinc acetylacetonate hydrate (0.79 mmol), and tin (IV) bis(acetylacetonate) dichloride (0.75 mmol) in 6 mL of OLA was prepared under argon atmosphere in a glove box at 65 °C. A 4.5 mmol of sulphur in OLA was prepared and heated to 65 °C. Then, 12 mL of OLA in the flask was evacuated for 5 min, purged with argon at room temperature. The flask was then heated under vacuum to 130 °C and then increased to 250 °C at which point the sulphur solution was injected and allowed to completely mix for 20 s. This was followed by the rapid injection of the cation precursor solution and allowed to react under argon atmosphere for 60 min. The reaction was then cooled to room temperature, and the product nanoparticles are washed by isopropanol. The main improvement found in this method was the sulphur solution is injected first and followed by precursor solution. The CZTS ink was deposited onto glass by the doctor blade method [144, 145].

The other non-vacuum deposition technique is called the printed screen deposition method. It was performed by Zhou et al. in 2010. The CZTS microparticles were prepared by using wet ball milling. Then, the mixture was dried in a vacuum oven at 40 ^{o}C for 24 h. After that, it was followed by the sintering method at 600 ^{o}C in a quartz tube furnace in a high-purity argon atmosphere for 2 h. The CZTS was wet ball milled and vacuum dried again. The as-prepared CZTS particles were dispersed in isopropanol, stirred for 6h and mixed with ethyl cellulose, which was dissolved in isopropanol to prepare the ink for the

screen printing. Then, the ink of CZTS was printed onto Mo-coated polyimide substrate. The band gap, sheet resistance, carrier concentration, and hall mobility of the screen-printed CZTS layers were 1.49 eV, 2.42×10^{3} Ω, 3.81×10^{18} cm^{-3} and 12.61 $cm^{2}V^{-1}s^{-1}$ respectively. The PV device based on the screen-printed CZTS with a structure of Al/Al:ZnO/CdS / CZTS/ Mo/polyimide showed a 0.49% of efficiency [146].

Mali et al. (2012) synthesised CZTS by successive ionic layer adsorption and reaction (SILAR). The CZTS was deposited onto fluorine doped tin oxide (FTO)-coated glass substrate by immersion of the substrate in a solution of copper sulphate, zinc sulphate and tin sulphate, which was then put in distilled water. Then, it was immersed in sodium sulphate and distilled water. These processes were done at various repeat deposition cycles (10, 20, 30 and 40), and these films were dried at 50 °C for 30 min. The XRD measurement showed the formation of a kesterite structure of the CZTS films. The sample of CZTS at 40 cycles had large particles with a uniform average grain size of about 100 nm. Also, the best PV efficiency was achieved by this sample at 0.396 % [147]. The same group synthesised the kesterite CZTS using the SILAR technique. Some improvements were made, and it achieved a efficiency of 1.85% under 30 $mWcm^{-2}$ illumination [148]. In summery the highest efficiency in each different deposition techniques is summarised in the Table 2.3.

Table 2.3 Highest research device efficiency of CZTS using different deposition techniques.

Deposition method	Efficiency η %	Open circuit voltage V_{oc} mV	Short circuit current density J_{sc} $mAcm^{-2}$	Fill factor FF %
Co-sputtering	11.01	730.6	21.7	69.3
evaporation	9.19	708	21.6	60
PLD	5.2	616	17.9	47.9
electrodeposition	7.3	567	22	58.1
spray pyrolysis	5.8	647	14.9	61
Sol-gel Spin coating	6.17	521	19.13	62
SILAR*	1.85	0.280	3.19	62

* Sample was recorded at 30 mW/cm^2 illumination at room temperature

2.3: References

1. Fonash, S., *Solar Cell Device Physics*. 2010: Elsevier Science.

2. Nelson, J., *The Physics of Solar cells*. 2003, UK: Imperial College press.

3. Würfel, P., *Physics of Solar Cells: From Basic Principles to Advanced Concepts*. 2009: Wiley.

4. Smestad, G.P., *Optoelectronics of Solar Cells*. 2002: Society of Photo Optical.

5. *Standard Solar Spectra https://www.pveducation.org/pvcdrom/appendices/standard-solar-spectra* [cited 18/11/2018].

6. Fonash, S.J., *Solar Cell Device Physics*. Solar Cell Device Physics (Second Edition), ed. S.J. Fonash. 2010, Boston: Academic Press.

7. Fahrenbruch , A.L. and R.H. Bube, *Fundamentals of Solar Cells: Photovoltaic Solar Energy Conversion*. 1 ed. 1983, London: Academic Press.

8. Solanki, C.S., *Solar Photovoltaic: Fundamentals, Technologies and Applications*. 2 ed. 2011, Delhi: PHI Learning Private Limited.

9. Paier, J., et al., *Cu_2ZnSnS_4 as a potential photovoltaic material: A hybrid Hartree-Fock density functional theory study*. Physical Review B, 2009. **79**(11): p. 8.

10. Lutz, J., et al., *Semiconductor Power Devices: Physics, Characteristics, Reliability*. 2011: Springer Berlin Heidelberg.

11. Brennan, K.F., *The Physics of Semiconductors: With Applications to Optoelectronic Devices*. 1999, UK: Cambridge University Press.

12. Rockett, A., *The Materials Science of Semiconductors*. 2007: Springer US.

13. Yacobi, B.G., *Semiconductor Materials An Introduction to Basic Principles*. 2004, USA: Kluwer Academic Publishers.

14. Sze, S.M. and K.N. Kwok, *Physics of Semiconductor Devices*. 2006: Wiley.

15. Godse, A. and U. Bakshi, *Semiconductor Devices & Circuits*. 2008: Technical Publications.

16. Dasgupta, N. and A. Dasgupta, *Semiconductor devices: Modelling and technology*. 2004: PHI Learning.

17. van Sark, W., *Teaching the relation between solar cell efficiency and annual energy yield.* European Journal of Physics, 2007. **28**(3): p. 415-427.

18. Rauschenbach, H.S., *Solar Cell Array Design Handbook: The Principles and Technology of Photovoltaic Energy Conversion*. 2012: Springer Netherlands.

19. Liu, C.L., et al., *An Asymmetrical Fuzzy-Logic-Control-Based MPPT Algorithm for Photovoltaic Systems.* Energies, 2014. **7**(4): p. 2177-2193.

20. Suryawanshi, M.P., et al., *CZTS based thin film solar cells: a status review.* Materials Technology, 2013. **28**(1-2): p. 98-109.

21. Wang, H.X., *Progress in Thin Film Solar Cells Based on Cu_2ZnSnS_4.* International Journal of Photoenergy, 2011: p. 10.

22. Bube, R.H., *Photovoltaic Malterials*. 2 ed. 2006, London: Imperial College Press.

23. Sukhatme, S., P & Nayak, J. K. , *Solar Energy: Principles of Thermal Collection and Storage*. 3 ed. 2008, New Delhi: Tata MCGRAW-HILL Publishing Company Limited.

24. Guha, S., et al., *Enhancement of open circuit voltage in high-efficiency amorphous-silicon alloy solar-cells.* Applied Physics Letters, 1986. **49**(4): p. 218-219.

25. Kayes, B.M., et al. *27.6% conversion efficiency, a new record for single-junction solar cells under 1 sun illumination*. in *Photovoltaic Specialists Conference (PVSC), 2011 37th IEEE*. 2011. IEEE.

26. Syum, Z. and H. Woldeghebriel, *The structure and electronic properties of (GaAs)(n) and Al/In-doped (GaAs)(n) (n=2-20) clusters.* Computational and Theoretical Chemistry, 2014. **1048**: p. 7-17.

27. Mangla, O. and S. Roy, *A study on aberrations in energy band gap of quantum confined gallium arsenide spherical nanoparticles.* Materials Letters, 2015. **143**: p. 48-50.

28. Akinlami, J.O. and A.O. Ashamu, *Optical properties of GaAs.* Journal of Semiconductors, 2013. **34**(3): p. 032002.

29. Green, M.A., et al., *Solar cell efficiency tables (version 48).* Progress in Photovoltaics: Research and Applications, 2016. **24**(7): p. 905-913.

30. Wu, X., *High-efficiency polycrystalline CdTe thin-film solar cells.* Solar Energy, 2004. **77**(6): p. 803-814.

31. Chelvanathan, P., M.I. Hossain, and N. Amin, *Performance analysis of copper-indium-gallium-diselenide (CIGS) solar cells with various buffer layers by SCAPS*. Current Applied Physics, 2010. **10**(3): p. S387-S391.

32. Persson, C., *Thin-film ZnO/CdS/$CuIn_{1-x}Ga_xSe_2$ solar cells: Anomalous physical properties of the $CuIn_{1-x}Ga_xSe_2$ absorber*. Brazilian Journal of Physics, 2006. **36**(3B): p. 948-951.

33. Decock, K., J. Lauwaert, and M. Burgelman, *Characterization of graded CIGS solar cells*, in *Proceedings of Inorganic and Nanostructured Photovoltaics*, G. Beaucarne, et al., Editors. 2010, Elsevier Science Bv: Amsterdam. p. 49-54.

34. Wu, J.L., Hirai, Y., Kato, T., Sugimoto, H., Bermudez, V.,. *New world record efficiency up to 22.9% for $Cu(In,Ga)(Se,S)_2$ thin-film solar cell*. in *7th World Conference on Photovoltaic Energy Conversion (WCPEC-7)*. 2018. Waikoloa, HI, USA.

35. Chen, S., et al., *Crystal and electronic band structure of Cu_2ZnSnX_4 (X=S and Se) photovoltaic absorbers: First-principles insights*. Applied Physics Letters, 2009. **94**(4).

36. Fthenakis, V., *Sustainability of photovoltaics: The case for thin-film solar cells*. Renewable & Sustainable Energy Reviews, 2009. **13**(9): p. 2746-2750.

37. Shockley, W. and H.J. Queisser, *Detailed Balance Limit of Efficiency of P-N Junction Solar Cells*. Journal of Applied Physics, 1961. **32**(3).

38. Paier, J., et al., *Cu_2ZnSnS_4 as a potential photovoltaic material: A hybrid Hartree-Fock density functional theory study*. Physical Review B, 2009. **79**(11).

39. Rios, L.E.V., et al., *Existence of off-stoichiometric single phase kesterite*. Journal of Alloys and Compounds, 2016. **657**: p. 408-413.

40. Schorr, S., *The crystal structure of kesterite type compounds: A neutron and X-ray diffraction study*. Solar Energy Materials and Solar Cells, 2011. **95**(6): p. 1482-1488.

41. Valakh, M.Y., et al., *Optically induced structural transformation in disordered kesterite Cu_2ZnSnS_4*. Jetp Letters, 2013. **98**(5): p. 255-258.

42. Lu, X.T., et al., *Wurtzite Cu_2ZnSnS_4 nanocrystals: a novel quaternary semiconductor*. Chemical Communications, 2011. **47**(11): p. 3141-3143.

43. Luo, Q., et al., *Controllable Synthesis of Wurtzite Cu_2ZnSnS_4 Nanocrystals by Hot-Injection Approach and Growth Mechanism Studies*. Chemistry-an Asian Journal, 2014. **9**(8): p. 2309-2316.

44. Li, M., et al., *Synthesis of Pure Metastable Wurtzite CZTS Nanocrystals by Facile One-Pot Method*. Journal of Physical Chemistry C, 2012. **116**(50): p. 26507-26516.

45. Nagoya, A., et al., *Defect formation and phase stability of Cu_2ZnSnS_4 photovoltaic material.* Physical Review B, 2010. **81**(11).

46. Abermann, S., *Non-vacuum processed next generation thin film photovoltaics: Towards marketable efficiency and production of CZTS based solar cells.* Solar Energy, 2013. **94**: p. 37-70.

47. Chilate, V.A. and K.S. Srinadh, *Status of CZTS Thin Films and Future Prospect of CZTS Nanocrystal Synthesis by Three Step Hybrid Technology.*

48. Bao, W. and M. Ichimura, *Influence of Secondary Phases in Kesterite-Cu_2ZnSnS_4 Absorber Material Based on the First Principles Calculation.* International Journal of Photoenergy, 2015: p. 6.

49. Kumar, M., et al., *Strategic review of secondary phases, defects and defect-complexes in kesterite CZTS-Se solar cells.* Energy & Environmental Science, 2015.

50. Wu, C.Z., et al., *Hexagonal Cu_2SnS_3 with metallic character: Another category of conducting sulfides.* Applied Physics Letters, 2007. **91**(14): p. 3.

51. Just, J., et al., *Secondary phases and their influence on the composition of the kesterite phase in CZTS and CZTSe thin films.* Physical Chemistry Chemical Physics, 2016. **18**(23): p. 15988-15994.

52. Burton, L.A., et al., *Synthesis, Characterization, and Electronic Structure of Single-Crystal SnS, Sn_2S_3, and SnS_2.* Chemistry of Materials, 2013. **25**(24): p. 4908-4916.

53. Just, J., et al., *Determination of secondary phases in kesterite Cu_2ZnSnS_4 thin films by x-ray absorption near edge structure analysis.* Applied Physics Letters, 2011. **99**(26).

54. Berg, D.M., et al., *Discrimination and detection limits of secondary phases in Cu_2ZnSnS_4 using X-ray diffraction and Raman spectroscopy.* Thin Solid Films, 2014. **569**: p. 113-123.

55. Brandl, M., et al., *In-situ X-ray diffraction analysis of the recrystallization process in Cu_2ZnSnS_4 nanoparticles synthesised by hot-injection.* Thin Solid Films, 2015. **582**: p. 269-271.

56. Zhou, B., D. Xia, and Y. Wang, *Phase-selective synthesis and formation mechanism of CZTS nanocrystals.* RSC Advances, 2015. **5**(86): p. 70117-70126.

57. Schurr, R., et al., *The crystallisation of Cu_2ZnSnS_4 thin film solar cell absorbers from co-electroplated Cu-Zn-Sn precursors.* Thin Solid Films, 2009. **517**(7): p. 2465-2468.

58. Scragg, J.J., et al., *New routes to sustainable photovoltaics: evaluation of Cu_2ZnSnS_4 as an alternative absorber material.* physica status solidi (b), 2008. **245**(9): p. 1772-1778.

59. Wang, K.J., et al., *Structural and elemental characterization of high efficiency Cu_2ZnSnS_4 solar cells.* Applied Physics Letters, 2011. **98**(5): p. 3.

60. Jiang, F., et al., *Preparation and Optoelectronic Properties of Cu_2ZnSnS_4 Film.* Journal of the Electrochemical Society, 2012. **159**(6): p. H565-H569.

61. Yan, Z.G., et al., *Growth of Cu_2ZnSnS_4 thin films on transparent conducting glass substrates by the solvothermal method.* Materials Letters, 2013. **111**: p. 120-122.

62. Fontané, X., et al., *In-depth resolved Raman scattering analysis for the identification of secondary phases: Characterization of Cu_2ZnSnS_4 layers for solar cell applications.* Applied Physics Letters, 2011. **98**(18): p. 181905.

63. Fernandes, P.A., P.M.P. Salome, and A.F.d. Cunha, *Growth and Raman scattering characterization of Cu_2ZnSnS_4 thin films.* Thin Solid Films, 2009. **517**(7): p. 2519-2523.

64. Fernandes, P.A., P.M.P. Salome, and A.F.d. Cunha, *A study of ternary Cu_2SnS_3 and Cu_3SnS_4 thin films prepared by sulfurizing stacked metal precursors.* Journal of Physics D-Applied Physics, 2010. **43**(21).

65. Kheraj, V., et al., *Synthesis and characterisation of Copper Zinc Tin Sulphide (CZTS) compound for absorber material in solar-cells.* Journal of Crystal Growth, 2013. **362**: p. 174-177.

66. Fernandes, P.A., P.M.P. Salomé, and A.F.d. Cunha, *Study of polycrystalline Cu_2ZnSnS_4 films by Raman scattering.* Journal of Alloys and Compounds, 2011. **509**(28): p. 7600-7606.

67. Price, L.S., et al., *Atmospheric pressure chemical vapor deposition of tin sulfides (SnS, Sn_2S_3, and SnS_2) on glass.* Chemistry of Materials, 1999. **11**(7): p. 1792-1799.

68. Han, J., et al., *Crystallization behaviour of co-sputtered Cu_2ZnSnS_4 precursor prepared by sequential sulfurization processes.* Nanotechnology, 2013. **24**(9): p. 8.

69. Lin, X., et al., *Structural and optical properties of Cu_2ZnSnS_4 thin film absorbers from ZnS and Cu_3SnS_4 nanoparticle precursors.* Thin Solid Films, 2013. **535**(0): p. 10-13.

70. Chen, S., et al., *Classification of Lattice Defects in the Kesterite Cu_2ZnSnS_4 and Cu2ZnSnSe$_4$ Earth-Abundant Solar Cell Absorbers.* Advanced Materials, 2013. **25**(11): p. 1522-1539.

71. Chen, S.Y., et al., *Defect physics of the kesterite thin-film solar cell absorber Cu_2ZnSnS_4.* Applied Physics Letters, 2010. **96**(2): p. 3.

72. Yu, K. and E.A. Carter, *Determining and Controlling the Stoichiometry of Cu_2ZnSnS_4 Photovoltaics: The Physics and Its Implications.* Chemistry of Materials, 2016. **28**(12): p. 4415-4420.

73. Romero, M.J., et al., *A Comparative Study of the Defect Point Physics and Luminescence of the Kesterites Cu_2ZnSnS_4 and $Cu_2ZnSnSe_4$ and Chalcopyrite $Cu(In,Ga)Se_2$.* 2012 38th Ieee Photovoltaic Specialists Conference (Pvsc), 2012: p. 3349-3353.

74. Azimi, H., Y. Hou, and C.J. Brabec, *Towards low-cost, environmentally friendly printed chalcopyrite and kesterite solar cells.* Energy & Environmental Science, 2014. **7**(6): p. 1829-1849.

75. Yeh, M., C. Lee, and D. Wuu, *Influences of synthesizing temperatures on the properties of Cu_2ZnSnS_4 prepared by sol–gel spin-coated deposition.* Journal of Sol-Gel Science and Technology, 2009. **52**(1): p. 65-68.

76. Biswas, K., S. Lany, and A. Zunger, *The electronic consequences of multivalent elements in inorganic solar absorbers: Multivalency of Sn in Cu_2ZnSnS_4.* Applied Physics Letters, 2010. **96**(20).

77. Tanaka, K., et al., *Cu_2ZnSnS_4 thin film solar cells prepared by non-vacuum processing.* Solar Energy Materials and Solar Cells, 2009. **93**(5): p. 583-587.

78. Romero, M.J., et al., *Comparative study of the luminescence and intrinsic point defects in the kesterite Cu_2ZnSnS_4 and chalcopyrite $Cu(In,Ga)Se_2$ thin films used in photovoltaic applications.* Physical Review B, 2011. **84**(16).

79. Huang, D. and C. Persson, *Band gap change induced by defect complexes in Cu_2ZnSnS_4.* Thin Solid Films, 2013. **535**: p. 265-269.

80. Poornima, N., et al., *Defect Analysis Of CZTS Thin Films Using Photoluminescence Technique.* Solid State Physics, Vol 57, 2013. **1512**: p. 464-465.

81. Chen, S.Y., et al., *Intrinsic point defects and complexes in the quaternary kesterite semiconductor Cu_2ZnSnS_4.* Physical Review B, 2010. **81**(24).

82. Ito, K. and T. Nakazawa, *Electrical and optical-properties of stannite-type quaternary semiconductor thin-films.* Japanese Journal of Applied Physics Part 1-Regular Papers Short Notes & Review Papers, 1988. **27**(11): p. 2094-2097.

83. Seol, J.S., et al., *Electrical and optical properties of Cu_2ZnSnS_4 thin films prepared by rf magnetron sputtering process.* Solar Energy Materials and Solar Cells, 2003. **75**(1-2): p. 155-162.

84. Tanaka, T., et al., *Preparation of Cu_2ZnSnS_4 thin films by hybrid sputtering.* Journal of Physics and Chemistry of Solids, 2005. **66**(11): p. 1978-1981.

85. Fernandes, P.A., P.M.P. Salome, and A.F.d. Cunha, *Precursors' order effect on the properties of sulfurized Cu_2ZnSnS_4 thin films.* Semiconductor Science and Technology, 2009. **24**(10).

86. Fernandes, P.A., et al., *Cu_2ZnSnS_4 solar cells prepared with sulphurized dc-sputtered stacked metallic precursors.* Thin Solid Films, 2010. **519**(21): p. 7382-7385.

87. Fernandes, P.A., et al., *Admittance spectroscopy of Cu_2ZnSnS_4 based thin film solar cells.* Applied Physics Letters, 2012. **100**(23).

88. Leitao, J.P., et al., *Study of optical and structural properties of Cu_2ZnSnS_4 thin films.* Thin Solid Films, 2011. **519**(21): p. 7390-7393.

89. Leitao, J.P., et al., *Photoluminescence and electrical study of fluctuating potentials in Cu_2ZnSnS_4-based thin films.* Physical Review B, 2011. **84**(2): p. 024120.

90. Shin, S.W., et al., *Studies on Cu_2ZnSnS_4 (CZTS) absorber layer using different stacking orders in precursor thin films.* Solar Energy Materials and Solar Cells, 2011. **95**(12): p. 3202-3206.

91. Pawar, S.M., et al., *Synthesis of Cu_2ZnSnS_4 (CZTS) absorber by rapid thermal processing (RTP) sulfurization of stacked metallic precursor films for solar cell applications.* Materials Letters, 2014. **118**: p. 76-79.

92. Dhakal, T.P., et al., *Characterization of a CZTS thin film solar cell grown by sputtering method.* Solar Energy, 2014. **100**: p. 23-30.

93. Lin, Y.P., et al., *Preparation of Cu_2ZnSnS_4 (CZTS) sputtering target and its application to the fabrication of CZTS thin-film solar cells.* Journal of Alloys and Compounds, 2016. **654**: p. 498-508.

94. Yan, C., et al., *Boost V_{oc} of pure sulfide kesterite solar cell via a double CZTS layer stacks.* Solar Energy Materials and Solar Cells, 2017. **160**: p. 7-11.

95. Feng, Y., et al., *The dependence of open-circuit voltage on the element component in Cu_2ZnSnS_4 film solar cells.* Surface & Coatings Technology, 2017. **320**: p. 65-69.

96. Feng, W.M., et al., *Influence of Annealing Temperature on CZTS Thin Film Surface Properties.* Journal of Electronic Materials, 2017. **46**(1): p. 288-295.

97. Feng, Y., et al., *A low-temperature formation path toward highly efficient Se-free Cu_2ZnSnS_4 solar cells fabricated through sputtering and sulfurization.* Crystengcomm, 2016. **18**(6): p. 1070-1077.

98. Yan, C., et al., *Cu_2ZnSnS_4 solar cells with over 10% power conversion efficiency enabled by heterojunction heat treatment.* Nature Energy, 2018. **3**(9): p. 764-772.

99. Katagiri, H., et al., *Preparation and evaluation of Cu_2ZnSnS_4 thin films by sulfurization of E-B evaporated precursors.* Solar Energy Materials and Solar Cells, 1997. **49**(1-4): p. 407-414.

100. Friedlmeier, T.M.W., N.; Walter,Th.; Dittrich, H.; and Schock, H.-W. , *Heterojunctions based on Cu_2ZnSnS_4 and $Cu_2ZnSnSe_4$ thin films.* 1997: p. 4.

101. Katagiri, H., et al., *Development of CZTS-based thin film solar cells.* Thin Solid Films, 2009. **517**(7): p. 2455-2460.

102. Katagiri, H., et al., *Characterization of Cu_2ZnSnS_4 thin films prepared by vapor phase sulfurization.* Japanese Journal of Applied Physics Part 1-Regular Papers Short Notes & Review Papers, 2001. **40**(2A): p. 500-504.

103. Katagiri, H., et al., *Solar cell without environmental pollution by using CZTS thin film*. Proceedings of 3rd World Conference on Photovoltaic Energy Conversion, Vols a-C, ed. K. Kurokawa, et al. 2003. 2874-2879.

104. Kobayashi, T., et al., *Investigation of Cu_2ZnSnS_4 based thin film solar cells using abundant materials.* Japanese Journal of Applied Physics Part 1-Regular Papers Brief Communications & Review Papers, 2005. **44**(1B): p. 783-787.

105. Schubert, B.-A., et al., *Cu_2ZnSnS_4 thin film solar cells by fast coevaporation.* Progress in Photovoltaics, 2011. **19**(1): p. 93-96.

106. Wang, K., et al., *Thermally evaporated Cu_2ZnSnS_4 solar cells.* Applied Physics Letters, 2010. **97**(14): p. 3.

107. Shin, B., et al., *Thin film solar cell with 8.4% power conversion efficiency using an earth-abundant Cu_2ZnSnS_4 absorber.* Progress in Photovoltaics, 2013. **21**(1): p. 72-76.

108. Sakai, N., H. Hiroi, and H. Sugimoto. *Development of Cd-free buffer layer for Cu_2ZnSnS_4 thin-film solar cells*. in *Photovoltaic Specialists Conference (PVSC), 2011 37th IEEE*. 2011. IEEE.

109. Hiroi, H., N. Sakai, and H. Sugimoto, *Development of high efficiency Cu_2ZnSnS_4 solar cells and modules.* 26th EU PVSEC, 2011.

110. Kato, T., et al. *Characterization of front and back interfaces on Cu_2ZnSnS_4 thin-film solar cells*. in *27th European photovoltaic solar energy conference and exhibition*. 2012.

111. Hiroi, H., N. Sakai, and H. Sugimoto. *Cd-free 5× 5 cm^2 sized Cu_2ZnSnS_4 submodules*. in *Photovoltaic Specialists Conference (PVSC), 2011 37th IEEE*. 2011. IEEE.

112. Sakthivel, S. and V. Baskaran, *Photovoltaic Study of CZTS Thin Films Grown by Vacuum Evaporation and Chemical Bath Deposition Methods.* An International Research Journal of Nano Science & Technology, 2015. **Nano Vision Vol. 5, Issue 7-9, July-September, 2015 (Pages 169-294)**.

113. Cazzaniga, A., et al., *Ultra-thin Cu_2ZnSnS_4 solar cell by pulsed laser deposition.* Solar Energy Materials and Solar Cells, 2017. **166**: p. 91-99.

114. Vanalakar, S.A., et al., *A review on pulsed laser deposited CZTS thin films for solar cell applications.* Journal of Alloys and Compounds, 2015. **619**: p. 109-121.

115. Moriya, K., K. Tanaka, and H. Uchiki, *Fabrication of Cu_2ZnSnS_4 thin-film solar cell prepared by pulsed laser deposition.* Japanese Journal of Applied Physics Part 1-Regular Papers Brief Communications & Review Papers, 2007. **46**(9A): p. 5780-5781.

116. Moriya, K., K. Tanaka, and H. Uchiki, *Cu_2ZnSnS_4 thin films annealed in H_2S atmosphere for solar cell absorber prepared by pulsed laser deposition.* Japanese Journal of Applied Physics, 2008. **47**(1): p. 602-604.

117. Pawar, S.M., et al., *Effect of laser incident energy on the structural, morphological and optical properties of Cu_2ZnSnS_4 (CZTS) thin films.* Current Applied Physics, 2010. **10**(2): p. 565-569.

118. Moholkar, A.V., et al., *Synthesis and characterization of Cu_2ZnSnS_4 thin films grown by PLD: Solar cells.* Journal of Alloys and Compounds, 2011. **509**(27): p. 7439-7446.

119. Jin, X., et al., *Pulsed laser deposition of $Cu_2ZnSn(S_xSe_{1-x})_4$ thin film solar cells using quaternary oxide target prepared by combustion method.* Solar Energy Materials and Solar Cells, 2016. **155**: p. 216-225.

120. Scragg, J.J., P.J. Dale, and L.M. Peter, *Towards sustainable materials for solar energy conversion: Preparation and photoelectrochemical characterization of Cu_2ZnSnS_4.* Electrochemistry Communications, 2008. **10**(4): p. 639-642.

121. Scragg, J.J., P.J. Dale, and L.M. Peter, *Synthesis and characterization of Cu_2ZnSnS_4 absorber layers by an electrodeposition-annealing route.* Thin Solid Films, 2009. **517**(7): p. 2481-2484.

122. Scragg, J.J., D.M. Berg, and P.J. Dale, *A 3.2% efficient Kesterite device from electrodeposited stacked elemental layers.* Journal of Electroanalytical Chemistry, 2010. **646**(1-2): p. 52-59.

123. Araki, H., et al., *Preparation of Cu_2ZnSnS_4 thin films by sulfurization of co-electroplated Cu-Zn-Sn precursors.* physica status solidi (c), 2009. **6**(5): p. 1266-1268.

124. Ge, J., et al., *A 5.5% efficient co-electrodeposited ZnO/CdS/Cu_2ZnSnS_4/Mo thin film solar cell.* Solar Energy Materials and Solar Cells, 2014. **125**: p. 20-26.

125. Ennaoui, A., et al., *Cu_2ZnSnS_4 thin film solar cells from electroplated precursors: Novel low-cost perspective.* Thin Solid Films, 2009. **517**(7): p. 2511-2514.

126. Ahmed, S., et al., *A High Efficiency Electrodeposited Cu_2ZnSnS_4 Solar Cell.* Advanced Energy Materials, 2012. **2**(2): p. 253-259.

127. Nakayama, N. and K. Ito, *Sprayed films of stannite Cu_2ZnSnS_4.* Applied Surface Science, 1996. **92**(0): p. 171-175.

128. Kamoun, N., H. Bouzouita, and B. Rezig, *Fabrication and characterization of Cu_2ZnSnS_4 thin films deposited by spray pyrolysis technique.* Thin Solid Films, 2007. **515**(15): p. 5949-5952.

129. Kishore Kumar, Y.B., et al., *Preparation and characterization of spray-deposited Cu_2ZnSnS_4 thin films.* Solar Energy Materials and Solar Cells, 2009. **93**(8): p. 1230-1237.

130. Prabhakar, T., J. Nagaraju, and Ieee, *Ultrasonic spray pyrolysis of CZTS solar cell absorber layers and characterization studies.* 35th Ieee Photovoltaic Specialists Conference, 2010: p. 1964-1969.

131. Prabhakar, T. and J. Nagaraju. *Device parameters of Cu_2ZnSnS_4 thin film solar cell.* in *Photovoltaic Specialists Conference (PVSC), 2011 37th IEEE*. 2011. IEEE.

132. Larramona, G., et al., *Efficient Cu_2ZnSnS_4 solar cells spray coated from a hydro-alcoholic colloid synthesized by instantaneous reaction.* Rsc Advances, 2014. **4**(28): p. 14655-14662.

133. Nguyen, T.H., et al., *Cu_2ZnSnS_4 thin film solar cells with 5.8% conversion efficiency obtained by a facile spray pyrolysis technique.* Rsc Advances, 2015. **5**(95): p. 77565-77571.

134. Tanaka, K., N. Moritake, and H. Uchiki, *Preparation of thin films by sulfurizing sol–gel deposited precursors.* Solar Energy Materials and Solar Cells, 2007. **91**(13): p. 1199-1201.

135. Tanaka, K., et al., *Chemical composition dependence of morphological and optical properties of Cu_2ZnSnS_4 thin films deposited by sol-gel sulfurization and Cu_2ZnSnS_4 thin film solar cell efficiency.* Solar Energy Materials and Solar Cells, 2011. **95**(3): p. 838-842.

136. Maeda, K., et al., *Influence of H_2S concentration on the properties of Cu_2ZnSnS_4 thin films and solar cells prepared by sol–gel sulfurization.* Solar Energy Materials and Solar Cells, 2011. **95**(10): p. 2855-2860.

137. Jiang, M., et al., *Cu_2ZnSnS_4 polycrystalline thin films with large densely packed grains prepared by sol-gel method.* Journal of Photonics for Energy, 2011. **1**.

138. El Kissani, A., et al., *Synthesis, annealing, characterization, and electronic properties of thin films of a quaternary semiconductor; copper zinc tin sulfide.* Spectroscopy Letters, 2016. **48**(5): p. 343-347.

139. Tiwari, D., et al., *Cu_2ZnSnS_4 thin films by simple replacement reaction route for solar photovoltaic application.* Thin Solid Films, 2014. **551**(0): p. 42-45.

140. Guo, Q., H.W. Hillhouse, and R. Agrawal, *Synthesis of Cu_2ZnSnS_4 nanocrystal ink and its use for solar cells.* Journal of the American Chemical Society, 2009. **131**(33): p. 11672-11673.

141. Steinhagen, C., et al., *Synthesis of Cu_2ZnSnS_4 Nanocrystals for Use in Low-Cost Photovoltaics.* Journal of the American Chemical Society, 2009. **131**(35): p. 12554-+.

142. Guo, Q., et al., *Fabrication of 7.2% Efficient CZTSSe Solar Cells Using CZTS Nanocrystals.* Journal of the American Chemical Society, 2010. **132**(49): p. 17384-17386.

143. Mendez-Lopez, A., et al., *Synthesis and Characterization of Colloidal CZTS Nanocrystals by a Hot-Injection Method.* Journal of Nanomaterials, 2016.

144. Miskin, C.K., et al., *9.0% efficient $Cu_2ZnSn(S,Se)_4$ solar cells from selenized nanoparticle inks.* Progress in Photovoltaics, 2015. **23**(5): p. 654-659.

145. Miskin, C.K., et al., *High Efficiency Cu_2ZnSnS_4 Nanocrystal Ink Solar Cells through Improved Nanoparticle Synthesis and Selenization.* 2013 Ieee 39th Photovoltaic Specialists Conference (Pvsc), 2013: p. 34-37.

146. Zhou, Z.H., et al., *Fabrication of Cu_2ZnSnS_4 screen printed layers for solar cells.* Solar Energy Materials and Solar Cells, 2010. **94**(12): p. 2042-2045.

147. Mali, S.S., et al., *Synthesis and characterization of Cu_2ZnSnS_4 thin films by SILAR method.* Journal of Physics and Chemistry of Solids, 2012. **73**(6): p. 735-740.

148. Mali, S.S., et al., *Novel synthesis of kesterite Cu_2ZnSnS_4 nanoflakes by successive ionic layer adsorption and reaction technique: Characterization and application.* Electrochimica Acta, 2012. **66**(0): p. 216-221.

Chapter 3: Experimental Methods and Characterization Techniques

3.1: Experimental methods

3.1.1: CZTS nanoparticle synthesis

The CZTS nanocrystal inks were synthesised via the hot injection method by using oleylamine as a solvent [1]. By using the hot injection technique, synthesis parameters such as composition, shape, phase and particle size distribution were controlled easily. In this method as shown in Figure 3.1, a 100 ml volume three necked-flask was used to mix the salts; two necks were connected to a Schlenk line to either purge the reaction with argon gas or evacuate with a vacuum. The other neck was used to monitor temperature and inject the sulphur solution. In this method, the nanoparticles were synthesised with 0.4 g of copper (II) acetylacetonate, 0.2 g of zinc (II) acetylacetonate and 0.3 g tin (IV) bis(acetylacetonate) dichloride as metal sources, which were heated in 12 ml oleylamine to 140 ^{o}C under vacuum and degassed for 30 min with stirring and purged with argon several times. Then, a solution of 0.1 g elemental sulphur in 3 ml oleylamine was injected into the mixture after the temperature was increased to 225 ^{o}C and left the mixture for 30 min. after that the mixture left to cool to 30 ^{o}C in air. Then, 5 ml of toluene and 40 ml of isopropanol were added into the solution, and the nanoparticles were collected using the centrifuge at 10000 rpm for 10 min. The supernatant was then decanted. Afterwards, 20 ml of toluene and 10 ml of isopropanol were added to mixture and centrifuged at 8000 rpm for 10 min, the supernatant was decanted again. These processes were repeated twice, the resultant CZTS powder was dried under vacuum and prepared as a high concentration ink by suspending in hexanethiol as a solvent (200 mg of CZTS in 1 ml of hexanethiol).

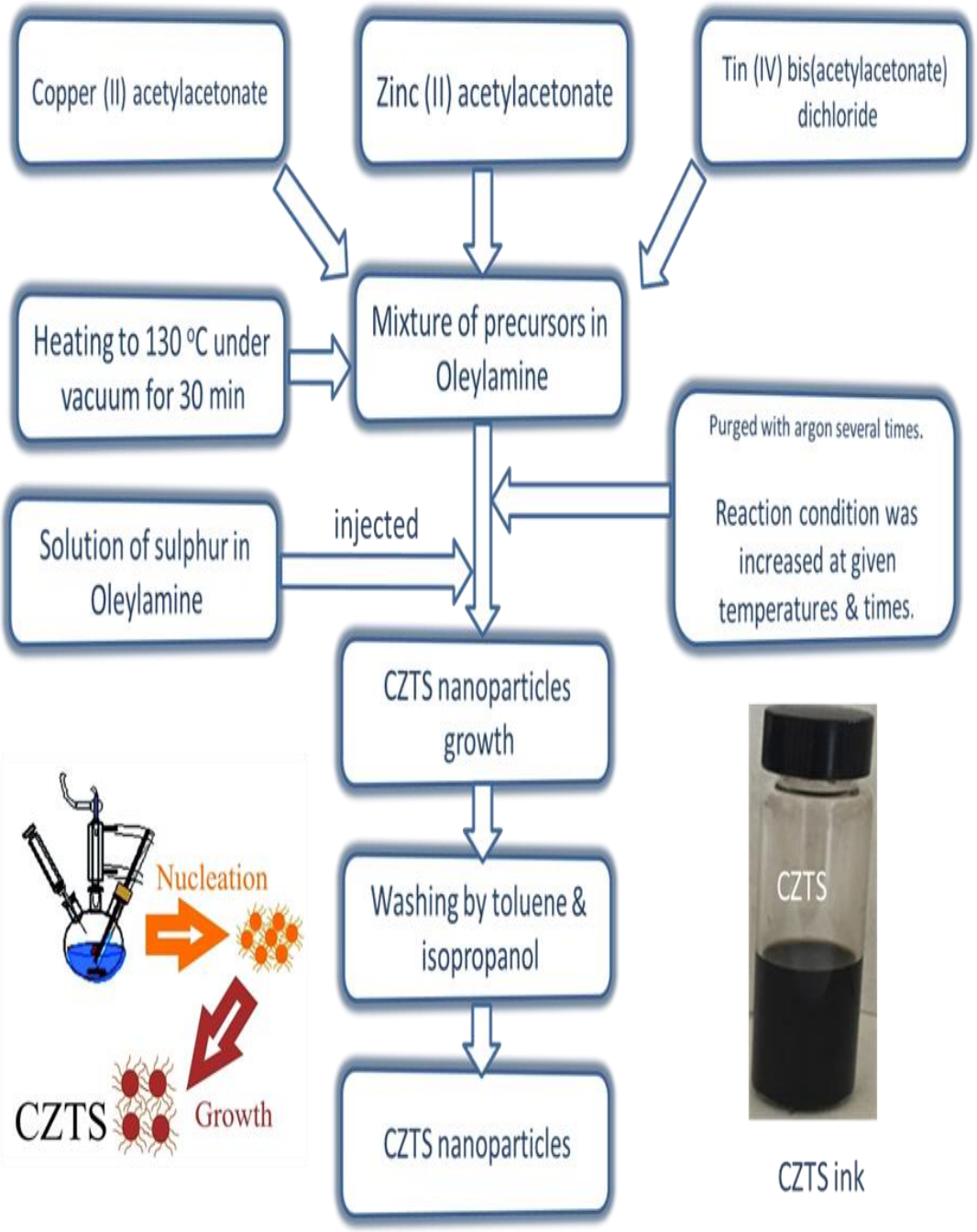

Figure 3.1 Schematic diagram for CZTS fabrication process.

3.1.2: CZTS nanoparticles thin film deposition techniques

The CZTS nanoparticles were deposited onto glass substrate by the spin coating technique. The glass was cleaned by washing with acetone, methanol and distilled water for ten minutes in ultrasonic bath. Then, the glass was dried by using nitrogen flow. The high concentration of CZTS ink (200 mg/ml in hexanethiol solvent) was dropped onto the glass placed in a spin coater which spins at high speed; 2500 rpm for 10 second to achieve a highly uniform film. The samples are then preheated in air at 150 ^{o}C for 30 seconds and 300 ^{o}C for 30 seconds. These steps were repeated 8 times to get a suitable thickness of CZTS layer which is around 1 to 2 μm.

3.1.3: Annealing process

The CZTS thin films on substrates were loaded in the furnace tube manually. After that the two ends of the tube caps were connected to different valves; a vacuum pump, exhaustion line, nitrogen and H_2S supplies. For an N_2 atmosphere where different annealing temperature, time and ramping rate conditions were applied, the tube was evacuated by using a rotary vacuum pump and the furnace tube was filled with N_2 gas. For a H_2S atmosphere, after rotary vacuum pump closing a mix gas of H_2S and N_2 with a composition ratio of 20:80 was introduced and it was left to fill the tube and the pressure monitored until it reached the desired pressure of 0.15 atm and the gas supply was then closed. For furnace annealing treatments, various temperatures, times and ramping rates were applied. The processes commenced at 300 ^{o}C for with a ramping rate of 10 ^{o}C/ min for 1 h under N_2 atmosphere. After that the furnace was left to cool naturally overnight. These processes were repeated for different temperatures 400, 500 and 600 ^{o}C, and for different times 0.5, 1.5 and 2 h, and different ramping rates 5, 15 and 20 ^{o}C/ min. Lastly, after the annealing treatment was finished under a (20%) H_2S + (80%) N_2 atmosphere, the furnace tube was flushed several times with nitrogen gas and vented.

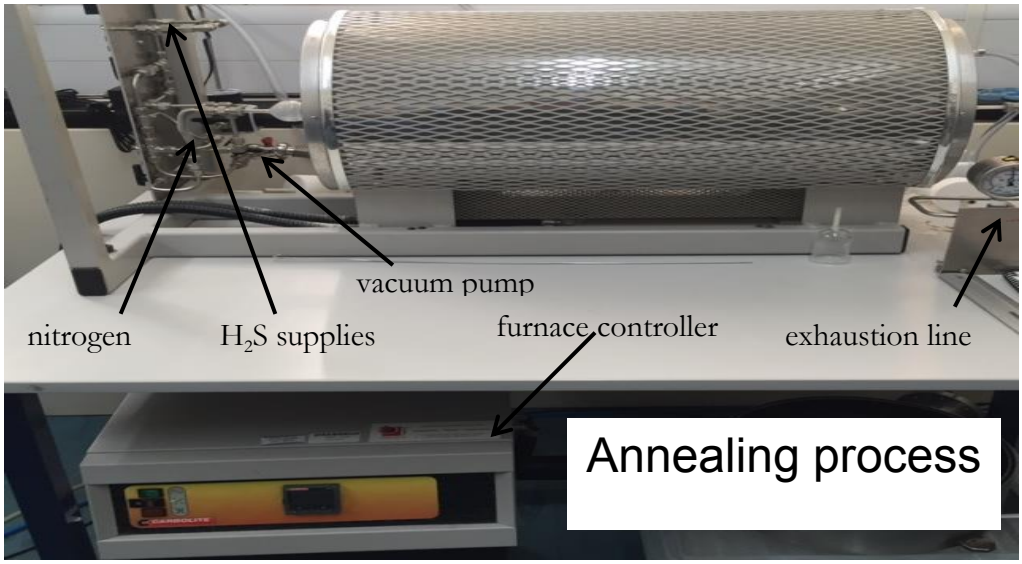

Figure 3.2 Annealing process by using furnace

3.1.4: Device fabrication

3.1.4.1: Mo deposition

Mo films were deposited by using high vacuum sputter system. The clean glass substrate and Mo target were placed onto the instrument and left in the system under vacuum overnight to reach a suitable vacuum pressure of 6×10^{-6} Torr. Then, the voltage and current were set at 650 V and 0.11 A respectively. For film deposition, the argon valve was opened and the DC was switched on. Then the pressure decreased to ~ 3×10^{-3} Torr voltage dropped to 285 V. The gate-valve and current control were manually adjusted as necessary to maintain constant pressure and current at 0.11 A, and then the plasma was ignited. In this instrument the deposition rate was 1 Å/sec. The sputter time for each pressure was chosen to yield a film having a nominal thickness of 600 nm. Due to fabrication issues of the Mo sputtering machine these processes were used for films in chapter 6, but in chapter 7 Mo foils were used instead of Mo thin films.

3.1.4.2: Chemical bath deposition of CdS (CBD-CdS)

There are numerous recipes in the literature for the successful fabrication of CdS layers by using the chemical bath deposition (CBD) technique [2-6], and also by the use of RF sputtering systems [7] and by thermal evaporation method [8]. However, chemical bath

deposition is a simple way to deposit CdS onto a CZTS, it is low cost and achieves the high efficiency. A deposition solution containing $CdSO_4$ (2.5 mM), NH_4OH (15 ml) and CSN_2H_4 (10 mM) was diluted in distilled (DI) water and placed on a water-jacket beaker, which was itself placed on hot plate stirrer. The total volume of the solution was 150 ml. After that, a substrate was placed into the beaker and soaked in the solution before adding the thiourea. Then the thiourea was added and the substrate was placed again in the beaker and then the measurement time was started to deposit 70 nm. After the time finished, the substrate was rinsed by DI water and dried by N_2 flow. Figure 3.3 shows a diagram of the apparatus used for the CBD-CdS deposition.

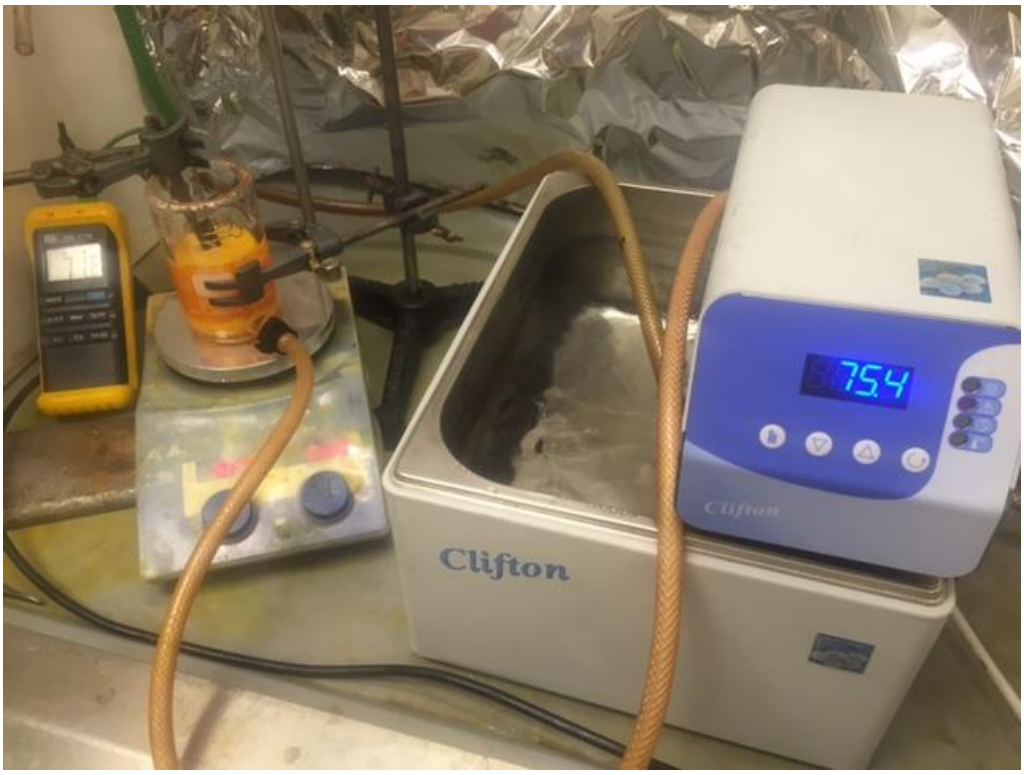

Figure 3.3 A diagram of the apparatus used for the CBD-CdS deposition

3.2: Characterisation Techniques

Many techniques were used in this study to characterise and analyse the CZTS nanoparticles. However, in this section the background physics of all of the instruments will be discussed in detail.

3.2.1: X-ray diffraction

When accelerated electrons from a negative cathode filament move towards a positive tungsten target anode, two types different mechanisms of x-rays can be generated. When the electrons interact with target, the electrons pass close to positive charge nucleus and the coulombic forces are present, leading to deceleration of the electron and change its direction causing a significant loss of electron kinetic energy which is converted to x-ray radiation with energy equal to the kinetic energy lost by the initial electron energy. This process is called bremsstrahlung (braking radiation) [9]. If however the electron has sufficient energy; greater than the target shell binding energy; to eject the electron from its shell (K-shell), leaving a hole (vacancy) in the inner shell (K-shell), this hole (vacancy) will be filled by an electron from the outer shells (L and M shells), leading to loss of energy and emission of x-ray radiation which is equal to the difference energy between two shells. This is the characteristic x-ray generation as shown in Figure 3.4 [10, 11].

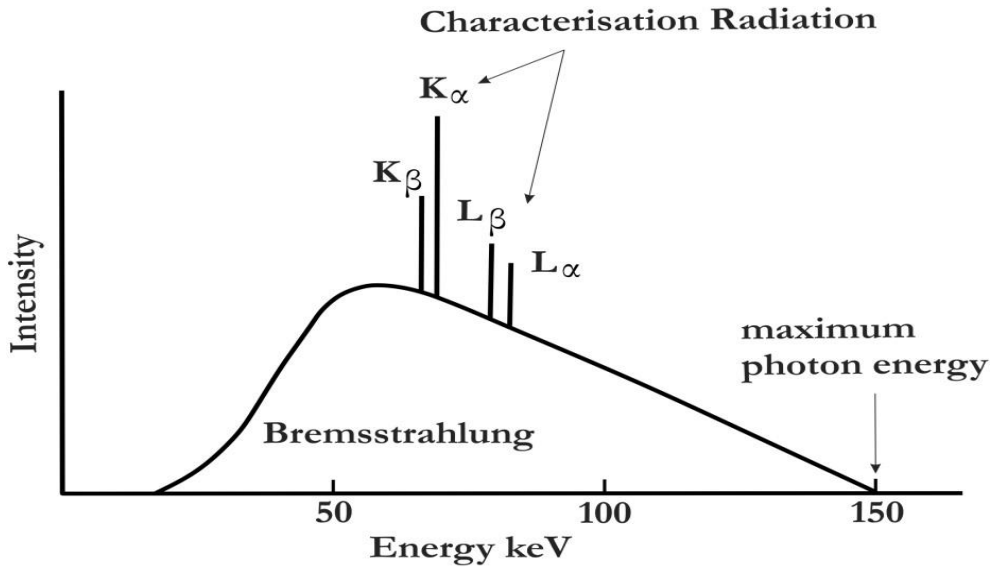

Figure 3.4 Two types of x ray radiations are produced; bremsstrahlung and characterisation radiation. Bremsstrahlung is continuous spectra, whereas characteristic radiation is discrete spectra which shows K_α and K_β which is due to electrons fill vacancies from L and M shells to K shell [12, 13].

When the produced x-ray as described above, hits the atom (sample), which is usually a crystalline substance at the right distance and angle, constructive interferences and diffraction rays will be produced. Also, some patterns interfere with each other and cancel each other out. Bragg studied [14] the relationship between the wavelength, the angle of the x-ray and the internal spacing in the crystal.

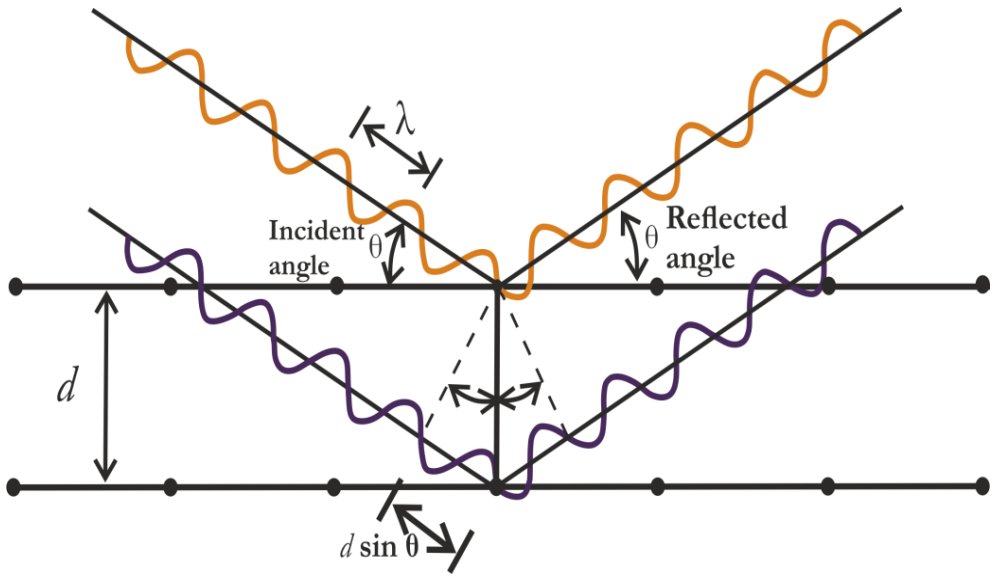

Figure 3.5 Bragg's law suppose that the crystal may be divided into many parallel planes. When the x- ray with wavelength λ is incident the parallel planes at angle θ, it will reflect by angle equal to the incident angles. The distance between two parallel planes is *d*.

This relation is given by the formula, which is called Bragg's law.

$$n\lambda = 2d \sin\theta \qquad (3.1)$$

where λ: wavelength of the incident x ray, θ: the angle between the incident rays and the surface of the crystal, d: spacing between the layers and n: is an integer [15, 16]. The sample is in a powder form that contains a large number of crystallites in a random orientation placed in the x-ray path. The scattering of the x-ray will be detected by an appropriate detector from the planes in these crystallites at correct angles to achieve Bragg's law. As a result, each lattice space in the crystal will give rise to a cone of diffraction from a single crystallite within the powder sample, Figure 3.5. The peak intensities will be recorded on the computer, and the d spacing values will be calculated using Bragg's equation [17].

Because the CZTS has a tetragonal structure, as the literature review suggests [10, 18], the inter-planer spacing and lattice parameters are the following, according to Bragg's law:

$$n\lambda = 2d_{hkl}\sin\theta \qquad (3.2)$$

$$\frac{1}{d_{hkl}^{\,2}} = \frac{h^2+k^2}{a^2} + \frac{l^2}{c^2} \qquad (3.3)$$

The grain size or thickness of the crystallite layer is inversely proportional to the full width at half-maximum (FWHM) of the peaks. It is given by the Scherrer's formula [19]:

$$x = \frac{0.9\lambda}{D\cos\theta} \qquad (3.4)$$

where x : grain size, D: full width at half-maximum (FWHM) at (112) peak, λ: wavelength for Cu Kα (0.154 nm) and θ: Bragg angle of diffraction (peak position). The x-ray diffraction instrument consists of an x-ray source, a goniometer, a sample holder, a radiation detector and a signal processor and readout. The x-ray diffraction provides useful information, such as a determination of the crystal structure, phase identification, determination of grain size and thin film composition [20-23]. In this work the XRD peaks will be used to provide information for peak positions which can determine the crystal system as well as the particle sizes. Also, the inter-planer *d* spacing and lattice parameters will be determined. XRD measurements will be taken for all samples by using Cu-K_α x-ray in Bruker d7 diffractometers.

3.2.2: Raman spectroscopy

This is one of the most important techniques that are used to provide extensive information regarding the crystal's structure, composition and secondary phases. Especially in this work to identify the purity of CZTS films as well as secondary phases. Raman scattering is an inelastic scattering of monochromatic light (laser), which means that the scattering energy of the photon incident are absorbed by the sample and re-emitted as photons. The energy of these photons shifts up or down in comparison with the incident photon energy.

When the incident photons interact with the sample, the scattering process occurs. When the incident photons excite the electron into a virtual state (it is an imaginary intermediate

energy state with a short life time), the electrons can return to the ground state and emit the photons with energy equal to that of the incident photon. This process is called Rayleigh scattering (elastic scattering) [24]. When the electrons relax back down and shift up or down to vibrational energy states (ground state), the Raman Effect occurs [25]. These shifts provide information about vibrational, rotational and other low frequency transitions in molecules as shown in Figure 3.6.

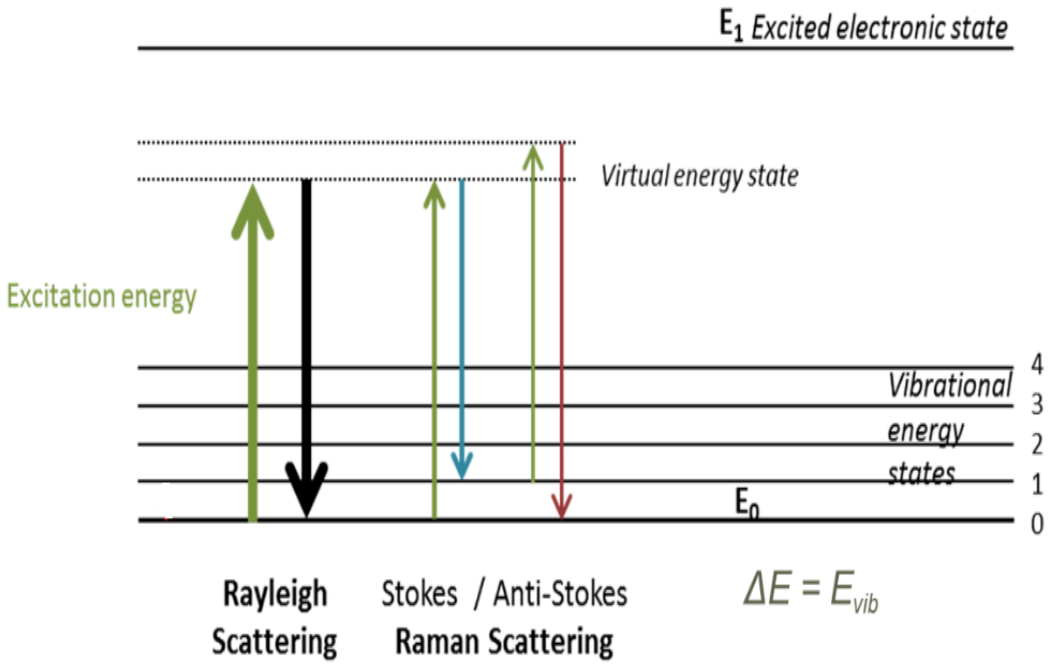

Figure 3.6 Energy level diagram shows Rayleigh and Raman scattering processes. E_o is the vibrational energy state and E1 is the excited electronic state. V= 0 is the ground vibrational energy state, V=1, 2, 3 and 4 are the first, second, third and fourth vibration [25].

However, when the energy of the incident photon moves from the virtual state to the vibrational state (phonon state) and emits a photon with less energy of the incident photon, this leads to what is known as stokes Raman scattering. On the other hand, when the electron in the vibrational, excited state (phonon state) becomes excited to a higher virtual state and come back down to the ground state, emitting photons with more energy than those of the incident energy, this leads to what is known as anti-stokes Raman scattering. The energy level diagrams for the Rayleigh, Stokes and anti-Stokes scattering schemes are

presented in Figure 3.6. The Raman spectrum consists of the following types of Rayleigh scattering peaks: those with high intensity and wavelength as excitation photons, those with a series of Stokes-shifted peaks, with low intensity and longer wavelengths, those with a series of anti-Stokes shifted peaks and with lower intensity and shorter wavelengths [26-28].

The Raman spectra will be taken by using horiba JY lab RAM-HR microscope.

3.2.3: Electron microscopy

3.2.3.1: Transmission electron microscopy (TEM)

TEM is one of tools that used to analyse CZTS structure. In the TEM, electrons transmit through the sample and are detected and analysed by using advanced computer programming. An electron beam of high energy is required to produce high resolution and transmission, typically 200 keV is used as shown in Figure 3.7 [29]. The electromagnetic lenses act to focus the electrons transmitted. The condenser lenses are used to control the electron illumination of the sample. Also, other lenses such as objective and projector lenses are used to produce the diffraction pattern on the fluorescent screen [20, 30]. There are many functions can be used in TEM to analysis the particles such as contrast imaging to show particles' images and calculate size of particles. Also, High Resolution Electron Microscopy (HREM) used to study the atomic structure of the material and calculate d spacing. Moreover, Selected Area Electron Diffraction (SAED) gives information about lattice parameters and point groups of a crystal. TEM in addition is used to provide chemical analysis and the chemical composition of elements can be determined by energy dispersive x-ray (EDX). The TEM measurements will be taken by using JEOL 2100F FEG TEM, with operation voltage at 200 kV.

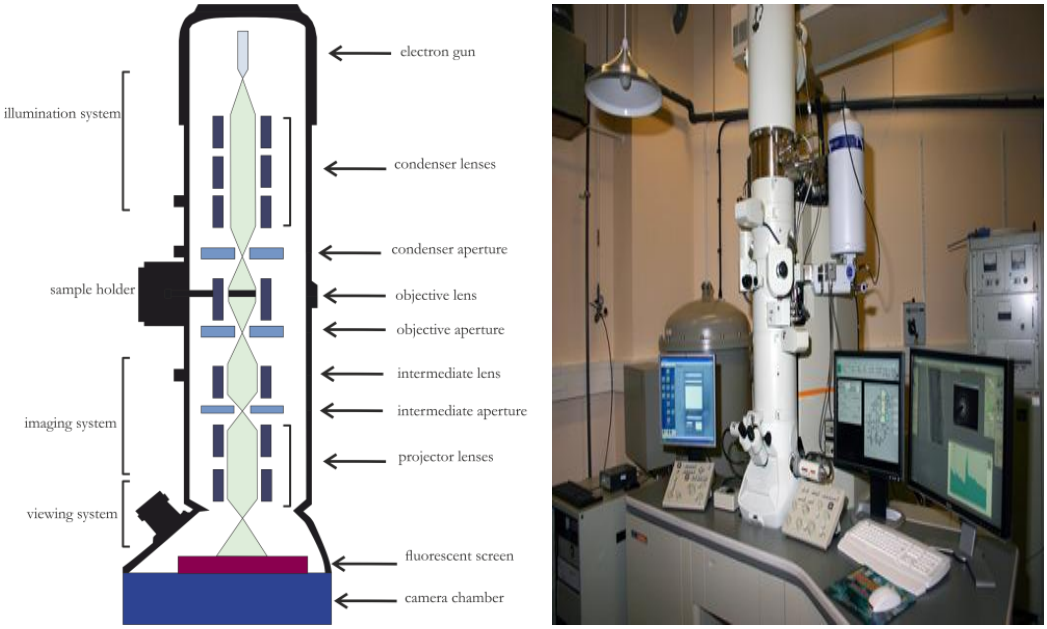

Figure 3.7 TEM instrument, in the left diagram, it is the cross section of the main part of TEM instrument. It consists of an electron gun for generating the electron beam, two condenser lenses and apertures, an objective lens and aperture, projector lenses, a viewing system and a camera chamber.

3.2.3.2: Scanning electron microscopy SEM

The main differences between TEM and SEM are the focused electrons in TEM transmitted through the sample whereas in SEM the electron beam is scanned over the sample surface. In this instrument, the electron column consists of an electron gun and two or more lenses operating under high vacuum as shown in Figure 3.8. The electron gun is to provide a large and stable current in small electron beam. The electrons were accelerated between cathode and anode by a voltage 1-50 eV in the electron gun chamber [31-33]. Three electron beam parameters are defined when the electron hits the sample surface these are electron probe diameter, electron probe current and electron probe convergence. In the SEM there are one to three condenser lenses which are used to demagnify the image of the crossover in the electron gun. The final lens in the SEM column is called the objective lens which is used to focus the image by controlling the movement of the probe crossover along the z-axis of the column. The objective lens is the strongest lens with high current flow through it, liquid cooling is required [32].

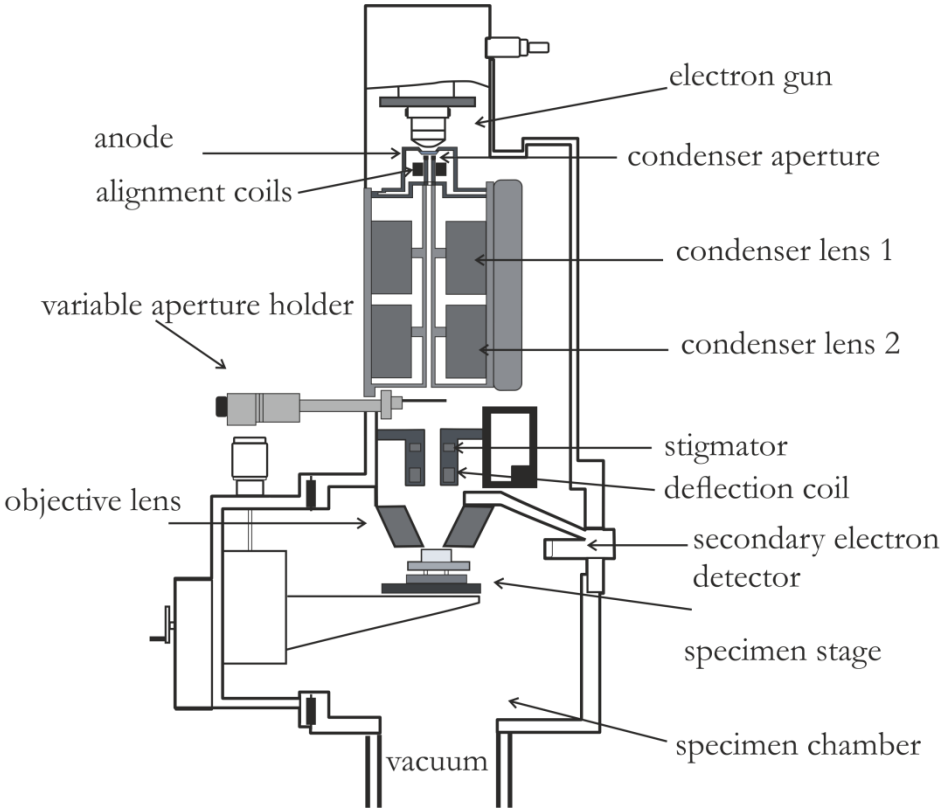

Figure 3.8 SEM instrument consists of electron gun, anode and cathode, condenser aperture, two condenser lens, variable aperture holder, stigmator and deflection coil, objective lens, secondary electron detectors and specimen chamber which contains specimen stage and connects to vacuum system [34, 35].

When the electron beam hits the sample surface, the electrons penetrate the surface of sample to a depth of a few microns and many types of interactions with the electrons are possible; these are either an elastic or inelastic scattering with atoms of the specimen, Figure 3.9 such as secondary electrons (SE), backscattered electrons (BSE) and characteristic x-rays [32, 36].

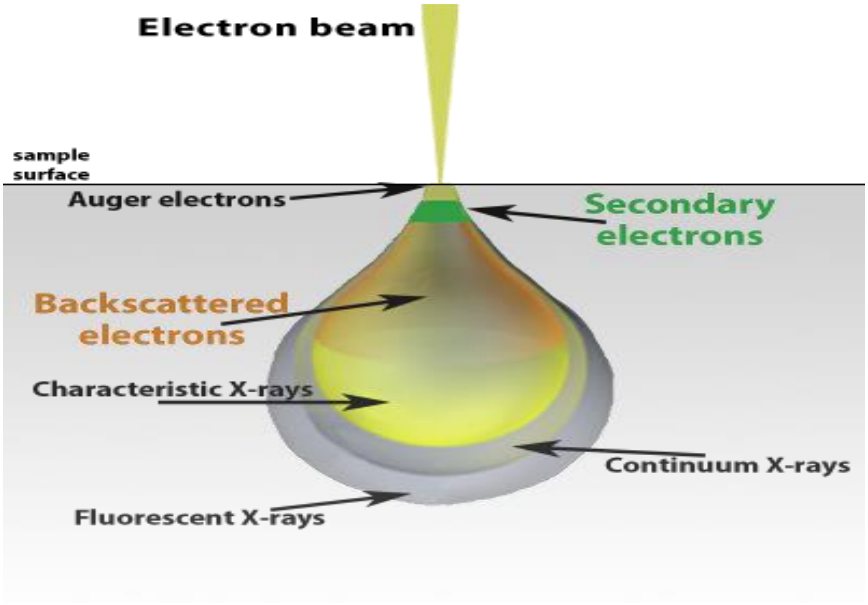

Figure 3.9 Different types of electron beam interaction with surface of the sample; Auger electrons, secondary electrons, backscattering electrons, characteristic x-rays, continuum x-rays and fluorescent x-rays [37].

The secondary electrons are emitted from the surface of sample by using low accelerating voltage and play the important roles for surface imaging. Not only the incident beam lost its energy by excited electrons on the surface but also go through backscattering within the sample surface and the scale depth of BSE is greater than SE depending in the energy of incident beam (accelerating potential). SEM instrument in addition can use emitted x ray characterization to analyses the composition of elements. However, when the electron beam ejects the electron in the core level and creates the vacancy, the electron in outer level with high energy falls down and fills the vacancy at low energy level and emits a photon with an energy equivalent to difference of energy between high and low level [36, 38]. The SEM measurements will be taken by using the Hitachi SU-70 FEG SEM to image the CZTS film surfaces and calculate the particle sizes as well as EDX spectroscopy to determine the chemical compositions of CZTS elements by INCA software in Hitachi SU-70 SEM.

3.2.3.3: Focused ion beam (FIB)

Focused ion beam (FIB) is a useful instrument used in this work to image the surface of materials such as CZTS films, CdS films as well as cross section images of CZTS solar devices. Moreover, it can be used to produce transmission SEM sample to study the cross section image of CZTS devices. However, FIB system consists of dual beam; ion beam and electron beam, sample stage, vacuum system, detectors and camera. Electron beam column is vertically oriented to the sample stage. This beam can be used for high resolution scanning electron images as well as to determine the chemical composition of the sample with EDS detector. The electron energies can be between 0.1 and 30 keV. Ion beam column is tilted to an angle of 52° and consists of positive charged gallium ions. The beam can be used to generate secondary electrons and ions which can be used to form images. The electron will interact with sample as discussed in section 3.2.3.2. For cross section images, the sample stage was tilted at 52^{o} and a platinum layer was deposited on the sample surface to protect underlying layers from ion beam and then followed by milling of the trench on the surface which was lastly polished at low current.

3.2.3.4: Electron backscatter diffraction (EBSD)

Electron backscatter diffraction (EBSD) technique is used to analyse crystal microstructure including phase identification and fractions, type of grain boundary, grain size, and crystal orientation. EBSD consists of a holder which can be tilted to 70^{o} on SEM device or by using pretilted holder, a phosphor screen, a sensitive digital camera for viewing the pattern from the phosphor screen and specialized computer software (Aztec) used to analyse electron backscattered patterns. Typically, an EBSD system is attached to an SEM device and the accelerated electron beam hitting on the crystal specimen, that is tilted to about 70° and the incident beam with an angle of 20° with the sample, will be backscattered in all directions. The backscattered electrons meeting Bragg's condition and will form Kikuchi diffracted patterns on the phosphor screen, which then can be captured by the camera. The electron will interact with sample as discussed in section 3.2.3.2.

3.2.4: Photoluminescence (PL) spectroscopy

This is a very sensitive technique that is used to study various properties of semiconductors. PL spectroscopy is not a destructive optical technique. It is used to evaluate the various dopants and impurities' levels in semiconductors. The PL spectroscopy instrument requires a suitable laser beam with an appropriate emission-characteristics spectrometer for a high-spectral resolution and appropriate detector [39].

There are three main processes involved in PL performance; absorption, excitation and emission as shown in Figure 3.10. When the laser photons are absorbed by the materials, this leads to an excitation the electron from a lower energy level (valence band or defect level near valence band) to higher energy states (conduction or defect near conduction level). Thermalisation happens next the hot electrons and holes lose energy by emitting phonons to thermalize with lattice. The next process is the relaxation of the excitation electrons as they relax from conduction level to valence level and emit a photon. All these process are radiative recombination i.e they lead to the release of a photon. On the other hand, when electrons relax from the conduction band to an intermediate energy state (deep defect level) or from this level to the valence band and hence release a phonon, these processes are called non-radiative recombination. Figure 3.10 shows the different process of radiative and non-radiative recombination when the excitation electrons relax to lower energy levels [40, 41] .

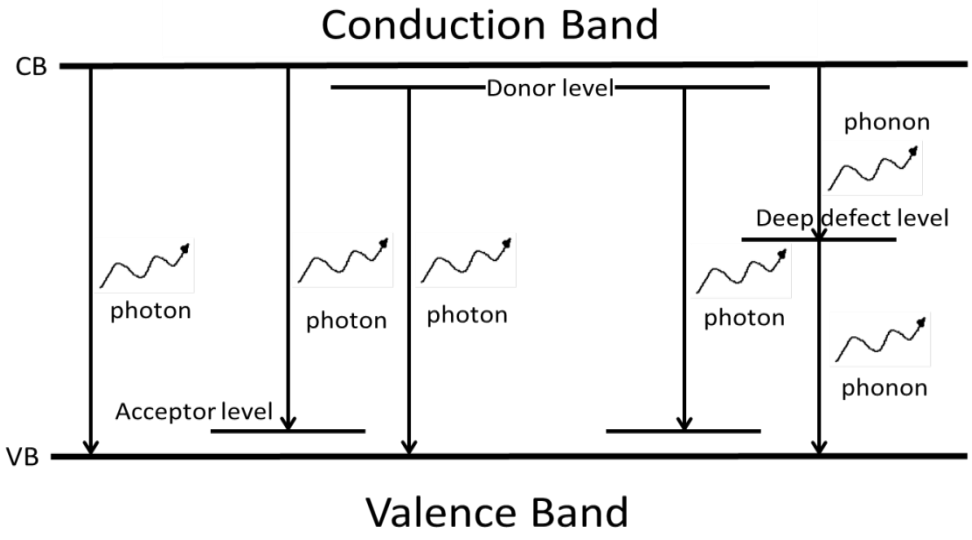

Figure 3.10 Different PL process for radiative and non-radiative recombination paths

It is clear that there are three main path ways available which lead to the emission photons; band to band recombination (BB), where the electrons from the conduction band return back to the valence band and emission of photons with energy equal to band gap E_g i.e

$$E = h\nu \tag{3.5}$$

where, E is photon energy, h is blank constant and ν is frequency of light.

Other recombinations exist when carriers transfer from the energy band to defect levels (either acceptor or donor level) in the band gap, this process is called band to impurities recombination (BI). This is recombination can be described by the following equation:

$$I = \sqrt{(h\nu - E_g + E_i)/k_B T}\exp\left(-\frac{h\nu - E_g + E_i}{k_B T}\right) \tag{3.6}$$

Where, E_g is the band gap of the materials, E_i is the ionisation energy of the donor or acceptor, k_B is the Boltzmann constant and T is the sample temperature. The photoluminescence energy maximum is described by $h\nu_{\max} = E_g - E_i$.

The existence of a high concentration of acceptors and donors under low temperature, the donor-acceptor pair recombination (DAP) was detected as shown in the Figure 3.10 and also it is emitted photons. This is recombination also can be described by the following equation [42],

$$h\nu_{\max} = E_g - \left(E_A + E_D\right) + \frac{e^2}{4\pi\varepsilon_o\varepsilon r} \tag{3.7}$$

Where, $E_A + E_D$ are the acceptor and donor ionisation energies respectively, e is electron charge, ε_o is the permittivity of vacuum, ε is the static dielectric constant and r is the distance between the donor and acceptor ions. However, the most important term in this equation is $\frac{e^2}{4\pi\varepsilon_o\varepsilon r}$ which describes the coulomb interaction between both donor and acceptor. It is clear that when increasing the excitation power of PL, the photogeneration of electrons and holes also will increase, which leads to increased screening of Coulomb interaction between donor and acceptor ions and as result due to strength of Coulomb force the emission line will shift to a higher energy. The PL measurements are used to

provide information on the energy band gap, impurity levels, carrier lifetime and recombination mechanisms. Moreover, there is extensive useful information that can be obtained from peak energy, peak width and peak intensity [20, 43].

Moreover, there are other recombination process that can occur in the CZTS materials, depending on the level of dopant and the defects concentration which form spatial fluctuation in the band gap edge and electrostatic potential. This leads to perturbation in the band structure and the broad distribution of defect levels can form a band-tail. For instance a band tail which is due to band gap fluctuations can be induced by varying anion and cation concentrations and a band tail which is due to electrostatic potential fluctuations induced by the variation in dopant (donor and acceptor) concentration [44, 45] is also possible. However, when the maximum of the conduction band corresponds spatially to the minimum of the valence band, where both absorption and emission (recombination) occur at the same point, this process is called band gap fluctuation, whereas, electrostatic potential fluctuation occurs due to a high concentration of defects and impurities. The absorption and recombination when the minimum of the conduction band and the maximum of the valance band correspond spatially together leads to these process happening at different locations via tunnelling, this process is called electrostatic potential fluctuation. Both band gap, and electrostatic potential fluctuations have detrimental effects in photovoltaic device performance by reducing the open circuit voltage [46].

However, the average well depth of fluctuating potential is given by [47, 48]

$$\gamma = \sqrt{2\pi N_T r_o}\,\frac{e^2}{\varepsilon} \tag{3.8}$$

where N_T is the concentration of donor and acceptor impurities, e is the electron charge, ε and is the relative permittivity, r_o is Debye screening radius which can be given by [47]

$$r_o = \left(\frac{a_o}{4}\right)^{1/2}\left(\frac{\pi}{3n}\right)^{1/6} \tag{3.9}$$

where a_o is the Bohr radius of the isolated shallow donor or acceptor state and n is the concentration of free charge.

Moreover, the absorption coefficient α and fluctuation potential can be given by [46].

$$\alpha = \alpha_o \exp\left(-\frac{2}{5\sqrt{\pi}}\right)\left(\frac{E_g - E}{\gamma/2}\right)^{5/4} \qquad (3.10)$$

where α is the absorption coefficient, and a_o is the proportional constant, and the γ for optical transition is given by [46, 49].

$$\gamma^5 = \left(\frac{e^2}{4\pi\varepsilon_r\varepsilon_o}\right)^4 \frac{N_T^2\hbar^2}{m_r} \qquad (3.11)$$

where, ε is the relative dielectric permittivity, N_T is the total charge defects density, $\hbar$ is reduced Plank constant and m_r is the reduced mass of the electron and hole which is equal to $m_r = (m_e m_h)/(m_e + m_h)$.

The PL measurements will be taken to identify the defects and recombination types. In this work PL measurements will be taken by using Ar ion laser as the excitation source with excitation laser wavelength 514 nm (green line laser). The samples will placed under vacuum in cryostat (Cryomech ST405) and cooled to 3 K for low-temperature measurements. Two filters are used to remove laser light as OG 550 and OG 570.The data were collected by using lab view software.

3.2.5: UV-Vis Spectrophotometer

The UV-Vis spectrophotometer is an optical instrument that is used to measure the intensities of light absorbance, transmittance and reflectance by a sample as a function of its wavelength. A light beam with a particular wavelength is passed through the sample and along the reference path. Then, these light beams converge on the detector [50]. When light passes through the reference sample, the intensities are observed and referred to as initial intensity I_o. When light passes through the sample, the intensities are recorded as transmitted intensity I. When the sample does not absorb light, the initial intensity is equal to the transmitted intensity. But the intensity becomes less than I_o when the sample absorbs the light. In general, in the UV-Vis spectrophotometer, when the energy of photon reaches to the energy required for electron to move from its energy state (ground state) to high energy level (excitation state) these processes is basis of absorbance spectroscopy. The Beer-Lambert law is the basic principle of the absorbance analysis [51]. This law is defined as:

$$T = I/I_o = 10^{-kcl} \tag{3.12}$$

$$A = \log(1/T) = \log I_o/I = -\alpha cl \tag{3.13}$$

where A is absorbance, T is transmittance, I is transmitted intensity , I_o is incident intensity, k is constant, l is the length of light path through the cuvette and c is the sample concentration [52]. The absorption coefficient (α) depends on the incident wavelength and can be determined by transmittance (T) and reflectance (R) measurements as the following equation [39]:

$$\alpha = \frac{1}{x}\ln\left[\frac{(1-R)^2}{T}\right] \tag{3.14}$$

The thickness x of the film can be calculated from the absorbance spectrum when the absorption coefficient is known [53]. It is related to absorbance by the absorbance coefficient (α) via Beer-Lambert law:

$$\frac{I}{I_o} = \exp(-\alpha x) = 10^A \quad , \quad x = \frac{-\ln 10^A}{\alpha} \tag{3.15}$$

However, the energy band gap E_g depends on the absorption coefficient as the following equation (3.16) [54]:

$$\alpha h\nu = C\left(h\nu - E_g\right)^{1/n} \tag{3.16}$$

Where, C is constant, h is plank's constant, $h\nu$ is the incident photon energy eV, n is a constant related to the band structure; which is equal to 2 for a direct band gap bulk semiconductor. The energy band gap can be estimated by extrapolating the linear portion of the curve $(\alpha h\nu)^2$ versus photon energy. This is commonly referred to as a Tauc plot.

The UV-Vis spectrophotometer will use to estimate the energy band gap of CZTS under different parameters. In this works the UV-Vis measurements will be taken using a Shimadzu UV-3600 UV/Vis spectrometer.

3.2.6: Current – voltage *(I-V)* measurement device

Solar cell devices are characterised by applying an external voltage cross the cell and measuring the current passing through the cell. To measure I-*V* characteristic of PV solar cells devices, a Keithely 2400 device and labVIEW for windows was used. The PV device is linked with keithely device and a computer. Then, the measurement of current was collected and transferred to a computer programme to draw the relationship between voltage (*V*) and current density (*J*) from this curve useful information will be collected as mentioned in chapter 2.1.4 [20]. The devices were illuminated by solar simulator.

3.3: References

1. Guo, Q., H.W. Hillhouse, and R. Agrawal, *Synthesis of Cu_2ZnSnS_4 nanocrystal ink and its use for solar cells.* Journal of the American Chemical Society, 2009. **131**(33): p. 11672-11673.

2. Hong, C.W., et al., *Chemically Deposited CdS Buffer/Kesterite Cu_2ZnSnS_4 Solar Cells: Relationship between CdS Thickness and Device Performance.* Acs Applied Materials & Interfaces, 2017. **9**(42): p. 36733-36744.

3. Cantas, A., et al., *Importance of CdS buffer layer thickness on Cu_2ZnSnS_4-based solar cell efficiency.* Journal of Physics D-Applied Physics, 2018. **51**(27): p. 14.

4. Aguilera, M.L.A., et al., *Improving the optical and crystalline properties on CdS thin films growth on small and large area by using CBD technique.* Revista Mexicana De Fisica, 2016. **62**(2): p. 129-134.

5. Li, J.K., *Preparation and properties of CdS thin films deposited by chemical bath deposition.* Ceramics International, 2015. **41**: p. S376-S380.

6. Qu, Y.T., G. Zoppi, and N.S. Beattie, *The role of nanoparticle inks in determining the performance of solution processed $Cu_2ZnSn(S,Se)_4$ thin film solar cells.* Progress in Photovoltaics, 2016. **24**(6): p. 836-845.

7. Tao, J.H., et al., *7.1% efficient co-electroplated Cu_2ZnSnS_4 thin film solar cells with sputtered CdS buffer layers.* Green Chemistry, 2016. **18**(2): p. 550-557.

8. Memarian, N., et al., *Deposition of Nanostructured CdS Thin Films by Thermal Evaporation Method: Effect of Substrate Temperature.* Materials, 2017. **10**(7): p. 8.

9. Shapiro, J., *Radiation Protection: A Guide for Scientists, Regulators, and Physicians*. 2002, Cambridge Massachusetts and London, England: Harvard University Press.

10. Massa, W. and R.O. Gould, *Crystal Structure Determination*. 2013, Germany: Springer Berlin Heidelberg.

11. Als-Nielsen, J. and D. McMorrow, *Elements of Modern X-ray Physics*. 2011, UK: Wiley.

12. *Imaging in medicine, http://www.open.edu/openlearn/ocw/mod/oucontent/view.php?id=2562&printable=1*. [cited 25/09/2017].

13. Cullity, B.D. and S.R. Stock, *Elements of X-ray Diffraction*. 2013, UK: Pearson education limited.

14. Agrawal, R., G. Jain, and R. Sharma, *Solid State and Nuclear Physics*. 2008, India: Krishna Prakashan.

15. Dyson, N.A., *X-rays in Atomic and Nuclear Physics*. 2005, UK: Cambridge University Press.

16. Waseda, Y., E. Matsubara, and K. Shinoda, *X-Ray Diffraction Crystallography: Introduction, Examples and Solved Problems*. 2011, Germany: Springer Berlin Heidelberg.

17. Singh, A.K., *Advanced X-ray Techniques in Research and Industry*. 2005, Netherlands: IOS Press.

18. Chen, J., et al., *Influences of synthesis conditions on chemical composition of Cu_2ZnSnS_4 nanocrystals prepared by one pot route*. Journal of Materials Science-Materials in Electronics, 2014. **25**(2): p. 873-881.

19. Koch, C., et al., *Structural Nanocrystalline Materials: Fundamentals and Applications*. 2007, UK: Cambridge University Press.

20. Yacobi, B.G., *Semiconductor Materials An Introduction to Basic Principles*. 2004, USA: Kluwer Academic Publishers.

21. Kittel, C., *Introduction to Solid State Physics*. 2007, USA: Wiley.

22. Suryanarayana, C. and M.G. Norton, *X-Ray Diffraction: A Practical Approach*. 2013, USA: Springer Science & Business Media.

23. Mittemeijer, E.J. and U. Welzel, *Modern Diffraction Methods*. 2013, Germany: Wiley-VCH.

24. Ferraro, J.R. and K. Nakamoto, *Introductory Raman Spectroscopy*. 2012, UK: Academic Press Limited.

25. Schrader, B., *Infrared and Raman Spectroscopy: Methods and Applications*. 2008, Germany: Wiley-VCH.

26. Richard, L.M., *Raman Spectroscopy for Chemical Analysis*. 2005, USA: John Wiley & Sons.

27. Perkowitz, S., *Optical Characterization of Semiconductors: Infrared, Raman, and Photoluminescence Spectroscopy*. 2012, UK: Academic Press Limited.

28. Vandenabeele, P., *Practical Raman Spectroscopy: An Introduction*. 2013, UK: Jon Wiley & sons.

29. Reimer, L., *Transmission Electron Microscopy: Physics of Image Formation and Microanalysis*. 2013, Germany: Springer Berlin Heidelberg.

30. Buseck, P., J. Cowley, and L.R. Eyring, *High-Resolution Transmission Electron Microscopy: and Associated Techniques*. 1989, USA: Oxford University Press.

31. Egerton, R.F., *Physical Principles of Electron Microscopy: An Introduction to TEM, SEM, and AEM*. 2016, Switzerland: Springer International Publishing.

32. Goldstein, J., et al., *Scanning Electron Microscopy and X-ray Microanalysis: Third Edition*. 2012, USA: Springer US.

33. Slayter, E.M. and H.S. Slayter, *Light and Electron Microscopy*. 1992, UK: Cambridge University Press.

34. *Scanning Electron Microscopy https://cmrf.research.uiowa.edu/sites/cmrf.research.uiowa.edu/files/styles/large/public/sem1.gif?itok=uzYuMy9J*. [cited 26/09/2017].

35. Lyman, C.E., et al., *Scanning Electron Microscopy, X-Ray Microanalysis, and Analytical Electron Microscopy: A Laboratory Workbook*. 2012, USA: Springer US.

36. Holt, D.B. and D.C. Joy, *SEM Microcharacterization of Semiconductors*. 2013, UK: Academic Press Limited.

37. *Nanoscience Instruments, Sample-Electron Interaction http://www.nanoscience.com/files/5114/5678/8470/electronbeaminteraction_w.png*. [cited 26/09/2017].

38. Williams, D.B. and C.B. Carter, *Transmission Electron Microscopy: A Textbook for Materials Science*. 2009, USA: Springer Science & Business Media.

39. Fox, M., *Optical Properties of Solids*. 2010, UK: Oxford University Press.

40. Nelson, J., *The Physics of Solar Cells*. 2003, UK: Imperial College press.

41. Bergman, L. and J.L. McHale, *Handbook of Luminescent Semiconductor Materials*. 2016, USA: CRC Press.

42. Gershon, T., et al., *Photoluminescence characterization of a high-efficiency Cu_2ZnSnS_4 device*. Journal of Applied Physics, 2013. **114**(15).

43. Seshan, K., *Handbook of thin-film deposition processes and techniques*. 2 ed. 2002, USA: Noyes Publications.

44. Mendis, B.G., et al., *Nanometre-scale optical property fluctuations in Cu_2ZnSnS_4 revealed by low temperature cathodoluminescence.* Solar Energy Materials and Solar Cells, 2018. **174**: p. 65-76.

45. Rey, G., et al., *On the origin of band-tails in kesterite.* Solar Energy Materials and Solar Cells, 2018. **179**: p. 142-151.

46. Gokmen, T., et al., *Band tailing and efficiency limitation in kesterite solar cells.* Applied Physics Letters, 2013. **103**(10): p. 5.

47. Halliday, D.P., et al., *Luminescence of Cu_2ZnSnS_4 polycrystals described by the fluctuating potential model.* Journal of Applied Physics, 2013. **113**(22): p. 10.

48. Luryi, S., B.I. Shklovskii, and A.L. Efros, *Electronic Properties of Doped Semiconductors*. 2013, Germany: Springer Berlin Heidelberg.

49. Wagner, M., et al., *Characterization of $CuIn(Ga)Se_2$ Thin Films.* physica status solidi (a), 1998. **167**(1): p. 131-142.

50. Owen, T., *Fundamentals of Modern UV-visible Spectroscopy: Primer*. 2000, USA: Agilent Technologies.

51. Lajunen, L.H.J. and P. Perämäki, *Spectrochemical Analysis by Atomic Absorption and Emission*. 2004, UK: Royal Society of Chemistry.

52. Jha, A., *Inorganic Glasses for Photonics: Fundamentals, Engineering, and Applications*. 2016, UK: John Wiley & Sons.

53. Wardle, B., *Principles and Applications of Photochemistry*. 2009, UK: John Wiley & Sons.

54. Tumbul, A., et al., *Structural, morphological and optical properties of the vacuum-free processed CZTS thin film absorbers.* Materials Research Express, 2018. **5**(6).

Chapter 4: Synthesis and characterisation of Cu_2ZnSnS_4 (CZTS) nanoparticle solution inks under different fabrication conditions

4.1: Introduction

CZTS was fabricated using a non-vacuum technique especially designed to be a single stage hot injection method, the spin coating technique was used to grow layers of CZTS nanoparticles as an ink onto glass substrates. This method has been successfully utilised by several groups [1-3] with non-vacuum deposition techniques such as drop casting and spin coating methods [1, 4-7]. The aim of this chapter is to focus on the synthesis and characterisation of (CZTS) nanoparticles by hot injection techniques with different synthesis conditions such as temperature and time. According to many studies, the best solar cells have been achieved with copper poor zinc rich region in the narrow range of (Cu/Zn+Sn) =0.79 to 0.85 and (Zn/Sn) =1.05 to 1.25 [8-12]. In this work the composition ratios of (Cu/Zn+Sn) and (Zn/Sn) were chosen as 0.85 and 1.25 respectively.

4.2: Synthesis of CZTS nanoparticles ink:

CZTS nanoparticles were synthesised as described in chapter 3.1 under non-stoichiometric compositions; 1.35 mmol of copper (II) acetylacetonate, 0.80 mmol of zinc (II) acetylacetonate and 0.75 mmol of tin (IV) bis(acetylacetonate) dichloride as metal sources and a solution of 4 mmol of elemental sulphur in 4.5 ml oleylamine was injected into the mixture. The reaction temperature was increased at given temperature to allow the nanoparticles growth by setting temperature to 185, 205, 225, 245, 265 ^{o}C for 30 min under argon atmosphere. Subsequently, 5 ml of toluene and 40 ml of isopropanol were added into the solution, and the nanoparticles were collected using a centrifuge at 10000 rpm for 10 min after cooling the solution to 60 ^{o}C at room atmosphere. These process repeated at different reaction time 0.5, 1, 1.5 and 2 h with fixed temperature at 225 ^{o}C were synthesised to study the effect of different reaction time.

4.3: Results and discussion

4.3.1: The effect of reaction temperature

In the synthesis of CZTS method, the reaction temperature was varied from 185 to 265 °C and the reaction time was set as a constant of 30 min.

4.3.1.1: SEM & EDX measurements

As shown in figure 4.1, it was found that the shape of CZTS nanoparticles was spherical, dispersive nanoparticles and aggregate together at 185 to 225 °C due to high surface energy and Van der Waals force. Whereas, at 245 °C and 265 °C the shape of CZTS nanoparticles becomes smoother and the size of the nanoparticles gradually increase with increasing temperatures.

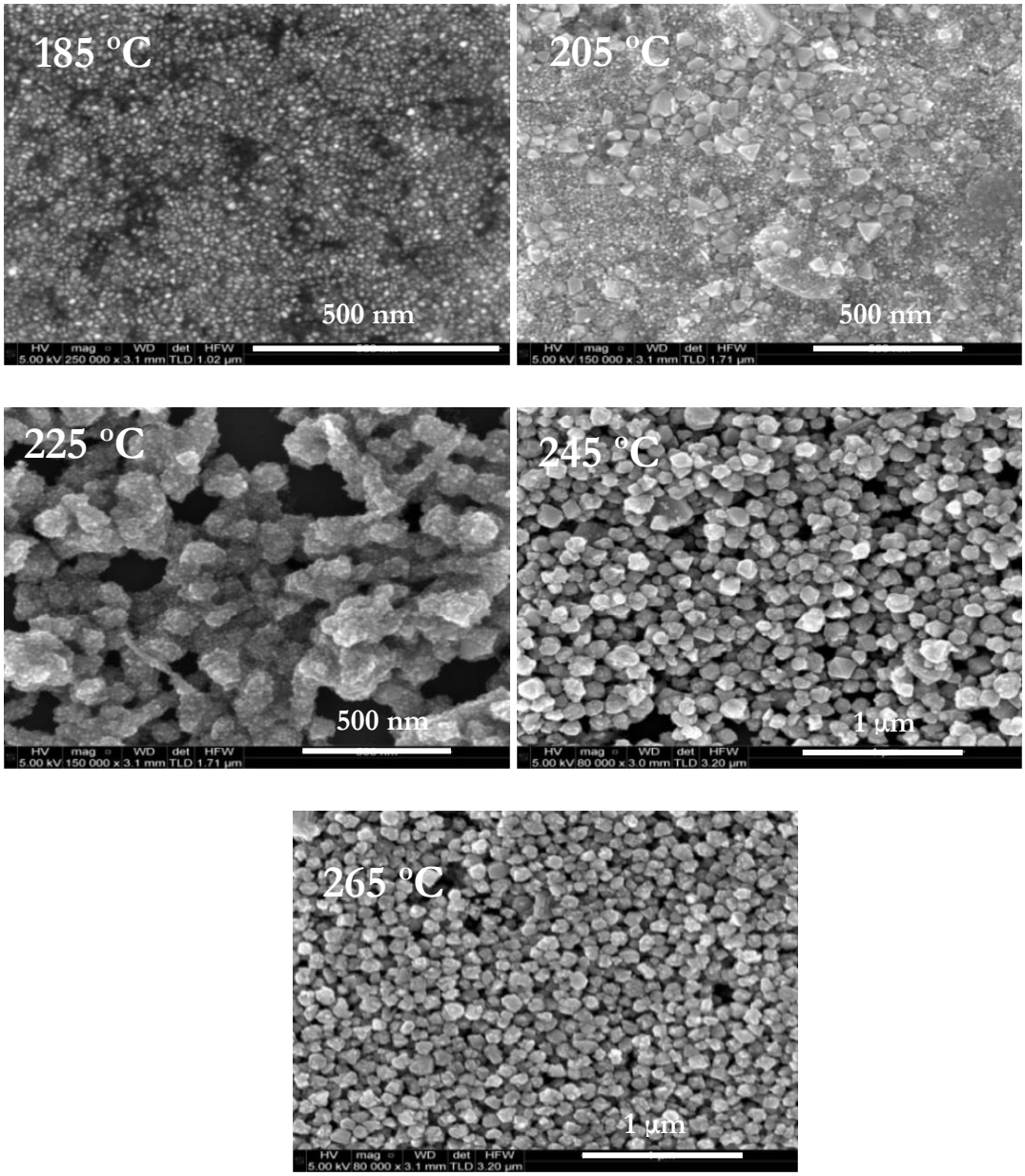

Figure 4.1 SEM images of the surface of CZTS films at different reaction temperature 185, 205, 225, 245 and 265 °C.

Energy dispersive x-ray spectroscopy EDX was performed to examine the overall composition of CZTS as synthesised nanoparticles. Figure 4.2 shows the chemical composition of copper, zinc, tin and sulphur of CZTS at different temperatures. In general, the Cu and Sn decreased with increasing temperature, whereas, Zn increased with increasing reaction temperature. Also, S was slightly increased with increasing reaction temperature.

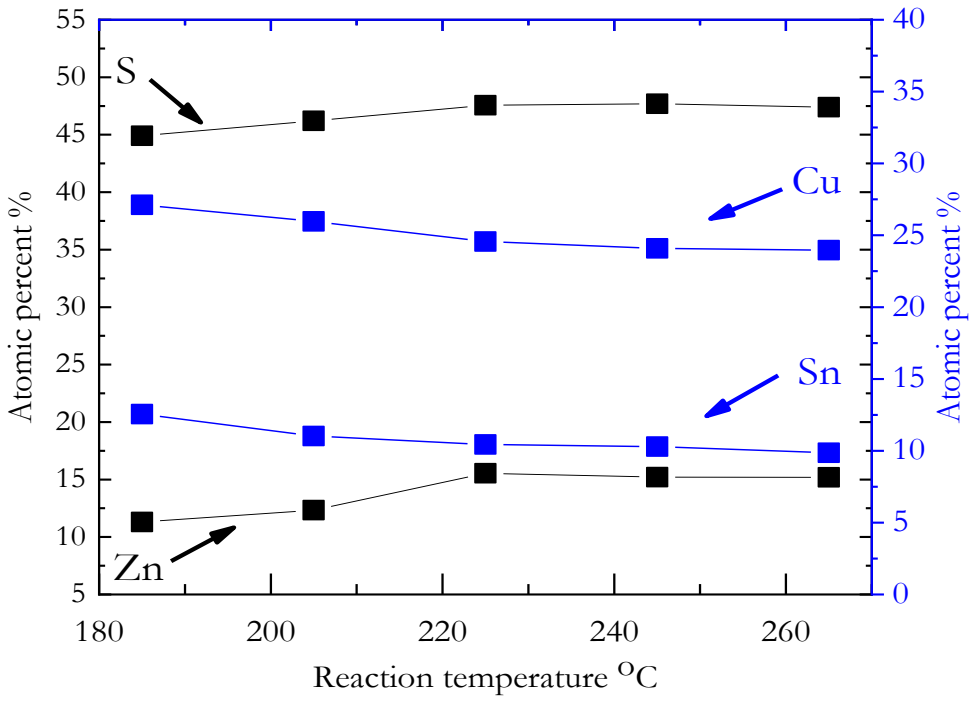

Figure 4.2 Chemical composition of as synthesis CZTS nanoparticles under different reaction temperatures.

Table 4.1 shows the chemical ratio based on CZTS nanoparticles. It can be seen by EDX measurements that the content of Zn and S increased with increasing temperature until 225 °C. Moreover, the atomic percent of Cu and Sn decreased with increasing the temperature. However, the compositional ratio was Cu/ (Zn + Sn) = 1.14, 1.11, 0.95, 0.94 and 0.96, and Zn/Sn = 0.90, 1.12, 1.49, 1.48 and 1.54 for 185, 205, 225, 245 and 265 °C respectively. However, the ratio of S/ Metal is lower than 1, which means that the sulphur content is deficient in all samples.

Table 4.1 Chemical composition and element ratios of CZTS nanoparticles with different reaction temperatures.

Temperature (°C)	Cu/(Zn+Sn)	Zn/Sn	S/(Cu+Zn+Sn)
185	1.14	0.90	0.88
205	1.11	1.12	0.94
225	0.95	1.49	0.94
245	0.94	1.48	0.96
265	0.96	1.54	0.97

4.3.1.2: TEM measurements

Transmission electron microscopy (TEM), high resolution TEM (HRTEM) and selected area electron diffraction (SAED) are shown in Figure 4.3, it can be seen that the size of particle increase with increasing reaction temperature and most of the nanocrystals are spherical. Also, most of nanoparticles' sizes agree with XRD measurements using Scherrer's equation.

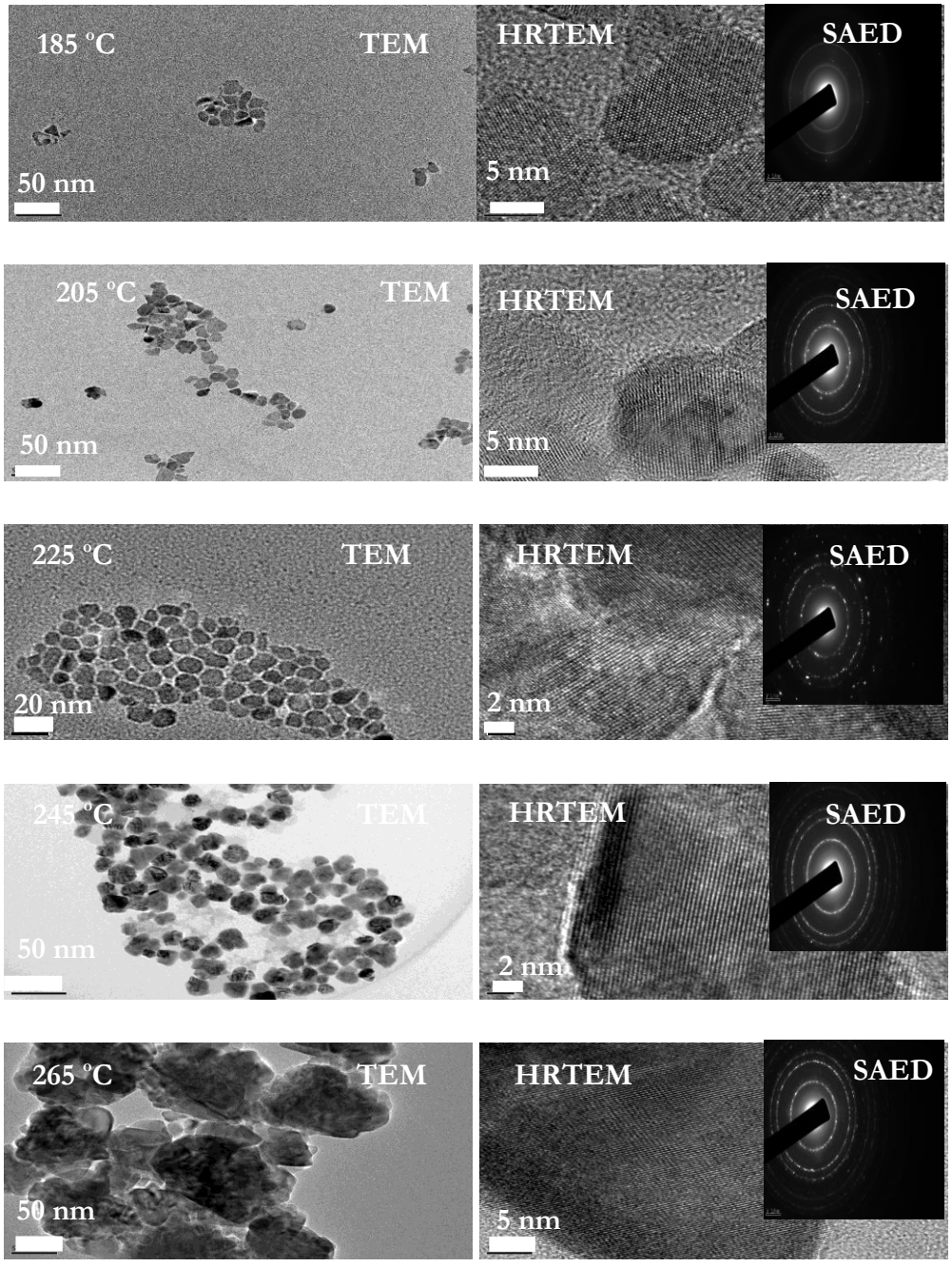

Figure 4.3 TEM, HRTEM and SAED of CZTS at 185, 205, 225, 245 and 265 °C for 0.5 h.

Further study to confirm the structure of the synthesised nanoparticles using HRTEM analysis was carried out and all of lattices of CZTS nanoparticles were revealed to be highly crystalline. Moreover, the inter-planar spacing *d* was measured to be 3.1 and 1.9 Å, corresponding to the (112) and (220) planes of the kesterite phase, respectively, and also in complete agreement with XRD measurements. SAED images show the three main brightness rings which correspond to 112, 200 and 220 planes of CZTS with tetragonal structure.

4.3.1.3: X-ray diffraction and rietveld refinement analysis:

Figure 4.4 shows the X-ray powder diffraction patterns of CZTS nanoparticles which were synthesised under different temperature from 185 °C to 265 °C. It is found that there are main diffraction peaks which are in good agreement with high intensity reflection of kesterite type structure of CZTS such as (112), (200), (220), (312) and (400/008) which are located at 28.8, 33.3, 47.8, 56.5 and 69.1° respectively according to JCPDS card number 26-0575. However, due to the similarity between KT and ST structures, the presence of ST structure is not excluded based on XRD data. Also, there are other peaks at 26.1, 31.1 and 51.1° which match the diffraction patterns of (210), (211) and (213) planes of wurtzite type structures of CZTS which were observed. Moreover, these peaks may correspond to $Cu_{2-x}S$ and SnS_2 secondary phases for samples produced at 245 and 265 °C.

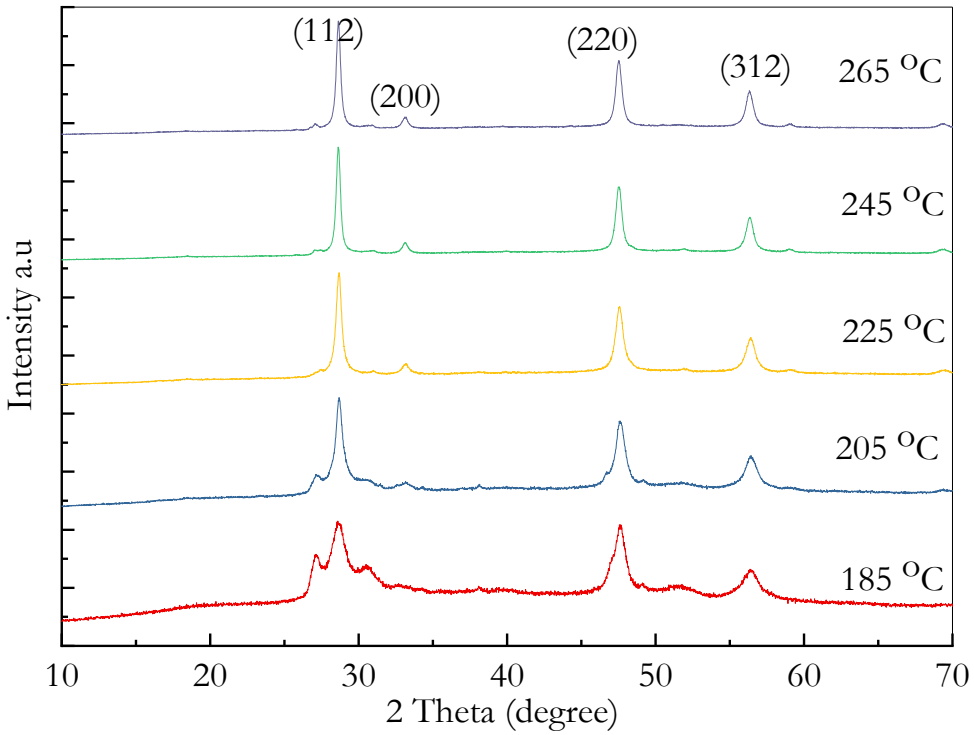

Figure 4.4 XRD pattern of as synthesis CZTS nanoparticles under different reaction temperatures.

However, due to the wurtzite structure having diffraction peaks at 28.6, 47.7 and 56.6° similar to kesterite structure, these peaks can be marked to (002), (230) and (232) planes of wurtzite structure or (112), (220) and (312) planes of kesterite structure [13, 14]. Moreover, due to the existence of a weak peak around 33.2°, this proves the existence of CZTS with kesterite structure in all samples, so, it can be said that all samples contain the wurtzite-kesterite mixed phase. It is clear that the peak intensities increase with increasing reaction temperature and become sharper. The average of CZTS nanoparticles size was calculated by using Scherrer's equation [15, 16] depending on the peaks width,

$$x = \frac{0.9\lambda}{D\cos\theta} \tag{4.1}$$

where λ is the wavelength of x-ray (Cu K_α = 0.154 nm), D is the full width at half maximum (FWHM) of the diffraction peaks and θ is the Bragg's angle. The average crystallite size of CZTS synthesised at 185, 205, 225, 245 and 265 °C were about 13, 28, 37, 48 and 49 nm respectively. It confirms that the size of crystallites was increased with

increasing reaction temperatures. The interplaner distance and lattice constant a and c were calculated by using the equation [17]:

$$\frac{1}{d_{hkl}^{\ 2}} = \frac{h^2 + k^2}{a^2} + \frac{l^2}{c^2} \qquad (4.2)$$

The interplaner distance was found close to values reported in the literature, and was calculated for *d* (112) and *d* (220) planes. The values were around 3.12 and 1.91 Å respectively and match well with lattice spacing measured from TEM measurements. These values slightly increase with increasing reaction temperature. Rietveld refinement analysis was used to confirm the phase purity of CZTS. Also, the lattice constants were calculated by using TOPAS software for kesterite and wurtzite structures as shown in the Table 4.2.

Table 4.2 Lattice parameters at different synthesis temperatures from rietveld refinement analysis.

Synthesis temperatures (°C)	**185**	**205**	**225**	**245**	**265**
Lattice parameters (Å)					
CZTS (kest) a	5.451	5.472	5.446	5.439	5.434
CZTS (kest) c/2	5.409	5.345	5.378	5.383	5.385
CZTS (wurt) a	3.829	3.821	3.792	3.803	3.822
CZTS (wurt) c/2	3.160	3.144	3.140	3.137	3.145

As shown Figure 4.5, the CZTS nanoparticles have a mixed structure between kesterite and wurtzite. The lattice constant CZTS (kest) a is in the range 5.434-5.472 Å and CZTS (kest) c is in the range 10.818-10.69 Å, which means that (a) values decreased and (c) values increased with increasing reaction temperatures for kesterite structure.

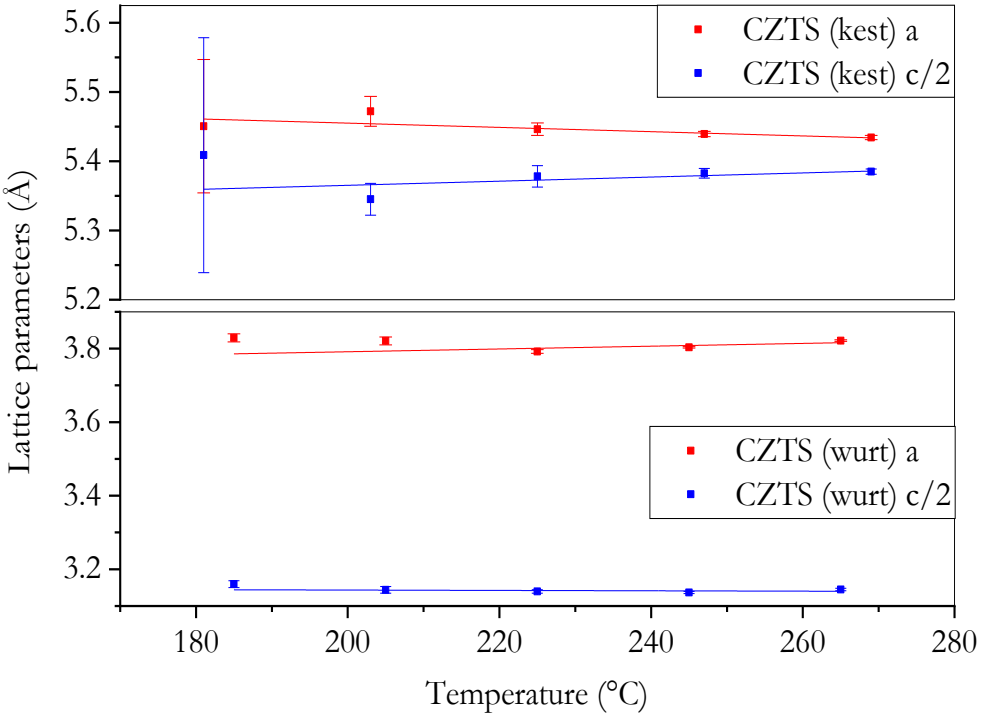

Figure 4.5 Lattice constant values at different CZTS synthesis temperatures.

Moreover, the lattice constant CZTS (wurt) a is in the range 3.829-3.822 Å and CZTS (wurt) c is in the range 6.32-6.29 Å, which means that (a) and (c) values had a small trend to smaller values with increasing reaction temperatures for wurtize structures. Those results from XRD and Rietveld refinement measurements agree with many literature reports [18-22] . However, due to the similarity between CZTS, CTS (copper tin sulphide) and c-ZnS structure, it is difficult using XRD pattern to distinguish in the angle position at major peaks. Raman spectroscopy was therefore used to identify whether secondary phases present in the samples.

4.3.1.4: Raman measurements:

Raman measurement of CZTS at different synthesis temperatures in Figure 4.6 show the main and strong peak located at 334 cm^{-1} for 180 °C, 336 cm^{-1} for 205 °C, 337 cm^{-1} for 225, 245 and 265 °C, with other small peaks located at 250, 265, 286, 355, and 370 cm^{-1} at all synthesis temperatures Additional peak located at 366 cm^{-1} for 225, 245 and 265 °C, and all these peaks confirming that all films were a single phase of CZTS.

The main peaks were located at 334, 336 and 337 cm^{-1} and are due to A asymmetry vibrational modes and related to sulphur vibration [23-26]. However, at 185 ^{o}C, the peak at 334 cm^{-1} is likely to be a result of mixed kesterite and wurtzite structure [27-29], whereas the peaks at 336 and 337 cm^{-1} with small shoulder peaks at 286 and 370 cm^{-1} can be well attributed to the scattering of kestrite CZTS phase [30, 31].

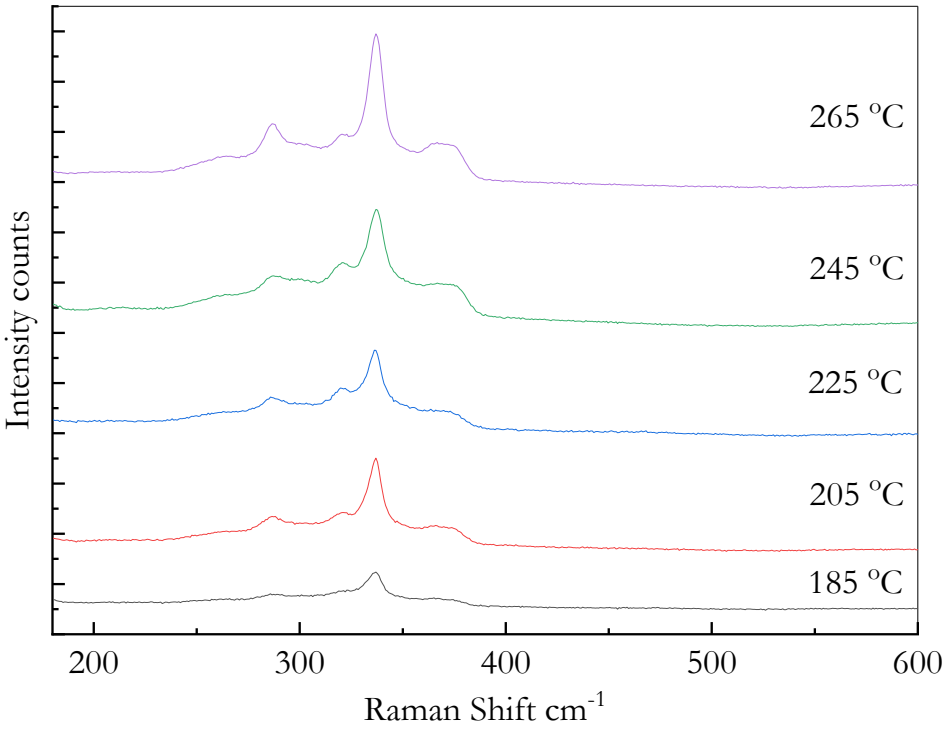

Figure 4.6 Raman spectrum of as synthesis CZTS nanoparticles under different reaction temperatures.

However, there are other peaks which may correspond to secondary phases such as a peak at 300 cm^{-1} for 185, 205, 225 and 245 ^{o}C which corresponds to SnS_2 and at 304 cm^{-1} for 265 ^{o}C samples which corresponds to Sn_2S_3 or Cu_2SnS_3 secondary phases [32-34]. All samples present the Cu_3SnS_4 secondary phase at 320 cm^{-1} [35-37]. Also, all samples except 225 ^{o}C had a small peak at 262 cm^{-1} which was assigned to $Cu_{2-x}S$ [21, 38-40]. There is no evidence of ZnS secondary phase at 271 and 351 cm^{-1} [41, 42], and $Cu_{2-x}S$ at 475 cm^{-1}.

4.3.1.5: Optical measurement

The optical band gap of CZTS nanoparticles has been calculated from the absorption spectrum using the form of the Tauc relation $(Ahv) = C(hv - E_g)^n$ where C is a constant, A is absorbance, E_g is the average band gap of the material and n depends on the type of transition and equal to ½, for direct band gap. The average band gap was estimated from the intercept of linear portion of the $(Ahv)^2$ vs. Energy Band gap plots.

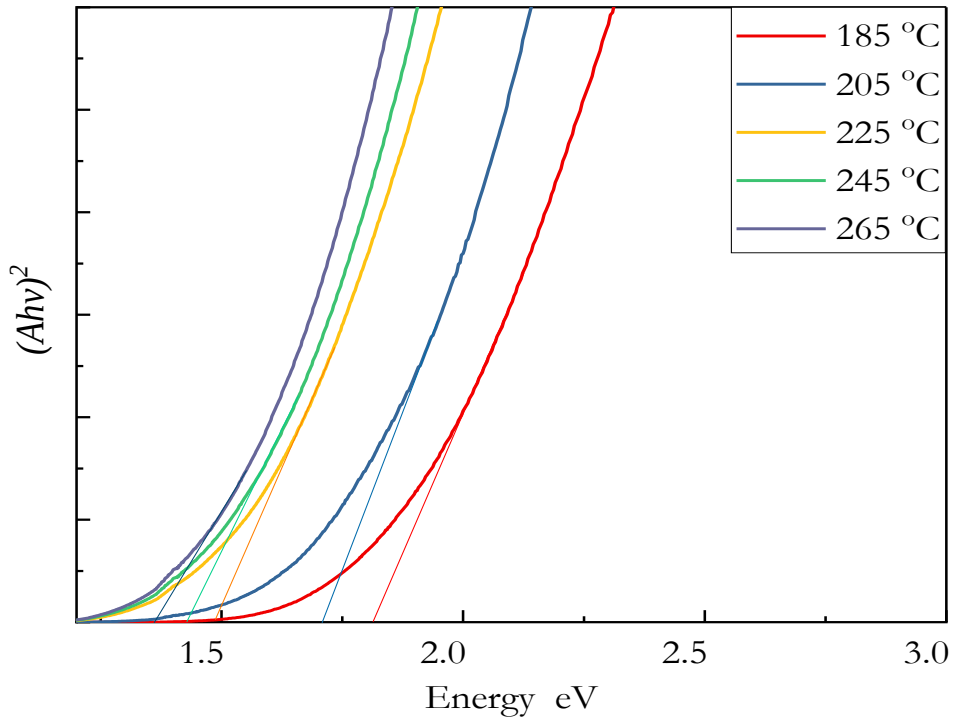

Figure 4.7 Energy band gap from UV–vis absorption spectra and calculated by Tauc plot of the CZTS nanocrystals at different temperatures.

The energy band gap spectra of as-synthesised CZTS nanoparticles were measured by using a UV–vis spectrophotometer as shown in Figure 4.7. The band gap energy values of samples under various reaction temperatures were calculated from absorption spectra to be 1.81, 1.75, 1.49, 1.40 and 1.32 eV corresponded to the reaction temperature of 185, 205, 225, 245 and 265 °C respectively for CZTS films.

However, due to the results above from SEM, TEM, EDX, Raman measurement and UV-Vis measurements, the sample synthesis at 225 °C for 0.5 h has less secondary phases and

has optimum size and shape and optical properties which make it suitable condition to thin film solar cells.

4.3.2: Effect of reaction time on CZTS

The effects of reaction time on the properties of CZTS nanoparticles with a fixed reaction temperature of 225 °C were also studied, and the reaction time was in the range from 0.5 to 2 h.

4.3.2.1: SEM & EDX measurements

As shown in Figure 4.8, it was found that the shape of CZTS nanoparticles was irregular, dispersive and aggregated together and the size of the nanoparticles gradually increased with increasing time. Moreover, the particles at 1.5 and 2.0 h became bigger with more irregular shapes.

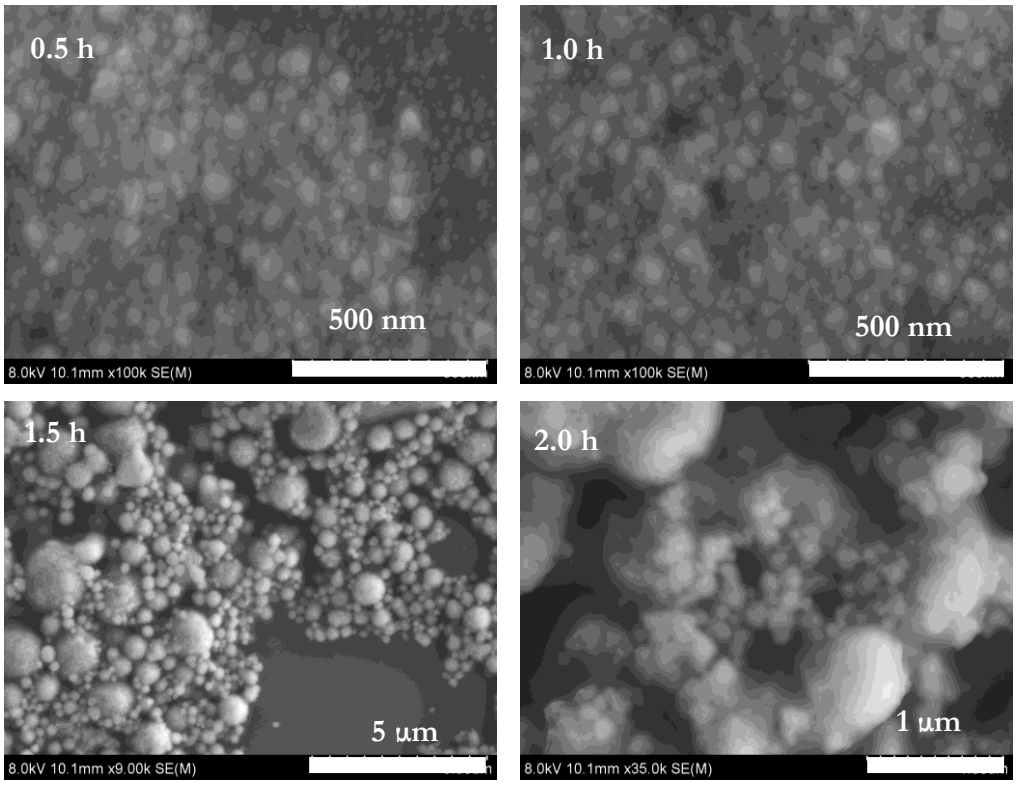

Figure 4.8 SEM of CZTS at 225 °C for 0.5 h, 1 h, 1.5 h and 2 h.

Table 4.3 shows the element ratios and atomic percent. It can be seen by EDX measurements that the contents of Sn and Zn slightly increased with increasing the reaction time. Moreover, the atomic percent of Cu and S decreased with increasing the reaction time. However, the compositional ration was Cu/ (Zn+Sn) = 0.95, 0.88, 0.83 and 0.72, and Zn/Sn = 1.49, 1.24, 1.41 and 1.37at 0.5, 1.0, 1.5 and 2.0 h respectively.

Table 4.3: Element ratios of CZTS nanoparticles with different reaction times determined by EDX.

Time h	Cu/(Zn+Sn)	Zn/Sn	S/(Cu+Zn+Sn)
0.5	0.95	1.49	0.94
1.0	0.88	1.24	0.95
1.5	0.83	1.41	0.94
2.0	0.72	1.37	0.92

However, it can be seen that the ratios of S/ Metal is less than 1, which means that the sulphur is inefficient in all samples. In general, the contents of Sn and Zn increased with increasing reaction time and the contents of S and Cu decreased with increasing reaction time as shown in Figure 4.9.

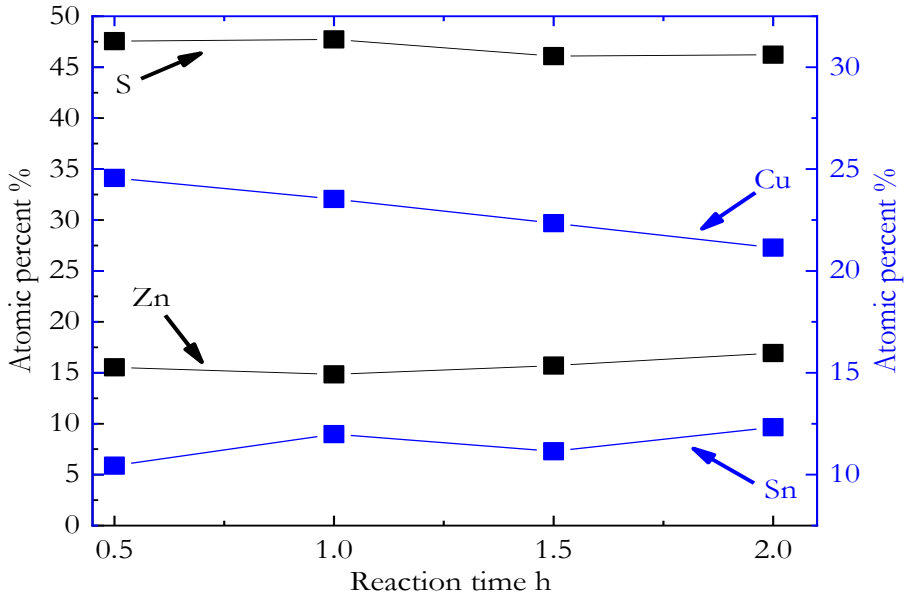

Figure 4.9 Chemical composition of as synthesis CZTS nanoparticles at different reaction times.

4.3.2.2: TEM measurements

As shown in Figure 4.10, the size of particle increases with increasing reaction time. Also, most of nanoparticles' size agrees closely with XRD measurements using Scherrer's equation.

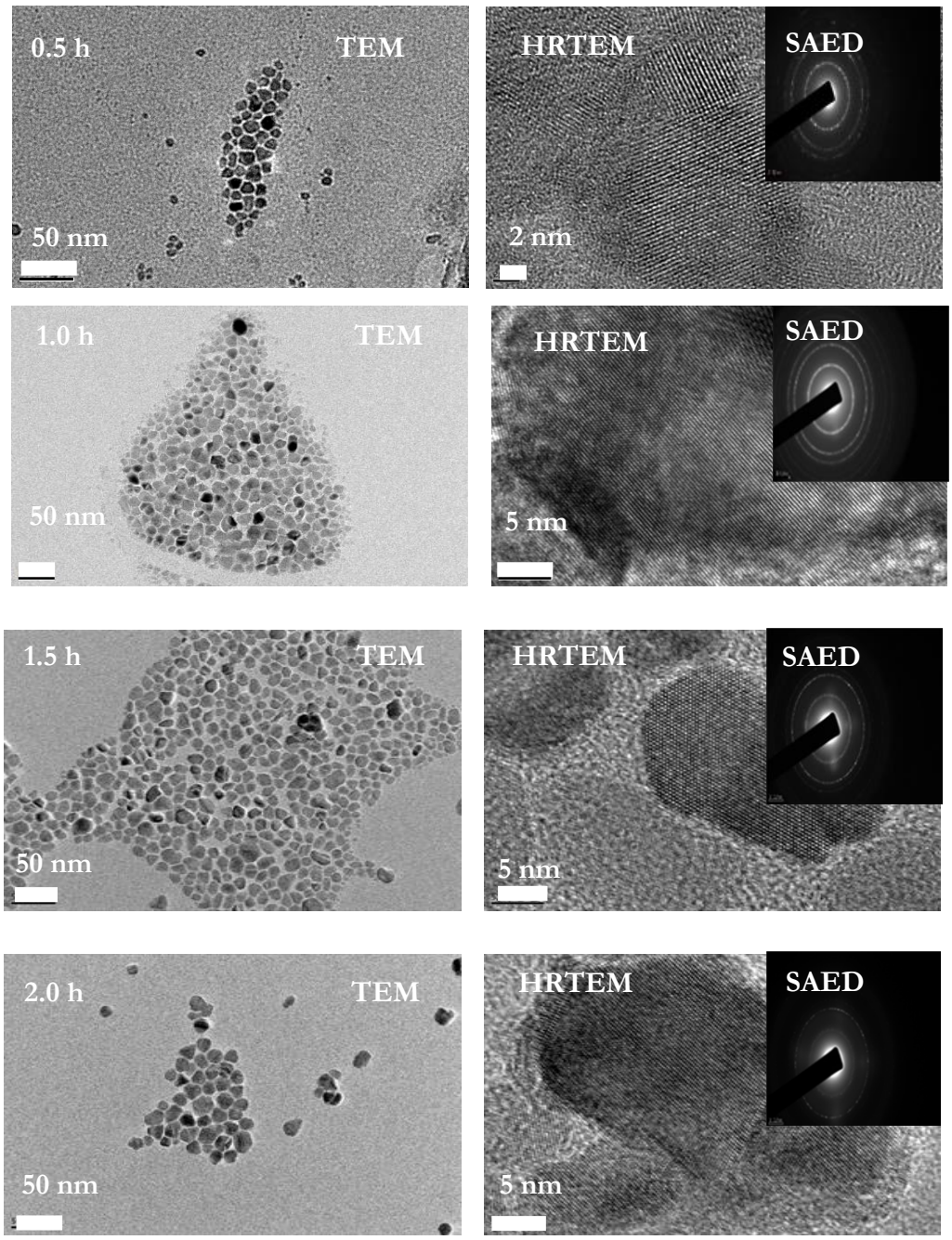

Figure 4.10 TEM, HRTEM and SAED of CZTS fabricated at 225 °C for 0.5 h, 1.0 h, 1.5 h and 2.0 h.

Moreover, the *d* spacing was calculated from HRTEM and also completely agrees with XRD measurements which is close to 3.1 and 1.9 Å, which corresponds to the (112) and (220) planes. SAED images show the three brightness rings this corresponds to 112, 200 and 220 planes. In general, the size of particles increases with increasing reaction times.

X ray diffraction and rietveld refinement analysis:

Figure 4.11 shows the XRD diffraction patterns of CZTS nanoparticles which were synthesised under different time from 0.5 h to 2 h. It is found that there are four main diffraction peaks which correspond to the plane of kesterite type structure such as (112), (200), (220) and (312) which are located at 28.6, 33.1, 47.6 and 56.3° respectively according to JCPDS card number 26-0575. Moreover, from peak widths, the size of crystallite was calculated by using Scherrer's equation. The average crystallite size of CZTS synthesised at 0.5, 1.0, 1.5 and 2.0 h were 37.1, 35.1, 41.2 and 45.8 nm, which confirms the size of particles increase with increasing reaction time. The CZTS nanoparticles have a mixed structure between kesterite and wurtzite.

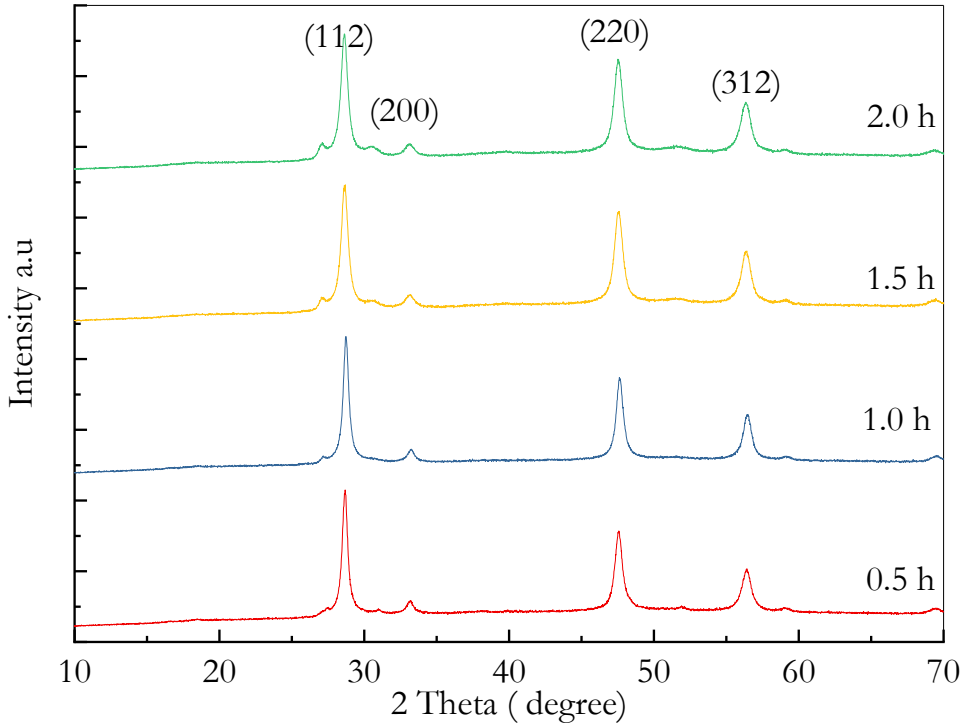

Figure 4.11 XRD of CZTS nanoparticles synthesis at 225 oC at different times.

The lattice constant CZTS (kest) a is 5.438 Å and CZTS (kest) c is 10.724 Å, which means that (a) values decreased slightly and (c) values increased with increasing reaction time for kesterite structure as shown in Figure 4.12.

Table 4.4 Lattice parameters at different synthesis times from rietveld refinement analysis.

Reaction times (h)	**0.5**	**1**	**1.5**	**2**
	Lattice parameters (Å)			
CZTS (kest) a	5.446	5.439	5.435	5.430
CZTS (kest) c/2	5.350	5.346	5.373	5.379
CZTS (wurt) a	3.790	3.816	3.817	3.818
CZTS (wurt) c/2	3.138	3.166	3.158	3.151

the lattice constant CZTS (wurt) a is 3.829 Å and CZTS (wurt) c is 6.32 Å, which means that (a) and (c) values had a small tend to small values with increasing reaction time for wurtize structure as shown in Figure 4.12.

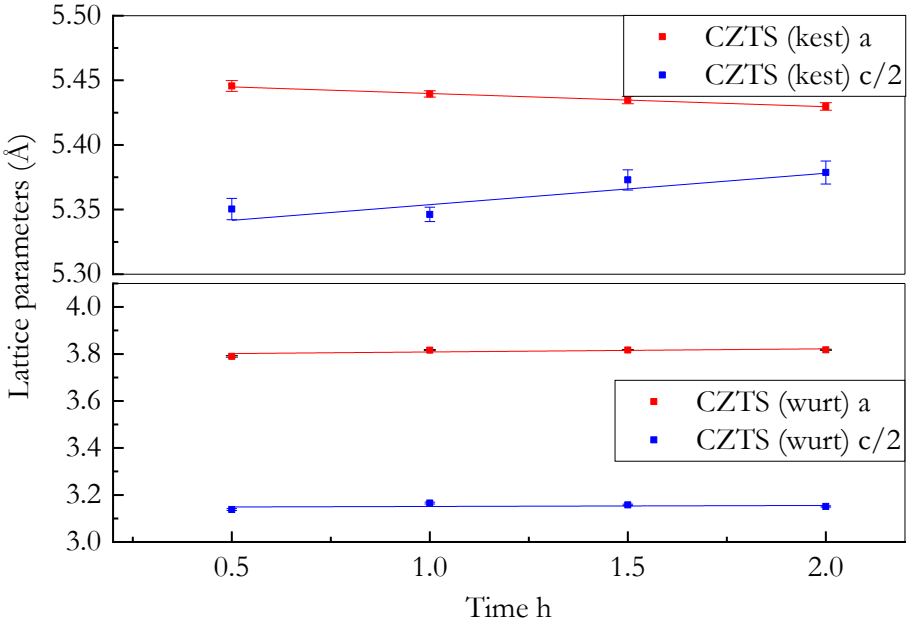

Figure 4.12 Lattice constant for as-synthesised CZTS under different reaction times.

4.3.2.3: Raman Measurement

Raman measurements shown in Figure 4.13 confirmed that the main peaks for different synthesis times of CZTS were at 337 cm^{-1} for 0.5 h and 1.0 h, and at 336 cm^{-1} for 1.5 h and 2.0 h. also, other small peaks at in range (280-286 cm^{-1}), (352-355 cm^{-1}) and (370-375 cm^{-1}) have been observed and assigned to CZTS nanoparticles, and these peaks are corresponding to the A1 mode of single phase CZTS [43, 44]. Also, the peak at 320 cm^{-1} assigned to Cu_3SnS_4 [45, 46] in all samples except that synthesised at 1 h condition where the main peak become more narrow and sharper than other conditions which indicated the crystallinity was improved at this synthesis time.

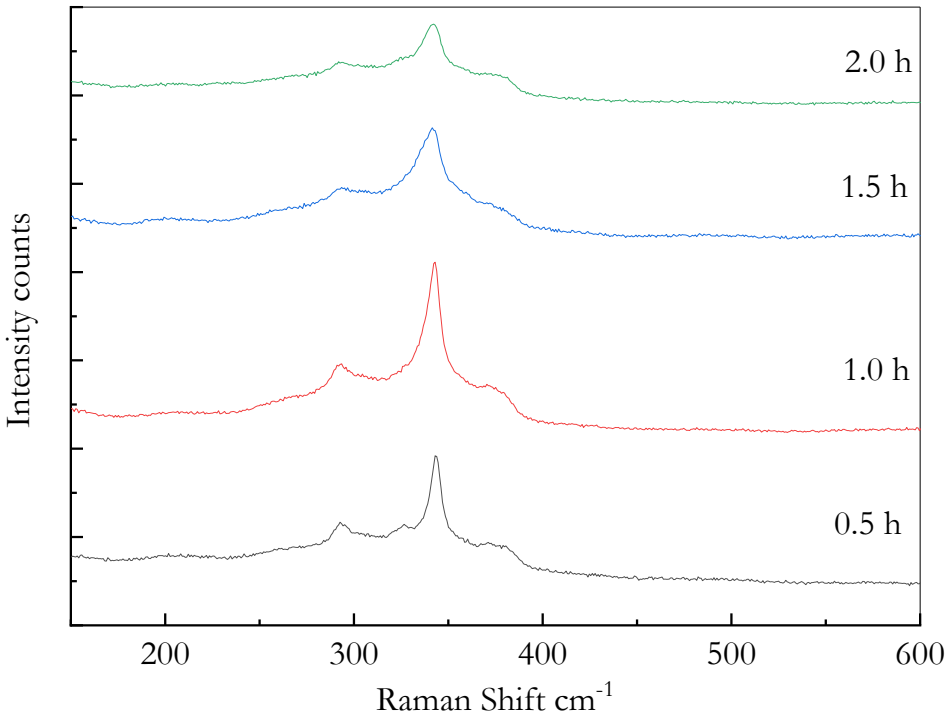

Figure 4.13 Raman measurements of as synthesis CZTS nanoparticles under different reaction times.

There is a peak at 264 cm^{-1} for $Cu_{2-x}S$ for 1.5 and 2 h. However, there is no evidence for peaks at 271 cm^{-1} and 352 cm^{-1} for all samples which correspond to phonon energies for ZnS [47, 48]. Also, no peaks located at 220 cm^{-1} for SnS, 315 cm^{-1} for SnS_2 and (470-475 cm^{-1}) for $Cu_{2-x}S$ [47] .

4.3.2.4: Optical Measurement

The energy band gap of all samples under different reaction time 0.5, 1.0, 1.5 and 2.0 h were calculated to be 1.49, 1.54, 1.61 and 1.70 eV respectively. It can be seen that the energy band gap has increased with increasing reaction time as shown in Figure 4.14.

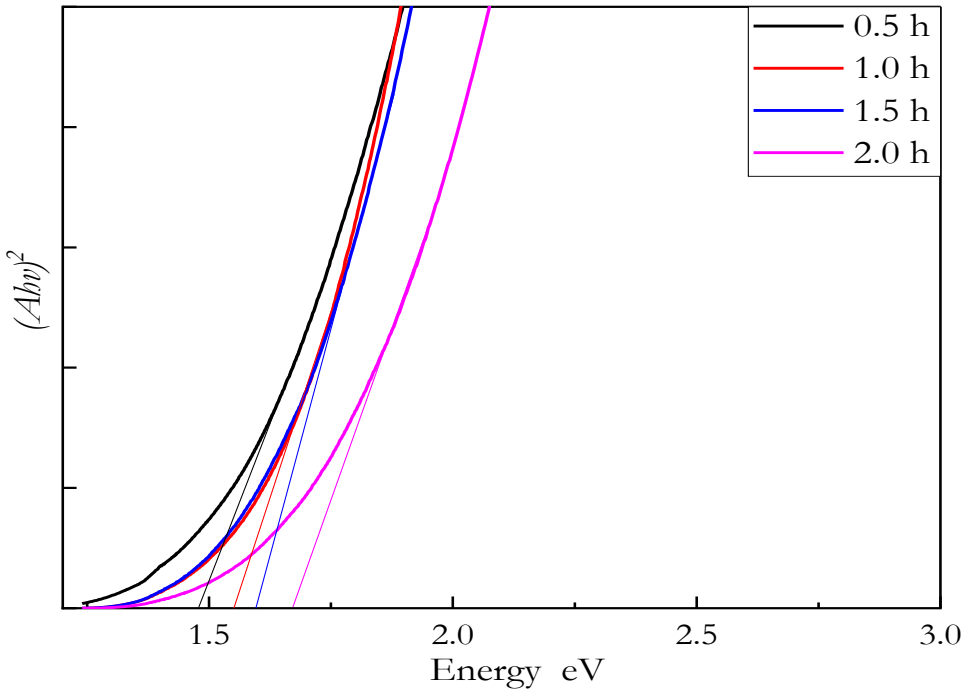

Figure 4.14 UV–vis–NIR absorption spectra and dependence of $(Ahν)^2$ on hν of the CZTS nanocrystals prepared at different times.

4.4: Conclusion

Hot injection synthesis route towards kesterite CZTS nanoparticles at different conditions (temperature and time) were studied. These conditions have significant effects on the CZTS nanoparticles on structure, composition, shape and optical properties. The sizes of CZTS under different temperatures differ from 19 nm to 48 nm. Also, the composition of elements was changed with increasing temperature and time. The band gaps of all samples were in the range between 1.5 and 1.9 eV and decreased with increasing reaction temperature whereas increasing with increasing reaction time. Many techniques were used to investigated structure and optical properties for all samples. From the above results we can say that the optimum conditions which are suitable for synthesising a high quality CZTS absorber thin film is 225 °C at 1.0 h.

4.5: References

1. Guo, Q., H.W. Hillhouse, and R. Agrawal, *Synthesis of Cu_2ZnSnS_4 nanocrystal ink and its use for solar cells.* Journal of the American Chemical Society, 2009. **131**(33): p. 11672-11673.

2. Steinhagen, C., et al., *Synthesis of Cu_2ZnSnS_4 Nanocrystals for Use in Low-Cost Photovoltaics.* Journal of the American Chemical Society, 2009. **131**(35): p. 12554-+.

3. Riha, S.C., B.A. Parkinson, and A.L. Prieto, *Solution-Based Synthesis and Characterization of Cu_2ZnSnS_4 Nanocrystals.* Journal of the American Chemical Society, 2009. **131**(34): p. 12054-+.

4. Yongtao, Q., et al., *Influence of reaction conditions on the properties of solution-processed Cu_2ZnSnS_4 nanocrystals.* Materials Research Express, 2014. **1**(4): p. 045040.

5. Guo, Q., et al., *Fabrication of 7.2% Efficient CZTSSe Solar Cells Using CZTS Nanocrystals.* Journal of the American Chemical Society, 2010. **132**(49): p. 17384-17386.

6. Zhang, K.D., et al., *Preparation of Cu_2ZnSnS_4 thin films using spin-coating method with thermolysis and annealing.* Journal of Sol-Gel Science and Technology, 2015. **73**(2): p. 452-459.

7. Majula, L., et al., *Spin-coated Kesterite CZTS Thin Films for Photovoltaic Applications.* Journal of the Korean Physical Society, 2015. **67**(6): p. 1078-1081.

8. Katagiri, H., et al., *Development of CZTS-based thin film solar cells.* Thin Solid Films, 2009. **517**(7): p. 2455-2460.

9. Platzer-Björkman, C., et al., *Influence of precursor sulfur content on film formation and compositional changes in Cu_2ZnSnS_4 films and solar cells.* Solar Energy Materials and Solar Cells, 2012. **98**(0): p. 110-117.

10. Tanaka, K., et al., *Chemical composition dependence of morphological and optical properties of Cu_2ZnSnS_4 thin films deposited by sol-gel sulfurization and Cu_2ZnSnS_4 thin film solar cell efficiency.* Solar Energy Materials and Solar Cells, 2011. **95**(3): p. 838-842.

11. Xie, M., et al., *Preparation and Characterization of Cu_2ZnSnS_4 Thin Films and Solar Cells Fabricated from Quaternary Cu-Zn-Sn-S Target.* International Journal of Photoenergy, 2013.

12. Liu, J.P., et al., *Fabrication and characterization of kesterite Cu_2ZnSnS_4 thin films deposited by electrostatic spray assisted vapour deposition method.* Physica Status Solidi a-Applications and Materials Science, 2015. **212**(1): p. 135-139.

13. Berg, D.M., et al., *Discrimination and detection limits of secondary phases in Cu_2ZnSnS_4 using X-ray diffraction and Raman spectroscopy.* Thin Solid Films, 2014. **569**: p. 113-123.

14. Luo, Q., et al., *Controllable Synthesis of Wurtzite Cu_2ZnSnS_4 Nanocrystals by Hot-Injection Approach and Growth Mechanism Studies.* Chemistry-an Asian Journal, 2014. **9**(8): p. 2309-2316.

15. Mkawi, E.M., et al., *Solvent solution-dependent properties of nonstoichiometric cubic Cu_2ZnSnS_4 nanoparticles.* Chemical Physics Letters, 2014. **608**(0): p. 393-397.

16. Willardson, R.K. and A.C. Beer, *Semiconductors and Semimetals*. 1972: Elsevier Science.

17. Chen, J., et al., *Influences of synthesis conditions on chemical composition of Cu_2ZnSnS_4 nanocrystals prepared by one pot route.* Journal of Materials Science: Materials in Electronics, 2014. **25**(2): p. 873-881.

18. Gurieva, G., et al., *Cu_2ZnSnS_4 thin films grown by spray pyrolysis: characterization by Raman spectroscopy and X-ray diffraction.* Physica Status Solidi C: Current Topics in Solid State Physics, Vol 10, No 7-8, 2013. **10**(7-8): p. 1082-1085.

19. Li, Z.G., et al., *Phase-Selective Synthesis of Cu_2ZnSnS_4 Nanocrystals using Different Sulfur Precursors.* Inorganic Chemistry, 2014. **53**(20): p. 10874-10880.

20. Li, M., et al., *Synthesis of Pure Metastable Wurtzite CZTS Nanocrystals by Facile One-Pot Method.* Journal of Physical Chemistry C, 2012. **116**(50): p. 26507-26516.

21. Ahmad, R., et al., *A comprehensive study on the mechanism behind formation and depletion of Cu_2ZnSnS_4 (CZTS) phases.* Crystengcomm, 2015. **17**(36): p. 6972-6984.

22. Brandl, M., et al., *In-situ X-ray diffraction analysis of the recrystallization process in Cu_2ZnSnS_4 nanoparticles synthesised by hot-injection.* Thin Solid Films, 2015. **582**: p. 269-271.

23. Mitzi, D.B., et al., *The path towards a high-performance solution-processed kesterite solar cell.* Solar Energy Materials and Solar Cells, 2011. **95**(6): p. 1421-1436.

24. Grossberg, M., et al., *Photoluminescence study of disordering in the cation sublattice of Cu_2ZnSnS_4.* Current Applied Physics, 2014. **14**(11): p. 1424-1427.

25. Sarswat, P.K. and M.L. Free, *An investigation of rapidly synthesized Cu_2ZnSnS_4 nanocrystals.* Journal of Crystal Growth, 2013. **372**: p. 87-94.

26. Kosyak, V., M.A. Karmarkar, and M.A. Scarpulla, *Temperature dependent conductivity of polycrystalline Cu_2ZnSnS_4 thin films.* Applied Physics Letters, 2012. **100**(26): p. 263903.

27. Tan, J.M.R., et al., *Understanding the Synthetic Pathway of a Single-Phase Quarternary Semiconductor Using Surface-Enhanced Raman Scattering: A Case of Wurtzite Cu_2ZnSnS_4 Nanoparticles.* Journal of the American Chemical Society, 2014. **136**(18): p. 6684-92.

28. Lu, X.T., et al., *Wurtzite Cu_2ZnSnS_4 nanocrystals: a novel quaternary semiconductor.* Chemical Communications, 2011. **47**(11): p. 3141-3143.

29. Zhao, Z.Y., et al., *Electronic structure and optical properties of wurtzite-kesterite Cu_2ZnSnS_4.* Physics Letters A, 2013. **377**(5): p. 417-422.

30. Caballero, R., et al., *Non-stoichiometry effect and disorder in Cu_2ZnSnS_4 thin films obtained by flash evaporation: Raman scattering investigation.* Acta Materialia, 2014. **65**: p. 412-417.

31. Valakh, M.Y., et al., *Optically induced structural transformation in disordered kesterite Cu_2ZnSnS_4.* Jetp Letters, 2013. **98**(5): p. 255-258.

32. Bahramzadeh, S., H. Abdizadeh, and M.R. Golobostanfard, *Controlling the morphology and properties of solvothermal synthesized Cu_2ZnSnS_4 nanoparticles by solvent type.* Journal of Alloys and Compounds, 2015. **642**: p. 124-130.

33. Mkawi, E., et al., *Dependence of Copper Concentration on the Properties of Cu_2ZnSnS_4 Thin Films Prepared by Electrochemical Method.* Int. J. Electrochem. Sci, 2013. **8**: p. 359-368.

34. Tiong, V.T., et al., *Phase-selective hydrothermal synthesis of Cu_2ZnSnS_4 nanocrystals: the effect of the sulphur precursor.* Crystengcomm, 2014. **16**(20): p. 4306-4313.

35. Weber, A., et al., *In-situ XRD on formation reactions of Cu_2ZnSnS_4 thin films*, in *Physica Status Solidi C - Current Topics in Solid State Physics, Vol 6, No 5*, S. Sadewasser, et al., Editors. 2009, Wiley-V C H Verlag Gmbh: Weinheim. p. 1245-+.

36. Schorr, S., et al., *In-situ investigation of the kesterite formation from binary and ternary sulphides.* Thin Solid Films, 2009. **517**(7): p. 2461-2464.

37. Ozdal, T. and H. Kavak, *Comprehensive analysis of spin coated copper zinc tin sulfide thin film absorbers.* Journal of Alloys and Compounds, 2017. **725**: p. 644-651.

38. Fontané, X., et al., *In-depth resolved Raman scattering analysis for the identification of secondary phases: Characterization of Cu_2ZnSnS_4 layers for solar cell applications.* Applied Physics Letters, 2011. **98**(18): p. 181905.

39. Fernandes, P.A., P.M.P. Salome, and A.F.d. Cunha, *Growth and Raman scattering characterization of Cu_2ZnSnS_4 thin films.* Thin Solid Films, 2009. **517**(7): p. 2519-2523.

40. Xie, H., et al., *Formation and impact of secondary phases in Cu-poor Zn-rich $Cu_2ZnSn(S_{1-y}Se_y)_4$ ($0 \leq y \leq 1$) based solar cells.* Solar Energy Materials and Solar Cells, 2015. **140**: p. 289-298.

41. Ahmed, S., et al., *A High Efficiency Electrodeposited Cu_2ZnSnS_4 Solar Cell.* Advanced Energy Materials, 2012. **2**(2): p. 253-259.

42. Fairbrother, A., et al., *Development of a Selective Chemical Etch To Improve the Conversion Efficiency of Zn-Rich Cu_2ZnSnS_4 Solar Cells*. Journal of the American Chemical Society, 2012. **134**(19): p. 8018-8021.

43. Ghediya, P. and T. Chaudhuri, *Doctor-blade printing of Cu_2ZnSnS_4 films from microwave-processed ink*. Journal of Materials Science: Materials in Electronics, 2015. **26**(3): p. 1908-1912.

44. Mirbagheri, N., et al., *Synthesis of ligand-free CZTS nanoparticles via a facile hot injection route*. Nanotechnology, 2016. **27**(18): p. 85603-85603.

45. Fernandes, P.A., P.M.P. Salomé, and A.F.d. Cunha, *Study of polycrystalline Cu_2ZnSnS_4 films by Raman scattering*. Journal of Alloys and Compounds, 2011. **509**(28): p. 7600-7606.

46. Fernandes, P.A., P.M.P. Salome, and A.F.d. Cunha, *A study of ternary Cu_2SnS_3 and Cu_3SnS_4 thin films prepared by sulfurizing stacked metal precursors*. Journal of Physics D-Applied Physics, 2010. **43**(21).

47. Gao, Y., et al., *Understanding the growth mechanism of wurtzite Cu_2ZnSnS_4 nanocrystals and the photodegradation properties*. Materials & Design, 2017. **123**: p. 24-31.

48. Wang, Y., et al., *Influence of sintering temperature on screen printed Cu_2ZnSnS_4 (CZTS) films*. Journal of Alloys and Compounds, 2012. **539**(0): p. 237-241.

Chapter 5: A study of the effect of different Copper and Zinc compositions

5.1: Introduction

Synthesis of CZTS nanoparticle inks is a competitive processes for thin film solar cells because the defects and secondary phases are present during their formation such as ZnS, Cu_xS, SnS and Cu_2SnS_3 [1, 2]. However, these secondary phases have either positive or negative roles in CZTS devices. For instance, secondary phases act as carrier barriers and form traps at interfacial layers which leads to decrease the efficiency of CZTS nanoparticle devices [3] and for more details see chapter 2. There are many factors that limit CZTS device efficiency with synthesis conditions such as temperature and reaction duration, composition control and secondary phase's formation. Controlling Cu and Zn content are one of the important factors for high efficiency under copper poor and zinc rich composition. Therefore, Cu poor conditions can reduce the concentration of complex defects such as $[Cu_{Zn}+Sn_{Zn}]$ which leads to form electron trapping states in the CZTS absorber layer [4, 5]. Moreover, increasing Zn content leads to increase the grain size which reduces the series resistance of CZTS thin film solar cells, but excess Zn content also leads to form ZnS secondary phase. Moreover, Cu and Zn compositions play an important role to determine the p-type conductivity of CZTS and also the hole concentration [6, 7] However, as the pure CZTS region on the phase diagram is too small, controlling the element compositions plays an important role in CZTS properties [8, 9]. Furthermore, the efficiency of CZTS relies on the chemical composition. For instance, the highest efficiencies of CZTS devices are obtained in the narrow composition range close to 0.80-0.85 and 1.10-1.25 for Cu/Zn+Sn and Zn/Sn respectively which suggests the Cu poor and Zn rich composition is favourable [9, 10].

The aim of this work is to study the effect of the material composition of copper content and zinc content on the structure, morphological and optical properties of CZTS thin films.

5.2: Sample preparation

5.2.1: CZTS synthesis

The nanoparticles for this study were prepared in similar formation to the previous chapter with some changes described in the Tables 5.1 and 5.2. In this study stoichiometric and non-stoichiometric batches were synthesised to study the effect of chemical compositions on structure, optical and electrical properties for CZTS nanoparticle inks.

Table 5.1 Different composition of Copper prepared in mmol units.

	copper (II) acetylacetonate	**zinc (II) acetylacetonate**	**tin (IV) bis(acetylacetonate) dichloride**
C1	1.86	0.75	0.75
C2	1.5	0.75	0.75
C3	1.30	0.75	0.75

Table 5.2 Different composition of zinc prepared in mmol units.

	copper (II) acetylacetonate	**zinc (II) acetylacetonate**	**tin (IV) bis(acetylacetonate) dichloride**
S1	1.5	0.75	0.75
S2	1.44	0.87	0.75
S3	1.44	0.94	0.75
S4	1.44	1.09	0.75

These mixtures were heated in an oleylamine solution to 140 ^{o}C under vacuum and degassed for 30 min and then purged with argon several times. Next, the reaction temperature was increased to 225^{o}C, and then the solution of 4 mmol of elemental sulphur in 4.5 ml oleylamine was injected into the mixture and was kept for 1 h under argon atmosphere. Subsequently, 5 ml of toluene and 40 ml of isopropanol were added into the solution, and the nanoparticles were collected using a centrifuge at 10000 rpm for 10 min after cooling the solution to 60 ^{o}C at room atmosphere. The supernatant was then decanted. Afterwards, 20 ml of toluene and 10 ml of isopropanol were added and the

suspension was centrifuged at 8000 rpm for 10 min, and the supernatant was decanted again and this step was repeated three times. These steps were repeated for each batch.

5.2.2: Thin film preparation

The CZTS nanoparticles were deposited on glass by spin coating technique. The glass was cleaned by using acetone, methanol and distilled water for ten minutes for each step. Then, the glass was dried by a using nitrogen flow. The high concentration of CZTS ink 200 mg/ml in hexanethiol solvent was dropped on the glass at high speed 2500 rpm for 10 seconds to achieve a uniform film and followed by preheating process at different temperatures; at 150 ^{o}C for 30 seconds and then at 300 ^{o}C for 30 seconds in air. Lastly, the above process repeated several time to obtain a favourable film thickness.

5.3: Results and discussion

5.3.1: Investigation of the effect of different Cu content on CZTS structure

X-ray diffraction (XRD) pattern of CZTS nanocrystals at different Copper compositions are given in Figure 5.1. Characteristic peaks for nanocrystals are clearly observed on XRD patterns. The as-synthesized CZTS nanocrystals showed five intensive XRD peaks centred at 2θ = 28.6°, 33.1°, 47.5° , 56.3° and 69.1° corresponding to planes (112), (200), (220), (312) and (008) respectively for all samples (C1= Cu rich, C2= stoichiometric and C3= Cu poor), which are similar to those reported for CZTS powders (JCPD 26-0575) These peak positions are in excellent agreement with other XRD measurements reported in the literature [11].

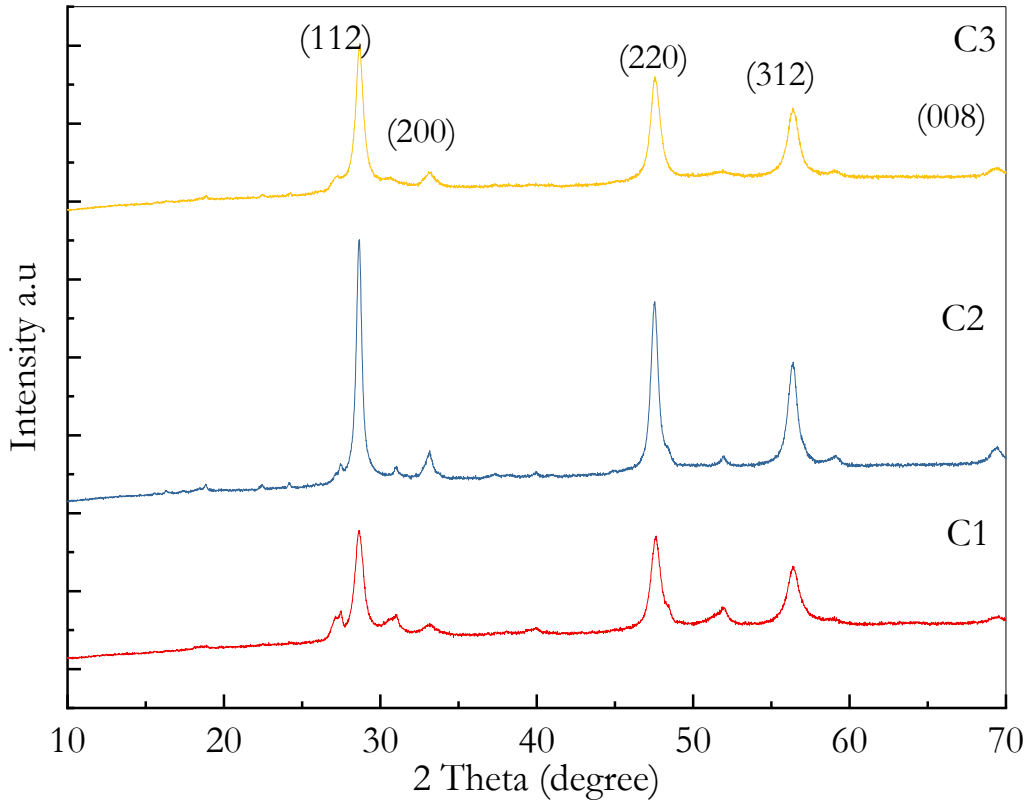

Figure 5.1 XRD patterns of CZTS Nanocrystals at different Cu content.

Moreover, there are small peaks at 27.0° which may correspond to SnO_2 or SnS secondary phases for all samples [12, 13]. However, in addition to 27.0° (100) there are peaks at 31.2°

(101) and 51.8° (103) in C1 and C2 samples which disappears in C3 sample which corresponds to wurtzite CZTS structure [10, 14-16].

The average particle size of the nanocrystals was calculated from the (112) diffraction peaks at 28.6° by using Debye-Sherrer's equation which gives 24.3, 39.3 and 31.8 nm for C1 , C2 and C3 samples respectively. Moreover, the *d* spacing was calculated as 0.31 and 0.19 nm for (112) and (220) planes for all samples, which is also confirmed by TEM analysis. This agrees with many studies [15, 17].

The structure and phase purity of the CZTS nanocrystals were investigated using Raman analysis. The Raman spectra of CZTS nanocrystals are presented in Figure 5.2, the characteristic peaks of CZTS are clearly observed on spectrum. A strong Raman peak at 336 cm^{-1} for Cu rich, 337 cm^{-1} ideal and 338 cm^{-1} for C3 which shifted to higher wavenumber as a result of changing the copper compositions. Small peaks are observed at 287-289, 364 and 370 cm^{-1} corresponded to the A1 mode of single phase of CZTS which also is associated with the presence of a disordered kestrite phase [7, 18].

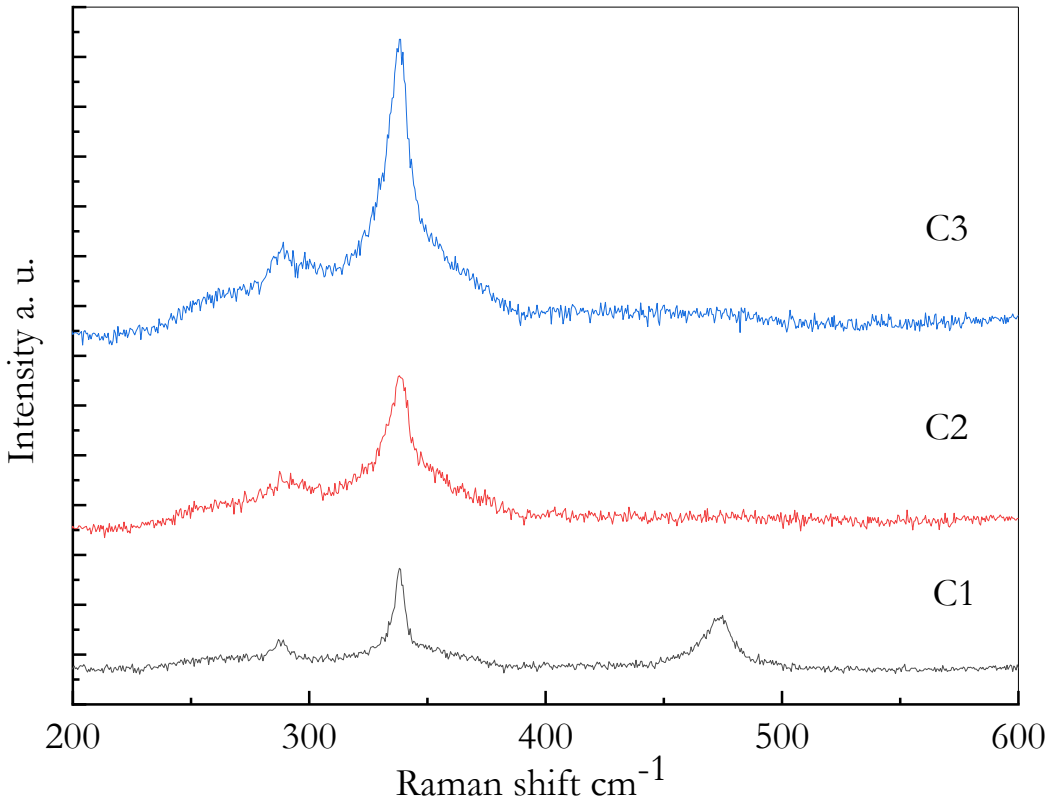

Figure 5.2 Raman shifts of CZTS nanocrystals at different Cu content.

However, in sample C1, there are others small peaks at 318 cm^{-1} which indicate Cu_2SnS_3. However, there is no significant indication of phase separation for Sn_2S_3 at 304 cm^{-1} and ZnS at 355 cm^{-1} In C2 and C3 samples [19, 20]. Moreover, there is no evidence for $Cu_{2-x}S$ at 475 cm^{-1} for all samples except C1 sample [21, 22]. Since no other crystalline forms were observed in the Raman spectrum, it is strongly suggested that the structure of the CZTS samples shows a single crystallinity on C2 and C3 samples [23, 24].

TEM images in Figure 5.3, shows that there are no extreme changes in nanoparticle size due to the change in composition. C3 shows some larger particles but the bulk of the particles across the images have no significant change in the sizes of the particles.

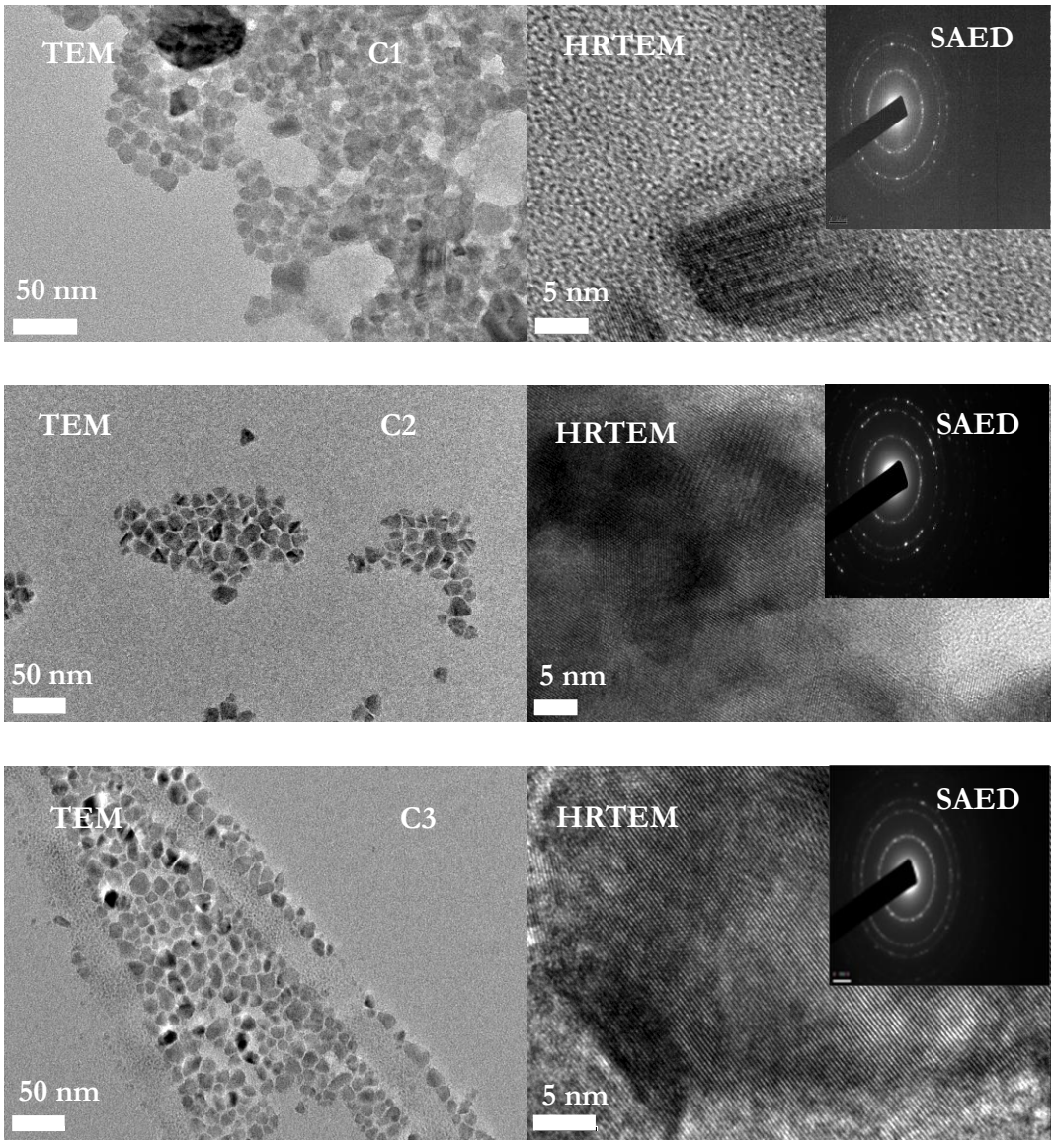

Figure 5.3 TEM, SAED and HRTEM images for CZTS nanoparticles under variable Cu content.

The particles at different Cu content appear to have a range of different shapes and sizes. The average particles sizes were calculated as 43.06±1.45, 44.93±1.35 and 48.42±2.47 nm for C1, C2 and C3 samples respectively. The SAED images provide the plane spacing which were found as 0.31 nm and 0.19 nm for single crystalline particles which corresponds to the (112) and (220) planes of tetragonal CZTS, yielding the most intense reflections in the XRD pattern. Moreover, the HRTEM images show three brightness rings which correspond to (112), (220) and (312) planes [25, 26]. As bigger CZTS nanoparticles are favourable for high efficiency; the copper poor composition is the best to achieve this goal. Also, this condition leads to formation of copper vacancies which increase the opportunity for formation of shallow acceptor levels in CZTS films.

From optical absorption using a Tauc plot the band gap energies were found to be 1.35, 1.45 and 1.50 eV for C1, C2 and C3 samples respectively, which is in a good agreement with the literature as shown in Figure 5.4 [27]. The band gap values are quite close to the optimum band gap required for a solar cell absorber layer. Moreover, this result confirms that different content of Cu leads to change of size of particles such as the ideal sample has a large grain size compared with Cu rich and Cu poor samples [10, 28].

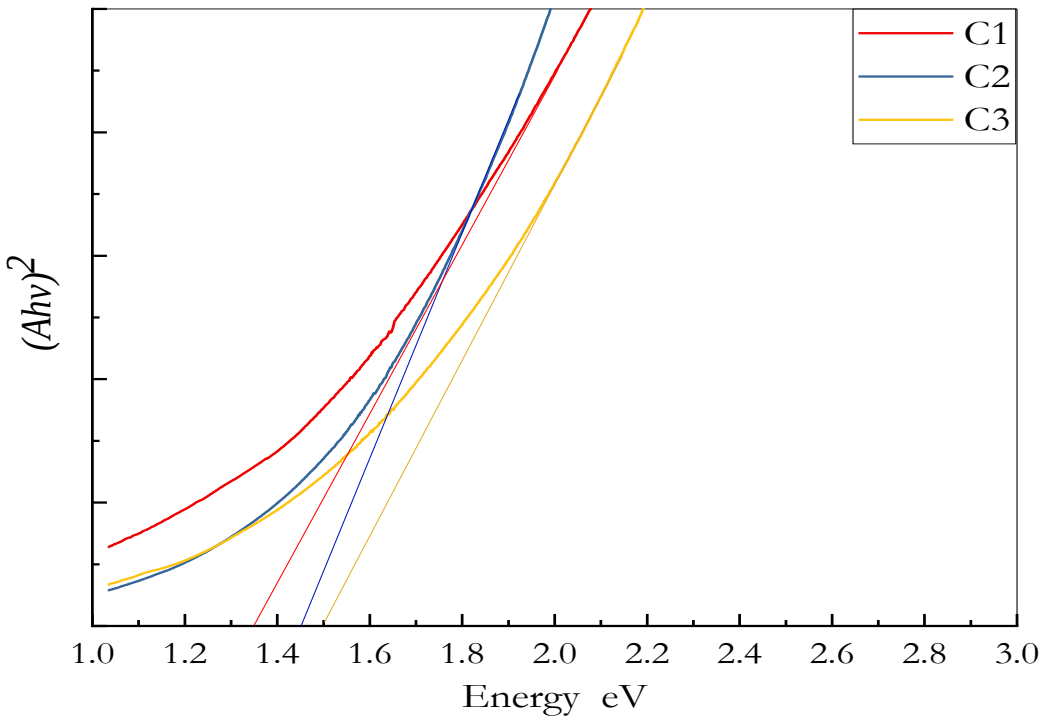

Figure 5.4 Band gap for different Cu content samples from Tauc plot.

The decrease of energy band gap with increasing Cu content is due to increasing the crystallinity, presence of narrow band gap of Cu_2SnS_3 phase or thickness of the films. Also, another reason which may influence the band gap is the disorder between Zn and Cu cation under different composition that is used. According to the above results the sample under Cu poor content has good properties to be suitable materials for CZTS absorber layer to fabricate a solar cell.

5.3.2: Investigation of the effect of Zn content

X-ray diffraction (XRD) pattern of different CZTS nanocrystal compositions are given in Figure 5.5. Characteristic peaks for nanocrystals are clearly observed in XRD patterns. The as-synthesized CZTS nanocrystals showed four intensive XRD peaks centered at 2θ = 28.7°, 33.1°, 47.5° and 56.3° corresponding planes to (112), (200), (220) and (312), respectively for all samples, which are similar to those reported for CZTS powders (JCPD 26-0575). Moreover, there are small peaks at 27.13°, 30.58° and 51.56° in sample S4 which may correspond to wurizite structure.

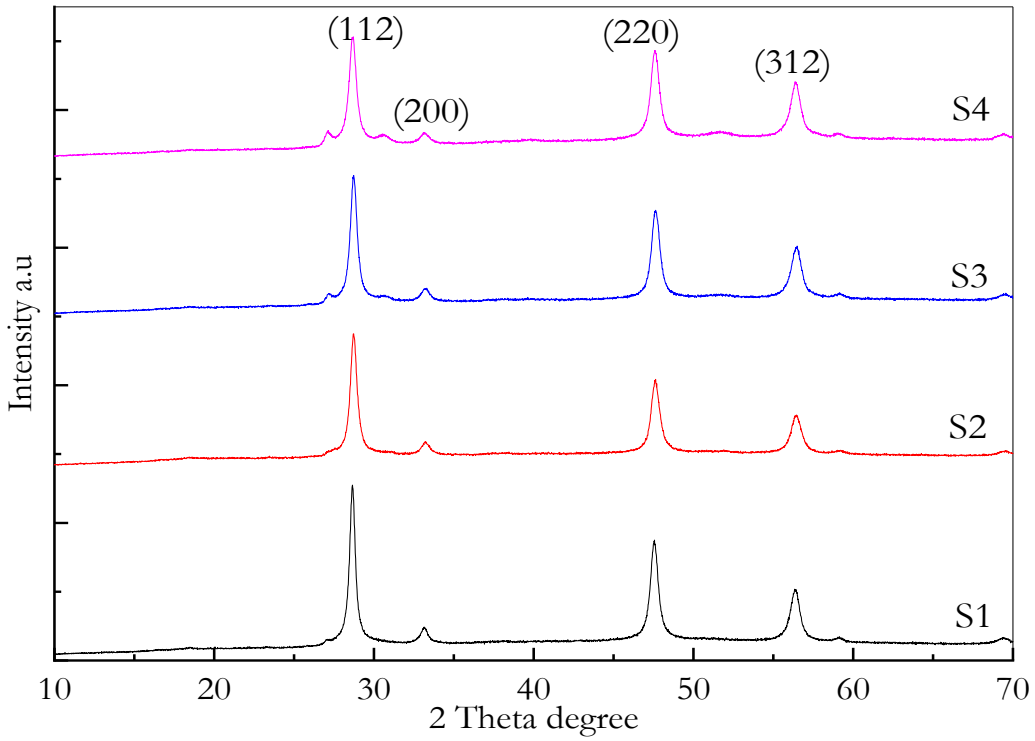

Figure 5.5 XRD patterns of CZTS nanocrystals at different Zn content.

The average particle size of the nanocrystals was calculated from the (112) diffraction peaks at 28.7° using the Debye-Sherrer equation giving values in the range 39.4, 34.1, 32.2 and 29.5 nm for S1, S2, S3 and S4 respectively. Moreover, the *d* spacing for (112) and (220) planes were calculated equal to 0.31 and 0.19 nm for all samples, which is also confirmed by TEM analysis.

The structure and phase purity of the CZTS nanocrystals were investigated by using Raman analysis. The Raman spectra of CZTS nanocrystals are presented in Figure 5.6. The characteristic peaks of CZTS are clearly observed. Raman can show the structure of CZTS, and it is found that the disordered kesterite (DKS) phase has the greatest intensity at a peak of 335 cm^{-1}. This is expected due to the nature of the composition, in which all the samples are non-stoichiometric and therefore forming a disordered phase. Normally, the kesterite structure shows A1 mode at 338 cm^{-1}.

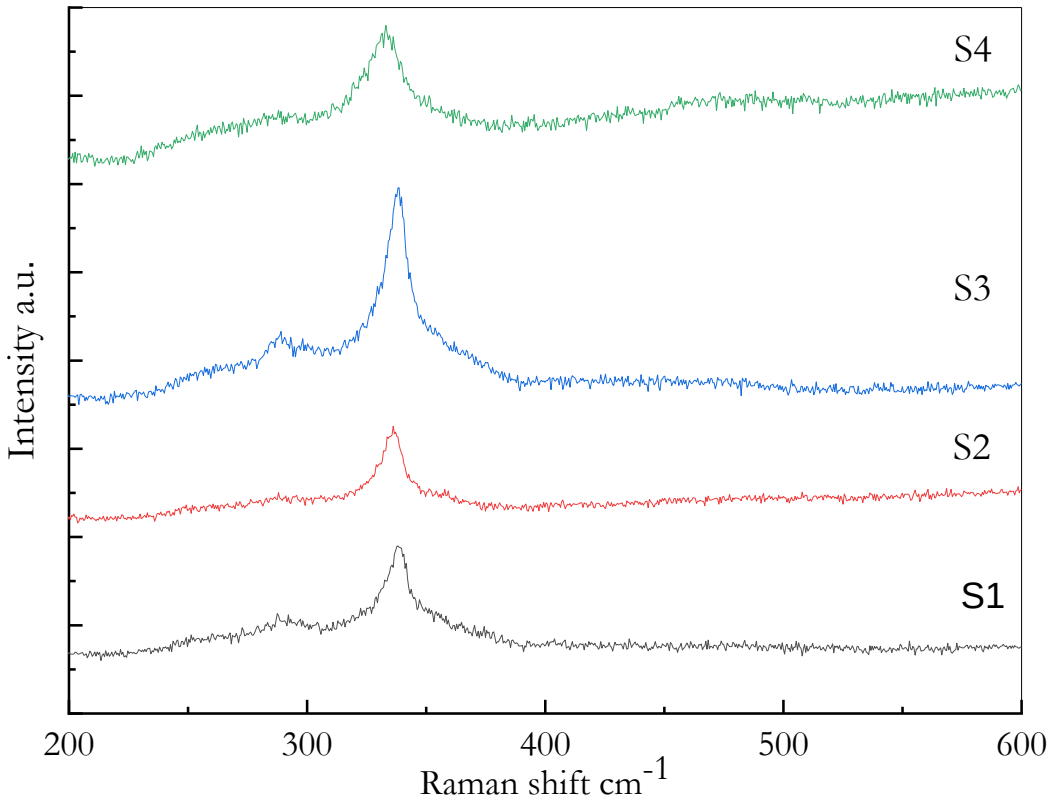

Figure 5.6 Raman spectrums of CZTS Nanocrystals at different Zn content.

However, the strong peak at 335 cm^{-1} is related to the presence of local structural inhomogeneity within the disordered cation sublattice antisites. However, the characteristic peaks of CZTS are clearly observed in the spectrum. A strong Raman peak at in the range 334-336 for all samples, and small peaks at 286-289 and 364 cm^{-1} corresponded to the A1 mode of single phase of CZTS. However, there are others small peaks at 320 cm^{-1} Cu_2SnS_3 in all samples except S3. Moreover, there is no evidence for $Cu_{2-x}S$ at 475 for all samples.

Figure 5.7 shows transmission electron microscopy (TEM) images and selected area diffraction (SAED) patterns of the as synthesized CZTS nanocrystals. As can be clearly seen from Figure 5.7, most of the nanocrystals are spherical with a range of sizes. The nanocrystals have an average size in the range of 44.93±1.35, 45.18±1.42, 52.46±1.47 and 49.05±0.91 nm for S1, S2, S3 and S4 respectively. To further study crystallinity and confirm the structure of the particles, HRTEM analysis was done and all of the *d* spacing of the synthesized CZTS nanocrystals revealed the crystalline nature. Moreover, interplaner spacing of 0.31 nm and 0.19 nm were measured and attributed to the (112) and (220) crystallographic planes. The SAED pattern of the nanocrystals, in which three main diffraction rings correspond to (112), (220) and (312) planes of CZTS nanocrystals. The diffraction rings are discontinuous and consist of sharp spots, which indicate that the nanocrystals are well crystallized. These results are consistent with the XRD data.

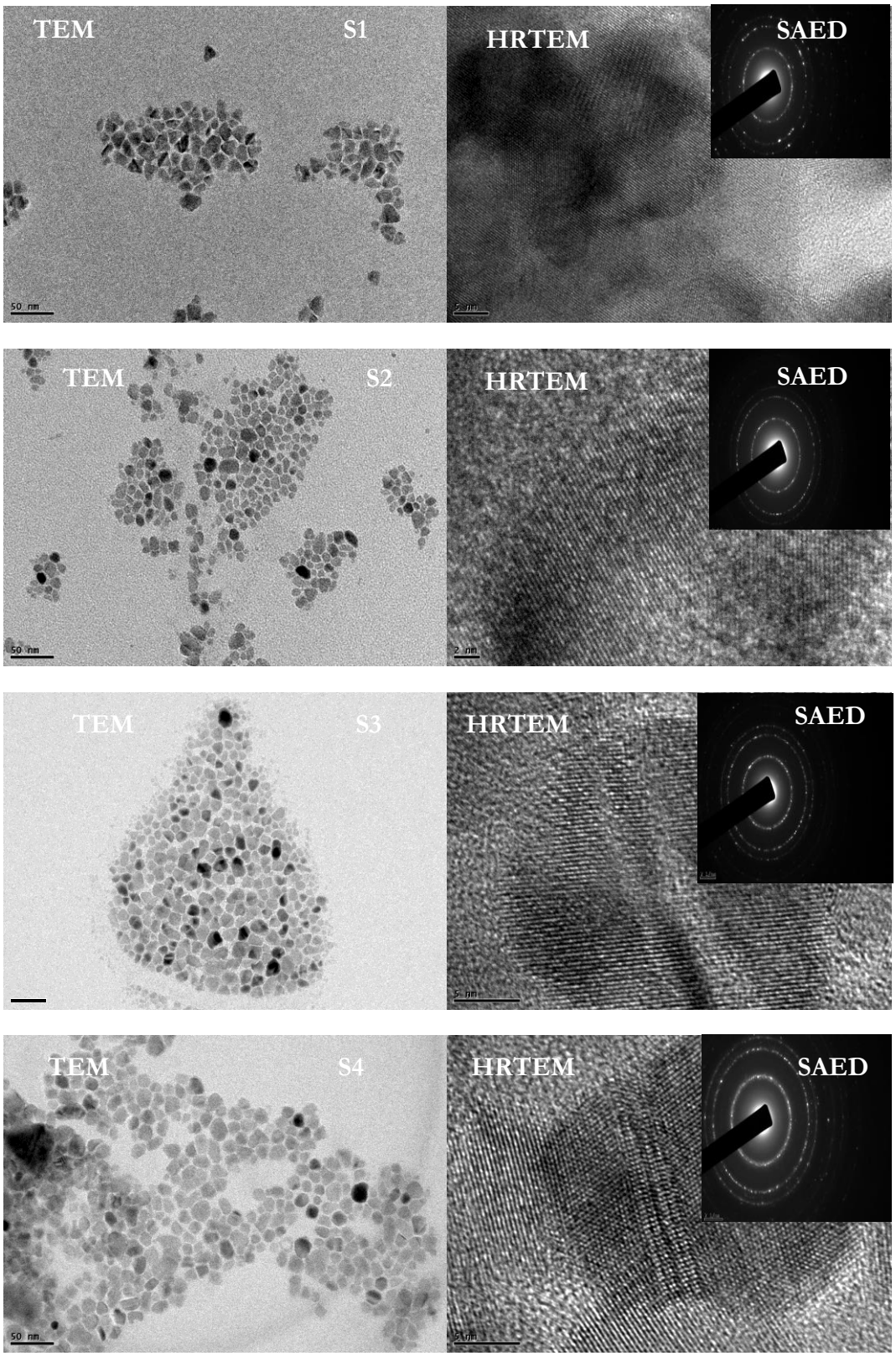

Figure 5.7 TEM, SAED and HRTEM images for CZTS nanoparticles under variable Zn content.

Energy-dispersive X-ray spectroscopy (EDX) was performed to examine the overall homogeneity and composition of CZTS of the synthesised nanocrystals. The EDX results from CZTS nanocrystals are presented in Table 5.3. It can be seen that, the values of elemental composition of the nanoparticle based CZTS thin film are Cu (25.03, 24.38, 23.31 and 23.42), Zn (12.49, 12.75, 13.86 and 14.51), Sn (11.79, 11.85, 11.35 and 11.31), and S (50.49, 51.03, 50.04 to 50.49) for S1, S2, S3 and S4 respectively. The Cu/ (Zn + Sn), Cu/Zn and S/metal ratios were calculated and estimated (1.03, 0.99, 0.92 and 0.91), (1.06, 1.08, 1.22 and 1.28) and (1.02, 1.04, 1.03 and 1.02) for S1, S2, S3 and S4 respectively. Under different Zn content, the ratio of Zn/Sn increases with increasing Zn content with a slight decrease in the Sn amount. Also, the ratio of Cu/ (Zn+Sn) decreased with increasing Zn amounts. However, all samples are still under copper poor zinc rich condition after synthesis except sample S1.

Table 5.3: Chemical composition determined from Energy-dispersive X-ray spectroscopy (EDX).

	Cu%	Zn%	Sn%	S%	Cu/(Zn+Sn)	Zn/Sn	S/(Cu+Zn+Sn)
S1	25.03	12.49	11.79	50.49	1.03	1.06	1.02
S2	24.38	12.75	11.85	51.03	0.99	1.08	1.04
S3	23.31	13.86	11.35	50.04	0.92	1.22	1.03
S4	23.42	14.51	11.31	50.49	0.91	1.28	1.02

The optical absorption spectra for all samples were recorded in the wavelength range of 400-1500 nm at room temperature and the optical band gap of CZTS nanoparticles has been calculated from the absorption spectrum using the Tauc relation $(Ahv) = C(hv - E_g)^n$ where C is a constant, A is absorbance, E_g is the average band gap of the material and n depends on the type of transition and equal to 1/2, for a direct band gap semiconductor as shown in the Figure 5.8.

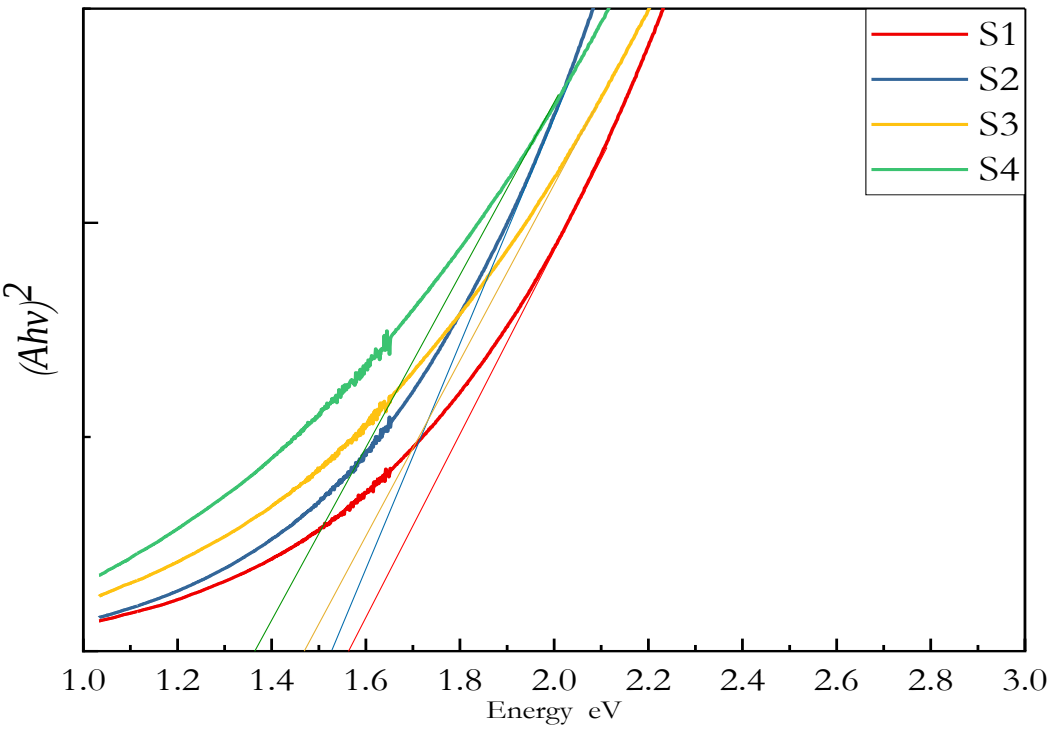

Figure 5.8 Energy band gaps of different Zn content using Tauc plot.

The average band gap was estimated from the extrapolating the linear portion of the $(Ahv)^2$ vs. hv curves. The band gap energies were found to be 1.57, 1.54, 1.48 and 1.36 eV for S1, S2, S3 and S4 respectively, which is in a good agreement with the literature [29-31]. These band gap values are quite close to the optimum band gap required for solar cell absorber layer. Table 5.4 shows the band gap of each sample. It can be seen clearly that there is a relationship between the copper-zinc ratio and the band gap.

Table 5.4: Band gaps for each sample calculated.

Sample	Cu/(Zn+Sn)	Zn/Sn	Band Gap (eV)
S1	1.03	1.06	1.57 ±0.05
S2	0.99	1.08	1.54 ±0.04
S3	0.92	1.22	1.48 ±0.05
S4	0.91	1.28	1.36 ±0.03

A decrease in copper/increase in zinc decreases the resulting band gap. The background noise between 1.38-1.55 eV is the result of a detector change within the UV-Vis spectrometer. The change in energy band gap may be due to either particles size or to be concentration of Cu / Zn content.

5.4: Conclusion

X-ray diffraction, Raman spectroscopy, TEM, EDX and UV-Vis spectroscopy have been used to describe the nature of CZTS thin films fabricated using the hot injection method with different copper-zinc ratios. Spin coating deposition methods have used to investigate how best to create a uniform film.

X-ray diffraction and Raman spectroscopy showed the majority of the CZTS may be in a kesterite and disordered kesterite or stannite phases in all ideal and Zn rich samples. XRD data also confirmed the presence of the mix kesterite and wurtzite CZTS structure in Cu rich sample. Raman results are inconclusive to determine if the CZTS has any significant kesterite or stannite structures due to broad peaks within the spectra. The strong peak at 335 cm^{-1} is related to the presence of local structural inhomogeneity within the disordered cation sublattice antisites. There is no evidence for $Cu_{2-x}S$ at 475 for all samples except Cu rich sample.

Transmission electron microscopy showed the nanoparticles made were between 44.9 nm and 52.5 nm in diameter, the maximum being S3. Ultraviolet-visible spectroscopy showed the band gap of the films varies between 1.38 eV and 1.55 eV, increasing in energy with a decreasing copper concentration. As well as increasing zinc concentrations decrease the resulting band gap and they in the range between 1.38 and 1.55 eV. The change in energy band gap is related with change of CZTS particles size as shown in XRD and TEM measurements. It will conclude that the energy band gap also depends on the Cu and Zn concentrations.

Overall, the CZTS nanoparticle ink shows promise for use as the absorber layer in PV devices due to the suitable band gap and simple deposition and nanoparticles size. However, as the PL and Raman spectroscopy data show, there are a significant amount of secondary phases present and further effort needs to be made for these to be reduced.

5.5: References

1. Kumar, M., et al., *Strategic review of secondary phases, defects and defect-complexes in kesterite CZTS-Se solar cells.* Energy & Environmental Science, 2015.

2. Just, J., et al., *Secondary phases and their influence on the composition of the kesterite phase in CZTS and CZTSe thin films.* Physical Chemistry Chemical Physics, 2016. **18**(23): p. 15988-15994.

3. Bao, W. and M. Ichimura, *Influence of Secondary Phases in Kesterite-Cu_2ZnSnS_4 Absorber Material Based on the First Principles Calculation.* International Journal of Photoenergy, 2015. **2015**: p. 6.

4. Chen, S., et al., *Classification of Lattice Defects in the Kesterite Cu_2ZnSnS_4 and Cu2ZnSnSe$_4$ Earth-Abundant Solar Cell Absorbers.* Advanced Materials, 2013. **25**(11): p. 1522-1539.

5. Tanaka, K., T. Shinji, and H. Uchiki, *Photoluminescence from Cu_2ZnSnS_4 thin films with different compositions fabricated by a sputtering-sulfurization method.* Solar Energy Materials and Solar Cells, 2014. **126**: p. 143-148.

6. Ruan, C.-H., et al., *Electrical properties of $Cu_xZn_ySnS_4$ films with different Cu/Zn ratios.* Thin Solid Films, 2014. **550**: p. 525-529.

7. Li, X.R., et al., *Investigation of Cu_2ZnSnS_4 thin films with controllable Cu composition and its influence on photovoltaic properties for solar cells.* Journal of Alloys and Compounds, 2017. **694**: p. 833-840.

8. Xie, H., et al., *Formation and impact of secondary phases in Cu-poor Zn-rich $Cu_2ZnSn(S_{1-y}Se_y)_4$ ($0 \leq y \leq 1$) based solar cells.* Solar Energy Materials and Solar Cells, 2015. **140**: p. 289-298.

9. Chen, G.L., et al., *Formation mechanism of secondary phases in Cu_2ZnSnS_4 growth under different copper content.* Materials Letters, 2017. **186**: p. 98-101.

10. Mitzi, D.B., et al., *The path towards a high-performance solution-processed kesterite solar cell.* Solar Energy Materials and Solar Cells, 2011. **95**(6): p. 1421-1436.

11. Jao, M.H., et al., *Synthesis and Characterization of Wurtzite Cu_2ZnSnS_4 Nanocrystals.* Japanese Journal of Applied Physics, 2012. **51**(10): p. 3.

12. Mirbagheri, N., et al., *Synthesis of ligand-free CZTS nanoparticles via a facile hot injection route.* Nanotechnology, 2016. **27**(18): p. 85603-85603.

13. Zhang, J., et al., *Effects of Sulfurization Temperature on Properties of CZTS Films by Vacuum Evaporation and Sulfurization Method.* International Journal of Photoenergy, 2013: p. 6.

14. Gao, Y., et al., *Understanding the growth mechanism of wurtzite Cu_2ZnSnS_4 nanocrystals and the photodegradation properties.* Materials & Design, 2017. **123**: p. 24-31.

15. Luo, Q., et al., *Controllable Synthesis of Wurtzite Cu_2ZnSnS_4 Nanocrystals by Hot-Injection Approach and Growth Mechanism Studies.* Chemistry-an Asian Journal, 2014. **9**(8): p. 2309-2316.

16. Mendez-Lopez, A., et al., *Synthesis and Characterization of Colloidal CZTS Nanocrystals by a Hot-Injection Method.* Journal of Nanomaterials, 2016.

17. Azimi, H., Y. Hou, and C.J. Brabec, *Towards low-cost, environmentally friendly printed chalcopyrite and kesterite solar cells.* Energy & Environmental Science, 2014. **7**(6): p. 1829-1849.

18. Yang, K.J., et al., *Effects of the compositional ratio distribution with sulfurization temperatures in the absorber layer on the defect and surface electrical characteristics of Cu_2ZnSnS_4 solar cells.* Progress in Photovoltaics, 2015. **23**(12): p. 1771-1784.

19. Lin, X., et al., *Structural and optical properties of Cu_2ZnSnS_4 thin film absorbers from ZnS and Cu_3SnS_4 nanoparticle precursors.* Thin Solid Films, 2013. **535**(0): p. 10-13.

20. Ennaoui, A., et al., *Cu_2ZnSnS_4 thin film solar cells from electroplated precursors: Novel low-cost perspective.* Thin Solid Films, 2009. **517**(7): p. 2511-2514.

21. Fernandes, P.A., P.M.P. Salomé, and A.F.d. Cunha, *Study of polycrystalline Cu_2ZnSnS_4 films by Raman scattering.* Journal of Alloys and Compounds, 2011. **509**(28): p. 7600-7606.

22. Fernandes, P.A., P.M.P. Salome, and A.F.d. Cunha, *Growth and Raman scattering characterization of Cu_2ZnSnS_4 thin films.* Thin Solid Films, 2009. **517**(7): p. 2519-2523.

23. Ahmad, R., et al., *Facile synthesis and post-processing of eco-friendly, highly conductive copper zinc tin sulphide nanoparticles.* Journal of Nanoparticle Research, 2013. **15**(9).

24. Leitao, J.P., et al., *Study of optical and structural properties of Cu_2ZnSnS_4 thin films.* Thin Solid Films, 2011. **519**(21): p. 7390-7393.

25. Riha, S.C., B.A. Parkinson, and A.L. Prieto, *Solution-Based Synthesis and Characterization of Cu_2ZnSnS_4 Nanocrystals.* Journal of the American Chemical Society, 2009. **131**(34): p. 12054-+.

26. Wei, M., et al., *Synthesis of spindle-like kesterite Cu_2ZnSnS_4 nanoparticles using thiorea as sulfur source.* Materials Letters, 2012. **79**(0): p. 177-179.

27. Katagiri, H., *Cu_2ZnSnS_4 thin film solar cells.* Thin Solid Films, 2005. **480**: p. 426-432.

28. Khoshmashrab, S., et al., *Effects of Cu content on the photoelectrochemistry of Cu_2ZnSnS_4 nanocrystal thin films*. Electrochimica Acta, 2015. **162**: p. 176-184.

29. Malerba, C., et al., *Stoichiometry effect on Cu_2ZnSnS_4 thin films morphological and optical properties*. Journal of Renewable and Sustainable Energy, 2014. **6**(1): p. 011404.

30. Singh, O.P., et al., *Effect of sputter deposited Zn precursor film thickness and annealing time on the properties of Cu_2ZnSnS_4 thin films deposited by sequential reactive sputtering of metal targets*. Materials Science in Semiconductor Processing, 2016. **52**: p. 38-45.

31. Boutebakh, F.Z., et al., *Zinc molarity effect on Cu_2ZnSnS_4 thin film properties prepared by spray pyrolysis*. Journal of Materials Science-Materials in Electronics, 2018. **29**(5): p. 4089-4095.

Chapter 6: The effect of annealing conditions temperature, reaction time, ramping rate and atmosphere on CZTS thin film properties

6.1: Introduction

The annealing process is important for CZTS nanocrystal thin films, to achieve high efficiency devices. However, controlling annealing parameters and their effects on CZTS device properties are still not well understood and also still a current research question. Many studies have looked at some of these parameters. For instance, Wang et al. [1] studied the effect of temperature on CZTS films fabricated by evaporation, they found that annealing under high temperature leads to the film's surface decomposition but that it also increases the grain growth. Short annealing times also enhance throughput. It is well known that good crystallinity requires higher growth temperature, however, to avoid losing Sn during the deposition, the deposition needs be carried out at low temperature and followed by an increase temperature post deposition to improve crystallinity [1, 2]. The annealing of the CZTS film at 530 °C for 10 min in sulphur vapour eliminated all the secondary phases, and diffusion of sulphur in the film during the annealing process enhanced the crystallinity of the film [3]. Fukano et al. also studied the effect of annealing process on CZTS electrical properties. The surface of CZTS thin films deposited by a sputtering technique which was followed by a sulfurisation process using a (5%) H_2S +(95%) N_2 atmosphere at 580 °C for different time lengths (10-60 min) was analysed by scanning spreading resistance microscopy (SSRM). The spreading resistance (SR) increased with increasing annealing time up until 30 min; this is probably caused by a decrease in point defects due to stabilization of the CZTS crystal grains. At 30 min, the SR of the whole CZTS absorber layer becomes as large as the SR of the CdS buffer layer whereas for long time periods close to 60 min the SR of the whole CZTS absorber layer becomes low, and the lowest SR areas are formed at the CZTS grain boundaries, this is probably caused by an increase in the carrier density induced by point defects in the CZTS crystals. The increased point defects are supposedly Cu substitutions at Zn sites (Cu_{Zn}), which are dominant acceptors in p-type CZTS crystals which means that the SR is strongly dependent on the holding time of the sulfurisation [4]. The aim of the work reported in this chapter is to study the effect of varying annealing parameters: temperature, time, ramping

rate and atmosphere on CZTS thin films synthesised by the hot injection method and deposited by a spin coating approach by investigating crystal structure and optical properties.

6.2: Experimental Details

CZTS nanoparticles were prepared by using the hot injection method which was explained in detail in chapter 3. The CZTS ink was deposited on a Mo layer on glass substrate by using the spin coating technique. The as-deposited films were annealed at different annealing temperatures, times, ramping rates and in different atmospheres. The CZTS thin film's substrates were loaded in the furnace tube manually. After that the two ends of the tube caps were connected to different valves; a vacuum pump, exhaustion line, nitrogen and H_2S supplies. For an N_2 atmosphere where different annealing temperature, time and ramping rate conditions were applied, the tube was evacuated by using a rotary vacuum pump and the furnace tube was filled with N_2 gas. For a H_2S atmosphere, after rotary vacuum pump closing a mix gas of H_2S and N_2 with a composition ratio of 20:80 was introduced and left to fill the tube and the pressure monitored until it reached the desired pressure of 0.15 atm and the gas supply was then closed. For furnace annealing treatments, various temperatures, times and ramping rates were applied. The processes commenced at 300 ^oC for with a ramping rate of 10 ^oC/ min for 1 h under N_2 atmosphere. After that the furnace was left to cool slowely overnight. These processes were repeated for different temperatures 400, 500 and 600 ^oC, and for different times 0.5, 1.5 and 2 h, and different ramping rates 5, 15 and 20 ^oC/ min. Lastly, after the annealing treatment was finished under a (20%) H_2S + (80%) N_2 atmosphere, the furnace tube was flushed several times with nitrogen gas and vented. After annealing, the films were further characterized for their structural, morphological, compositional, and optical properties.

6.3: Results and Discussion

6.3.1: Annealing effect under different temperature

The X-ray diffraction patterns of the annealed CZTS films at various annealing temperatures for 1 h under N_2 atmosphere are shown in Figure 6.1. The peaks located at 18.22, 28.51, 33.11, 47.41, 56.24 and 69.50° which correspond to the characteristic (101), (112), (200), (220), (312) and (008) kesterite structure [JCPDS card No: 26-0575]. Also, there are other peaks at 27.50° in samples at annealing temperature 300 and 400 °C. The peak at 40.61° in all samples corresponds to the Mo layer. However, in main CZTS characteristics peaks, secondary phases SnS_2 at 33.02 (JCPDS-83-1707), SnS at 45.80 (JCPDS-831758) and Cu_3SnS_4 at 37.27, 39.81, 51.80 are not observed [5, 6].

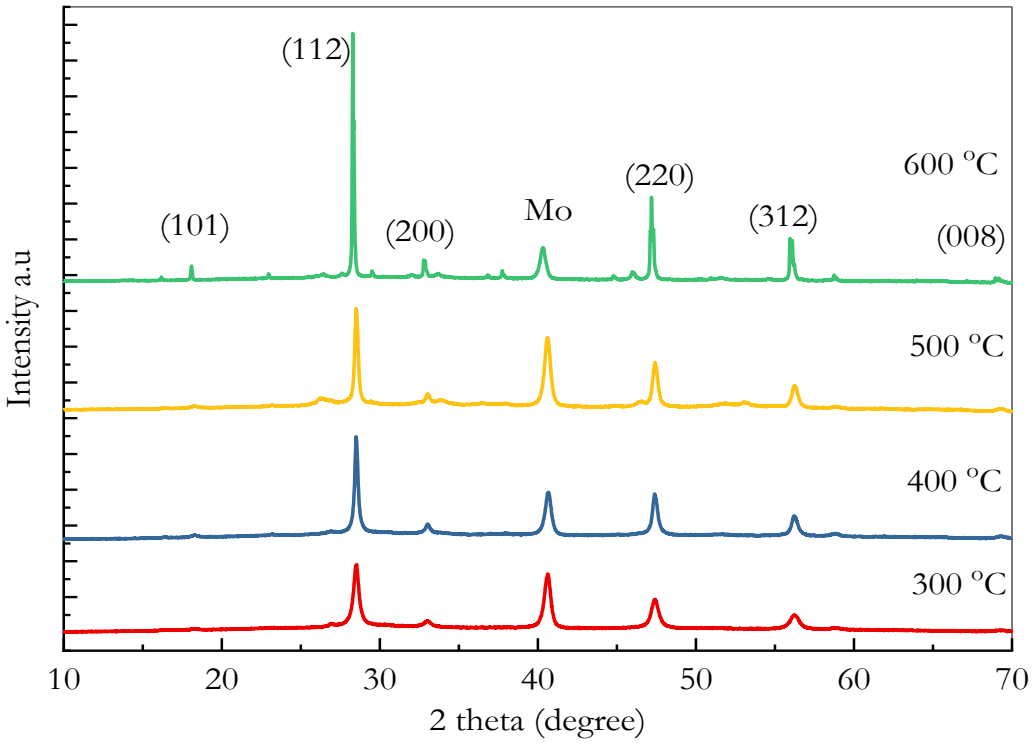

Figure 6.1 XRD of CZTS films at different annealing temperatures 300, 400, 500 and 600 °C

Due to the main peaks of CZTS were split to two peaks, the grain size of the crystallites were calculated for only the high intensity peak at 28.5 by using the Debye Sherrer equation and found to be 44.08 nm, 86.94 nm, 220.19 nm and 291.16 nm for annealing temperatures of 300, 400, 500 and 600 °C, respectively. It is clear that the size of CZTS nanoparticles

increase with increasing annealing temperatures. The d spacing was calculated for (112) and (220) planes which do not change with temperature and are found as 3.11 and 1.91 Å which agreed with many literature reports [7-9], which do not change with temperature.

Binary and ternary sulphides such as ZnS, $Cu_{2-x}S$ and Cu_2SnS_3 have similar x-ray peaks, leading to difficulties in distinguishing those phases by XRD. To investigate this further high resolution Raman spectra measurements of CZTS films at different annealing temperatures are shown in Figure 6.2. Peaks were fitted in Raman spectroscopy data and the intense peaks were around 338 cm^{-1} for all samples.

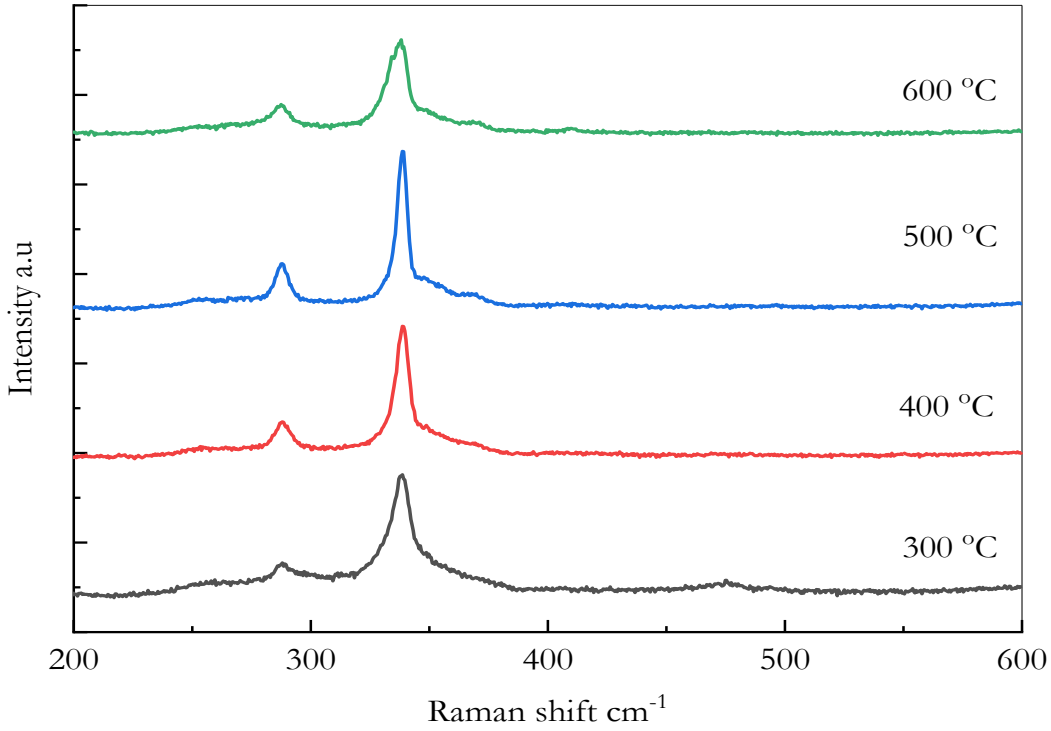

Figure 6.2 Raman measurements of CZTS films at different annealing temperatures 300, 400, 500 and 600 °C

However, the intense Raman peaks have a slight shift to lower wavenumber at 334 cm^{-1} for all samples except the sample which was annealed at 400 °C at 337 cm^{-1} [10]. For each sample, small peaks are formed in the shoulder were located at different wavenumbers. For instance, the sample annealed at 300 °C, the peaks located at 257, 289, 356 and 360 cm^{-1}, the sample annealed at 400 °C had peaks at 259, 288, 354 and 367 cm^{-1}, the sample annealed at 500 °C had peaks at 253, 280, 287, 351 and 367 cm^{-1} and the sample annealed at 600 °C, the peaks located at 266, 287, 351 and 368 cm^{-1} which is associated with single

CZTS phase. However, there is no evidence for secondary phases such as ZnS at 350 cm^{-1}, $CuSnS_3$ at 320 cm^{-1} and $Sn_{2-x}S$ at 475 cm^{-1} except for the sample annealed at 300 °C [11]. There are additional peaks at 313 cm^{-1} for the sample annealed at 600 °C and at 328 cm^{-1} for the sample annealed at 400 °C which corresponds to CZTS phase [12-14]. Therefore, all peaks contributed to different Raman modes, in the kesterite structure. The peak centred at 338 cm^{-1} is attributed to the main A mode; a slightly red-shifted peak at 334 cm^{-1} that causes broadening of the main peak represents most likely the partially disordered kesterite phase (DKS) or ST phase; and the peak centre at 287 cm^{-1} corresponds to the second A mode of kesterite and the peaks at 368 cm^{-1} can be attributed to E modes [15, 16].

Figure 6.3 shows the SEM images of the formation of CZTS microparticles where the nanoparticles demonstrating agglomeration with a non-uniform surface with non-homogeneous size distribution cracks. Also, samples annealed at 400 and 600 °C showed some bright and large particles which could be associated with secondary phases or incorporated elements during the reaction process.

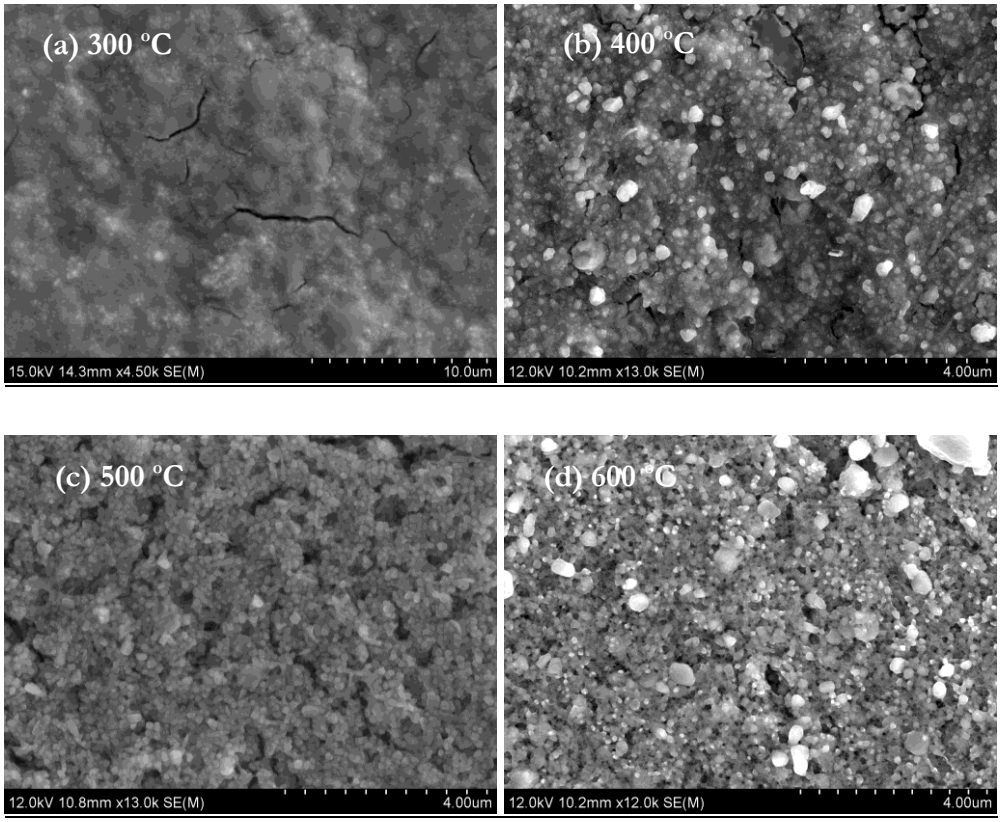

Figure 6.3 SEM images of CZTS thin films annealed at different temperatures (a) 300 °C, (b) 400 °C, (c) 500 °C and (d) 600 °C.

However, the image of the sample annealed at 500 °C for 1 h appears uniform and homogeneous with small voids and cracks. Also, the grain size of particles seem uniform and of nanoparticles scale, whereas others samples were largely aggregated. These particles are composed of primary crystallites with sizes larger than 1 μm. The conversion efficiency of solar cells is known to increase with an increase in the grain size of the absorber layer material. Therefore, larger grains are required for the fabrication of highly efficient solar cells. Voids and cracks on the absorber layer in thin film solar cells lead to low conversion efficiency because the generated carriers recombine. The large grain size in the absorber layer is important to both the minority carrier diffusion length and the recombination potential in polycrystalline thin film solar cells.

The effect of annealing temperature on CZTS compositions were studied by using EDX techniques as shown in Table 6.1. However, the composition of Cu/Zn+Sn, Zn/Sn and Cu/Sn show only little changes with increasing annealing temperatures except samples annealed at 600 °C which has a big change in its composition becoming close to a stoichiometric composition.

Table 6.1 Chemical compositions and elemental ratio of CZTS thin films prepared with different annealing temperatures measured by EDX .

	Chemical Composition %				**Element Ratio**			
Annealing temperature (°C)	S	Cu	Zn	Sn	Cu/(Zn+Sn)	Zn/Sn	Cu/Sn	S/Metal
300	44.9	25.98	19.11	13.33	0.80	1.43	1.95	0.76
400	43.71	26.65	18.82	12.52	0.85	1.50	2.13	0.75
500	49.03	23.96	15.39	12.18	0.87	1.26	1.97	0.97
600	48.77	24.89	11.63	11.4	1.04	1.02	2.01	1.02

It can be seen in Table 6.1 that the composition of Zn and Sn decreased with increasing annealing temperatures, leading to a decreasing Zn/Sn ratio except for the sample annealed at 400 °C. Moreover, samples annealed at 300 and 400 °C have insufficient sulphur content, whereas samples annealed at 500 and 600 °C nearly have sufficient sulphur content. As results have shown, controlling the element ratio in CZTS plays an important role on

CZTS structures and therefore on high efficiency solar cells devices. It is known that the CZTS solar cell with high efficiency was produced under Cu poor and Zn rich compositions.

6.3.2: Annealing effect over different time period

XRD and Raman measurements confirm that all samples which annealed over different time periods at 500 °C and ramping rate 10 °C/min are highly crystalline as shown in Figure 6.3. In XRD, all high intensity peaks at 18.6, 28.6, 33.3, 47.5, 56.7 and 69.8°match well with CZTS pattern reference (JCPDS 26-0575) corresponding to a kesterite structure. Also, the peak intensity of films increases with increasing annealing time which is due to the improvement of the crystallinity of CZTS thin films as shown in Figure 6.4. Moreover, the average particles sizes were calculated to be 200.57, 220.16, 229.61 and 236.58 nm for annealing times 30, 60, 90 and 120 minutes respectively.

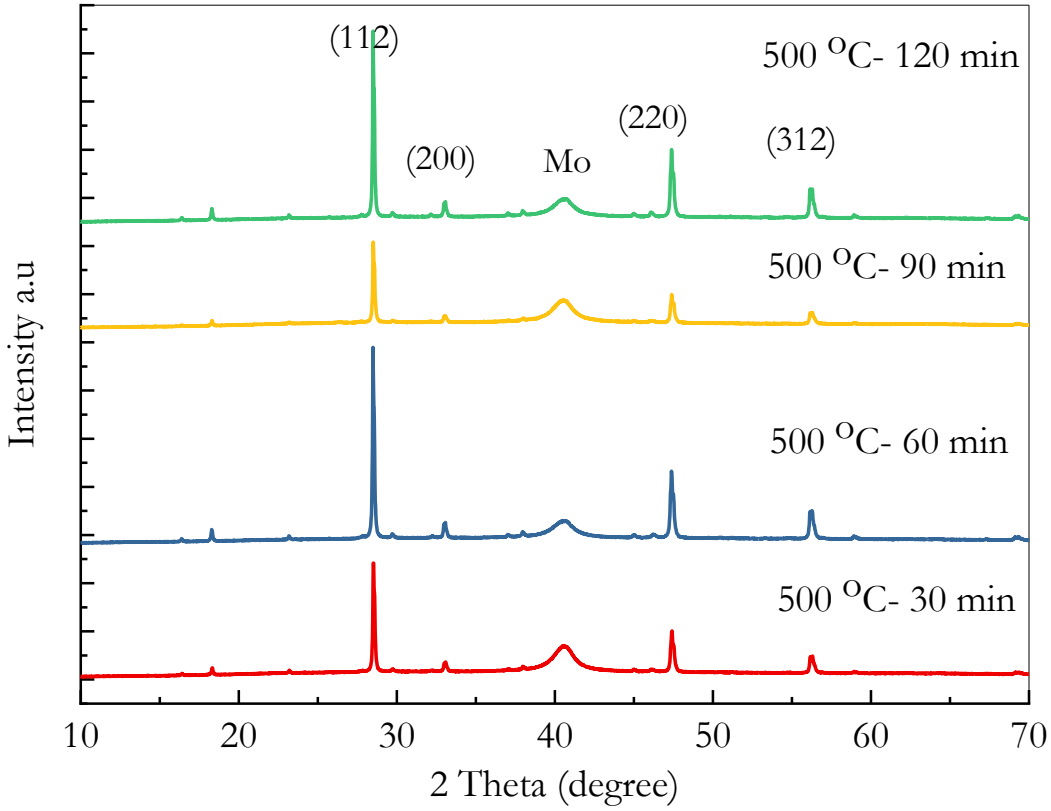

Figure 6.4 XRD of CZTS films at different annealing times 30, 60, 90 and 120 min at 500 °C.

The Raman measurements were done using a wavelength of 532 nm. The high resolution Raman spectra of the CZTS samples under different annealing times show the strong peak at 338 cm^{-1} which is associated with vibrations of sulphur atoms and three weak peaks at 287, 352 and 370 cm^{-1} as shown in Figure 6.5.

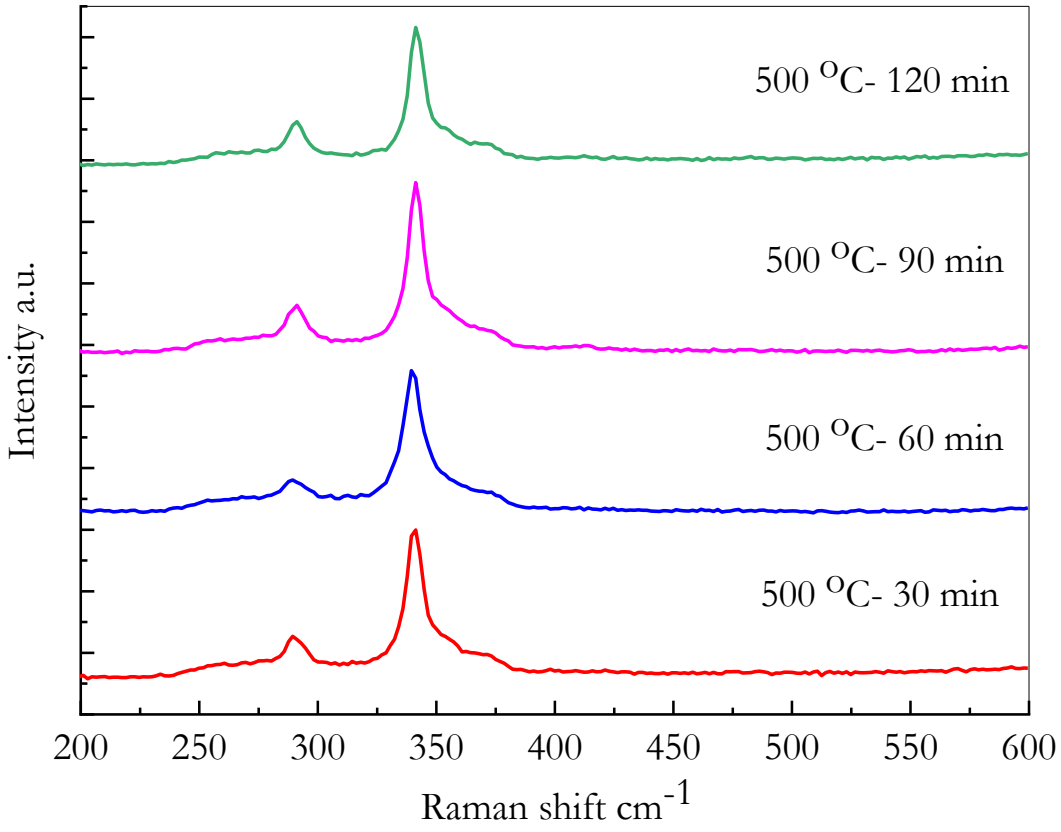

Figure 6.5 Raman measurements of CZTS films at different annealing times 30, 60, 90 and 120 min at 500 °C

Raman modes of CZTS have been reported with high intensity peaks in the range 333-339 cm^{-1} and low intensity peaks at 145, 165, 250-255, 286-289, 350-357, 360-365 and 370-375 cm^{-1}[17-19]. These shifts in frequency are due to disorder in the Cu and Zn cationic sites in the kesterite structure of CZTS thin films [20]. Also, the shape and position of intense peaks may be affected by defects in the material [21, 22]. However, the high intensity peaks in the range 335−337 cm^{-1} may also be assigned to a tetragonal CTS phase [15, 19], but the absence of its other two low shoulder peaks expected at 297 and 351 cm^{-1} [21, 23] rule out this phase being assigned. The weak peak at 304 cm^{-1} may be assigned to cubic-CTS or Sn_2S_3 phase in accordance with the reported data [15, 17, 24, 25].

SEM images in Figure 6.6 show the CZTS surface annealing under different times (30, 60, 90 and 120 min) under N_2 atmosphere at 500 °C.

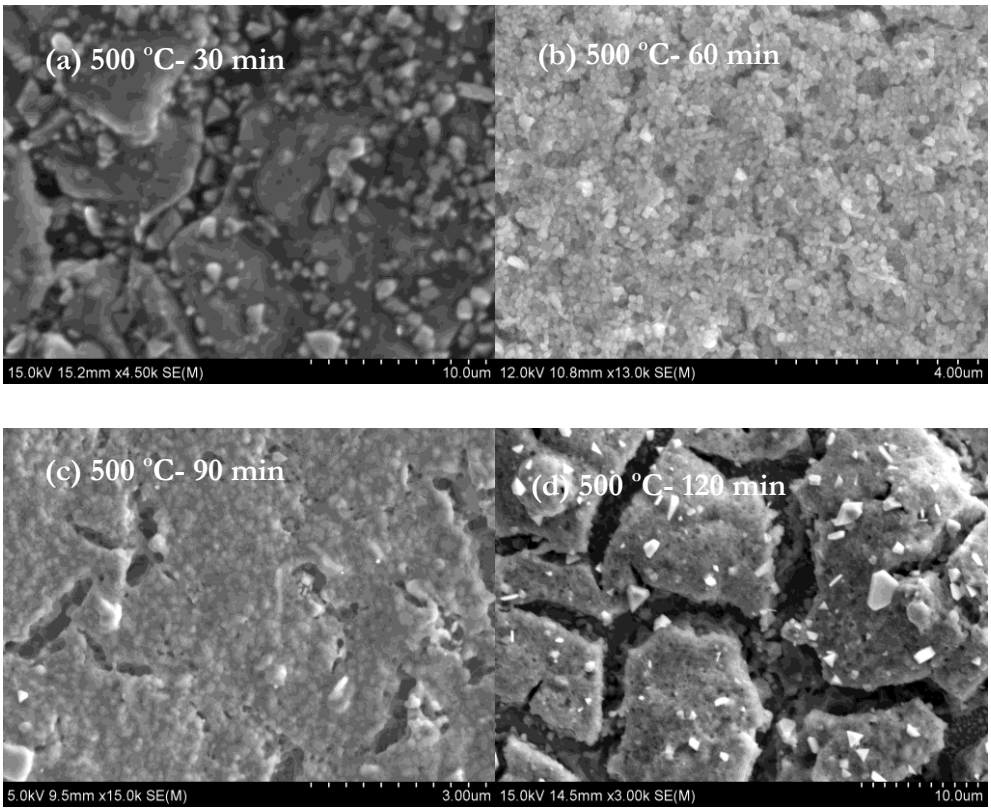

Figure 6.6 SEM images of CZTS thin films annealed at different times, (a) 30 min. (b) 60 min,(c) 90 min and (d) 120 min at 500 °C.

It can be seen that the annealing for long time (120 min) leads to lots of cracks in the surface and the CZTS sizes form large particles in the range of micrometres. Also, annealing at 2 h showed a small bright particle which may correspond to secondary phases also with different shapes, whereas annealing for 30 min showed some cracks in the surface with various shapes and sizes of particles. However, annealing at 90 min also showed some cracks with holes in the surface and merger of particles to form micron sized regions in some area of the film's surface. However, the sample annealed for 60 min showed the most uniform particles with regular shapes and sizes, but with some pinholes in the surface and CZTS particles still of the nanometre scale, concluding that the crystallinity improved, leading to form a dense morphological structure. Table 6.2 shows the atomic per cent

composition and ratios of Cu/(Zn + Sn), Cu/Zn, Zn/Sn, and S/(Cu + Zn + Sn) for CZTS thin films as functions of the annealing times for 30, 60, 90 and 120 min at temperature of 500 °C using EDX measurements. Annealing at different times shows no big changes in the S and Cu during the annealing process. Moreover, the Zn and Sn elements composition decreases with increasing annealing times.

Table 6.2 Chemical compositions and ratio of CZTS thin films prepared with different annealing times at temperature of 500 °C.

	Chemical Composition %				**Element Ratio**			
Annealing time min	S	Cu	Zn	Sn	Cu/(Zn+Sn)	Zn/Sn	Cu/Sn	S/Metal
30	48.08	24.31	15.59	13.06	0.85	1.19	1.86	0.91
60	49.03	23.96	15.39	12.18	0.87	1.26	1.97	0.95
90	49.51	24.54	12.39	11.41	1.03	1.09	2.15	1.02
120	49.55	24.35	11.17	10.71	1.11	1.04	2.27	1.07

It can be noticed that during the longer annealing times, the ratios of Cu/Zn+Sn, Cu/Sn and S/Metal increased with increasing annealing time and the films become stoichiometric at 90 min and Cu rich at 120 min, whereas the Zn/Sn decreased with increasing annealing times which leads to change the film composition from Cu poor Zn rich to nearly stoichiometric and Cu rich compositions. However, this change in the elemental compositions may affect the CZTS solar optical and electrical properties. For instance, Cu-rich CZTS thin films can assist the formation of passivated defect clusters such as [Cu_{Zn} + Sn_{Zn}] and [$2Cu_{Zn}$ + Sn_{Zn}] which produce a deep donor level in the band gap and hence reduce the band gap of CZTS. However, Zn rich films are necessary to form Zn_{Sn} acceptors and reduce the presence of Sn_{Zn} donors which lead to an increase in the conductivity of the CZTS thin film [26-28].

6.3.3: Annealing effect under different ramping rate

XRD and Raman measurements were performed to study the effects of different annealing ramping rates (5, 10, 15, 20 °C/min) at 500 °C for 1 h on structure as shown in Figure 6.7. Sharp peaks were located at 28.3, 33.2, 47.5 and 56.2° which can be attributed to the diffraction pattern of (112), (200), (220) and (312) planes of CZTS kesterite structure (JCPDS 26-0575). There is no additional peak which can be attributed to secondary phases in any samples except the sample annealed at 15 °C/min. In samples annealed at 15 °C/min, there are other peaks located at 46.4° which correspond to secondary phases Cu_2S [29]. Moreover, the average particle sizes calculated by Scherrer's equation were found to be 221.8, 220.2, 234.6 and 250.4 nm for different annealing ramping rate conditions.

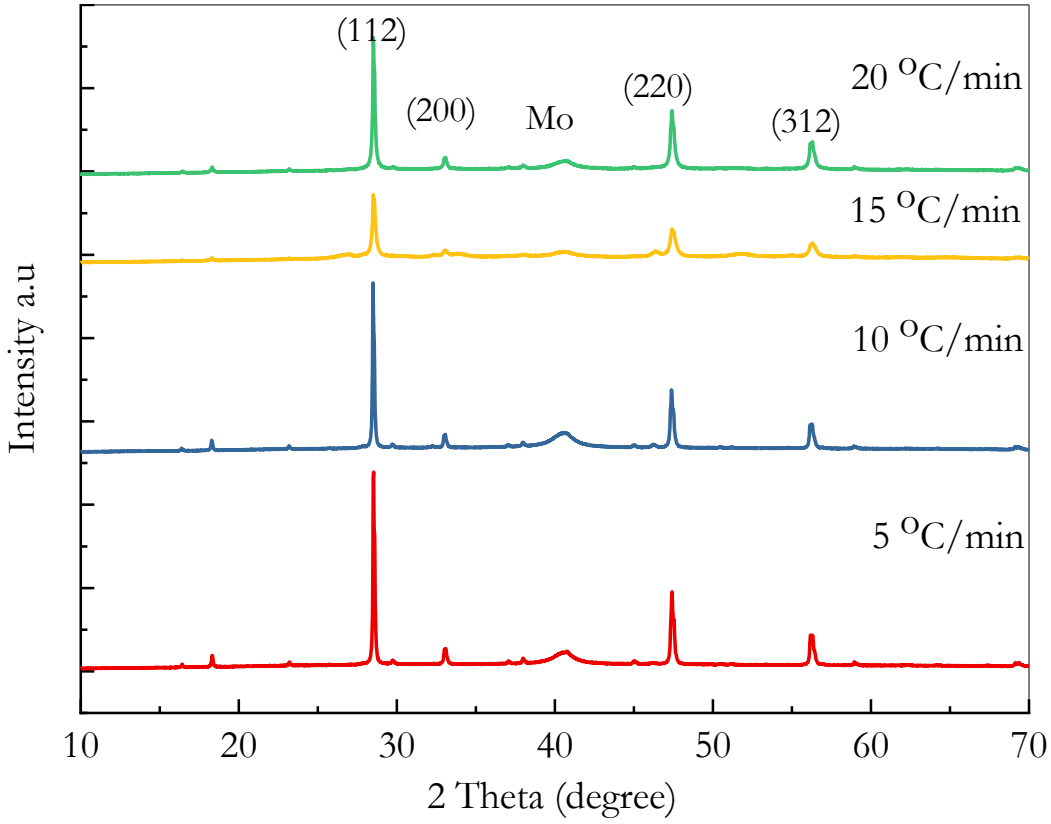

Figure 6.7 XRD of CZTS films at different annealing ramping rate 5, 10, 15 and 20 °C/min at 500 °C.

However, the main peaks for film annealed at 15 and 20 °C/min ramping rates were broader and less intensities compared with low ramping rates.

Raman spectroscopy was used in order to identify secondary phases. Figure 6.8 shows the sharp Raman peak at 338 cm^{-1} for all samples. Also, other small peaks at 255, 289, 360 and 370 cm^{-1} are identified as the main vibrational A1 mode for single phase CZTS. Also, there is a small peak at 310 cm^{-1} which can be attributed to Cu_2SnS_3, secondary phases. However, the presences of these five peaks in the Raman spectra confirm the formation of the CZTS phase. In addition, the sharp and strong major peak indicates the good crystalline quality of CZTS thin films.

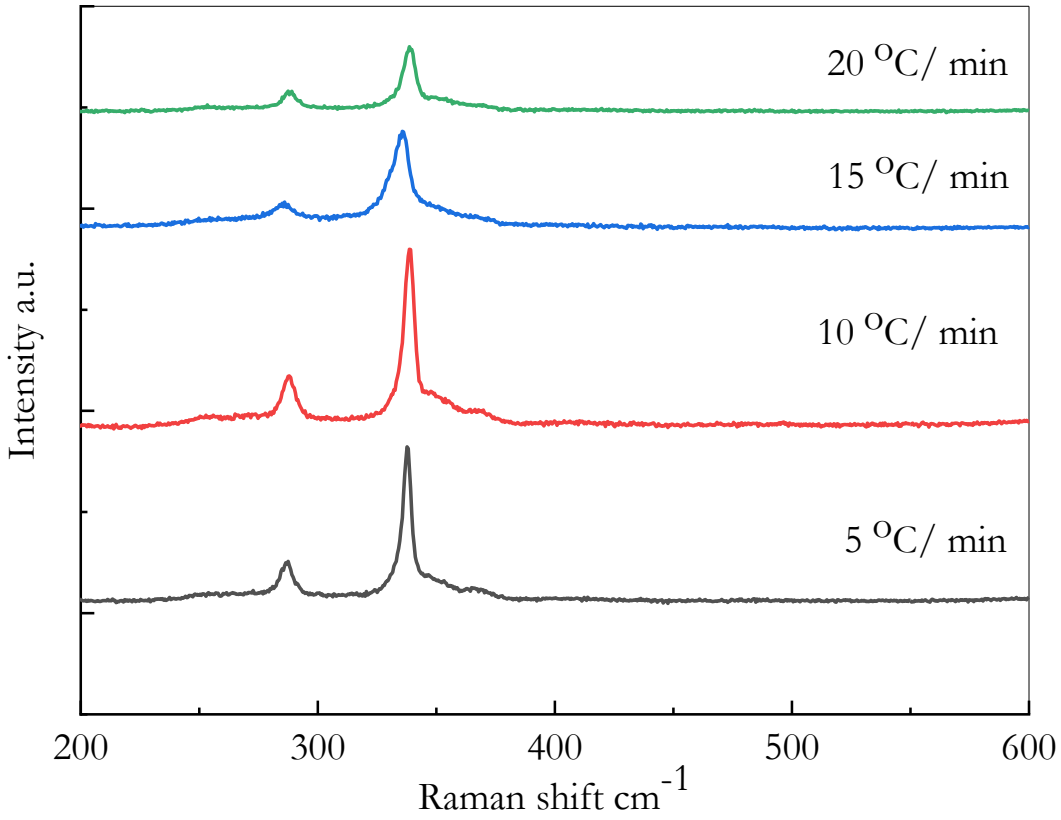

Figure 6.8 Raman measurements of CZTS films at different annealing ramping rate 5, 10, 15 and 20 °C/min at 500 °C.

The ZnS phase peaks located at 271 cm^{-1} and 352 cm^{-1} were not observed which indicates that the films form a single phase of CZTS. Also, there is no evidence for $Cu_{2-X}S$ secondary phases at 475 cm^{-1} [16, 23, 30-32].

The SEM images for samples annealed under different ramping rates show that the sample annealing under ramping rate at 15 and 20 °C/min have a small number of big particles

but at 5 °C/min have smaller particles. Also, the sample annealing at 10 °C/min has uniform particles of both shape and size as shown in Figure 6.9. The diameter of big particles of CZTS are up to 2 μm observed in the 15 °C/min sample. Also, the size of small nanometer particles have no big change with different ramping rates. However, a quick ramping rate up to 15 °C/min produces more cracks and holes on the surface of CZTS film.

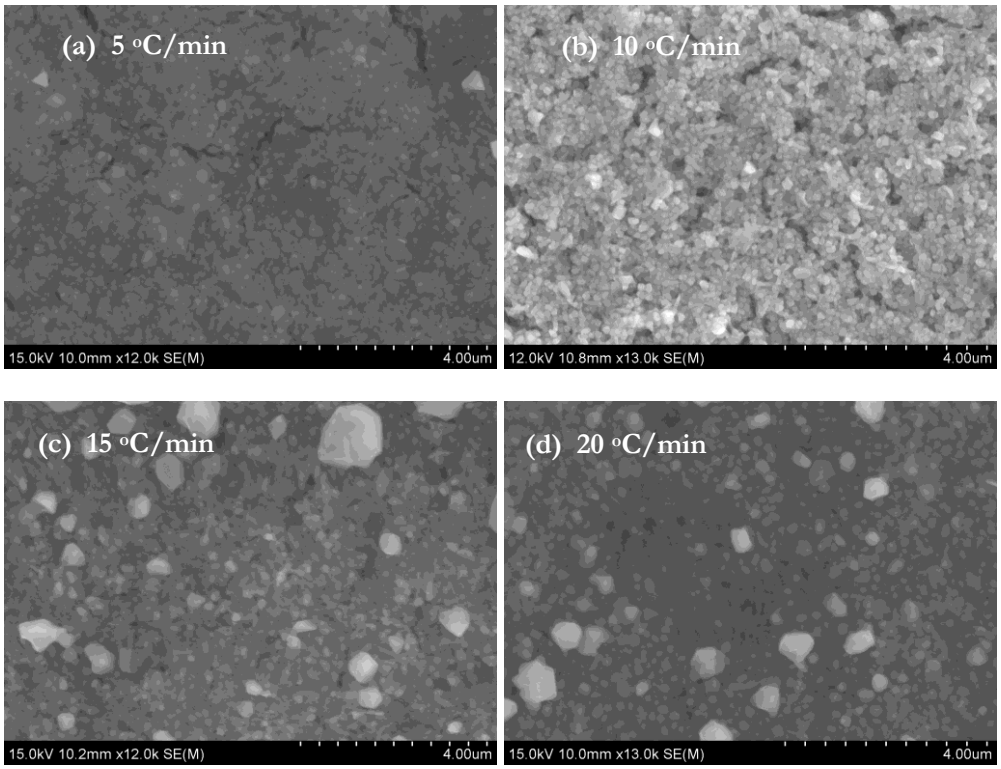

Figure 6.9 SEM images of CZTS thin films annealed at different ramping rates, (a) 5 °C/min, (b) 10 °C/min, (c) 15 °C/min and (d) 20 °C/min

In detail, annealing at low ramping rates at 5 °C/min showed some large particles with different sizes as in Figure 6.9 (a). Also, annealing at high ramping rate at 15 and 20 °C/min showed nonuniform distribution size and shape of CZTS particles as in Figures 6.9 (c) and (d). However, the uniform film produced from annealing at 10 °C/min improved the crystallinity compared with other ramping rate process as in Figure 6.9 (b). The ratio of CZTS elements in Cu/(Zn + Sn) were 0.91 for ramping rates at 5 and 15 °C/min , 0.93 for ramping rate at 20 °C/min and 0.87 for 10 °C/min ramping rate as shown in Table 6.3. The ratio of Zn/Sn was found to be 1.68, 1.26, 1.48 and 1.13 for 5, 10, 15 and 20 °C/min,

respectively. This is confirming that all samples are Cu-poor and Zn-rich compositions. Cu-poor condition leads to the formation of Cu vacancies, which generate shallow acceptors in CZTS, whereas a Zn-rich condition suppresses the Cu substitution at Zn sites, which increases deep acceptors. Studies indicate that Cu-poor and Zn-rich CZTS films have higher p-type conductivity and result in high efficiency solar cells [26, 33, 34].

Table 6.3 Chemical compositions and ratio of CZTS thin films prepared with different annealing ramping rates.

	Composition %				Ratio			
Annealing rate °C/min	S	Cu	Zn	Sn	Cu/(Zn+Sn)	Zn/Sn	Cu/Sn	S/Metal
5	47.32	25.68	17.62	10.47	0.91	1.68	2.45	0.88
10	49.03	23.96	15.39	12.18	0.87	1.26	1.97	0.95
15	47.33	24.96	16.41	11.07	0.91	1.48	2.25	0.90
20	48.52	24.37	13.85	12.27	0.93	1.13	1.99	0.96

6.3.4: Annealing effect under different atmosphere

In order to study the effect of annealing atmosphere (N_2 atmosphere and H_2S+N_2 atmosphere) on CZTS film properties, XRD, Raman spectroscopy, SEM and EDX measurements were carried out. In XRD measurements for annealing of samples in different atmospheres at 500 °C for 1 h and ramping rate at 10 min/°C, it can be seen that the main 6 peaks in shown Figure 6.10 are at 18.2°, 28.5°, 33.0°, 47.4°, 56.3° and 59.1° corresponding to planes (110), (112), (200), (220), (312) and (008) which match with kesterite structure of CZTS, according to JCPDS 26-0575. There were no notable peaks related to secondary phases such as binary or ternary sulphides such as ZnS, $Cu_{2-x}S$, and Cu_2SnS_3 from XRD, but they have similar diffraction patterns with CZTS owing to their similar zinc blend-type structures [34].

The particle size of CZTS nanoparticles is significantly altered by annealing atmosphere conditions under H_2S+N_2 atmosphere where the size of particles is close to 60 nm calculated from Debye Sherrer equation.

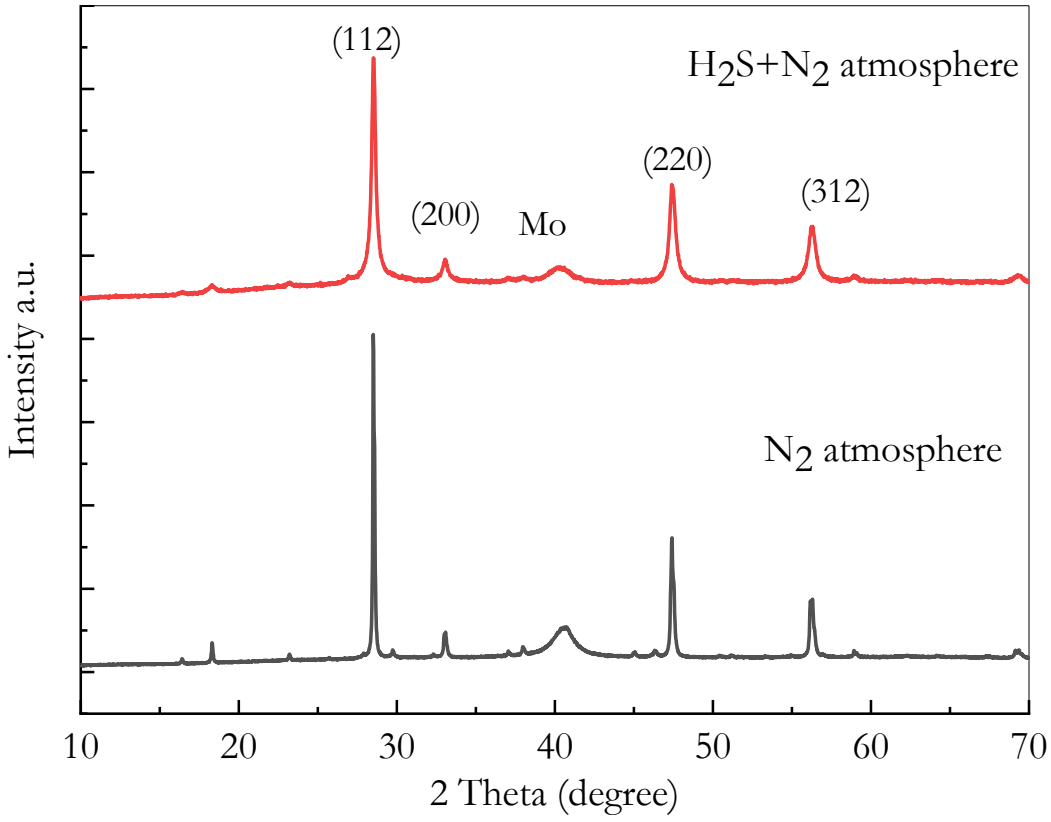

Figure 6.10 XRD of CZTS films at different annealing atmosphere H_2S+N_2 and N_2.

The Raman measurements in Figure 6.11 showed that the main peak of different CZTS samples under different annealing atmospheres was located at 338 cm^{-1}. Also, other small peaks were at 287, 335, 352 and 366 cm^{-1}, were seen in all samples, corresponding to a single CZTS phase. The spectra show that there are no additional peaks corresponding to secondary phases as discussed earlier.

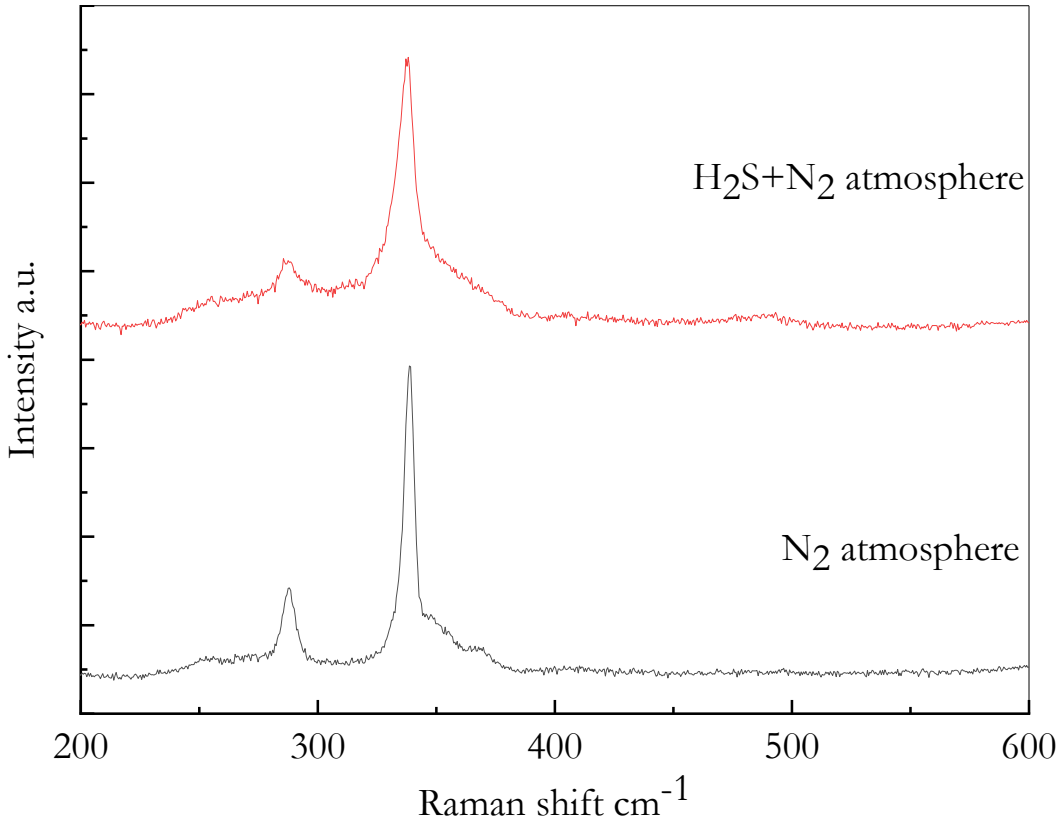

Figure 6.11 Raman measurements of CZTS films at different annealing atmosphere H_2S+N_2 and N_2.

The surface morphology of the films was observed by SEM, Figure 6.12 shows the CZTS film's images of samples annealed under different atmospheres. The film annealed at 500 °C for 1 h with 10 °C/min under N_2 atmosphere shows a polycrystalline film with some region of particles of dispersed grains with different size distribution. Also, the surface shows some cracks and holes. A similar trend is observed in the samples annealed under H_2S+N_2 atmosphere; here the size distribution is uniform with holes in some areas of the film surface as well as it has a more dense morphology.

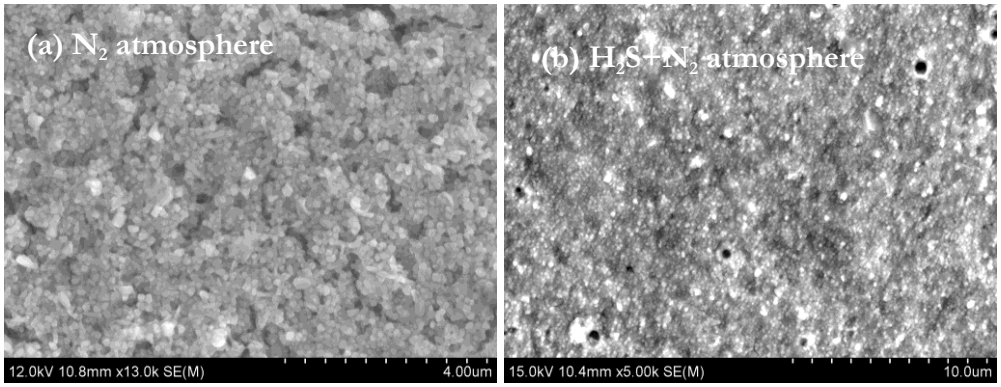

Figure 6.12 SEM images of CZTS thin films annealed at different atmospheres (a) N_2 atmosphere and (b) H_2S+N_2 atmosphere.

EDX studies in Table 6.4 showed the content of Cu, Zn and Sn decreased and S content increases when annealed under a H_2S+N_2 atmosphere, leading to a ratio of S/metal of above 1 which is providing a good indication that the sulfurization process is completed. Also, all films under different annealing atmospheres are still under Cu poor and Zn rich conditions which are favourable in high efficiency solar cells.

Table 6.4 Chemical compositions and ratio of CZTS thin films prepared with different annealing atmospheres.

	Composition %				**Ratio**			
Annealing atmosphere	S	Cu	Zn	Sn	Cu/Zn+Sn	Zn/Sn	Cu/Sn	S/Metal
N_2	49.03	23.96	15.39	12.18	0.87	1.26	1.97	0.95
H_2S+N_2	51.22	21.95	13.88	10.92	0.89	1.27	2.01	1.09

6.4: Conclusion

The CZTS nanoparticles were fabricated successfully by using the hot injection method and films were deposited by using spin coating techniques. The aims of this study were to investigate the influence of the annealing parameters such as temperature, length of time, ramping rate and atmosphere on CZTS thin films structure and optical properties. A range of techniques was used to analyse the prepared films. The XRD in all samples show the main peaks are close to 28.5, 33.2, 47.5 and 56.4^o which corresponds to kesterite, stannite or disordered kesterite structures. It is difficult to distinguish between all these structures

because the deviation between them is small. However, the Raman measurements confirm the single phase of CZTS thin film with a peak at 338 cm^{-1} and other small peak at 335 cm^{-1} in some annealing conditions. There was also evidence of some secondary phases. The intensity of peaks of XRD and Raman increased and become sharper with increasing the annealing conditions (temperatures, times and ramping rates) which indicates improvement in the crystallinity. However, these results suggest that the structure of these films may mix between kesterite and stannite structures which these results need to more structure investigations by using EBSD techniques. SEM was used to study the surface of CZTS films and show uniformly distributed films. EDX study indicated the chemical composition ratio of Cu/Zn+Sn, Zn/Sn, Cu/Sn and S/Metal affected by the annealing parameters and all ratios were greater than the initial compositions due to Zn and Sn losses partially during the preparation and annealing process. The crystallinity, structure and chemical composition of CZTS thin film increased and improved under H_2S+N_2 atmosphere. Based on this evidence it is concluded that annealing at 500 ^oC for 1 h with 10 ^oC/min under H_2S+N_2 atmosphere is a suitable condition for CZTS thin film formation for use in solar cell devices.

6.5: References

1. Wang, K., et al., *Thermally evaporated Cu_2ZnSnS_4 solar cells.* Applied Physics Letters, 2010. **97**(14): p. 3.

2. Shin, B., et al., *Thin film solar cell with 8.4% power conversion efficiency using an earth-abundant Cu_2ZnSnS_4 absorber.* Progress in Photovoltaics, 2013. **21**(1): p. 72-76.

3. Khalkar, A., et al., *Effect of Growth Parameters and Annealing Atmosphere on the Properties of Cu_2ZnSnS_4 Thin Films Deposited by Cosputtering.* International Journal of Photoenergy, 2013.

4. Fukano, T., S. Tajima, and T. Ito, . Applied Physics Express, 2013. **6**(6): p. 3.

5. Raiguru, J., et al., *Impact of Annealing Temperature on the Phase of CZTS with the Variation in Surface Morphological Changes and Extraction of Optical Bandgap*, in *National Conference on Processing and Characterization of Materials*. 2017, Iop Publishing Ltd: Bristol.

6. Bahramzadeh, S., H. Abdizadeh, and M.R. Golobostanfard, *Controlling the morphology and properties of solvothermal synthesized Cu_2ZnSnS_4 nanoparticles by solvent type.* Journal of Alloys and Compounds, 2015. **642**: p. 124-130.

7. Zhou, B., D. Xia, and Y. Wang, *Phase-selective synthesis and formation mechanism of CZTS nanocrystals.* RSC Advances, 2015. **5**(86): p. 70117-70126.

8. Ahmad, R., et al., *A comprehensive study on the mechanism behind formation and depletion of Cu_2ZnSnS_4 (CZTS) phases.* CrystEngComm, 2015. **17**(36): p. 6972-6984.

9. Chernomordik, B.D., et al., *Rapid facile synthesis of Cu_2ZnSnS_4 nanocrystals.* Journal of Materials Chemistry A, 2014. **2**(27): p. 10389-10395.

10. Khare, A., et al., *Calculation of the lattice dynamics and Raman spectra of copper zinc tin chalcogenides and comparison to experiments.* Journal of Applied Physics, 2012. **111**(8): p. 9.

11. Kumar, M., et al., *Strategic review of secondary phases, defects and defect-complexes in kesterite CZTS-Se solar cells.* Energy & Environmental Science, 2015.

12. Dimitrievska, M., et al., *Multiwavelength excitation Raman scattering study of polycrystalline kesterite Cu_2ZnSnS_4 thin films.* Applied Physics Letters, 2014. **104**(2).

13. Wang, Z.R., S. Elouatik, and G.P. Demopoulos, *Understanding the phase formation kinetics of nano-crystalline kesterite deposited on mesoscopic scaffolds via in situ multi-wavelength Raman-monitored annealing.* Physical Chemistry Chemical Physics, 2016. **18**(42): p. 29435-29446.

14. Sun, R.J., et al., *$Cu_2ZnSnSSe_4$ solar cells with 9.6% efficiency via selenizing Cu-Zn-Sn-S precursor sputtered from a quaternary target.* Solar Energy Materials and Solar Cells, 2018. **174**: p. 42-49.

15. Fernandes, P.A., P.M.P. Salomé, and A.F.d. Cunha, *Study of polycrystalline Cu_2ZnSnS_4 films by Raman scattering.* Journal of Alloys and Compounds, 2011. **509**(28): p. 7600-7606.

16. Patel, K., et al., *Cu_2ZnSnS_4 thin-films grown by dip-coating: Effects of annealing.* Journal of Alloys and Compounds, 2016. **663**: p. 842-847.

17. Wang, K.J., et al., *Structural and elemental characterization of high efficiency Cu_2ZnSnS_4 solar cells.* Applied Physics Letters, 2011. **98**(5): p. 3.

18. Yoo, H. and J. Kim, *Growth of Cu_2ZnSnS_4 thin films using sulfurization of stacked metallic films.* Thin Solid Films, 2010. **518**(22): p. 6567-6572.

19. Fontané, X., et al., *In-depth resolved Raman scattering analysis for the identification of secondary phases: Characterization of Cu_2ZnSnS_4 layers for solar cell applications.* Applied Physics Letters, 2011. **98**(18): p. 181905.

20. Caballero, R., et al., *Cu_2ZnSnS_4 thin films grown by flash evaporation and subsequent annealing in Ar atmosphere.* Thin Solid Films, 2013. **535**: p. 62-66.

21. Chalapathi, U., S. Uthanna, and V.S. Raja, *Growth of Cu_2ZnSnS_4 thin films by co-evaporation-annealing route: effect of annealing temperature and duration.* Journal of Materials Science-Materials in Electronics, 2018. **29**(2): p. 1048-1057.

22. Valakh, M.Y., et al., *Optically induced structural transformation in disordered kesterite Cu_2ZnSnS_4.* Jetp Letters, 2013. **98**(5): p. 255-258.

23. Fernandes, P.A., P.M.P. Salome, and A.F.d. Cunha, *A study of ternary Cu_2SnS_3 and Cu_3SnS_4 thin films prepared by sulfurizing stacked metal precursors.* Journal of Physics D-Applied Physics, 2010. **43**(21).

24. Fernandes, P.A., P.M.P. Salome, and A.F.d. Cunha, *Growth and Raman scattering characterization of Cu_2ZnSnS_4 thin films.* Thin Solid Films, 2009. **517**(7): p. 2519-2523.

25. Kumar, S., et al., *Study of CZTS nano-powder synthesis by hot injection method by variation of Cu and Zn concentrations*, in *Proceedings of the 2016 E-Mrs Spring Meeting Symposium T - Advanced Materials and Characterization Techniques for Solar Cells Iii*, S. Yerci, et al., Editors. 2016. p. 136-143.

26. Chen, S.Y., et al., *Intrinsic point defects and complexes in the quaternary kesterite semiconductor Cu_2ZnSnS_4.* Physical Review B, 2010. **81**(24).

27. Ruan, C.-H., et al., *Electrical properties of $Cu_xZn_ySnS_4$ films with different Cu/Zn ratios.* Thin Solid Films, 2014. **550**: p. 525-529.

28. Yeh, M., C. Lee, and D. Wuu, *Influences of synthesizing temperatures on the properties of Cu_2ZnSnS_4 prepared by sol–gel spin-coated deposition.* Journal of Sol-Gel Science and Technology, 2009. **52**(1): p. 65-68.

29. Mkawi, E., et al., *Dependence of Copper Concentration on the Properties of Cu_2ZnSnS_4 Thin Films Prepared by Electrochemical Method.* Int. J. Electrochem. Sci, 2013. **8**: p. 359-368.

30. Pawar, S.M., et al., *Synthesis of Cu_2ZnSnS_4 (CZTS) absorber by rapid thermal processing (RTP) sulfurization of stacked metallic precursor films for solar cell applications.* Materials Letters, 2014. **118**: p. 76-79.

31. El Kissani, A., et al., *Synthesis, annealing, characterization, and electronic properties of thin films of a quaternary semiconductor; copper zinc tin sulfide.* Spectroscopy Letters, 2016. **48**(5): p. 343-347.

32. Nguyen, D.C., S. Ito, and D.V.A. Dung, *Effects of annealing conditions on crystallization of the CZTS absorber and photovoltaic properties of $Cu(Zn,Sn)(S,Se)_2$ solar cells.* Journal of Alloys and Compounds, 2015. **632**: p. 676-680.

33. Chen, S., et al., *Crystal and electronic band structure of Cu_2ZnSnX_4 (X=S and Se) photovoltaic absorbers: First-principles insights.* Applied Physics Letters, 2009. **94**(4).

34. Park, H., Y.H. Hwang, and B.-S. Bae, *Sol-gel processed Cu_2ZnSnS_4 thin films for a photovoltaic absorber layer without sulfurization.* Journal of Sol-Gel Science and Technology, 2013. **65**(1): p. 23-27.

Chapter 7: Effect of absorber and buffer layers of solar cells performance

7.1: Introduction and review

CZTS solar cell devices consist of many layers. The first layer is a back contact, which is made from molybdenum (Mo) with a thickness between 500 and 700 nm is deposited via the sputtering technique on glass substrate. The second layer is the absorber layer; in this layer, the CZTS has a p-type thin film with thickness up to 2000 nm, and it is deposited on the Mo layer by spin coating method. Then, this is followed by the n-type CdS layer that is deposited by chemical bath deposition (CBD) with a thickness in the range of 70 nm to form the p-n junction. After that, the i:ZnO layer with a thickness of 50 nm is deposited on the CdS layer by the RF sputtering technique to avoid leakage. Next, Al:ZnO layer is deposited by the sputtering technique with a thickness 250 nm. Lastly, the Al grid is deposited on the transparent conducting oxide to achieve electrical contacts [1] [2].

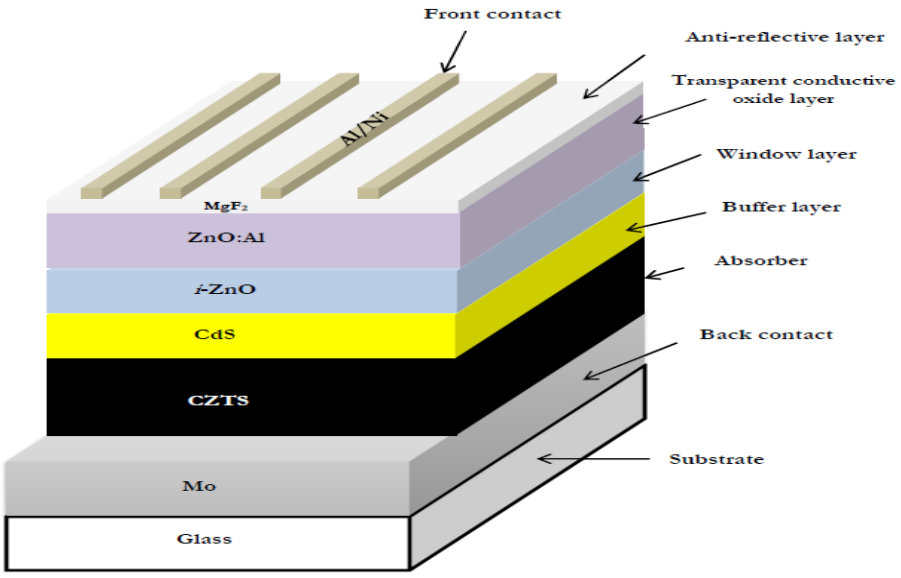

Figure 7.1 CZTS solar cells device consists of substrate, back contact layer, followed by the main layer in this project; absorber layer, buffer layer, window layer, Transparent oxide layer, grid layer and anti-reflective layer.

7.1.1: Back contact

The back contact layer works as a barrier for preventing diffusion of impurities from the substrate into the absorber layer and as electrode of the CZTS solar device. For good electronic device properties, formation of Ohmic contact for majority carrier (holes) from CZTS and low recombination rate for minority carrier (electrons) at CZTS/Mo or other back contact materials such as gold (Au), tungsten (W), palladium (Pd), platinum (Pt) and nickel (Ni). Mo is still the most common layer that is used as a back contact material for thin film solar cells because its stability at high temperature during the growth condition, its low price and excellent adhesion between glass substrates from one side and CZTS absorber. Also, the highest recorded conversion efficiency was performed by using Mo back contact [3].

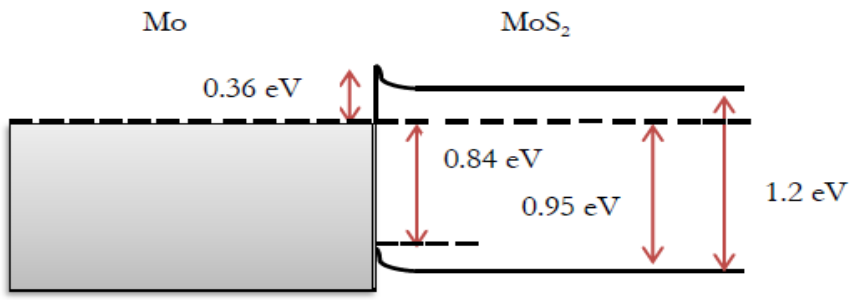

Figure 7.2 Interface between Mo layer in CZTS and intermediate layer MoS_2 [4].

However, during the fabrication and deposition of CZTS onto Mo substrate, the MoS_2 layer will be formed between Mo and CZTS interface as shown in figure 7.2 which have a negative effect on the solar cell device and its performance. MoS_2 increases the resistance to conduct the current and also the combination between MoS_2 and voids at Mo/CZTS interface increases the series resistance which leads to additional source of electrical loss in the device [4-6].

There are many techniques that were used to control interface reaction between Mo and CZTS. For instance, inserting a thin MoO_3 intermediate layer with thickness 20 nm can also prevent direct reaction between CZTS and Mo back contact and form MoS_2, and also prevent the formation of voids and secondary phases at back contact and absorber interface [7].

Liu et al recorded the high efficiency of ultrathin CZTS by applying the thin layer of Al_2O_3 at Mo/CZTS interface which leads to prevent the detrimental interface reaction and reduce the back contact recombination [8, 9]. The thin layer of titanium nitride (NiT) was used by Scragg's group which acts as a barrier layer that can passivate the interface reaction of Mo and CZTS and reduce formation of MoS_2 [10]. But TiN/CZTS interface contact induces a rather high resistance in the CZTS device [10].

Inserting the thin TiB_2 intermediate layer at Mo/CZTS interface acts to reduce formation of MoS_2 layer and reduce the series resistance and increase the efficiency of CZTS device by boosting J_{sc} and FF [11]. The presence of TiB_2 leads to degrade the CZTS crystallinity which leads to degradation of CZTS performance, it is important to optimise TiB_2 thickness to ensure acceptable MoS_2 thickness and large grain microstructure of CZTS absorber layer [11, 12].

In addition, applying the thin ZnO intermediate layer significantly improves the V_{oc}, J_{sc} and FF which increases the CZTS efficiency because this layer acts to reduce voids and secondary phases such as MoS_2 in the Mo/CZTS interface as well as reduce the series resistance and increase the shunt resistance which leads to improve the FF. The ZnO layer reduces generation of SnS_2 on the CZTS surface [13].

Moreover, another technique used to solve the back contact reaction is by inserting the thin carbon layer between Mo/CZTS. This layer acts to aggregate carbon at the inner walls of voids and reconnect CZTS with back contact which reduces the series resistance and boosts J_{sc} [14]. The thin layer of Ag [15, 16] also acts to reduce defects such as voids and inhibit the formation of MoS_2. Ultrathin Ti layer also has dual functions in CZTS solar cell; it prevents the formation of MoS_2 by blocking diffusion of S into Mo film and improves the crystalinity of CZTS. Also 20 nm of Ti increases the device efficiency to 3.94 % and V_{oc} to 541 mV [17]. Moreover, inserting thin bismuth (Bi) intermediate layer with thickness 20 nm acts to improve the CZTS device efficiency as well as increase the V_{oc} to 590 mV and also block diffusion of S to Mo to form MoS_2 and improve the crystallinity of synthesized CZTS [18].

7.1.2: Buffer layer

It is n-type layer which acts to form a junction with CZTS absorber layer (p-type). This buffer layer must have minimum recombination loss to photogenerated carrier and also minimum electrical resistance to transport the photogenerated carriers to the outer circuit. This requires the band gap of buffer layer to be as high as possible and the layer thickness as thin as possible to reduce recombination and series resistance which affects directly the solar performance in V_{oc}, J_{sc} and FF. There are many materials that are used in buffer layers such as CdS, In_2S_3, ZnO, ZnS, $Zn_{1-x}Sn_xO_y$, $Cd_{1-x}Zn_xS$ and $Zn_{1-x}Mg_xO$ [19, 20].

CdS is the most popular compound used as buffer layer and lots of CZTS thin film solar cell devices achieving high efficiency are based on CdS buffer layer with band gap 2.4 eV [21]. Also, in CdS, the surface recombination velocity value is 10^7 cms^{-1} for CdS /CZTS and a shunt resistance value is of 2×10^4 $\Omega.cm^2$ (area of solar cell device) [21]. However, the interface between CZTS and CdS has important role on CZTS device performance. Due to the difference in the kind of junction (n and p types), the band gap energy and electron affinity of CZTS and CdS, there are two different types of band alignments at CZTS and CdS interface; cliff-like hetrojunction and spike-like hetrojunction [22]. When the valance band edge of CZTS is higher than that for CdS while the conduction band edge of CZTS is lower than that for CdS, the spike-like hetrojunction is formed which is a type I heterojunction which requires that the CBO is small and positive and in the range $0 \text{ eV} < \Delta E_c < 0.41 \text{ eV}$ [23, 24]. Electrons can be thermally emitted out of the absorber into the buffer layer at a rate high enough such that large light currents can pass the interface which acts to reduce the interface recombination and increase the open circuit voltage which is a favourable hetrojuction interface in CZTS PV devices as shown in Figure 7.3 (a) and (b) [25]. However, if the CBO is too positive, a spike will form as well and it would block the light-generated electrons transfering from the CZTS to CdS layer [26].

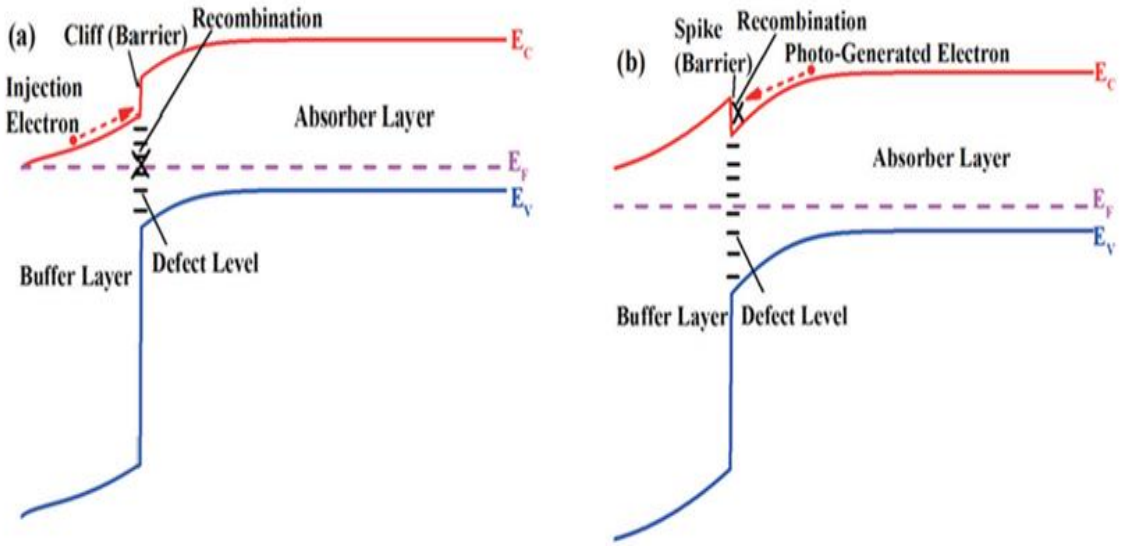

Figure 7.3 Different types of band alignments at CZTS absorber layer and buffer layer interface; (a) cliff-like hetrojunction and (b) spike-like hetrojunction [12, 24].

Whereas, when the valence band edge of CZTS was higher than that for CdS, while the conduction band edge of CdS lower than that of CZTS, the cliff hetrojunction is formed which is labelled to type II heterojunction which acts as a barrier against injected electrons from n type region. This increases the interface recombination and reduces CZTS device performance [26, 27]. On the other hand, a range of conduction and valence band offset values have been reported. For cliff CZTS/CdS, the CBO values are -0.06 eV [28], -0.14 eV [29], -0.2, -0.3[30] and -0.33 eV [30, 31]. For spike CZTS/CdS, the CBO are 0.2 eV [27], 0.41 eV [32] and 0.55 eV [33]. Therefore, CdS buffer layer has been reported as both conduction band offsets; spike and cliff CBO. As shown also in Figure 7.4 (a), other buffer materials are indeed spike like hetrojunction which affect directly the PV device CZTS.

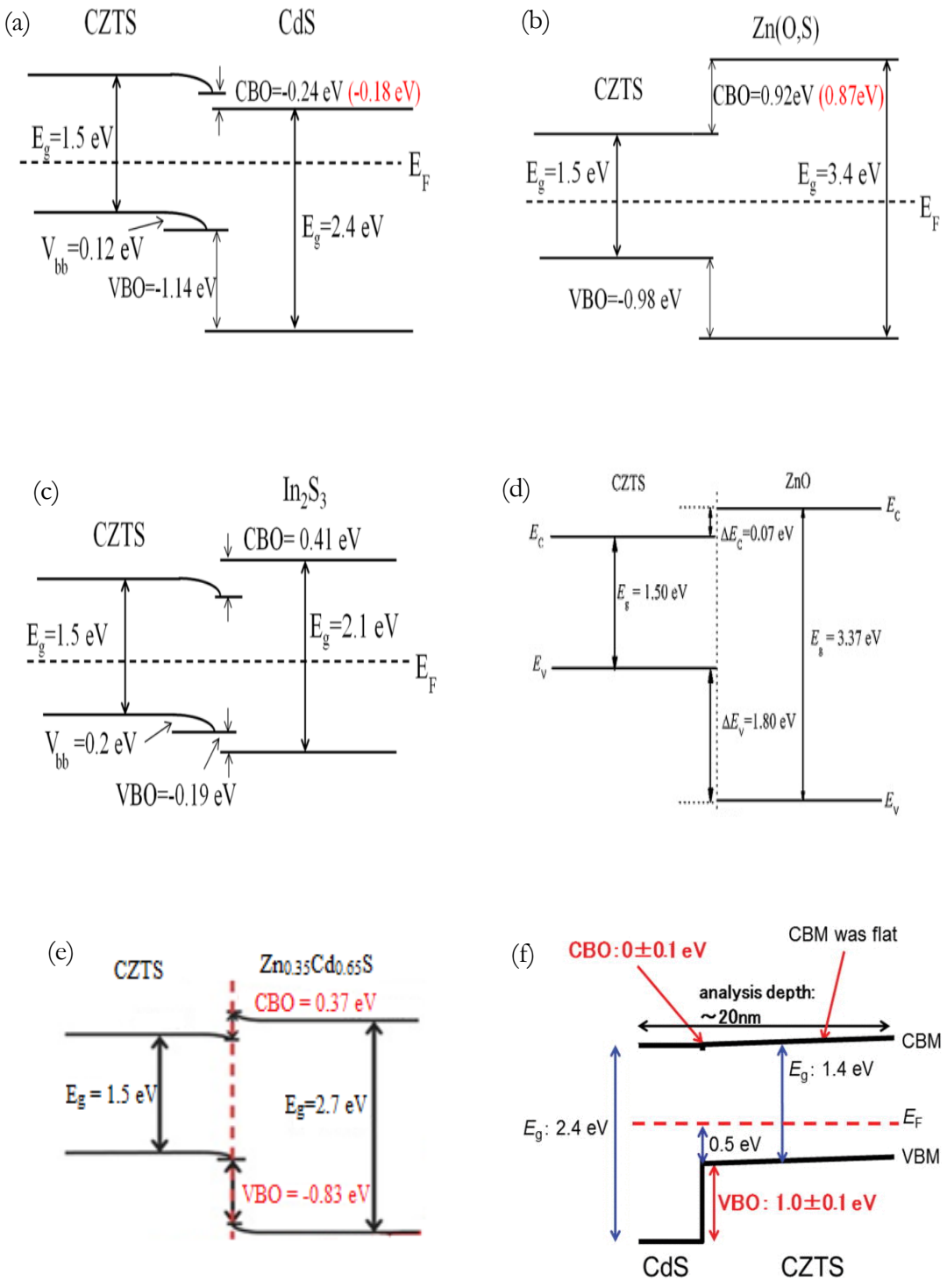

Figure 7.4 Different band offset diagram of different buffer materials (a) CdS ,(b) Zn(O,S), (c) In_2S_3, (d) ZnO, (e) $Cd_{1-x}Zn_xS$ and (f) CdS with CBO equal to zero and VBO equal to 1 eV.

In_2S_3 is an n type semiconductor with energy band gap close to 2.78 eV. The valence and conduction band offsets are determined to be 0.46 and 0.82 respectively which is too high for fabrication of high efficiency solar cells reduces J_{sc} [34]. Other study determined the bands offset at -0.19 eV for valence band offset and 0.41 eV for conduction band offset which indicate a spike like hetrojunction at In_2S_3/CZTS interface as shown in Figure 7.4 (c) [22].

$Cd_{1-x}Zn_xS$ has variable band gap energy in the range 2.4 eV to 3.7 eV which depends on a relative ratio of Cd and Zn. However, the band offsets strongly depend on the Zn composition which is a spike hetrojunction with moderate barrier height less than 0.41 eV when the Zn composition in $Cd_{1-x}Zn_xS$ is in the range 0.25 to 0.5 as shown in Figure 7.4 (e). Above that composition leads to reduce photocurrent, whereas smaller than 0.25 composition leads to increase recombination rate for majority carriers at the interface which reduces V_{oc} [35]. Other study [36] confirmed that improvement in V_{oc} was realized by applying $Zn_{0.35}Cd_{0.65}S$ buffer on CZTS solar cell and the efficiency was 9.2 % with highest V_{oc} of 762 mV and also the CBO changed from cliff to spike with this ratio changing. It is concluded that the Zn and Cd compositions have a strong effects on energy band gap as well as on CBO.

ZnO has 3.3 eV as band gap energy with n type semiconductor as well as abundant and nontoxic elements which makes it suitable for buffer layer. The CBO at CZTS/ZnO interface were calculated with positive value as 0.07 eV which is lower value for spike hetrojunction which is important for boosting the V_{oc} and it achieved a V_{OC} of 650 meV [37, 38]. On the other hand, ZnS with band gap close to 3.5 eV is alternative material for the buffer layer [39-41]. The 'spike-like' CBO of 0.86 eV was estimated at the CZTS/ZnS interface as shown in Figure 7.4 (d). A high content of ZnS limits the grain size of CZTS which leads to high series resistance and acts as a current blocking layer which leads to lower J_{sc} thus making it an unfavorable buffer layer in CZTS devices [42].

In $ZnO_{1-x}S_x$, the CBO at CZTS/Zn (O, S) interface depends on different S and O contents. When S/(S+O) ratio [42] x changes from 0 to 1, the CBO increases as the S content increased. The CBO can range from −0.23 eV for ZnO/CZTS to +1.06 eV for ZnS/CZTS. However, when x = 0.6 the CBO equal to 0.23 eV as a spike hetrojunction which improved solar PV performance [43] as shown in Figure 7.4 (b). On the other hand,

the large spiked barrier in this study [22] which is + 0.82 eV, will block the light-generated electrons transferred from the CZTS to the Zn (O, S) buffer layer, therefore the photocurrent is dramatically reduced. Therefore, the Zn (O, S) with an S/(S+O) ratio of 0.6 is the optimal CBO at 0.23 eV [43, 44].

Other possible buffer layers are $Zn_{1-x}Sn_xO_y$. The open circuit voltage is higher for the ZTO buffer devices as compared with their CdS reference cells which increase the device performance [45]. Also, by using thin layer of CdS as a double buffer layers in ZnSnO/CdS/CZTS showed a high open-circuit voltage of 810 mV which acts to reduce recombination. Moreover, $Zn_{1-x}Mg_xO$ is another material which could be used as a buffer layer. The large and variable band gaps are in the range between 3.3 eV and 4 eV [46] with controllable Conduction band offset which allows improved performances of PV cell. Besides, the conduction band alignment between ZMO and CZTS can be optimized via tuning the Mg/ (Zn + Mg) ratio [12, 47-49].

To passivise the interface defect on CZTS/CdS, the ultrathin SnO_2 intermediate layer with thickness 1.2 nm which was deposited by a SILAR method was applied. The CZTS solar cells devices with SnO_2 intermediate layers showed the higher open circuit voltage (V_{oc}) of 657 mV, short circuit current density (J_{sc}) of 20.5 and fill factor (FF) of 62.8%, compared to the CZTS device without the SnO_2 intermediate layers. The device performance was improved in the overall efficiency from 6.82% to 8.47% [50].

7.1.3: Window layer

ZnO is widely used as a window layer. It has an energy band gap in the range 3.29 to 3.33 eV [51, 52]. However, it is clear that the short-circuit current density J_{sc} strongly depends on the thickness of the ZnO window layer; increases in the window layer thickness from 10 up to 100 nm, the J_{SC} increases linearly which can be explained by the window layer thickness is high, the number of high energy absorbed photons is increased which leads to generate the higher number of electrons which contributing to the enhancement of the short-circuit current.

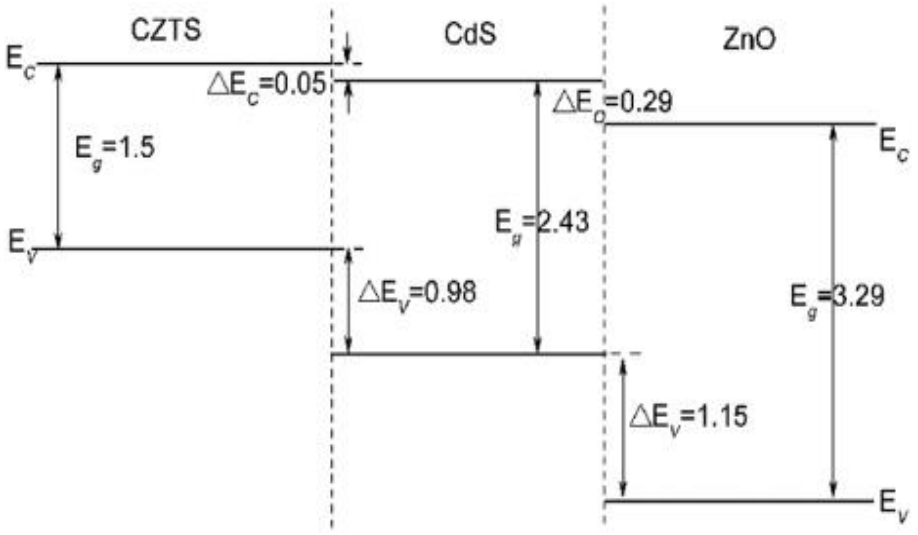

Figure 7.5 Interfaces between CZTS/CdS and CdS/ZnO.

Here also the interface between ZnO and CdS played the major influence for solar performance by recombination losses as shown in Figure 7.5. However, the high energy band gap of window layer is required to increase the amount of light passing through the cell to reach to buffer layer and absorber layer. Also, the window layer acts to minimise the leakage on CdS layer. A theoretical study confirms that the interface between CZTS/CdS and CdS/ZnO is a spike hetrojunction and the conduction-band offsets at both interfaces CZTS/CdS and CdS/ZnO are with values of 0.05 eV and 0.29 eV, respectively as shown in Figure 7.5 [53].

7.1.4: Transparent conducting layer

TCOs are employed as front electrodes in solar cells [54]. They act to collect the charge carriers and transport them to the collection grid. Transparent conducting layer needs some requirements such as highly conductive, low sheet resistance, transmittance of greater than 90% and high refractive index (typically more than 3). There are many materials that are used as transparent conducting oxides such as tin oxide (SnO_2), Indium Tin Oxide (ITO), Fluorine doped Tin Oxide (FTO), boron doped zinc oxide (ZnO:B), gallium doped zinc oxide (ZnO:Ga) [55], aluminium doped zinc oxide (ZnO:Al) [56, 57] and graphene [58]. However, the common used materials in CZTS devices are ITO and ZnO:Al. Park et al, presented the hybrid silver nanowire network ultrathin ITO as the transparent conductive electrode for CZTS. The device efficiency improved from 6.72 to 6.84% after introducing an intrinsic zinc oxide antireflective coating layer [59]. Despite the fact that ITO material

has good optical and electrical properties as TCO layer, but its quantity is limited, because of rare and high price of indium, it is replaced by (ZnO) structures doped with abundant and low cost elements, such as Al [55, 60] .

7.1.5: Anti-reflection layer

It is used in photovoltaic devices to reduce reflection of the incident illumination at the surface of a device [61]. The most common materials that are used as anti-reflection coatings are magnesium fluoride (MgF_2) [8] as well as ZnO [62] and Silicon dioxide (silica) SiO_2 [63]. However, MgF_2 is still the suitable anti-refection materials because adding this layer leads to an increase in the transmitting light and increases the J_{sc} and FF as well as efficiency [64, 65]. This layer does not apply in this thesis.

7.1.6: Grid contact

It is also called metal contact which acts to collect current from the cell and connects to the external circuit. There are many materials that are used as grid contacts such as Ni, Al, Au and Ag [17, 66-68]. Many techniques can be used to deposit these material on the transparent oxide layer (ZnO:Al) such as thermal evaporation, e-beam evaporation. Grid contact is one of current losses in solar devices and also the resistivity should be as low as possible to avoid losses [10, 69, 70].

The aim of this chapter is to study the effect of different thickness of CZTS layers on CZTS device performance.

7.2: Results and discussion

7.2.1: PL spectroscopy measurements of different CZTS thickness

The CZTS nanoccrystal inks were fabricated as mentioned in chapter 3. The CZTS films at different thickness were deposited by adding high concentration ink of 40 µL which equals 1 drop onto Mo foil substrate which was repeated many times to prepare many films with different thickness depending on the drops (4, 6, 8 and 10 drops) with their thickness found to be in the range 600 nm to 6 µm.

The PL peak arising from CZTS thin film is identified as the peaks in the range close to 1.39 to 1.55 eV in all samples. There are a number of luminescence features above the CZTS peak between the 1.6-2.0 eV energy ranges which are larger than the respective

sample's CZTS peak. As mentioned in chapter 5, PL measurements for non-annealing samples, peak energies have been compared to literature values of compounds that could be made during synthesis. Those considered are the metal sulphides such as CuS, ZnS, SnS, SnS_2, and Sn_2S_3, and the tertiary compounds Cu_2SnS_3 and Cu_3SnS_4. Some metal oxides are also recognized such as CuO, Cu_2O, ZnO, SnO and Sn_2O as these can be formed [71-73]. However, there are no trace for any possible secondary phases such as binary phases CuS at 1.0 2.38, 2.50, 2.56, 2.71 eV [74] Cu_2S at 1.22 eV [75], SnS and Sn_2S_3 as well as ternary phases Cu_2SnS_3 , Cu_3SnS_4 , $Cu_4Sn_7S_{16}$ and $Cu_2ZnSn_3S_8$ [76-79].

The temperature dependent PL measurements which are carried out at different temperatures at excitation laser power of 60 mW as well as the intensity dependent PL which is carried out at 4 K. Figure 7.6 show PL intensities as a function of temperature. It can be seen that the PL intensities increase with decreasing the temperature from RT to 4 K as well as the PL peak energies have a dependency on temperature which increase with decreasing temperature. Moreover, Figure 7.7 shows the PL intensity as a function of inverse temperature in an Arrhenius plot.

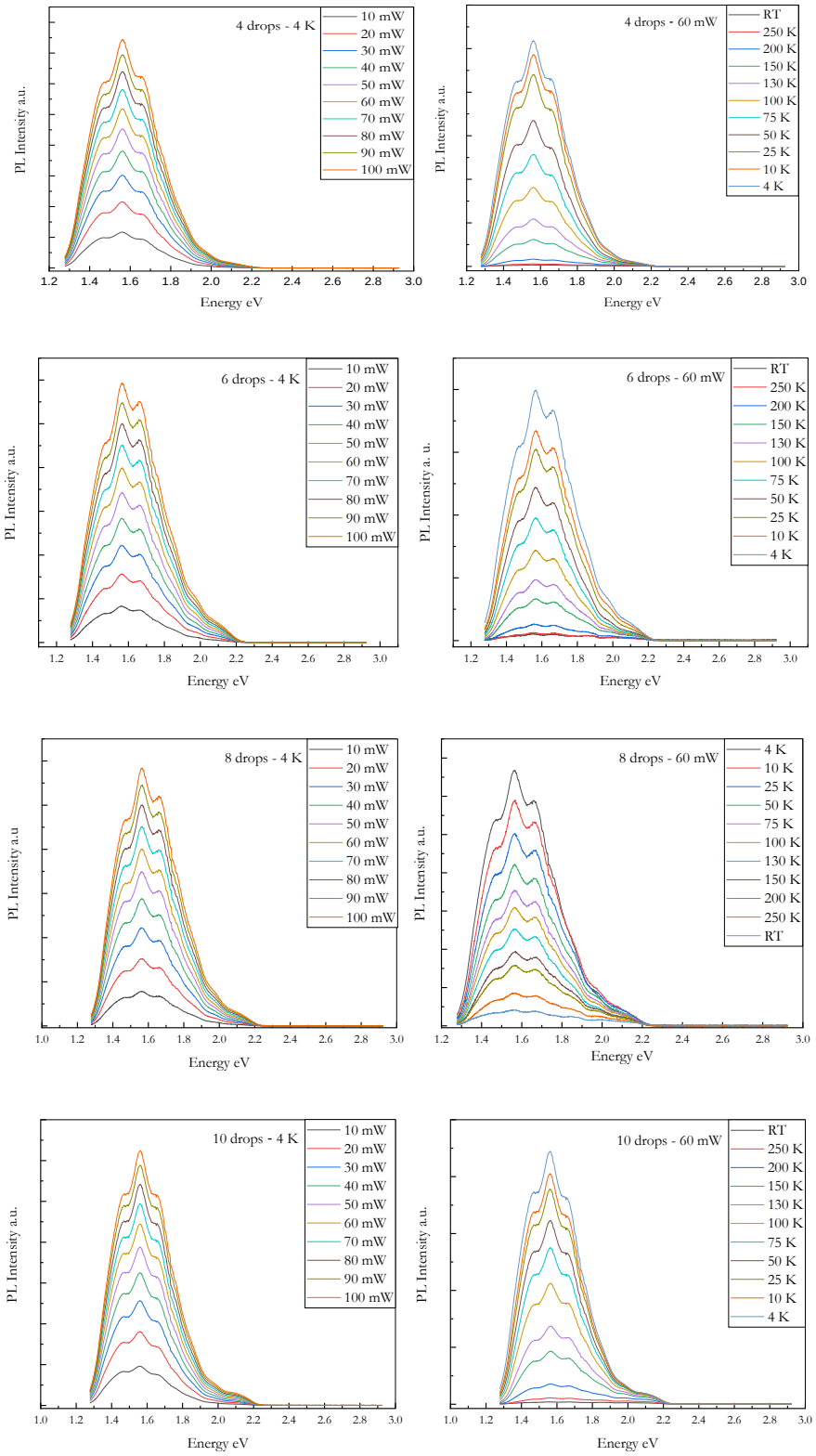

Figure 7.6 PL spectroscopy studies of the dependence on the temperature (right) and excitation power (left) of different CZTS thickness.

The PL spectroscopy studies the dependence on the temperature and excitation power of the peak energy position and intensity. Band gap of all peaks have a slight decrease of energy with increasing PL temperatures (red shift). In the range of changing temperature from low temperature 4 K to higher values (RT) the PL peak position shift to higher energy with decreasing temperatures. For example, P3 in all samples shifts by close to 10.4 meV for the peak energy of emission. Also, the shape of the spectra remains asymmetrical as the temperature increases. Moreover, the maximum intensity is at 1.55 eV for all samples.

However, using one activation energy model could not cover the whole data measurement points, therefore, the temperature dependence of the intensity of PL in CZTS is described by the best fitting function introduced by two activation energies as

$$I(T) = \frac{I_o}{1 + C_1 \exp\left(\frac{-E_1}{k_B T}\right) + C_2 \exp\left(\frac{-E_2}{k_B T}\right)} \tag{7.1}$$

where C_1 and C_2 are process rate parameters, E_1 and E_2 are the activation energies for the thermal excitation of charge carriers out of the radiative state to a higher energy non radiative state [80], T is the absolute temperature and k_B is the Boltzmann constant. The biexponential function represents the ground state and excited state for the luminescence transition. So, the activation energies for all peaks for all samples are shown in the Table7.1. The Figure (7.7) also shows that at low temperature < 100 K, the dependence of PL intensity is exponential whereas at high temperature the decrease of the PL intensity becomes steeper reflecting a difference in the activation energy E_1.

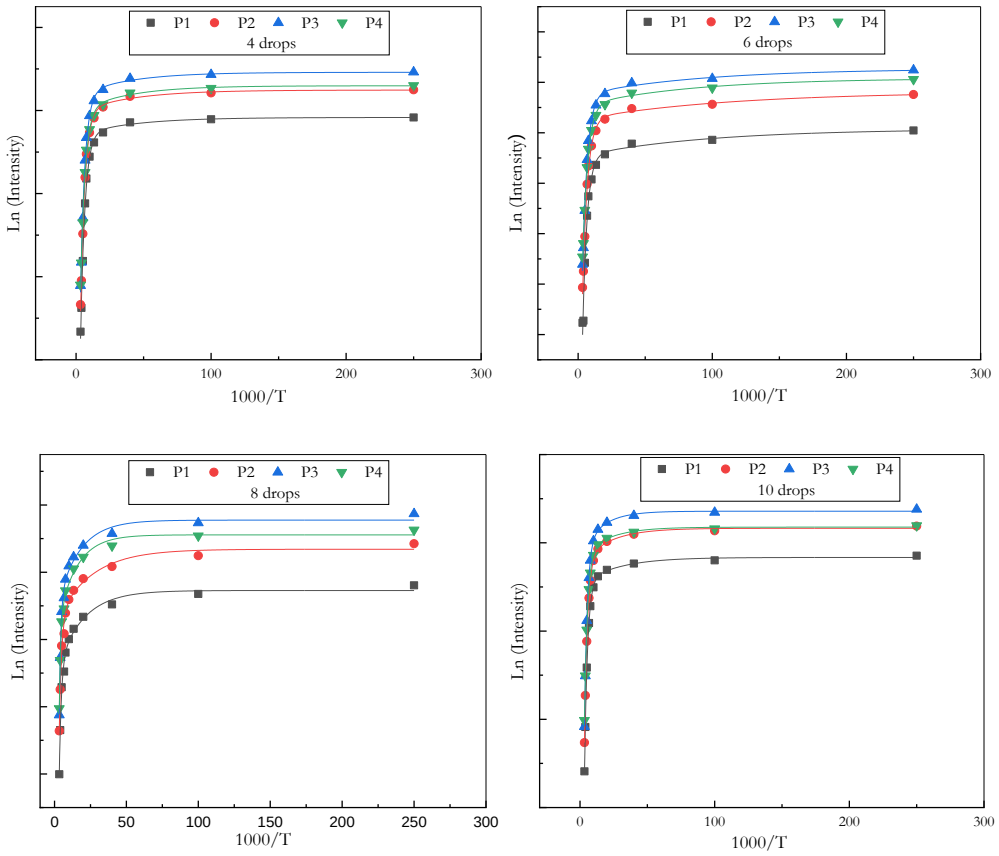

Figure 7.7 Arrhenius plots determine the thermal activation energies of different CZTS thickness.

The thermal activation energies were calculated from the temperature dependencies of the PL spectra using equation 7.1. It can be noticed that the activation energies in 4 and 10 drops are higher than that reported in many other studies, whereas for 6 and 8 drops are close with many literature values [81]. The table shows the activation energies of all samples with different thickness for the first four peaks. However, the activation energy E_1 and E_2 of P3 are 227 and 4.44, 150 and 1.66, 132 and 1.00 and 219 and 1.50 meV for 4, 6, 8 and 10 drops respectively. So, as the value of activation energies of P3 in 4 and 10 drops are higher than in 6 and 8 drops that confirms the defects levels are deeper in 4 and 10 drops. E1 and E2 measure the rate at which the ground state and excited state of the luminescence transition are depopulated. These results show that the nature of the luminescence levels does vary with film thickness and film treatment.

Table 7.1 the calculation of activation energies E_1 and E_2 from Arrhenius plots.

	Peaks	E_1 (eV)	E_2 (meV)
	P1	0.208	1.50
4 drops	**P2**	0.186	2.22
	P3	0.227	4.44
	P4	0.212	1.75
	P1	0.125	4.29
6 drops	**P2**	0.125	1.50
	P3	0.150	1.66
	P4	0.150	2.22
	P1	0.159	4.44
8 drops	**P2**	0.131	1.11
	P3	0.132	1.00
	P4	0.144	1.00
	P1	0.229	1.33
10 drops	**P2**	0.125	1.36
	P3	0.219	1.5
	P4	0.219	1.44

As shown in the Figure 7.8, as a result of the excitation power increasing, the PL peak energy suffers a slightly blue shift at rate of 0.88, 1.46, 1.53 and 1.32 meV/decade for CZTS thickness; 4, 6, 8, 10 drops at the main peak (high intensity) as well as for other peaks P1, P2 and P4, the range of energy shift are 3.00 and 0.20 meV/decade. Also, the PL intensity is related to excitation power by the power law $I \alpha P^k$ where I is the PL intensity, P is the related excitation power and k is adjustable parameter which has the value between 0 and 2. If k value is less than 1 the transition is related to defect transitions, whereas above 1 is related to excitonic transitions which depends to the concentration of both electron and holes in the conduction and valence bands. In the Figure 7.8 the k values for P3 are 0.79, 0.85, 0.87 and 0.84 which are less than 1. So, due to the k values being less than 1 these features are a result of donor-acceptor pair transition (DAP).

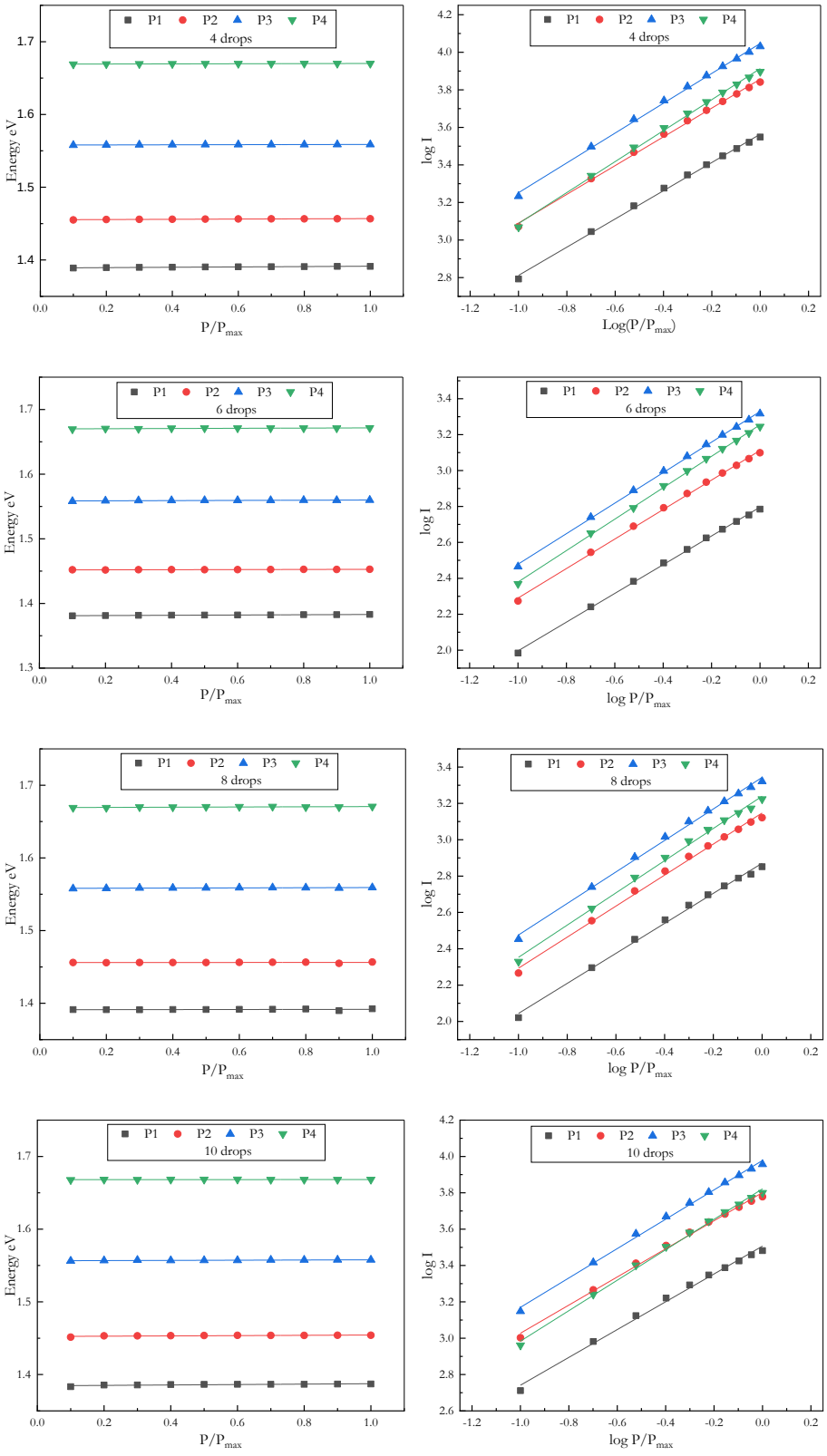

Figure 7.8 Laser power dependencies of PL bands peak positions (left) and intensity (right) of different CZTS thickness.

As seen in the Figures above, the PL measurement confirm the temperature and excitation power dependent with intensity of PL spectra. Due to the compositional ratio being Cu poor/Zn rich used to synthesise these films, there are many possible acceptor defects such as V_{Cu}, V_{Sn}, Cu_{Zn},Cu_{Sn}, and Zn_{Sn}, donor defects such as Zn_{Cu}, Zn_i and Sn_{Cu}, and defect clusters such as $[V_{Cu}+Zn_{Cu}]$, $[Cu_{Zn}+Zn_{Cu}]$, $[Zn_{Sn}+ 2Zn_{Cu}]$, and $[Cu_{Sn}+Sn_{Cu}]$ which are likely to be formed. As well as the defect clusters such as $[2Cu_{Zn}+Sn_{Zn}]$ can be produced relatively easily because their formation energy is as low as that of Cu_{Zn}. Therefore, in the CZTS-based absorber layer, it is possible to form various types of defects owing to the non-stoichiometry and secondary phase [82-85].

The Cu_{Zn} antisite defect has higher formation energy which acts as a deep acceptor level located about 100-150 meV above the valence band maxima (VBM) which be considered to be responsible for the intrinsic p-type conductivity of CZTS as reported by Chen. The copper vacancy (V_{Cu}) as well has comparatively lower energy of formation than Cu_{Zn} which contributes to a shallow acceptor level 20 meV above the VBM [83, 86]. Other accepter level defects can be found in CZTS with high energy formation such as V_{Zn}, Zn_{Sn} at 220 and 230 meV respectively [83, 87]. From first calculations [88, 89] which estimates the activation energy for defects such as Cu_{Zn} antisites as E ≈ 120 meV or 220 meV , copper vacancies V_{Cu}, as E ≈ 20 meV or 70 meV which are dominant acceptor type defects, as well as shallow donors such as Zn_{Cu} antisites as E ≈ 150 meV or 70 meV and Cu interstitials Cu_i, as E ≈ 150 meV or 50 meV [87, 90].

In CZTS, the main recombination processes can arise from different paths: band-to-tail recombination (BT) which is associated with a free electron and a hole which is localised in the valence band tail; band-to-band recombination (BB) that involves a free electron and a free hole; band-to-impurity (BI) recombination that involves an acceptor state or a donor state. Also, CZTS samples have properties of highly compensated and heavily doped semiconductors with fluctuating potentials [76, 91].

As shown in the Figures, the peak energies of the PL spectra are shifted to higher energy with few meV as the excitation powers increase. These shifts are a feature of DAP recombination and the peak energy of DAP transition is described by $h\nu=E_g-(E_D-E_A)+e^2/\varepsilon r$ where E_g is the energy brand gap, E_D is donor ionization energy, E_A is the acceptor ionization energy, e is the electron charge, ε is static dielectric constant and r is the distance

between donor and acceptor defects [92]. As a result of the excitation dependence of PL of CZTS, when the excitation power increases, the increased photocarriers will screen the coulomb interaction between the ionised donor and acceptor ions

As mentioned above, the DAP and BT models could be used to discuss the emission in CZTS. However, the DAP transition requires low doping level and as result charge carriers located at discrete donor and acceptor levels inside the band gap. On the other hand, BT transition created by electrostatic fluctuation potential due to highly doped and compensated CZTS which leads to large concentration of defects results in electrostatic fluctuation potential along the film which leads to tail states in the band gap [93].

However, as mentioned above all peaks have *k*-values less than 1 consistent with transitions in CZTS films with the peak (P3=1.55 eV) which may be related to CZTS. The values of *k* are in the range between 0.75 and 0.92 with uncertainty ±0.02 which are related with radiative transition involved defect levels. The PL peak energy has a blue shift to high energy with increasing excitation power. However, a small peak shift in the range between 1.0 and 4.0 meV/decade for all samples with different thickness. However, these results confirm the radiative transition involved defects and the electronic levels is influenced in similar way by fluctuating potential which leads to limitation of solar performance by decreasing the open circuit voltage and as well as limiting of solar efficiency.

7.2.2: Current–Voltage (IV) measurements

The device current–voltage (IV) characteristics yields important information about junction parameters such as: series resistance (Rs), diode ideality factor (n) and solar cell device parameters such as V_{oc}, I_{sc}, FF and efficiency. I–V curves of the samples were measured both in the dark and under illumination by using a solar simulator (AM 1.5 G irradiation, 100 $mWcm^{-2}$. The figures 7.9 for IV measurements of all devices show non photocurrent was generated for all devices with different thickness of CZTS layer. However, all devices also exhibit non-ohmic (nonlinear curve) behaviour.

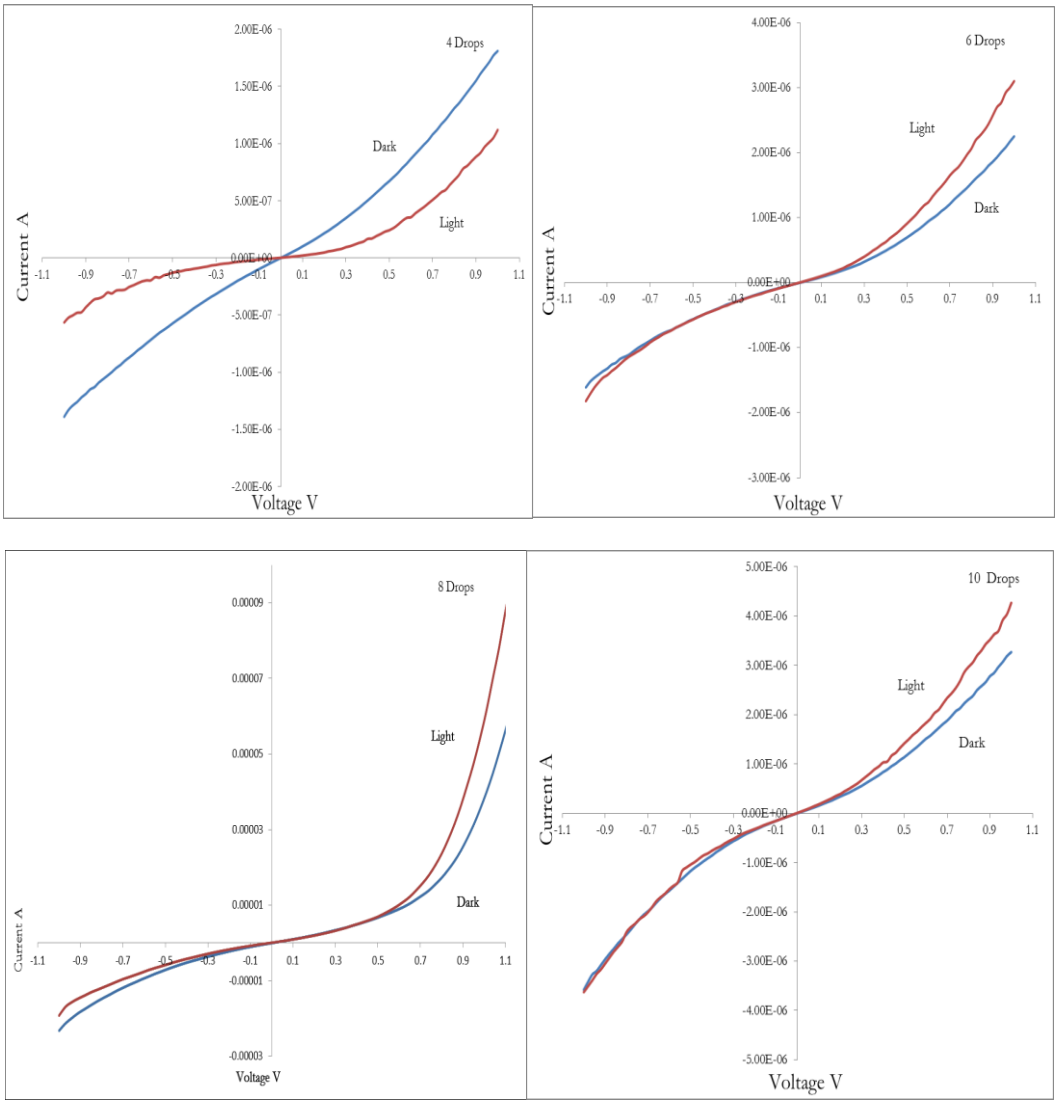

Figure 7.9 Current–voltage (IV) for different CZTS thickness.

The lack of good I-V characteristics for devices was found to be due to damage in layers as seen in Figures 7.10. The devices with structure Mo foil/CZTS/CdS/i-ZnO/ITO/Al have some damages in some layers as well as bad interface between CZTS and other layers such as CdS and ZnO layers which may explain this behaviour for I-V measurements. This damage in the device layers leads to loss current collection.

7.2.3: Cross section images of different devices

It can be seen in Figure 7.10 that the CZTS thin film solar cells have a strange structure especially in ZnO and ITO layers which have strange shapes. However, the device structure was Mo foil/CZTS/CdS/i-ZnO/ITO/Al grid. The zinc oxide layers which acts as transparent layer (window layer) were deposited by RF sputtering technique did not work correctly during the deposition process giving the shape.

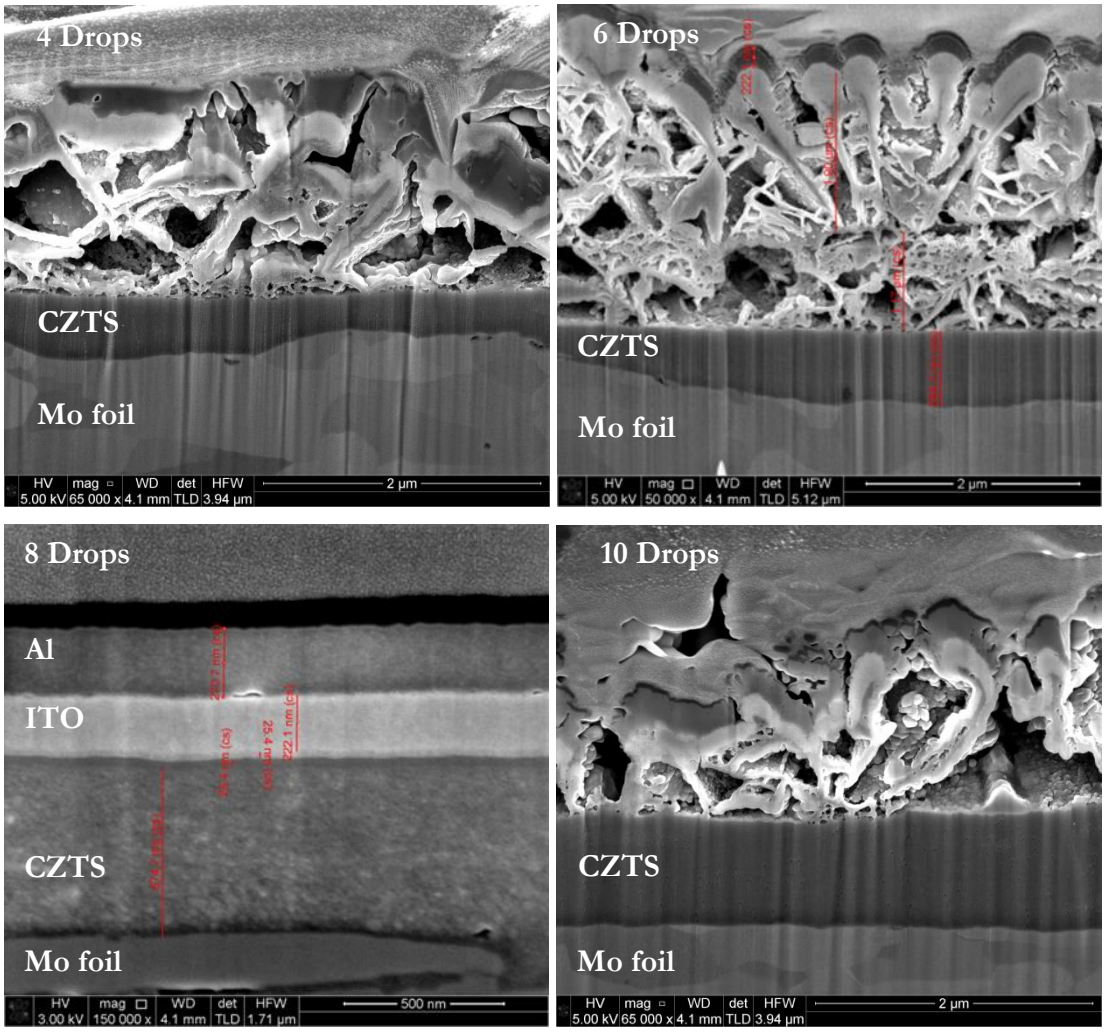

Figure 7.10 Cross sections of different CZTS devices with different thickness.

However, the main layer in this work is an absorber layer which is the second layer as shown in the figures above. These show depositing with uniform shape and structure with excellent adhesion between Mo foil and CZTS. Other issues could be seen in Figure 7.10

that the Mo foil surface did not look flat which also leads to non-uniformity thickness of CZTS along the film. As a result of depositing zinc oxide layer, the CdS layer is damaged and disappeared from the image which may affect the thickness of the underlying CZTS layer. Also, as the deposition of zinc oxide layers was done at the same time for all films, the same problem appeared in all films and the CdS layers which were deposited at different thickness; it is difficult to find this layer in all images. Lastly, all images confirm successful deposition of CZTS layer with thickness in the range between 600 nm and 6 µm.

Figures 7.11 shows the cross section of sample with thickness 8 drops. The left imaged shows the CZTS devices layers which are from bottom to top as Mo foil/ CZTS/ CdS/ ZnO/ ITO/ Al grid. It is cleared that this figure shows all layers of device with no cracks and holes. It can be seen also a black layer between Mo foil and CZTS which may correspond for MoS_2 secondary phase. The thickness of each layer CZTS/CdS/ZnO/ITO/ Al are determined as 675/25/25/222/207 nm respectively.

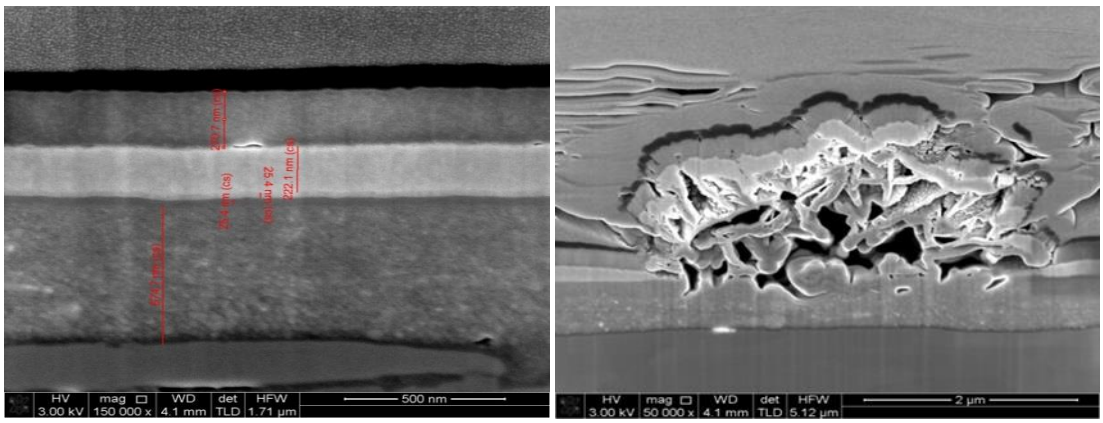

Figure 7.11 Cross section images from SEM for CZTS film with thickness 675 nm (left) and damage film (right).

However, this structure has not covered all film's surface and other region of the devices show strange shapes on the CdS layer which may correspond to CdO which damaged all layers. This damage can be used to explain why there was no photocurrent generation from I-V measurements because it leads to of loss the current collection.

Further investigations were done to identify this shape by fabricating new batches and take surface images for each batch. CZTS inks were deposited onto Mo foil substrate without annealing. It can be seen there is a smooth surface with some cracks, holes (bright particles) as shown in Figure 7.12.

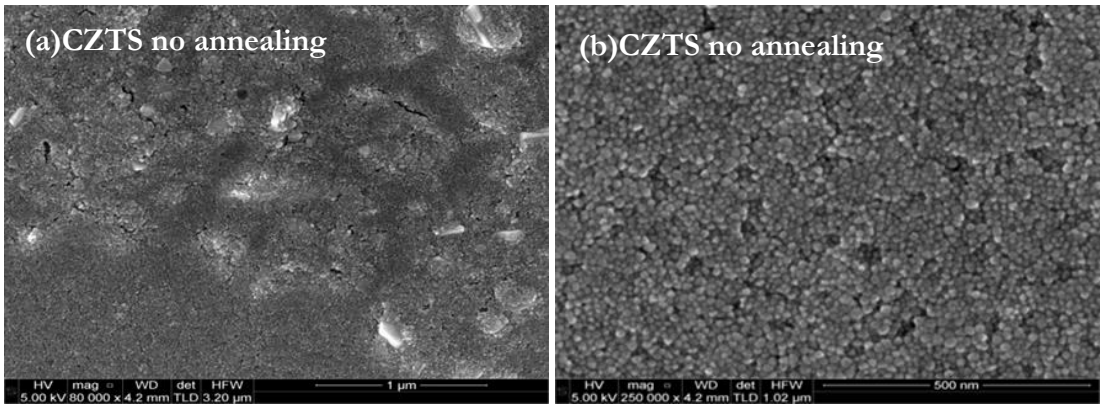

Figure 7.12 SEM images of non-annealed CZTS film at different magnification.

This film was annealed in furnace at 500 ^{o}C for 1 h under H_2S+N_2. Following this it can be seen a uniform film with some pinholes and some cracks in the surface as shown in Figure 7.13.

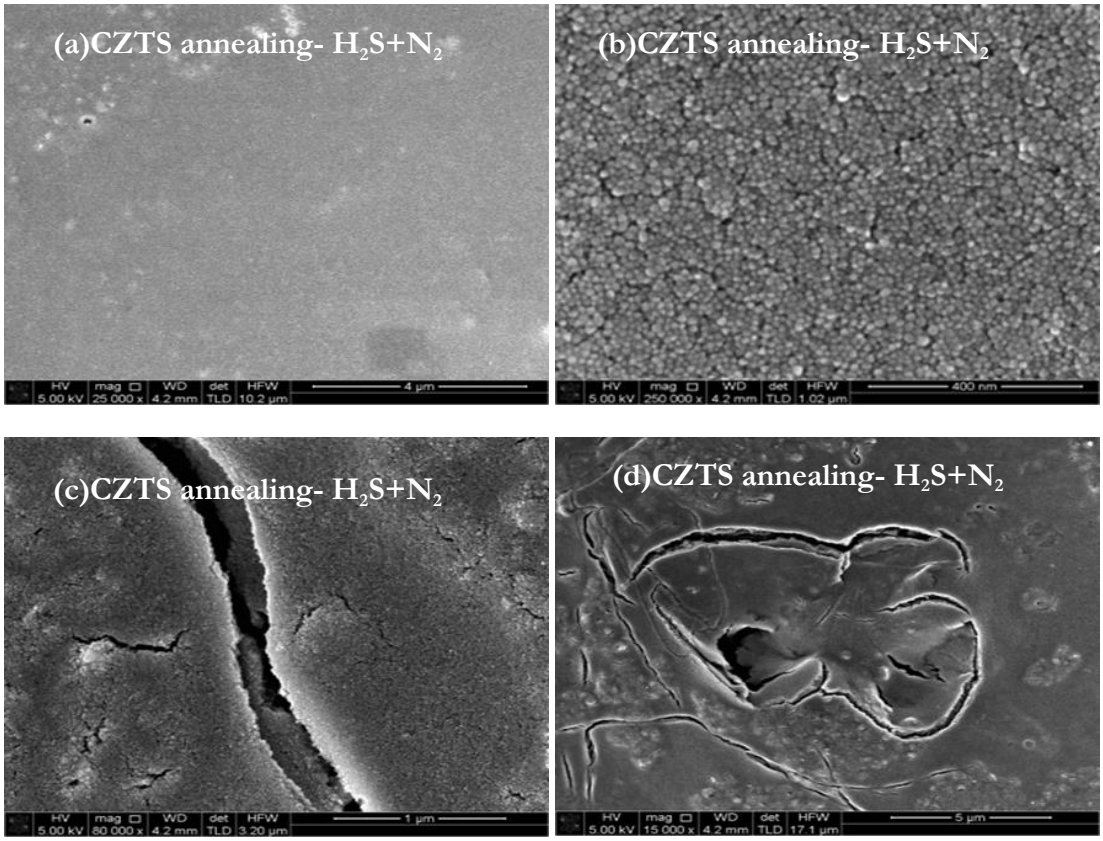

Figure 7.13 SEM images of CZTS film annealed under H_2S+N_2 atmosphere at different sites and magnification.

Images in Figure 7.14 show the films annealed at 500 °C for 1h under N_2 atmosphere. It can be seen there are large particles with different shape on the top, whereas small particles cover the film surface.

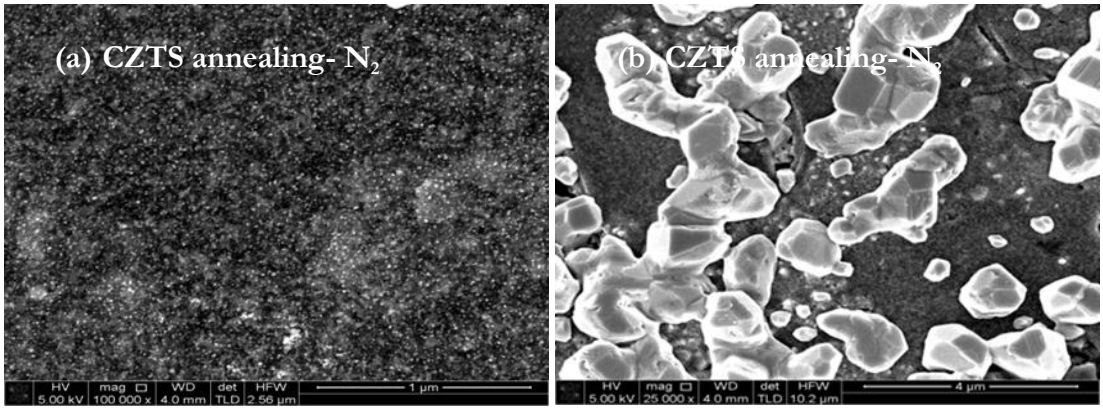

Figure 7.14 SEM images of CZTS film annealing under N_2 atmosphere at different sites and magnification.

Further investigations were done on the CdS layer. The Figure 7.15 shows CdS a layer that was deposited onto a Si wafer by chemical bath technique without annealing treatment. It is clear that the strange shape comes from this layer which is a CdO component with a diameter of about 15 μm. It also spreads and covers most of the surface of the film after annealing at 200 ^{o}C for 10 min under N_2 atmosphere.

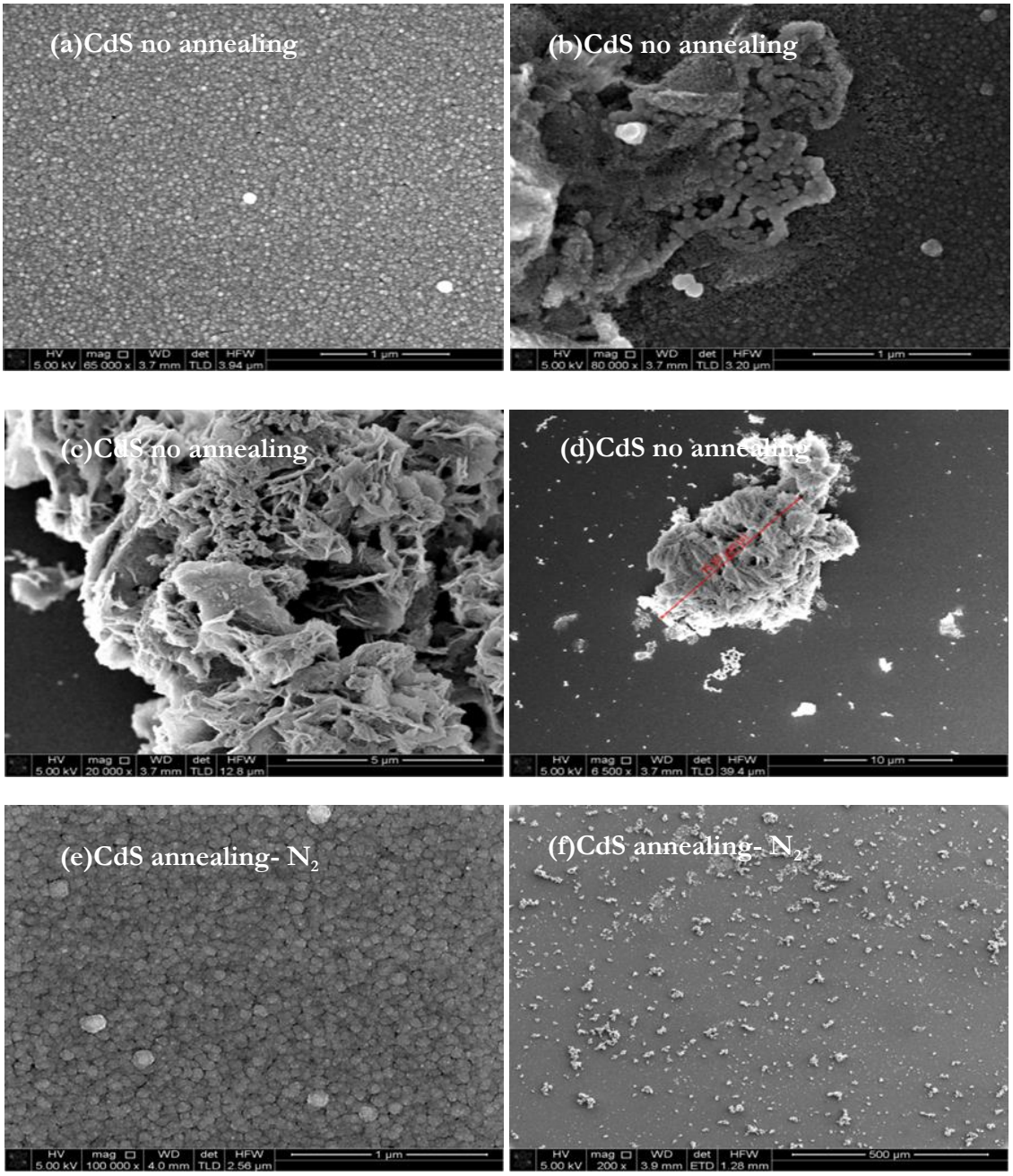

Figure 7.15 SEM images of CdS film (a,b,c and d) non-annealed films and (f and e)annealed film under N_2 atmosphere at 200 ^oC at different sites and magnification.

CdS was then deposited onto CZTS surface (annealed under H_2S+N_2 at 500 ^oC for 1 h). It can be seen that it was a thin layer which has not covered all CZTS surface as shown in Figure 7.16. There were some pinholes and cracks on the surface as well as the CdO which was formed during the deposition process which are clearly seen in the cross section images.

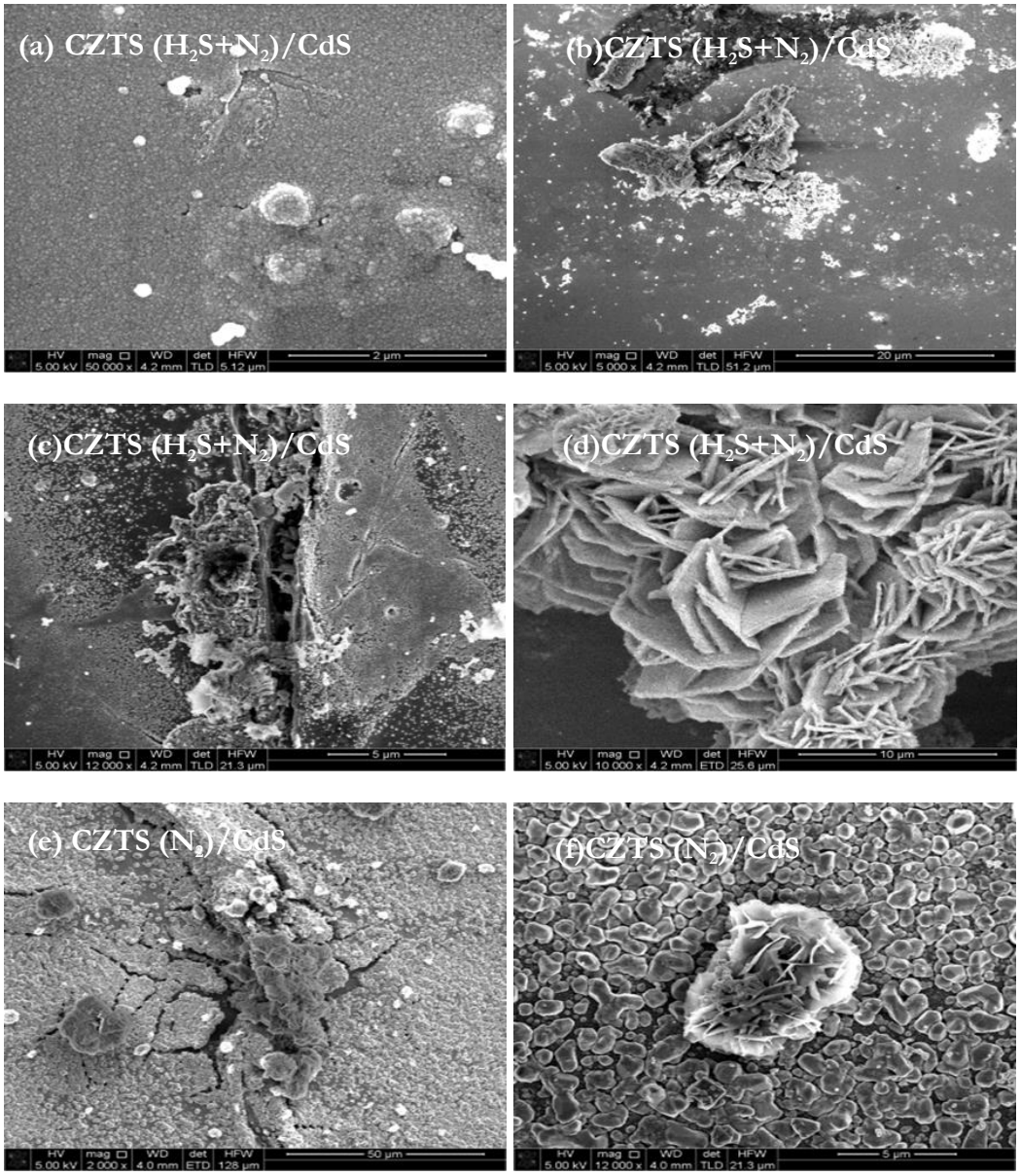

Figure 7.16 SEM images of CZTS/CdS at different annealing conditions of CZTS at different sites and magnification.

Cross-sectional SEM images were taken to investigate the crystal quality and elemental distributions of CZTS devices using EDS mapping from cross section images as shown in Figure 7.17. This confirms all elements that were used to fabricate the devices with layers as Mo foil/ CZTS / CdS /ZnO/ ITO/ Al grid. The images were taken at three different sites of the film to investigate each component in the device. The images confirm the CZTS film in the first for mapping images.

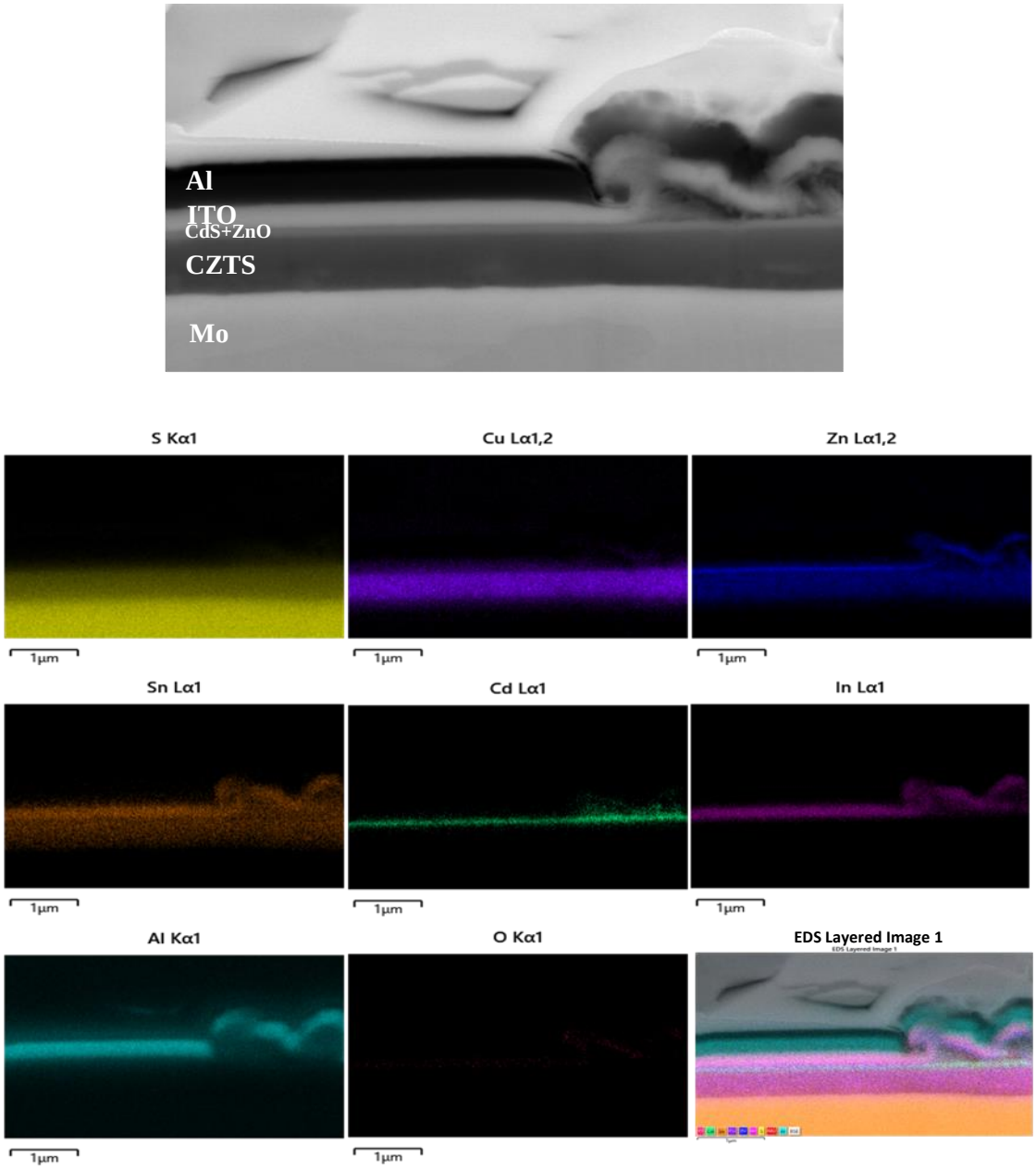

Figure 7.17 Cross sectional EDS -SEM mapping images for the compositional distribution of site 1 of CZTS device.

Images were also taken for other sites in the cross section images as shown in Figure 7.18 which also confirm the presence of all layers of device with some diffusion of elements at some points. For instance there is some Al in the surface of ZnO layer, also the strange shape may be due to CdO. Moreover, the Mo and S also overlap which may lead to form a thin layer of MoS_2.

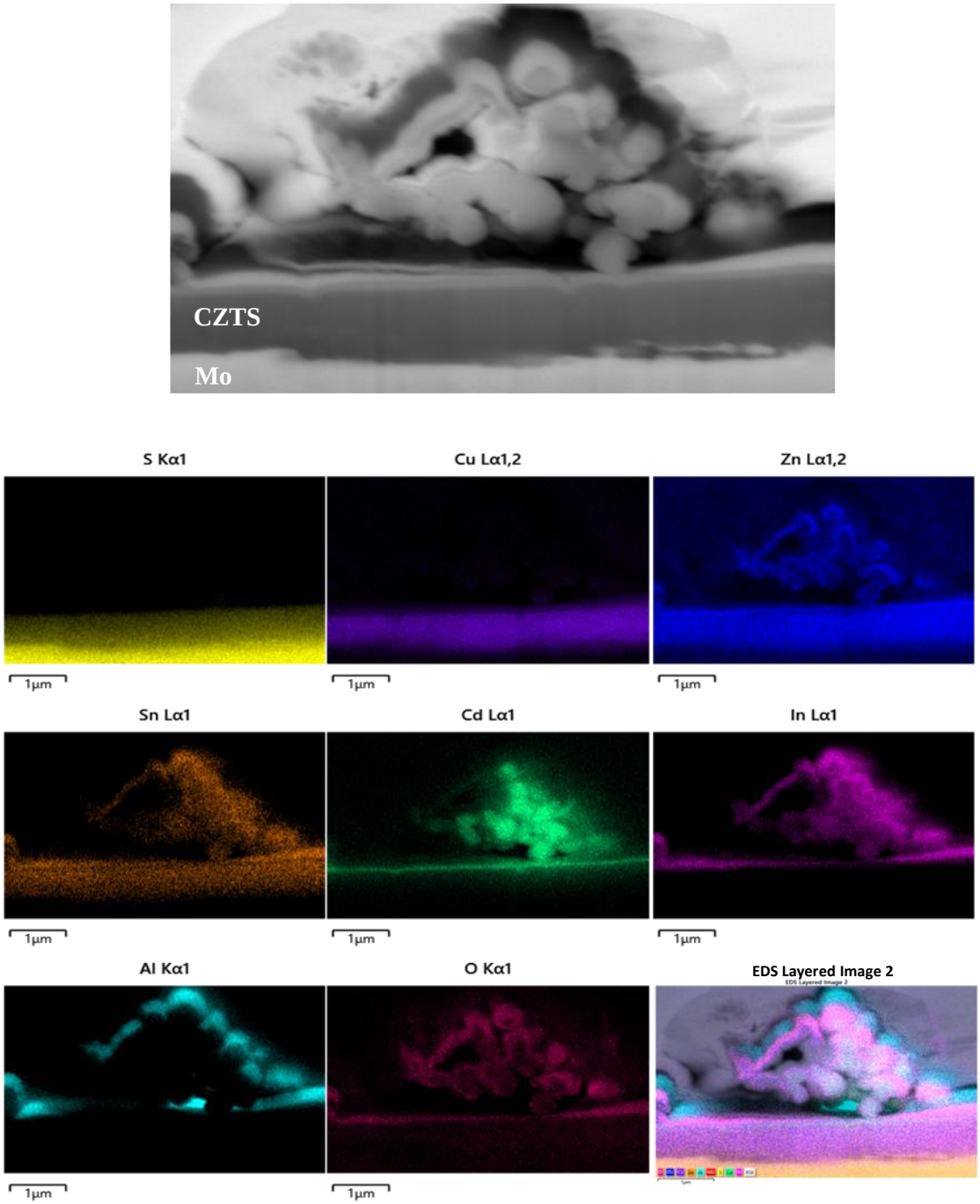

Figure 7.18 Cross sectional EDS -SEM mapping images for the compositional distribution of site 2 of CZTS device.

Images from site 3 confirm the results above for all elements showing a CZTS/ CdS / ZnO/ ITO / Al structure with uniform and homogeneous distribution as shown in Figure 7.19.

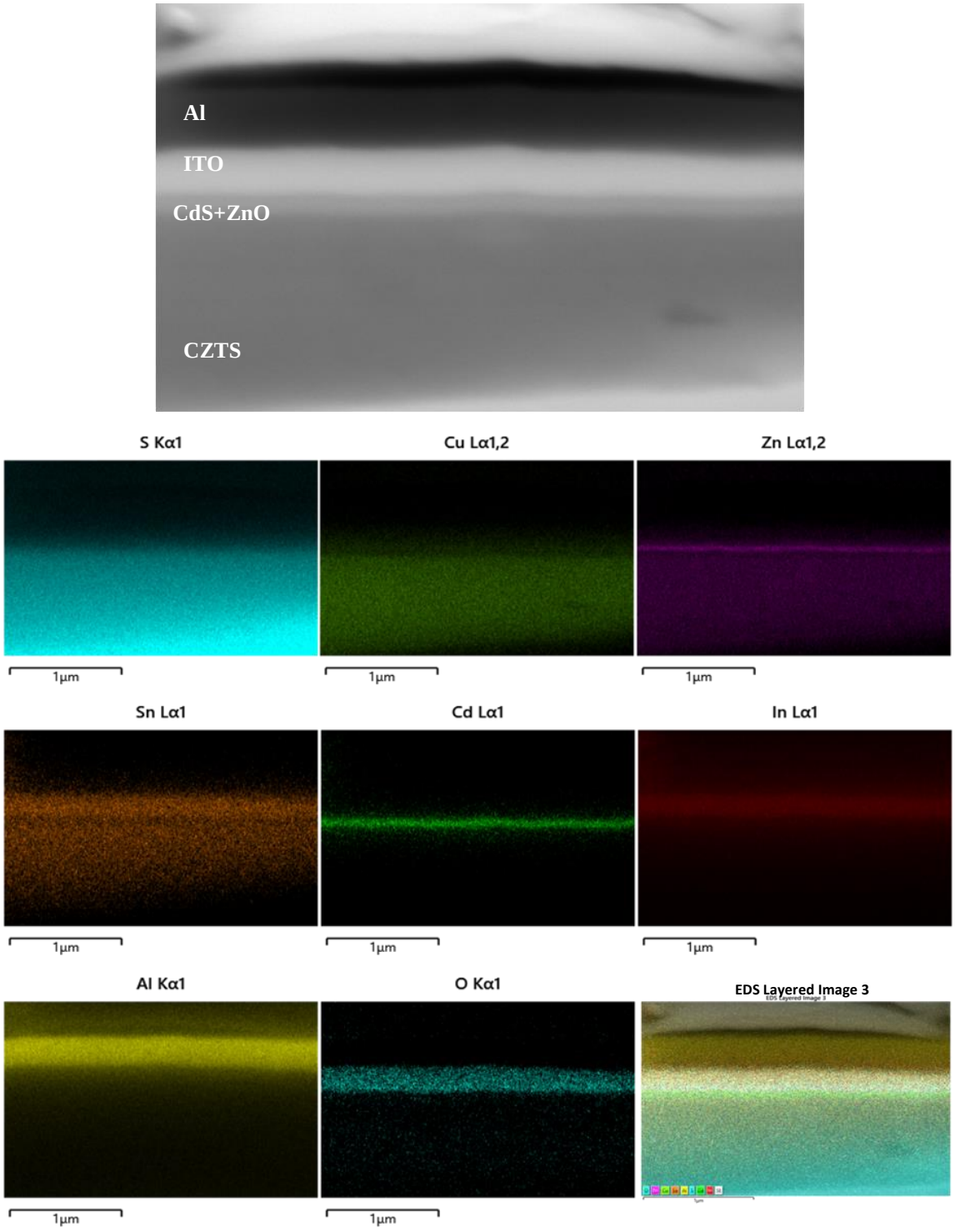

Figure 7.19 Cross sectional EDS –SEM mapping images for the compositional distribution of site 3 of CZTS device.

Scan line images were performance for all three sites in the cross section of devices. Figure 7.20 show the line scan from site 1 which also confirms uniform distribution of each element across the whole films and is similar to site 3 with no cracks and pinholes.

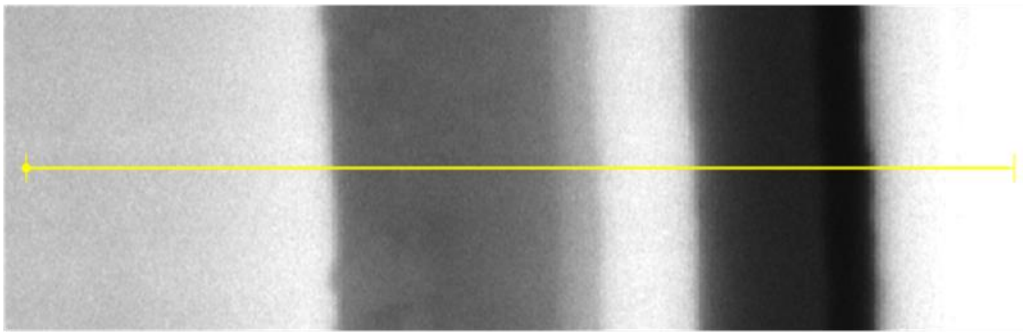

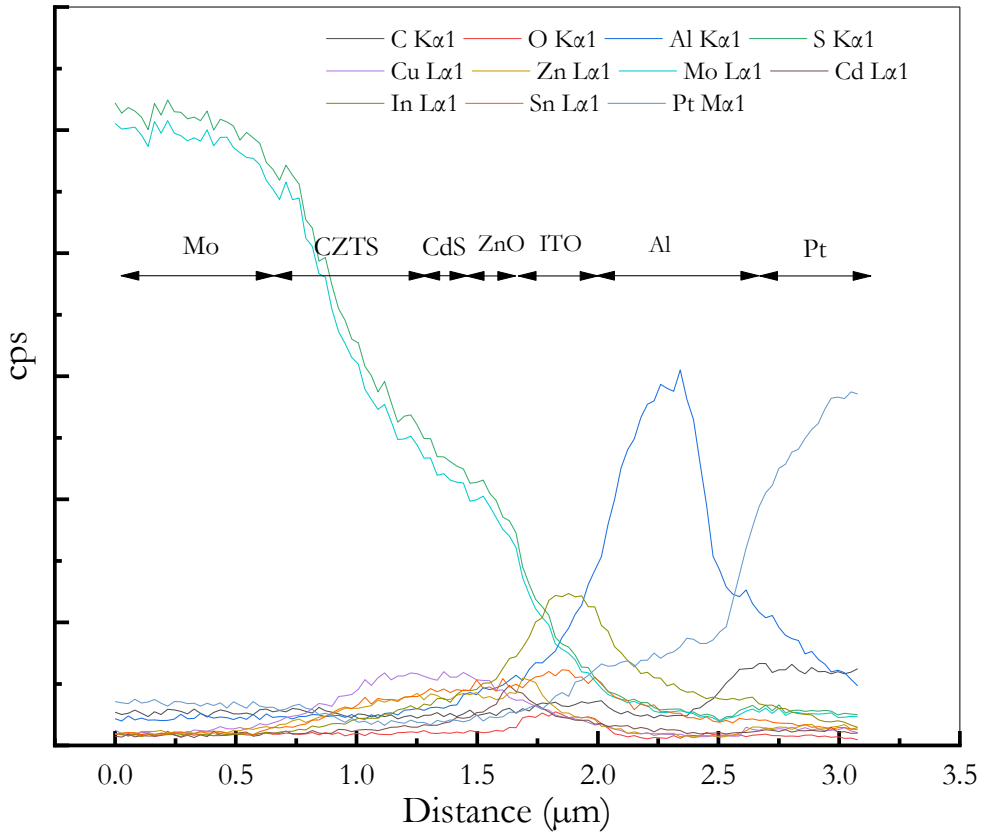

Figure 7.20 EDS line scan profiles on cross-section of CZTS thin film device (675 nm) site 1.

For site 2, it is clear that the CZTS and CdS layers were formed and then followed by complicated mixture layers. It can be seen a high intensity peak of Al_2O_3 layer above ZnO layer and the top of the film surface. As well as other elements as In, Zn, Sn, Cd, S, O and Al are in this Morphology as shown in Figure 7.21.

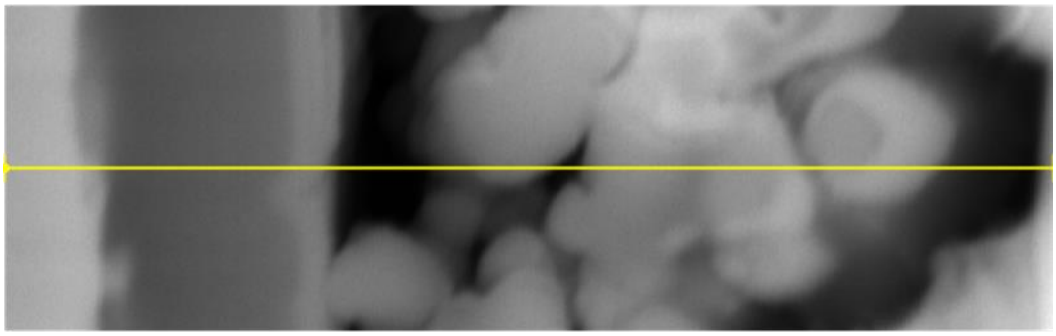

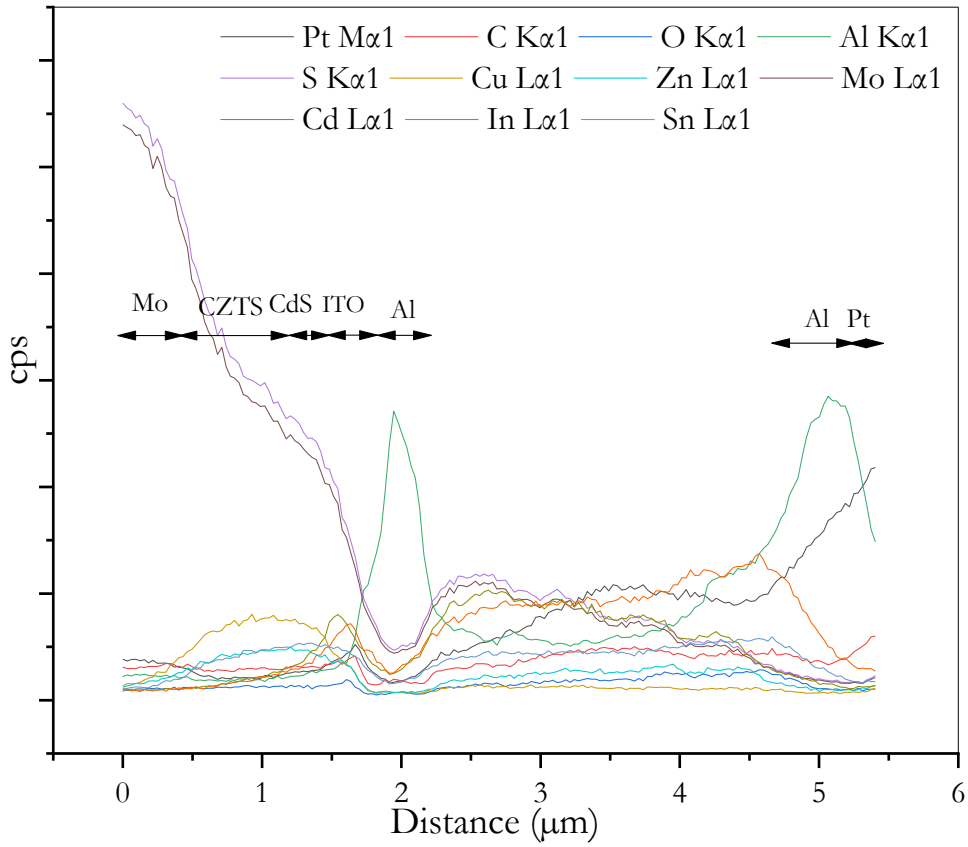

Figure 7.21 EDS line scan profiles on cross-section of CZTS thin film device (675 nm) site 2.

The cross-section EDS-SEM elemental profiles from line scan and elemental mapping images determined for site 3 are shown in Figure 7.22.

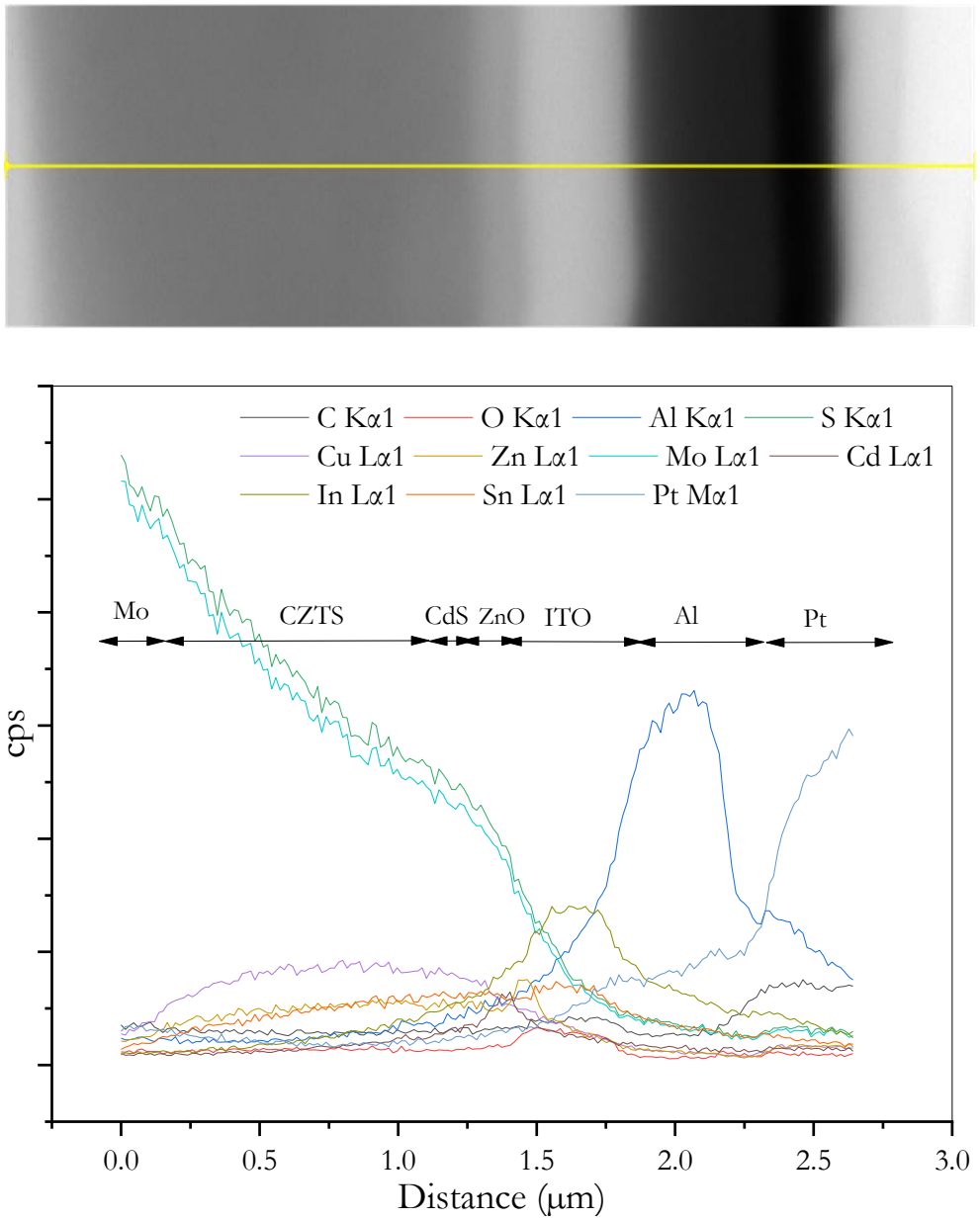

Figure 7.22 EDS line scan profiles on cross-section of CZTS thin film device (700 nm) site 3.

Due to the X-ray emission lines of Mo and S overlapping as the X-ray emission lines are 2.32 keV for the Mo Lα line and the S Kα line. So, this problem can be resolve by using wavelength dispersive spectroscopy (WDS) which has a higher resolution than EDS which can be resolve the energy peak of Mo and S elements [94]. On the other hand, the elements are distributed homogeneously across the cross-section region.

For electron backscatter diffraction (EBSD) profiles, the surface was milled and polished by using a Focused Ion Beam (FIB) at specific angle as shown in Figure 7.23. Band contrast images show the quality of EBSD pattern of the CZTS and grains as well. Also, Euler colours show the crystal orientation. The numbers 1 and 2 are different sites.

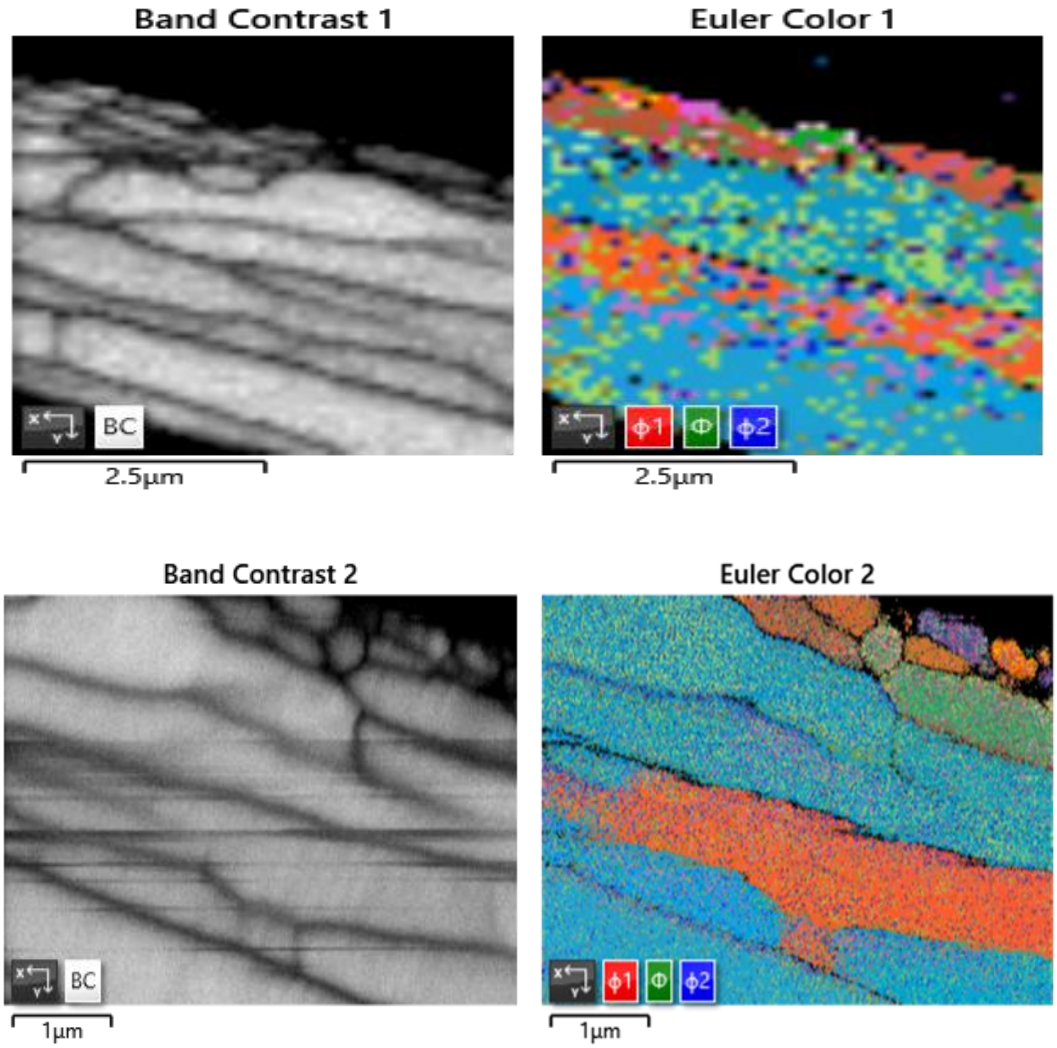

Figure 7.23 EBSD orientation map of a CZTS film at different site.

EBSD band contrast shows the quality of EBSD pattern and the grain size. The image confirms the presence of structure within the film profile. Bigger grains are observed to collect at the bottom of the layer with smaller grains moving to the top. The dark lines show variation in the band contrast image. The origin of the dark lines is not known but may correspond to layers from individual drops and subsequent drying process.

The Euler colour image shows the orientation angle of different grains. This indicates region of similar orientation throughout the cross section in a layer type configuration. This may correspond to layers in the deposition process. Although the orientation angle is known, the phase structure is not identified by EBSD. It is possible that the different orientation angle may indicate different structure (for example, kesterite or stannite) but this cannot be confirmed.

Compering images 1 and 2 at different location in the cross section shows that the layer type orientation behaviour varies with position along the cross section. It can be seen that there are distinct regions in the Euler colour diagrams at both location. This would indicate that there is a segregation of CZTS grains with the layer.

This is in contrast to other published EBSD results which show a completely random pattern in the orientation of grains. Further work is needed to elucidate the extent and origin of the layer type behaviour. Image 2 show smaller particles at the surface [95-98].

7.3: Conclusion

CZTS absorber layers were successfully synthesised and deposited onto Mo foil by spin coating technique. PL measurements showed many peaks in the range 1.3 eV to 2.0 eV. The peaks may correspond to CZTS in the range 1.3 eV to 1.6 eV, whereas other peaks may correspond to other secondary phases such as SnS, SnS_2, ZnS, CuS, Cu_2SnS_3 and Cu_2SnS_4. The temperature and laser excitation power dependence measurements were done to study the possible of existence defects in CZTS for different thickness of CZTS and CdS layers.

In CZTS, the PL activation energies E_1 and E_2 of the main peak were 227 and 4.44, 150 and 1.66, 132 and 1.00 and 219 and 1.50 meV for 4, 6, 8 and 10 drops respectively. So, as the values of activation energies in 4 and 10 drops are higher than in 6 and 8 drops that confirms the defects levels are deeper in 4 and 10 drops. So, the low activation energy values should be related to the presence of non-radiative defects that create energy levels close to the energy of the radiative states. The activation energy values at high temperature have higher activation energies. As a result of the excitation power increasing, the PL peak energy shows a slight blue shift at a rate of 0.88, 1.46, 1.53 and 1.32 meV/decade for CZTS thickness; 4, 6, 8, 10 drops at the main PL peak (high intensity) as well as for other peaks P1, P2 and P4, the range of energy shift are 3.00 and 0.20 meV/decade. The k values for P3 are 0.79, 0.85, 0.87 and 0.84 which are less than 1. As the k values are less than 1 these feature is as a result of defects related transitions. A model to describe our results is proposed from the fluctuating potential which leads to limitation of solar performance by decreasing the open circuit voltage as well as limiting of solar efficiency.

The devices current–voltage (IV) exhibits non-ohmic (nonlinear curve) behaviour. As a result of depositing zinc oxide layer, the CdS layer is damaged and disappeared from the image which may affect the CZTS layer. All images confirm that the successful deposition of CZTS layer with thickness in the range of 675 nm to 6 μm.

EDS-SEM measurements confirm the uniform distribution of elements of the cross section of CZTS devices at different sites and show there are some damage in some site of the film which explain no photocurrent collection in IV measurements. EBSD measurement shows the quality of EBSD pattern of the CZTS particles and displays the crystal orientation which needs further investigation to identify the crystal's phase structure.

7.4: References

1. Suryawanshi, M.P., et al., *CZTS based thin film solar cells: a status review.* Materials Technology, 2013. **28**(1-2): p. 98-109.

2. Wang, H.X., *Progress in Thin Film Solar Cells Based on Cu_2ZnSnS_4.* International Journal of Photoenergy, 2011: p. 10.

3. Ahmed, S., et al., *A High Efficiency Electrodeposited Cu_2ZnSnS_4 Solar Cell.* Advanced Energy Materials, 2012. **2**(2): p. 253-259.

4. Dhakal, T.P., et al., *Back Contact Band Offset Study of Mo-CZTS Based Solar Cell Structure by Using XPS/UPS Techniques*, in *2015 Ieee 42nd Photovoltaic Specialist Conference*. 2015, Ieee: New York.

5. Shin, B., N.A. Bojarczuk, and S. Guha, *On the kinetics of $MoSe_2$ interfacial layer formation in chalcogen-based thin film solar cells with a molybdenum back contact.* Applied Physics Letters, 2013. **102**(9): p. 4.

6. Dalapati, G.K., et al., *Impact of molybdenum out diffusion and interface quality on the performance of sputter grown CZTS based solar cells.* Scientific Reports, 2017. **7**: p. 12.

7. Park, J., et al., *The effect of thermal evaporated MoO_3 intermediate layer as primary back contact for kesterite Cu_2ZnSnS_4 solar cells.* Thin Solid Films, 2018. **648**: p. 39-45.

8. Liu, F.Y., et al., *Beyond 8% ultrathin kesterite Cu_2ZnSnS_4 solar cells by interface reaction route controlling and self-organized nanopattern at the back contact.* Npg Asia Materials, 2017. **9**: p. 8.

9. Vermang, B., et al., *Rear Surface Optimization of CZTS Solar Cells by Use of a Passivation Layer With Nanosized Point Openings.* Ieee Journal of Photovoltaics, 2016. **6**(1): p. 332-336.

10. Scragg, J.J., et al., *Effects of Back Contact Instability on Cu_2ZnSnS_4 Devices and Processes.* Chemistry of Materials, 2013. **25**(15): p. 3162-3171.

11. Liu, F.Y., et al., *Enhancing the Cu_2ZnSnS_4 solar cell efficiency by back contact modification: Inserting a thin TiB_2 intermediate layer at Cu_2ZnSnS_4/Mo interface.* Applied Physics Letters, 2014. **104**(5).

12. Gao, S., et al., *Interfaces of high-efficiency kesterite $Cu2ZnSnS(e)_4$ thin film solar cells.* Chinese Physics B, 2018. **27**(1): p. 018803.

13. Liu, X.L., et al., *Improving Cu_2ZnSnS_4 (CZTS) solar cell performance by an ultrathin ZnO intermediate layer between CZTS absorber and Mo back contact.* Physica Status Solidi-Rapid Research Letters, 2014. **8**(12): p. 966-970.

14. Zhou, F.Z., et al., *Improvement of J_{sc} in a Cu_2ZnSnS_4 Solar Cell by Using a Thin Carbon Intermediate Layer at the Cu_2ZnSnS_4/Mo Interface.* Acs Applied Materials & Interfaces, 2015. **7**(41): p. 22868-22873.

15. Cui, H., et al., *Improvement of Mo/Cu_2ZnSnS_4 interface for Cu_2ZnSnS_4 (CZTS) thin film solar cell application.* MRS Online Proceedings Library Archive, 2014. **1638**.

16. Cui, H.T., et al., *Boosting Cu_2ZnSnS_4 solar cells efficiency by a thin Ag intermediate layer between absorber and back contact.* Applied Physics Letters, 2014. **104**(4).

17. Guo, H.F., et al., *Dual function of ultrathin Ti intermediate layers in CZTS solar cells: Sulfur blocking and charge enhancement.* Solar Energy Materials and Solar Cells, 2018. **175**: p. 20-28.

18. Tong, Z.F., et al., *Modification of absorber quality and Mo-back contact by a thin Bi intermediate layer for kesterite Cu_2ZnSnS_4 solar cells.* Solar Energy Materials and Solar Cells, 2016. **144**: p. 537-543.

19. Olopade, M., O. Oyebola, and B. Adeleke, *Investigation of some materials as buffer layer in copper zinc tin sulphide (Cu_2ZnSnS_4) solar cells by SCAPS-1D.* Advances in Applied Science Research, 2012. **3**(6): p. 3396-3400.

20. Siebentritt, S., *Alternative buffers for chalcopyrite solar cells.* Solar Energy, 2004. **77**(6): p. 767-775.

21. Courel, M., J.A. Andrade-Arvizu, and O. Vigil-Galan, *Towards a CdS/Cu_2ZnSnS_4 solar cell efficiency improvement: A theoretical approach.* Applied Physics Letters, 2014. **105**(23): p. 4.

22. Yan, C., et al., *Band alignments of different buffer layers (CdS, Zn(O,S), and In_2S_3) on Cu_2ZnSnS_4.* Applied Physics Letters, 2014. **104**(17): p. 4.

23. Chen, H.J., et al., *Structural and photoelectron spectroscopic studies of band alignment at the Cu_2ZnSnS_4/CdS heterojunction with slight Ni doping in Cu_2ZnSnS_4.* Journal of Physics D-Applied Physics, 2016. **49**(33): p. 10.

24. Minemoto, T., et al., *Theoretical analysis of the effect of conduction band offset of window/CIS layers on performance of CIS solar cells using device simulation.* Solar Energy Materials and Solar Cells, 2001. **67**(1-4): p. 83-88.

25. Bao, W. and M. Ichimura, *First-Principles Study on Influences of Crystal Structure and Orientation on Band Offsets at the CdS/Cu_2ZnSnS_4 Interface.* International Journal of Photoenergy, 2012: p. 5.

26. Yin, L., et al., *Limitation factors for the performance of kesterite Cu_2ZnSnS_4 thin film solar cells studied by defect characterization.* Rsc Advances, 2015. **5**(50): p. 40369-40374.

27. Crovetto, A., et al., *Interface band gap narrowing behind open circuit voltage losses in Cu_2ZnSnS_4 solar cells.* Applied Physics Letters, 2017. **110**(8): p. 4.

28. Li, J., et al., *The band offset at CdS/Cu_2ZnSnS_4 heterojunction interface.* Electronic Materials Letters, 2012. **8**(4): p. 365-367.

29. Udaka, Y., et al., *Electronic structure of $Cu_2ZnSn(S_xSe_{1-x})_4$ surface and $CdS/Cu_2ZnSn(S_xSe_{1-x})_4$ interface*, in *Physica Status Solidi C: Current Topics in Solid State Physics, Vol 14 No 6*, M. Maiberg, W. Franzel, and R. Scheer, Editors. 2017, Wiley-V C H Verlag Gmbh: Weinheim.

30. Santoni, A., et al., *Valence band offset at the CdS/Cu_2ZnSnS_4 interface probed by x-ray photoelectron spectroscopy.* Journal of Physics D-Applied Physics, 2013. **46**(17): p. 5.

31. Bar, M., et al., *Cliff-like conduction band offset and KCN-induced recombination barrier enhancement at the CdS/Cu_2ZnSnS_4 thin-film solar cell heterojunction.* Applied Physics Letters, 2011. **99**(22): p. 3.

32. Haight, R., et al., *Band alignment at the $Cu_2ZnSn\ (S_xSe_{1-x})_4/CdS$ interface.* Applied Physics Letters, 2011. **98**(25): p. 253502.

33. Rondiya, S., et al., *CZTS/CdS: interface properties and band alignment study towards photovoltaic applications.* Journal of Materials Science-Materials in Electronics, 2018. **29**(5): p. 4201-4210.

34. Lin, L.Y., et al., *Band alignment at the In_2S_3/Cu_2ZnSnS_4 heterojunction interface investigated by X-ray photoemission spectroscopy.* Applied Physics a-Materials Science & Processing, 2014. **116**(4): p. 2173-2177.

35. Bao, W., Sachuronggui, and F.Y. Qiu, *Band offsets engineering at $Cd_xZn_{1-x}S/Cu_2ZnSnS_4$ heterointerface.* Chinese Physics B, 2016. **25**(12): p. 4.

36. Sun, K.W., et al., *Over 9% Efficient Kesterite Cu_2ZnSnS_4 Solar Cell Fabricated by Using $Zn_{1-x}Cd_xS$ Buffer Layer.* Advanced Energy Materials, 2016. **6**(12): p. 6.

37. Htay, M.T., et al., *A Cadmium-Free Cu_2ZnSnS_4/ZnO Hetrojunction Solar Cell Prepared by Practicable Processes.* Japanese Journal of Applied Physics, 2011. **50**(3): p. 4.

38. Yang, G., et al., *Band alignments at interface of Cu_2ZnSnS_4/ZnO heterojunction: An X-ray photoelectron spectroscopy and first-principles study.* Journal of Alloys and Compounds, 2015. **628**: p. 293-297.

39. Haque, F., et al., *Prospects of Zinc Sulphide as an Alternative Buffer Layer for CZTS Solar Cells from Numerical Analysis.* 2014 International Conference on Electrical and Computer Engineering. 2014, New York: Ieee. 504-507.

40. Kim, J., et al., *Optimization of sputtered ZnS buffer for Cu_2ZnSnS_4 thin film solar cells.* Thin Solid Films, 2014. **566**: p. 88-92.

41. Boutebakh, F.Z., et al., *Electrical properties and back contact study of CZTS/ZnS heterojunction.* Optik, 2017. **144**: p. 180-190.

42. Ericson, T., et al., *Zn(O, S) Buffer Layers and Thickness Variations of CdS Buffer for Cu_2ZnSnS_4 Solar Cells.* Ieee Journal of Photovoltaics, 2014. **4**(1): p. 465-469.

43. Lin, L.Y., et al., *Analysis of Effect of Zn(O,S) Buffer Layer Properties on CZTS Solar Cell Performance Using AMPS.* Chinese Physics Letters, 2016. **33**(10): p. 4.

44. Jani, M., D. Raval, and A. Ray, *Investigating the Band Alignment of Zn(O, S) with Kesterite Cu_2ZnSnS_4 Material for Photovoltaic Application.* Journal of Nano- and Electronic Physics, 2017. **9**(3): p. 4.

45. Platzer-Bjorkman, C., et al., *Reduced interface recombination in Cu_2ZnSnS_4 solar cells with atomic layer deposition $Zn_{1-x}Sn_xO_y$ buffer layers.* Applied Physics Letters, 2015. **107**(24): p. 4.

46. Ghosh, M. and A.K. Raychaudhuri, *Structural and optical properties of $Zn_{1-x}Mg_xO$ nanocrystals obtained by low temperature method.* Journal of Applied Physics, 2006. **100**(3): p. 7.

47. Bahfir, A., et al., *Study of novel ZnMgO buffer layer in CZTS solar cells.*

48. Bahfir, A., M. Boumaour, and M. Kechouane, *Prospects of potential ZnMgO front layer in CZTS solar cells.* Optik, 2018. **169**: p. 196-202.

49. Bahfir, A., et al., *Study of novel ZnMgO buffer layer in CZTS solar cells.* 2015.

50. Sun, H., et al., *Efficiency Enhancement of Kesterite Cu_2ZnSnS_4 Solar Cells via Solution-Processed Ultrathin Tin Oxide Intermediate Layer at Absorber/Buffer Interface.* ACS Applied Energy Materials, 2017. **1**(1): p. 154-160.

51. Gueddim, A., et al., *Characteristics and optimization of ZnO/CdS/CZTS photovoltaic solar cell.* Applied Physics a-Materials Science & Processing, 2018. **124**(2): p. 7.

52. Bundesmann, C., R. Schmidt-Grund, and M. Schubert, *Optical Properties of ZnO and Related Compounds*, in *Transparent Conductive Zinc Oxide*, K. Ellmer, A. Klein, and B. Rech, Editors. 2008, Springer-Verlag Berlin: Berlin. p. 79-124.

53. Dong, Z.Y., et al., *An experimental and first-principles study on band alignments at interfaces of Cu_2ZnSnS_4/CdS/ZnO heterojunctions.* Journal of Physics D-Applied Physics, 2014. **47**(7): p. 6.

54. Klein, A., et al., *Transparent Conducting Oxides for Photovoltaics: Manipulation of Fermi Level, Work Function and Energy Band Alignment.* Materials, 2010. **3**(11): p. 4892-4914.

55. Krawczak, E. and S. Gulkowski, *Electrical properties of aluminum contacts deposited by DC sputtering method for photovoltaic applications*, in *International Conference Energy, Environment and Material Systems*, M. Wzorek, G. Krolczyk, and A. Krol, Editors. 2017, E D P Sciences: Cedex A.

56. Aizawa, T., et al., *Investigation of ZnO:Al window layer of Cu_2ZnSnS_4 thin film solar cells prepared by non-vacuum processing*, in *Physica Status Solidi C: Current Topics in Solid State Physics, Vol 10, No 7-8*, M. Cavalleri, et al., Editors. 2013, Wiley-V C H Verlag Gmbh: Weinheim. p. 1050-1054.

57. Suman, R., et al., *Fabrication and characterization of SLG/Mo/CZTS/CdS/i-ZnO/Al:ZnO/Al thin film solar cell device.* Journal of Ovonic Research, 2015. **11**(5): p. 243-248.

58. Nikita, K.N., et al., *Exploring the Opportunity of Using Graphene as the Transparent Conducting Layer in CZTS-based Thin Film Solar Cells*, in *2016 3rd International Conference on Electrical Engineering and Information & Communication Technology*. 2016, Ieee: New York.

59. Park, J., et al., *Hybrid Ag Nanowire-ITO as Transparent Conductive Electrode for Pure Sulfide Kesterite Cu_2ZnSnS_4 Solar Cells.* Journal of Physical Chemistry C, 2017. **121**(38): p. 20597-20604.

60. Garcia-Valenzuela, J.A., J. Andreu, and J. Bertomeu, *Effect of the base pressure achieved prior deposition on the main properties of ZnO:Al films obtained by DC magnetron sputtering at room temperature for electrical contact use.* Journal of Vacuum Science & Technology A, 2017. **35**(2): p. 11.

61. Womack, G., et al., *Performance and durability of broadband antireflection coatings for thin film CdTe solar cells.* Journal of Vacuum Science & Technology A, 2017. **35**(2): p. 11.

62. Patel, M., et al., *A Study of the Applicability of ZnO Thin-Films as Anti-Reflection Coating on Cu_2ZnSnS_4 Thin-Films Solar Cell*, in *Indian Vacuum Society Symposium on Thin Films: Science & Technology*, N.K. Sahoo, D. Udupa, and D. Bhattacharyya, Editors. 2012, Amer Inst Physics: Melville. p. 97-99.

63. Ge, Z.Y., et al., *Enhanced omni-directional performance of copper zinc tin sulfide thin film solar cell by gradient index coating.* Applied Physics Letters, 2014. **104**(10): p. 4.

64. Wang, K., et al., *Thermally evaporated Cu_2ZnSnS_4 solar cells.* Applied Physics Letters, 2010. **97**(14): p. 3.

65. Feng, Y., et al., *Searching for a fabrication route of efficient Cu_2ZnSnS_4 solar cells by post-sulfuration of co-sputtered Sn-enriched precursors.* Journal of Materials Chemistry C, 2015. **3**(37): p. 9650-9656.

66. Boutebakh, F.Z., et al., *Thermal sulfurization effect on sprayed CZTS thin filmsproperties and CZTS/CdS solar cells performances.* Materials Research Express, 2018. **5**(1): p. 11.

67. Biccari, F., et al., *Fabrication of Cu_2ZnSnS_4 solar cells by sulfurization of evaporated precursors*, in *European Materials Research Society Conference Symposium: Advanced Inorganic Materials and Concepts for Photovoltaics*, G. Conibeer, et al., Editors. 2011, Elsevier Science Bv: Amsterdam.

68. Muhunthan, N., et al., *Interfacial properties of CZTS thin film solar cell.* Journal of Solar Energy, 2014. **2014**.

69. Jheng, B.T., P.T. Liu, and M.C. Wu, *A promising sputtering route for dense Cu_2ZnSnS_4 absorber films and their photovoltaic performance.* Solar Energy Materials and Solar Cells, 2014. **128**: p. 275-282.

70. Vigil-Galan, O., et al., *Toward a high Cu_2ZnSnS_4 solar cell efficiency processed by spray pyrolysis method.* Journal of Renewable and Sustainable Energy, 2013. **5**(5): p. 14.

71. Murali, D.S., et al., *Synthesis of Cu_2O from CuO thin films: Optical and electrical properties.* Aip Advances, 2015. **5**(4): p. 5.

72. Dobrozhan, O.A., et al., *Structural Properties of Cu_2ZnSnS_4 Thin Films Produced by Nanoink Spraying Process*, in *Proceedings of the 2017 Ieee 7th International Conference Nanomaterials: Application & Properties*, A.D. Pogrebnjak, et al., Editors. 2017, Ieee: New York.

73. Bosson, C.J., et al., *Polymorphism in Cu_2ZnSnS_4 and New Off-Stoichiometric Crystal Structure Types.* Chemistry of Materials, 2017. **29**(22): p. 9829-9839.

74. Chaki, S.H., J.P. Tailor, and M.P. Deshpande, *Covellite CuS - Single crystal growth by chemical vapour transport (CVT) technique and characterization.* Materials Science in Semiconductor Processing, 2014. **27**: p. 577-585.

75. Strater, H., et al., *Detailed photoluminescence studies of thin film Cu_2S for determination of quasi-Fermi level splitting and defect levels.* Journal of Applied Physics, 2013. **114**(23).

76. Tanaka, K., T. Shinji, and H. Uchiki, *Photoluminescence from Cu_2ZnSnS_4 thin films with different compositions fabricated by a sputtering-sulfurization method.* Solar Energy Materials and Solar Cells, 2014. **126**: p. 143-148.

77. Kurbatov, D.I., et al., *Luminescent and optical characteristics of zinc sulfide thin films produced by close-spaced vacuum sublimation.* 2010.

78. Saroja, A.M., et al., *Substrate temperature influence on the optical and electrical properties of spray deposited Sn_2S_3 thin films.* Optik, 2017. **130**: p. 245-254.

79. Tipcompor, N., S. Thongtem, and T. Thongtem, *Effect of microwave radiation on the morphology of tetragonal Cu_3SnS_4 synthesized by refluxing method.* Superlattices and Microstructures, 2015. **85**: p. 488-496.

80. Halliday, D.P., et al., *Luminescence of Cu_2ZnSnS_4 polycrystals described by the fluctuating potential model.* Journal of Applied Physics, 2013. **113**(22): p. 10.

81. Park, S.N., et al., *Solution-processed Cu_2ZnSnS_4 absorbers prepared by appropriate inclusion and removal of thiourea for thin film solar cells.* Rsc Advances, 2014. **4**(18): p. 9118-9125.

82. Yang, K.J., et al., *Effects of the compositional ratio distribution with sulfurization temperatures in the absorber layer on the defect and surface electrical characteristics of Cu_2ZnSnS_4 solar cells.* Progress in Photovoltaics, 2015. **23**(12): p. 1771-1784.

83. Chen, S., et al., *Classification of Lattice Defects in the Kesterite Cu_2ZnSnS_4 and Cu2ZnSnSe$_4$ Earth-Abundant Solar Cell Absorbers.* Advanced Materials, 2013. **25**(11): p. 1522-1539.

84. Chen, S.Y., et al., *Abundance of Cu-Zn + Sn-Zn and 2Cu(Zn) + Sn-Zn defect clusters in kesterite solar cells.* Applied Physics Letters, 2012. **101**(22): p. 4.

85. Yang, K.J., et al., *Comparison of chalcopyrite and kesterite thin-film solar cells.* Journal of Industrial and Engineering Chemistry, 2017. **45**: p. 78-84.

86. Ghediya, P.R. and T.K. Chaudhuri, *Temperature dependence electrical conduction of solution-processed CZTS films in dark and under light*, in *International Conference on Advances in Materials and Manufacturing Applications*, C.S.P. Rao and S. Basavarajappa, Editors. 2016, Iop Publishing Ltd: Bristol.

87. Krustok, J., et al., *Photoluminescence study of deep donor- deep acceptor pairs in Cu_2ZnSnS_4.* Materials Science in Semiconductor Processing, 2018. **80**: p. 52-55.

88. Chen, S.Y., et al., *Intrinsic point defects and complexes in the quaternary kesterite semiconductor Cu_2ZnSnS_4.* Physical Review B, 2010. **81**(24).

89. Han, D., et al., *Deep electron traps and origin of p-type conductivity in the earth-abundant solar-cell material Cu_2ZnSnS_4.* Physical Review B, 2013. **87**(15).

90. Van Puyvelde, L., et al., *Photoluminescence investigation of Cu_2ZnSnS_4 thin film solar cells.* Thin Solid Films, 2015. **582**: p. 146-150.

91. Grossberg, M., et al., *Microphotoluminescence study of Cu_2ZnSnS_4 polycrystals.* Journal of Photonics for Energy, 2013. **3**.

92. Tanaka, K., et al., *Donor-acceptor pair recombination luminescence from Cu_2ZnSnS_4 bulk single crystals.* Physica Status Solidi a-Applications and Materials Science, 2006. **203**(11): p. 2891-2896.

93. Teixeira, J.P., et al., *Radiative transitions in highly doped and compensated chalcopyrites and kesterites: The case of Cu_2ZnSnS_4.* Physical Review B, 2014. **90**(23).

94. Fernandes, P.A., P.M.P. Salomé, and A.F.d. Cunha, *Study of polycrystalline Cu_2ZnSnS_4 films by Raman scattering.* Journal of Alloys and Compounds, 2011. **509**(28): p. 7600-7606.

95. Rozeveld, S., et al., *Measurement of Grain Boundary Properties in Cu (ln, Ga) Se_2 Thin Films.* Microscopy Today, 2018. **26**(3): p. 32-39.

96. Moutinho, H.R., et al., *Epitaxial Growth of CZTS on Si Substrates Investigated with Electron Backscatter Diffraction*. 2014 Ieee 40th Photovoltaic Specialist Conference. 2014. 2379-2383.

97. Oo, W.M.H., et al., *Grain Size and Texture of Cu_2ZnSnS_4 Thin Films Synthesized by Cosputtering Binary Sulfides and Annealing: Effects of Processing Conditions and Sodium.* Journal of Electronic Materials, 2011. **40**(11): p. 2214-2221.

98. Kato, T., S. Muraoka, and H. Sugimoto, *Cross-sectional study on Cu_2ZnSnS_4 thin-film solar cells.* Small, 2011. **111**(001): p. 101.

Chapter 8: Conclusion and future work

The quaternary compound Cu_2ZnSnS_4 (CZTS) has potential properties for low cost thin film solar cells. It is composed of abundant elements as well non-toxic material, with desirable properties for thin film photovoltaic (PV) applications such as high absorption coefficient close to 10^{-4} cm^{-1} and band gap close to 1.5 eV. CZTS has been successfully fabricated by the non-vacuum hot injection method with a pure sulphur source. High concentration of CZTS nanoparticle inks were deposited onto clean glass by spin coating techniques with high speed (2500 rpm) for 10 second to study the CZTS nanoparticle ink quality.

Studying the influence of fabrication condition such temperature and time on structure and optical properties revealed that the conditions of temperature (185, 205,225, 245 and 265 ^oC) and time (0.5, 1.0, 1.5, and 2.0 h) have a significant effect on crystal structure, composition, morphology and band gap. For instance, the CZTS nanoparticles have a mixed structure between kesterite and wurtzite observed in XRD measurents. The average crystallite size of CZTS synthesised at 185, 205, 225, 245 and 265 ^oC were about 13, 28, 37, 48 and 49 nm respectively. It was also found that the size of particles increases with increasing reaction time at 37.1, 35.1, 41.2 and 45.8 nm for 0.5, 1.0, 1.5 and 2.0 h at 225 ^oC. However, Raman measurements confirmed that the main peaks for different fabrication conditions of CZTS were at 337 cm^{-1} which correspond to the A1 mode of single phase CZTS. Other Raman peaks at 320 cm^{-1} were assigned to Cu_3SnS_4 in all samples except that synthesised at 1 h where the main peak become narrower and sharper than at other fabrication conditions which indicated an improvement of the crystallinity. Moreover, the SEM and TEM measurements confirm that increasing the fabrication conditions leads to improvements in the crysallinty. EDX confirmed the compositional ratios which were Cu/ (Zn + Sn) = 1.14, 1.11, 0.95, 0.94 and 0.96, and Zn/Sn = 0.90, 1.12, 1.49, 1.48 and 1.54 for 185, 205, 225, 245 and 265 °C respectively. The compositional ratios were also found to be Cu/ (Zn+Sn) = 0.95, 0.88, 0.83 and 0.72, and Zn/Sn = 1.49, 1.24, 1.41 and 1.37at 0.5, 1.0, 1.5 and 2.0 h respectively at a temperature of 225 ^oC. Lastly, the band gaps of all samples were observed in the range between 1.5 and 1.9 eV. From the results above it is determined that the optimum condition suitable for synthesising a high quilty CZTS absorber layer is at

225 ^{o}C for 1.0 h. this gives an average nanoparticle size of 35 nm with an energy band gap close to 1.5 eV and a Cu-poor and Zn-rich composition.

Studying the influence of different copper and zinc compositions also revealed a strong impact of these compositions on CZTS properties. X-ray diffraction and Raman spectroscopy show the majority of the CZTS may be in a kesterite, disordered kesterite or stannite phases. XRD data also confirmed the presence of the mixed kesterite and wurtzite CZTS structure in Cu-rich (C1) and stoichiometry (C2) samples. Raman results are inconclusive in determining if the CZTS has any significant kesterite or stannite structures due to broad Raman peaks within the spectra. The strong peak at 335 cm^{-1} is related to the presence of local structural inhomogeneity within the disordered kesterite or stannite phases. There is no evidence for $Cu_{2-x}S$ at 475 cm^{-1} for all samples except C1. Transmission electron microscopy showed the nanoparticles were between 44.9 nm and 52.5 nm in diameter, the maximum occurring in sample S3. UV-vis spectroscopy showed the band gap of the films increasing with a decreasing copper concentration. It was also found that increasing zinc concentrations decrease the resulting energy band gaps in the range between 1.38 and 1.55 eV. The change in energy band gaps is related to change of concentration of Cu and Zn. It is concluded that the energy band gap depends on the Cu and Zn concentrations. Overall, the CZTS nanoparticle ink showed promise for use as the absorber layer in PV devices due to the suitable band gap and simple deposition and nanoparticle size. However, as Raman spectroscopy data show, there are a significant amount of secondary phases present and further effort needs to be made for these to be reduced.

Investigating the influence of the annealing parameters including temperature, time, ramping rate and atmosphere on CZTS thin films' structure and optical properties were achieved. The XRD in all samples showed the main peaks are 28.5, 33.2, 47.5 and 56.4^{o} which correspond to kesterite structures. Raman measurements also confirmed the presence of single phase CZTS thin films at 338 cm^{-1} with other small peak at 335 cm^{-1} in some annealing conditions. Some films also showed some secondary phases. Also, the intensities of peaks of XRD and Raman increased and became sharper with increasing the annealing conditions (temperature, time and ramping rate) as well as particle sizes which indicate improvements to the crystallinity. SEM was used to study the surface of CZTS films and showed uniformly distributed films. EDX study indicated the chemical

composition ratio of Cu/Zn+Sn, Zn/Sn, Cu/Sn and S/Metal was affected by the annealing parameters and all ratios were greater than the initial compositions due to partial Zn and Sn losses during the preparation and annealing process. The crystallinity, structure and chemical composition of CZTS thin films increased and improved under H_2S+N_2 atmosphere which demonstrated that annealing at 500 ^oC for 1 h with 10 ^oC/min under H_2S (20 %)+N_2 (80 %) atmosphere is a suitable condition for CZTS thin film formation for use in solar cell devices.

The thermal activation energies of defects in all samples were estimated from Arrhenius curves for different CZTS. For instance, the activation energies E_1 and E_2 of P3 were 227 and 4.44, 150 and 1.66, 132 and 1.00 and 219 and 1.50 meV for films of increasing thickness with4, 6, 8 and 10 drops respectively of CZTS ink. Higher activation energies confirm the defects levels are deep level states. The low activation energy values should be related to the presence of non-radiative defects that create energy levels close to the energy of the radiative states. The activation energy values at high temperature have higher activation energies. As a result of the excitation power being increased, the PL peak energy suffers a slight blue shift at the average rate of 1.32 meV/decade. The k values for P3 are 0.79, 0.85, 0.87 and 0.84 which are less than 1 and in the ranges 0.85 and 0.92 $\pm$0.02 for all samples. So, due to the k values being less than 1 these features are the result of defect related transitions. A model to describe our results is expected from the fluctuating potential which leads to limitation of solar device performance by decreasing the open circuit voltage as well as limiting solar device efficiency.

The device current–voltage (IV) in all devices exhibits non-ohmic (nonlinear curve) behaviour. As a result of depositing a zinc oxide layer, the CdS layer was damaged and disappeared from the cross section image which may affect the accurate determination thickness for the CZTS layer. All images confirm the successful deposition of CZTS layer with thickness in the range between 600 nm and 6 μm.

EDS-SEM measurements confirmed uniform distribution of all elements and clearly show all layers of CZTS devices. Also, the result confirms overlapping of Mo and S lines which requires using WDS to distinguish between them. EBSD measurement shows the crystal quality of CZTS absorber layer and phase orientation. This measurement requires further investigations to clearly identify the crystal structure.

This work has identified many issues that need further investigations and here some suggestions for future work are made. Different preparation chemical precursors and solvents as well as optimising deposition techniques including the drying process to get uniform films with high quality. Controlling the composition of the final CZTS device requires further development.

Controlling interface reactions between the layers of Mo/CZTS and CZTS/CdS requires further investigation to study their properties and their effects on CZTS device performance. Studying the passivation of secondary phases and diffusion of elements between layers using ultra-thin intermediate layers between the layers Mo/CZTS/CdS and their effects on CZTS device performance would also improve device performance.

Lastly, EBSD measurements require further study as mentioned in chapter 7 to identify the crystal structures and orientation phase by studying the films with and without annealing treatment as well as estimating the grain size and grain boundary. Finally, WDS can be used to identify the accurate composition of Cu and Zn.

This thesis has studied the complex chemical synthesis process used to produce CZTS nanoparticle inks and their subsequent deposition as thin films suitable for use in PV devices. The work has demonstrated that unable PV devices can be fabricated and has confirmed a range of parameters to optimise this process. Suggestions for further work should enable the production of high efficiency PV devices using this process.